

WETTING OF NON-RIGID SURFACES

NICASIO REAMONDO GERALDI

A thesis submitted in partial fulfilment of the requirements of
Nottingham Trent University for the degree of Doctor of Philosophy

May 13, 2015

This work is the intellectual property of the author. You may copy up to 5% of this work for private study, or personal, non-commercial research. Any re-use of the information contained within this document should be fully referenced, quoting the author, title, university, degree level and pagination. Queries or requests for any other use, or if a more substantial copy is required, should be directed to the owner of the Intellectual Property Rights.

Abstract

In the world of anti-wetting surfaces, many superhydrophobic substrates comprise rigid structures on rigid substrates. The development of a thin flexible substrate would allow new avenues to be explored to fully take advantage of the non-wetting properties of superhydrophobicity. This thesis presents a novel production method and subsequent analysis of thin, conformable, superhydrophobic films based on the embedding of carbon nano-particles (CNPs) into the surface of polydimethylsiloxane (PDMS) substrates. Firstly experiments were performed to determine the effects of surface roughness on the capillary origami process. It was found that the droplet wrapping process could be controlled with the appropriate choice of liquid. Using a wetting liquid would see an enhanced wrapping state whereas use of a dewetting liquid would see a complete suppression of the wrapping process. The second set of experiments concentrated on determining whether or not it is possible to reduce the drag force experienced on cylinders in a laminar flow situation. By comparing an uncoated cylinder to a CNP PDMS coated cylinder of equivalent diameter, it was determined that it is possible to reduce the drag by a maximum of 28%. The last tests were to determine the potential of the surface as a snail-repellent material. A set of experiments, designed to compare the repellent and adhesive properties of the surface were performed. It was seen that these surfaces show promise as a snail repellent surface. This surface is in keeping with the hypothesis of Shirtcliffe *et al.* [1] which states an effective snail repellent surface shows anti-adhesive properties and maintains a high receding contact angle in the presence of an anionic surfactant.

Acknowledgements

I would like to thank my Director of Studies, Dr. Michael Newton, and supervisors, Dr. Rob Morris and Prof. Glen McHale for their support and guidance through this challenging project and for always cracking the whip. Their knowledge and experience has been invaluable. I would also like to thank Dr. Fouzia Ouali for her contribution to the project. I also owe many thanks to my fellow Ph.D student, Joseph Brennan, for our valuable discussions in the lab.

I would like to show my gratitude to the technical staff, Dr. Stephen Elliott, David Parker and Gordon Arnott, for their knowledge and valuable experience. I am also grateful to Dr. Demothenes Koutsogeorgis, Dr. Nikolaos Kalfagiannis and the staff from Bruker for their help in collecting the AFM images.

I would like to thank all the members of staff and academics who I have had the pleasure to work beside at Nottingham Trent University. It has been a pleasure. Mention must also go to my colleagues in the office. Without them, my work life would not have been as enjoyable.

I owe my family and friends many thanks for their support throughout this period in my life. Without them, this would not have been possible.

Lastly, I am very grateful to Nottingham Trent University for the provision of a Ph.D. studentship.

Contents

Copyright Statement	i
Abstract	ii
Acknowledgements	iii
Abbreviations	1
Nomenclature	2
List of Figures	4
List of Tables	10
1 Background	11
1.1 Surface Tension	11
1.2 Capillary Length	12
1.3 Laplace Pressure	13
1.4 Spreading Parameter	13
1.5 Young’s Contact Angle	14
1.6 Contact Angle Hysteresis	15
1.7 Hydrophilicity and Hydrophobicity	17
1.8 Surface Free Energy Approach	19
1.9 Roughness	20
1.9.1 Wenzel Model	21
1.9.2 Cassie-Baxter Model	24
1.9.3 Cassie-Baxter or Wenzel?	26
1.10 Methods for Changing the Hydrophobicity	28
1.11 Improving the Hydrophobicity of PDMS	34

2	Methods	37
2.1	Development of the Superhydrophobic Thin Films	37
2.1.1	Trial Methods	37
2.1.2	Development of CNP Coated PDMS	45
2.1.3	Initial Production Method for Superhydrophobic PDMS	47
2.2	Suggested Work and Preliminary Tests	50
3	Capillary Origami	55
3.1	Background of Self-Assembly and Capillary Origami	55
3.2	Capillary Origami with a Novel Surface	61
3.2.1	Initial Experiments	61
3.2.2	Replication of Previous Work and Testing of Uncoated Substrates	62
3.2.3	Superhydrophobic Modification of the Wrapping Experiments	63
3.2.4	Liquid Determination	64
3.2.5	Determination of Young's Modulus for CNP Coated Surfaces	66
3.3	Results	68
3.3.1	Determination of the Young's Modulus	68
3.3.2	Replication of Uncoated PDMS Tests	74
3.3.3	Characterisation of the Carbon Nano-particle PDMS Films	76
3.3.4	Capillary Origami of Superhydrophobic Triangular Substrates	81
3.4	Discussion	84
3.5	Conclusions	87
3.6	Suggested work	88
4	Superhydrophobic Drag Reduction	90
4.1	Background	90
4.2	Drag Reduction Using CNP Coated PDMS	93
4.2.1	Flow Chamber Setup	93
4.2.2	Testing of Small Diameter Cylinders	94
4.2.3	Modification of the Soot Coating Process	94
4.2.4	Construction and Testing of Larger Diameter Cylinders	99
4.3	Results	101
4.3.1	Testing of Superhydrophobic Cylinders	101
4.3.2	Calculation of Drag Coefficient	102

4.4	Discussion	109
4.5	Conclusions	115
4.6	Suggested Work	115
5	Snail Repellent Surfaces	117
5.1	A Background to Snail Repellency	117
5.2	Investigation of CNP Coated PDMS as a Snail Deterrent Surface . .	122
5.2.1	Snail Type	122
5.2.2	Pot Comparison Tests	123
5.2.3	Maze Tests	124
5.2.4	Spin Tests	126
5.2.5	Fluorinert Modification of the Sooted Surfaces	128
5.2.6	Effect of Surface Tension on the Contact Angle for Different Surfaces	129
5.3	Results	130
5.3.1	Pot Comparison Tests	130
5.3.2	Maze Tests	137
5.3.3	Spin Tests	143
5.3.4	Surface Tension Tests	147
5.4	Discussion	149
5.5	Conclusions	151
5.6	Suggested Work	151
6	Summary	153
	References	155
	Published Work	173

Abbreviations

- AFM** - Atomic Force Microscopy
- CNP** - Carbon Nano-Particle
- CVD** - Chemical Vapour Deposition
- DRIE** - Deep Reactive Ion Etching
- ECA** - Ethyl Cyanoacrylate
- IPA** - Isopropanol (2-propanol)
- LBL** - Layer By Layer deposition
- LDA** - Laser Doppler Anemometer
- MEMS** - Microelectromechanical Systems
- PPI** - Points Per Inch
- PDMS** - Polydimethylsiloxane
- PECA** - Polyethylcyanoacrylate
- PTFE** - Polytetrafluoroethylene
- QCM** - Quartz Crystal Microbalance
- RPM** - Revolutions Per Minute
- SDS** - Sodium Dodecyl Sulphate
- SEM** - Scanning Electron Microscopy

Nomenclature

γ - surface tension

γ_{SV} - surface tension of the surface/vapour interface

γ_{SL} - surface tension of the surface/liquid interface

γ_{LV} - surface tension of the liquid/vapour interface

κ_B - bending rigidity

η - viscosity

ν - Poisson's space ratio

θ - angle

θ_A - advancing contact angle

θ_{CB} - Cassie-Baxter contact angle

θ_e - Young's contact angle

θ_R - receding contact angle

θ_T - contact angle depending on the wetting regime

θ_W - Wenzel contact angle

ρ - density

A - area

C - curvature

C_D - drag coefficient

d - diameter

E - Young's modulus

f_s - surface fraction

F - surface free energy

g - gravitational acceleration

h - thickness

I - moment of inertia
 L - Length
 L_C - capillary length
 L_{crit} - critical wrapping length
 L_{EC} - elastocapillary length
 L_S - slip length
 m - mass
 P - pressure
 r - roughness factor
 R - radius of curvature
 Re - Reynolds number
 R_C - critical droplet radius
 RPM - revolutions per minute
 S - spreading parameter
 U - velocity
 U_1 - free-stream velocity
 V_S - slip velocity
 w - width
 y - horizontal displacement
 y_{max} - maximum deflection

List of Figures

1.1	Illustration showing the unbalanced forces on a surface molecule compared to a molecule in the bulk of the liquid. The arrows indicate the attractive forces between the molecules.	12
1.2	Illustration showing how a droplet is deformed under the force of gravity.	12
1.3	Illustration of the outcomes of a positive or negative spreading parameter. If positive the liquid fully spreads but if negative, the liquid only partially spreads forming a spherical cap.	14
1.4	The contact angle of a liquid droplet is the angle, θ , made by the liquid/vapour interface at the contact point with the solid surface. . .	14
1.5	Illustration of the advancing (A) and receding (B) contact angles to determine the hysteresis.	16
1.6	Illustrations of the partial wetting states.	17
1.7	Illustration showing the change in area in the surface free energy approach.	19
1.8	Illustrations of the Wenzel and Cassie-Baxter models.	21
1.9	Illustration of the surface roughness. The lines represent the the 2D slice of a surface which enables the roughness to be determined in the direction of the cut.	21
1.10	Illustration of the Wenzel wetting state where the liquid infiltrates between surface features.	22
1.11	Illustration of the Cassie-Baxter wetting state where the liquid sits on top of the surface features.	24
1.12	Illustration of the change in apparent contact angle as the orientation of the surface changes.	26

2.1	Image of a droplet of water on a PDMS surface that has been treated with Granger's.	39
2.2	Images of water droplets on PDMS (red), PDMS cast on sandpaper (blue) and Granger's coated PDMS cast on sandpaper (green).	40
2.3	Graph of the contact angles for various grades of sandpaper for the PDMS, PDMS cast on sandpaper and Granger's coated PDMS cast on sandpaper.	40
2.4	Images of laser patterned acrylic plates.	41
2.5	Image of a droplet of water on PDMS cast on patterned plate.	41
2.6	Images of laser patterned PDMS surfaces showing the concave features. The largest features (far left) are approximately $100\mu m$ wide.	42
2.7	Images of a Loctite ECA Structure. There are 3 layers of ridges. The top layer is composed of the largest ridges that snake their way across the surface (top left). The middle layer is composed of a network of smaller ridges (top right). At the bottom is a layer of smaller wrinkles that cover the entire surface (bottom).	45
2.8	Image of an advancing droplet of water on an ECA surface.	46
2.9	Images showing the advancing (left) and receding (right) contact angle on an ethanol soot PDMS surface.	47
2.10	Images comparing the Static (left),the advancing (middle) and receding (right) contact angles for uncoated and CNP coated PDMS.	49
2.11	SEM images of the files and the substrates cast on the different surfaces.	53
3.1	Formation of a cube solely through the forces generated by a droplet of water.	61
3.2	Effect of a droplet of blue-dyed water on a PDMS triangular membrane: a) blue-dye water droplet causes the edges of the membrane to bend, b) initial triangular-shaped PDMS thin film with score lines for folding, c) the evaporating droplet causes the membrane to fold around it, and d) tetrahedron left after all the liquid has evaporated [2].	62

3.3	Sequence showing the six stages of a completely wrapped droplet of water on a PDMS triangular membrane as the water droplet evaporates.	62
3.4	Setup for the capillary origami tests. PDMS triangles are laid out on a hydrophobic surface in side length order.	63
3.5	Comparison of the wrapping process for uncoated(A) and CNP-coated(B) triangular PDMS substrates over time as the water droplet evaporates.	64
3.6	Contact angle for different concentrations of Isopropanol in water. . .	65
3.7	Illustration of the cantilever deflection set-up (sideview) used to measure the deflection of the PDMS beams. Both the camera and PDMS beam are mounted horizontally.	66
3.8	Illustration of the cantilever deflection set-up (top view) used to measure the deflection of the PDMS beams. The PDMS beam is perpendicular to the camera.	67
3.9	Illustration of the cantilever deflection test and key measurements. . .	68
3.10	Graph of maximum deflection versus length for uncoated PDMS. The line of best fit has been added in order to compare the Uncoated PDMS with the Soot-coated PDMS in Fig.3.11.	70
3.11	Graph of maximum deflection versus length for soot coated PDMS. The line of best fit is the same as that in Fig.3.10.	70
3.12	Wrapping sequences for uncoated and soot-coated membranes with water (a and b) and the azeotrope of allyl alcohol (c and d). Sequences b and d show how it is possible to see Cassie-Baxter and Wenzel wetting states on the same surface with the appropriate choice of liquid. . . .	74
3.13	Graph of L_{crit} against L_{EC} for water on uncoated PDMS triangular membranes. The dashed line shows the line of best fit being made to cross the origin replicating that by Py <i>et al.</i> [3].	75
3.14	Image of water droplets on the soot coated PDMS surface.	76
3.15	Images of the advancing, static and receding contact angles for water on PDMS.	77

3.16	Images of the advancing, static and receding contact angles for water on soot-coated PDMS.	77
3.17	Images of the advancing, static and receding contact angles for the azeotrope of allyl alcohol on PDMS.	78
3.18	Images of the advancing, static and receding contact angles for the azeotrope of allyl alcohol on soot-coated PDMS.	78
3.19	Atomic force microscopy of the soot coated PDMS surface.	79
3.20	Scanning electron microscopy of the soot coated PDMS surface.	80
3.21	Graph of the critical length, L_{crit} , versus the elastocapillary length, L_{EC} , for the 30% Isopropanol solution on soot PDMS membranes.	82
3.22	Graph of L_{crit} against L_{EC} for water and allyl alcohol on uncoated PDMS and soot coated PDMS triangular membranes.	83
3.23	Graph of γL_{crit}^2 against κ_B for water and allyl alcohol on uncoated PDMS and soot coated PDMS triangular membranes.	83
4.1	Illustration of the boundary conditions between a liquid and a solid.	91
4.2	Illustration of the air circulation that occurs in the plastron layer around as water moves around the object.	92
4.3	Illustration of the flow chamber used for drag reduction tests. The light blue region in which the sample is positioned, indicates the laminar flow segment of the chamber.	93
4.4	Illustration of the 6mm diameter cylinders used for the drag reduction tests.	94
4.5	Illustration of the scaled-up sooting method.	95
4.6	Illustration of the larger area sooting method.	98
4.8	Graph showing the drag coefficient verses Reynolds number for the uncoated brass cylinders.	103
4.9	Graph showing the drag coefficient verses Reynolds number for the uncoated brass cylinders and the first soot PDMS covered cylinder.	103
4.10	Graph showing the drag coefficient verses Reynolds number for the uncoated brass cylinders and the second soot PDMS covered cylinder.	104

4.11	Graph showing the drag coefficient verses Reynolds number for the uncoated brass cylinders and the third soot PDMS covered cylinder. .	104
4.12	Graph showing the drag coefficient verses Reynolds number for the uncoated brass cylinders and the forth soot PDMS covered cylinder. .	105
4.13	Graph showing the drag coefficient verses Reynolds number for the uncoated brass cylinders and the fifth soot PDMS covered cylinder. .	105
4.14	Graph showing the drag coefficient verses Reynolds number for the uncoated brass cylinders and the first soot PDMS covered cylinder after an ethanol rinse.	106
4.15	Graph showing the drag coefficient verses Reynolds number for the uncoated brass cylinders and the second soot PDMS covered cylinder after an ethanol rinse.	106
4.16	Chart comparing the average drag coefficient for the brass cylinders and the soot-coated cylinders. The dashed line shows the average drag coefficient for the brass cylinders.	107
4.17	Chart comparing the average drag coefficient for the Ethanol rinsed and non-rinsed cylinders. The dashed line shows the average drag coefficient for the brass cylinders.	107
4.7	Image of a soot PDMS covered cylinder during testing. The surface appears silvery due to the presence of a plastron layer. The black lines on the cylinder are the seams where the edges of the PDMS substrates meet.	108
4.18	Images of the third soot PDMS cylinder after testing.	112
4.19	Image of a soot PDMS covered cylinder after a test in the flow chamber. The matt black surface of the cylinder shows the surface remained dry throughout the test.	113
4.20	Image of the second soot PDMS covered cylinder after all testing. The ethanol rinse has caused the PDMS substrate to shrink.	114
5.1	Image of a common garden snail.	119
5.2	Images of the first of the three pot comparison tests.	124

5.3	Images of the second of the three pot comparison tests.	125
5.4	Image of the third pot comparison test.	125
5.5	Image of the zigzag maze surrounded by soot PDMS.	126
5.6	Image of the spin removal force determination experimental setup. . .	128
5.7	Image of a snail's footprint area being recorded.	129
5.8	Before and after images of the first pot comparison test. Soot coated PDMS(left), Polypropylene (middle) and Copper coated (right). . . .	132
5.9	Images of the second pot comparison test.	133
5.10	Images showing a snail dropping onto the pots from the top surface. .	134
5.11	Time-lapse images of the third pot comparison test.	135
5.12	Before and after images of the third pot comparison test.	136
5.13	Images of maze test setup.	138
5.14	Time-lapse images of a snail travelling upward on a vertically mounted sheet of acrylic.	140
5.15	Time-lapse images of a snail travelling the length of the path enclosed by soot PDMS.	141
5.16	Time-lapse images of a snail travelling over the soot surface during a vertical maze test.	142
5.17	Graph showing the average removal force for a given surface.	145
5.18	Graph showing the variation in footprint area with mass for maturing common garden snails.	145
5.19	Graph showing the difference in removal force, divided by the footprint area, for all test surfaces.	146
5.20	Graph of receding contact angle against surface tension for various surfaces.	148

List of Tables

2.1	Average dimensions of ridge structures on and replicated from the Bastard, Second and Smooth cut files.	52
2.2	Average contact angle for PDMS and soot PDMS cast on the 3 different files and a flat surface.	54
3.1	Deflection data for the uncoated PDMS.	72
3.2	Deflection data for the soot-coated PDMS.	73
3.3	Contact Angles for water and the azeotrope of allyl alcohol on PDMS and soot coated PDMS.	76
5.1	Table of results for the vertical acrylic sheet tests.	138
5.2	Table of results for the vertical soot PDMS maze tests.	139
5.3	Table of results for the horizontal soot PDMS maze tests.	143
5.4	Table showing the average force required to eject a snail from a given surface.	144
5.5	Table showing the average force per square metre to remove the snails from a given surface.	146

Chapter 1

Background

This first chapter focuses on the theory behind how solids and liquids interact and the different wetting regimes. This is followed by a review of the ways in which the hydrophobicity of a surface can be increased.

Wetting

1.1 Surface Tension

In order to understand the wetting behaviour of a liquid, we must first consider the the surface of a liquid. The cohesive forces between the molecules in the liquid pull equally on the molecules in the bulk of the liquid. At the surface, the molecules are not surrounded on all sides by like molecules and are therefore subjected to unbalanced forces (Fig.1.1). These unbalanced forces tend to pull the molecules inward, resulting in a surface tension γ . The surface tension acts to reduce the surface area to volume ratio in order to reduce the surface energy of the liquid. The surface tension is measured in units of force per unit length, Nm^{-1} , or equivalently as the energy per unit area, Jm^{-2} [4]. It is a a measure of the energy cost associated with generating an interface and is a measure of the energy difference per unit area between the bulk and the surface of a liquid.

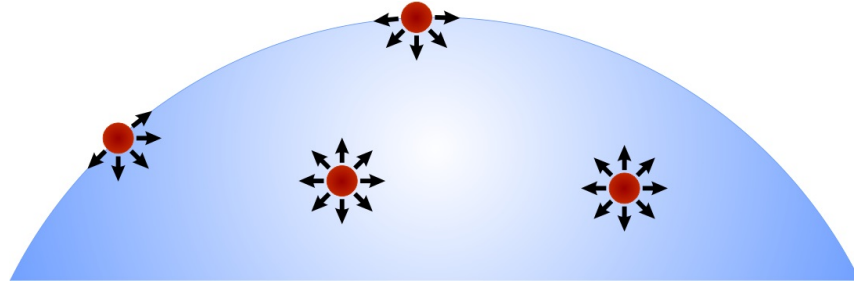


Figure 1.1: Illustration showing the unbalanced forces on a surface molecule compared to a molecule in the bulk of the liquid. The arrows indicate the attractive forces between the molecules.

1.2 Capillary Length

If a liquid is free to move it will do so in order to minimise the surface area. This is to find the minimum surface energy, depending on all the interfaces concerned. If the volume is small, this will be to form a spherical shape. This is dependent on the capillary length,

$$L_C = \sqrt{\frac{\gamma}{\rho g}} \quad (1.1)$$

Where ρ = density g = acceleration due to gravity

For water this is approximately 2.7mm . If the horizontal diameter of the droplet, d , is of the magnitude of the capillary length both the surface tension and the gravitational force act on the droplet. If d is much less than L_C , usually said to be one order of magnitude, the surface tension forces dominate over the gravitational forces, to form spherical droplet shapes (Fig.1.2).

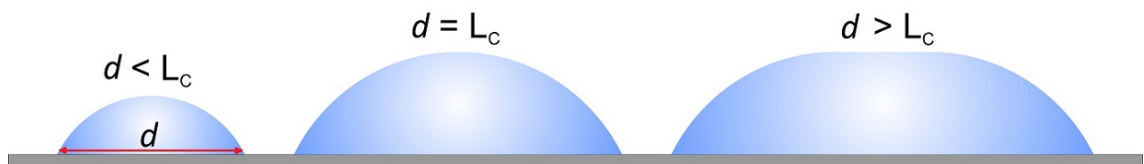


Figure 1.2: Illustration showing how a droplet is deformed under the force of gravity.

1.3 Laplace Pressure

The Laplace pressure is a consequence of the surface tension at the interface between the liquid and vapour phases. It is the difference between the pressures inside and outside of a droplet and can be calculated using the Young-Laplace equation [5],

$$\Delta P = P_{inside} - P_{outside} = \gamma \left(\frac{1}{R_1} + \frac{1}{R_2} \right) \quad (1.2)$$

Where R_1 & R_2 = principle radii of curvature of the droplet

γ = surface tension

P_{inside} = pressure inside the droplet

$P_{outside}$ = pressure outside the droplet

Equation 1.2 is commonly used to determine the pressure difference for spherical droplets or bubble. In this situation $R_1 = R_2$ and so equation 1.2 simplifies to

$$\Delta P = \gamma \left(\frac{1}{R} + \frac{1}{R} \right) = \frac{2\gamma}{R} \quad (1.3)$$

1.4 Spreading Parameter

Classicaly, we examine the surface tension between the three phases; solid, liquid and vapour. The surface tension between a liquid and air is denoted, γ_{LV} . For water $\gamma_{LV} = 72.8mN/m$ [6]. For a droplet on a surface we must also consider the solid/vapour, γ_{SV} , and the solid/liquid, γ_{SL} , interfaces. If we multiply the surface tension with the surface area, A , we get the total surface free energy, F . These three surface tensions help us define the spreading parameter, S , where,

$$S = \gamma_{SV} - (\gamma_{SL} + \gamma_{LV}) \quad (1.4)$$

When $S > 0$, a droplet will spread completely over a surface in order to reduce

its surface energy, resulting in a liquid film over the entire surface. This is to reduce the solid/vapour area underneath the liquid, as $\gamma_{SV} > \gamma_{SL} + \gamma_{LV}$. Reducing this area lowers the overall surface free energy of the system as it is preferential to have solid/liquid and liquid/vapour interfaces (Fig.1.3).

When $S < 0$, a partial wetting scenario is seen. The droplet does not spread over the surface but instead forms a spherical cap. The angle that the contacting edge of the droplet makes with the surface is called the contact angle, θ .

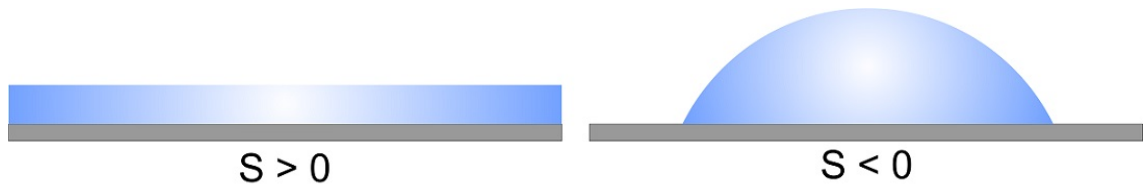


Figure 1.3: Illustration of the outcomes of a positive or negative spreading parameter. If positive the liquid fully spreads but if negative, the liquid only partially spreads forming a spherical cap.

A spherical cap is formed in this partial wetting state if the radius of the droplet is less than the capillary length for the liquid. If not, gravitational forces will flatten the top of the droplet (Fig.1.2).

1.5 Young's Contact Angle

Balancing the capillary forces acting at the contact line, also known as the triple line, allows determination of the contact angle (Fig.1.4).

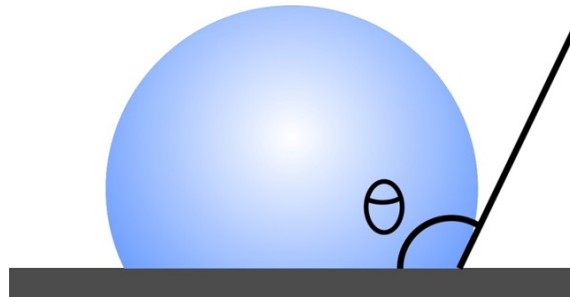


Figure 1.4: The contact angle of a liquid droplet is the angle, θ , made by the liquid/vapour interface at the contact point with the solid surface.

The angle is observed at the point where a liquid/vapour interface meets a solid interface. As surface tension is a force per unit length, it is possible to resolve the surface tensions in the horizontal plane and so at equilibrium γ_{SV} , γ_{SL} and $\gamma_{LV} \cos \theta_e$ are balanced so that,

$$\gamma_{SV} = \gamma_{SL} + \gamma_{LV} \cos \theta_e \quad (1.5)$$

This leads directly to Young's equation [7], where,

$$\cos \theta_e = \frac{\gamma_{SV} - \gamma_{SL}}{\gamma_{LV}} \quad (1.6)$$

The contact angle is independent of droplet size or volume. This means Young's equation is valid for all droplets on surfaces. Equation 1.6 was established for ideal solids which are smooth and chemically homogeneous. The angle is governed solely by the chemical nature of the three phases.

1.6 Contact Angle Hysteresis

For flat smooth surfaces it is possible for liquids to achieve contact angles as low as 0° . Oppositely, for flat surfaces, contact angles for water greater than 120° have not been experimentally observed, which were for fluoropolymer surfaces such as polytetrafluoroethylene (PTFE) [8]. These surfaces have the some of the lowest surface energies known and in order to achieve a greater contact angle with water, the development of a solid smooth surface with a lower surface tension would be needed.

The concept of flat smooth surfaces is generally unrealistic but there are some atomically flat surfaces. These include silicon wafers used in the microelectronics industry, cleaved mica, floated glass that has been cast on liquid tin in a process known as the Pilkington process and elastomers made by cross-linking of liquid films [4].

It is often found that surfaces contain defects. These can be chemical, such as stains, or physical defects like scratches or grooves. The physical defects may

be caused by fabrication processes. Alternatively surfaces may be composed of compressed grains which themselves produce roughness on the scale of the grains. For these non-flat surfaces the contact angle can have a range of values. The range of angles is known as the contact angle hysteresis.

If a droplet is deposited on a horizontal non-flat surface and the same liquid is slowly pumped into the droplet it will begin to expand, whilst the contact line remains stationary. As the volume increases, the contact angle also increases as the shape of droplet changes, beyond the value of θ_e until it reaches a threshold value, θ_A , known as the advancing contact angle. At this angle the contact line advances. A similar process occurs if the liquid is slowly pumped out of the droplet. The contact angle decrease below the value of θ_e until the threshold value, θ_R , is reached, known as the receding contact angle. At this point the droplet begins to recede. The difference between the advancing and receding angles, θ_A is known as the contact angle hysteresis (Fig.1.5).

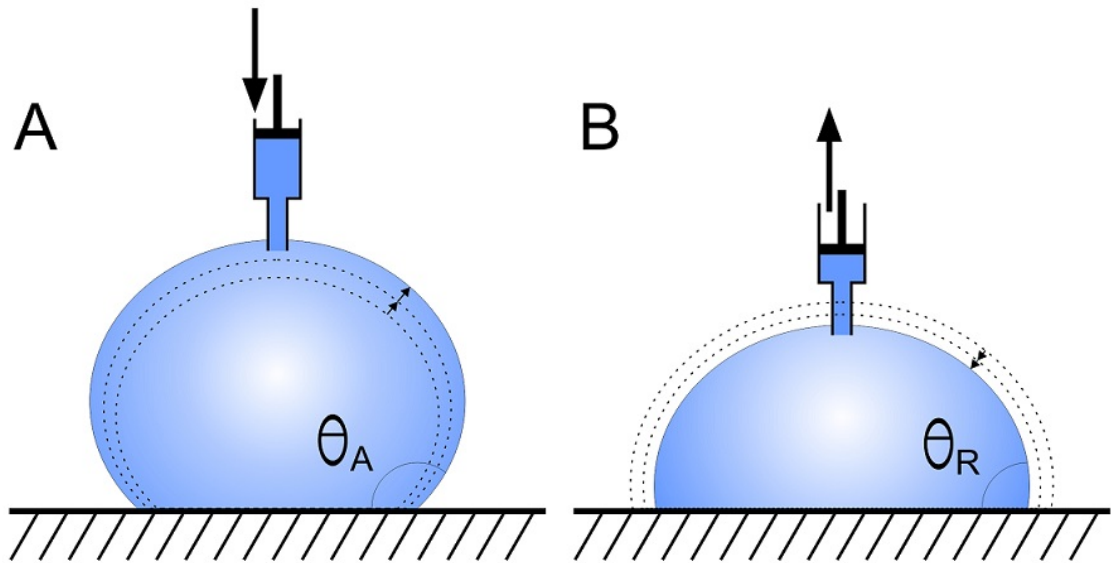


Figure 1.5: Illustration of the advancing (A) and receding (B) contact angles to determine the hysteresis.

As a result of the hysteresis, it is possible for droplets on an inclined plane to remain stationary, with the front of a droplet reluctant to wet oncoming surface features and for the rear of the droplet reluctant to de-wet features as the droplet is pinned on the surface features. The difference in the front and rear contact angles creates a Laplace pressure difference between the advancing and receding sides.

The difference in curvature between the advancing and receding fronts generates a force strong enough to resist gravitational forces, assuming the droplet is sufficiently small [9].

The hysteresis can be exploited e.g. it can be used to guide flow along a line of defects, but it can also be detrimental for example in the case of water droplets deposited on a window pane, which distort the transparency by scattering the light passing through.

1.7 Hydrophilicity and Hydrophobicity

A hydrophilic surface is one where the contact angle is less than 90° i.e. $\theta_e < 90^\circ$. A completely hydrophilic surface has a positive spreading parameter, $S > 0$, with a contact angle of zero, and so $\theta_e = 0^\circ$ making $\cos \theta_e = 1$. This means a droplet completely spreads forming a liquid film. Oppositely a completely hydrophobic surface, where $\theta_e = 180^\circ$ and $\cos \theta_e = -1$, is one where it is energetically favourable for a droplet to disassociate itself from the surface.

The change in sign for $\cos \theta_e$ in equation 1.6 can be used to define the behaviour of a liquid on a surface.

If $0 < \cos \theta_e \leq 1$ i.e. $\theta_e < 90^\circ$ then $\gamma_{SV} > \gamma_{SL}$ and the surface is considered hydrophilic (Fig. 1.6a).

If $0 > \cos \theta_e \geq -1$ i.e. $\theta_e > 90^\circ$ then $\gamma_{SV} < \gamma_{SL}$ and the surface is considered hydrophobic (Fig. 1.6b).

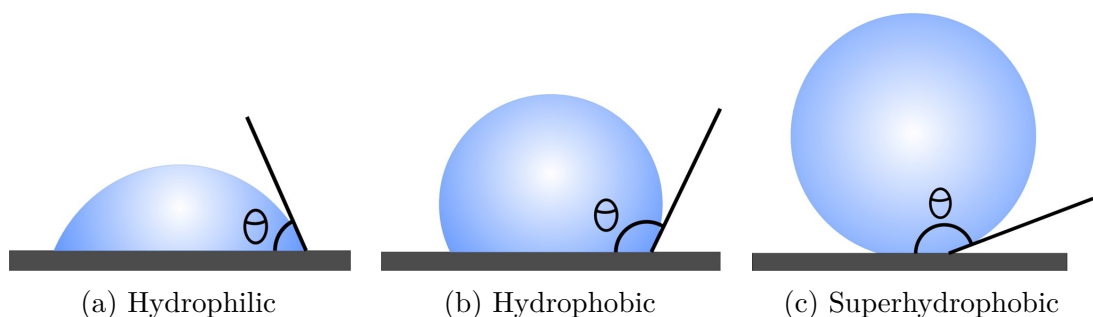


Figure 1.6: Illustrations of the partial wetting states.

It can be argued that if a droplet attaches itself to a surface then there must be some amount of hydrophilic behaviour and even with a contact angle greater than

90° , the wetting behaviour can be considered as a lesser hydrophilic state rather than hydrophobic [10,11].

At $\theta_e = 90^\circ$, $\gamma_{SV} = \gamma_{SL}$. At this angle there the change in energy when the liquid makes contact with the surface is equal. This results in a droplet forming a hemisphere on the surface as there is no advantage to the droplet wetting or dewetting the surface.

Superhydrophobicity can be achieved through the modification of a hydrophobic surface. By adding roughness, on the correct scale, the contact angle can be pushed upward of 150° . This is beyond that that has been seen with chemistry alone. Some also consider this to be superhydrophobic if the contact angle hysteresis is also low, $\Delta\theta < 10^\circ$ (Fig. 1.6c) [12]. The added roughness can be seen as a physical enhancement of the surface chemistry [13].

Nature has been the inspiration for many superhydrophobic surfaces. The leaves of the Sacred Lotus are covered in features that force water droplets to ball-up and roll off. As droplets of water roll over the surfaces of the leaves they pick up and carry away any dust or small dirt particles that they come into contact with. This has become known as the “lotus effect” [14–16]. Superhydrophobicity is quite common in nature, with many plants displaying contact angles in excess of 160° . These include Silver Wattle (*Acacia dealbata*), Peruvian lily (*Alstroemeria aurantiaca*), Taro (*Colocasia esculenta*), Lady’s Mantle (*Alchemilla mollis*) and Foxtail lily (*Eremurus robustus*) [15,17]. These plants have evolved to have hydrophobic leaves. The hierarchical structures over the surface of the leaves in combination with waxy-crystals amplify the dewetting state to take advantage of directed water droplets rolling off their surfaces.

Nature takes advantage of both hydrophobicity and hydrophilicity where plants and insects have evolved with modified surfaces in order to manage water droplets and channel them to desired areas or to harness surface tension to their advantage [18].

1.8 Surface Free Energy Approach

An alternative approach is to examine the surface free energy changes for a small movement of the contact line and to resolve the changes in energy over a small area.

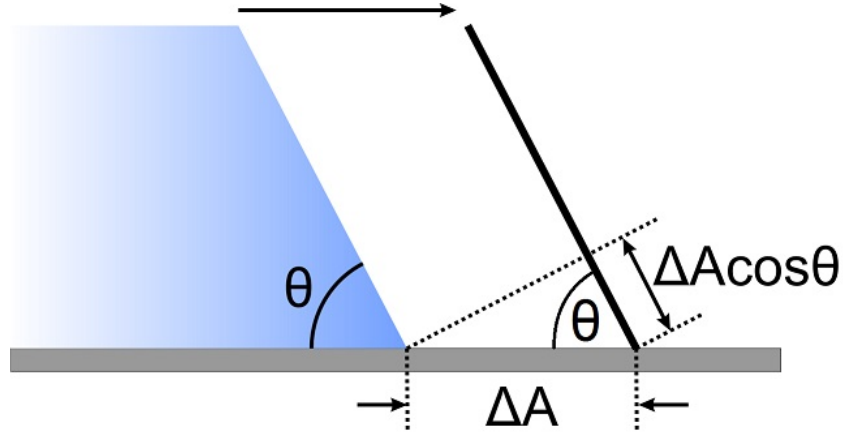


Figure 1.7: Illustration showing the change in area in the surface free energy approach.

If there is a small advance of the contact line by a small amount, with a change in contact area of ΔA , then there is a loss of solid/vapour area and a gain in both the solid/liquid and liquid/vapour areas (Fig.1.7). The change in energy is $(\gamma_{SL} - \gamma_{SV})\Delta A$, with the additional gain in the liquid/vapour area being $\gamma_{LV} \cos \theta_e \Delta A$. It is assumed that any change in θ_e is negligible due to the small distance moved by the contact line. The overall change in the surface free energy, ΔF , is,

$$\Delta F = (\gamma_{SL} - \gamma_{SV})\Delta A + \gamma_{LV} \cos \theta_e \Delta A$$

A local equilibrium of the contact line relates to a minimum in the surface free energy, so the change in energy for a small perturbation of the contact line can be considered to be zero. Therefore $\Delta F = 0$ and Young's equation (Eq.1.6) is recovered i.e.,

$$0 = (\gamma_{SL} - \gamma_{SV})\Delta A + \gamma_{LV} \cos \theta_e \Delta A$$

$$(\gamma_{SV} - \gamma_{SL})\Delta A = \gamma_{LV} \cos \theta_e \Delta A$$

$$\therefore \cos \theta = \frac{\gamma_{SV} - \gamma_{SL}}{\gamma_{LV}}$$

This approach assumes the contact line is free to move to examine changes in the local energy landscape. This in-turn relies on the absence of contact angle hysteresis (see section 1.6). This approach is also only valid for the area in the immediate vicinity of the contact line and does not apply to areas well inside or outside of the droplet away from the contact line [19, 20].

1.9 Roughness

Surface roughness is an important factor in determining the wetting characteristics of a surface. By understanding how a liquid behaves on various topographies it is then possible to tailor the roughness of a surface to control its wetting characteristics of that surface.

An issue that arises when analysing the wetting of rough surfaces is the change in the local contact angle as a liquid advances or recedes over defects on the surface. As the contact line moves over sharp defects, resolving the contact angle and capillary forces becomes more difficult [4, 21].

The wetting of rough hydrophobic surfaces can be examined from the two extremes. The first being the complete wetting of the surface, where the liquid penetrates in between all the topography. This was first described by Wenzel in the 1930's [22, 23]. The alternative extreme is where the liquid cannot penetrate between the surface features and no longer makes contact with the entire surface. This was first explored by Cassie and Baxter in the 1940's [24, 25].

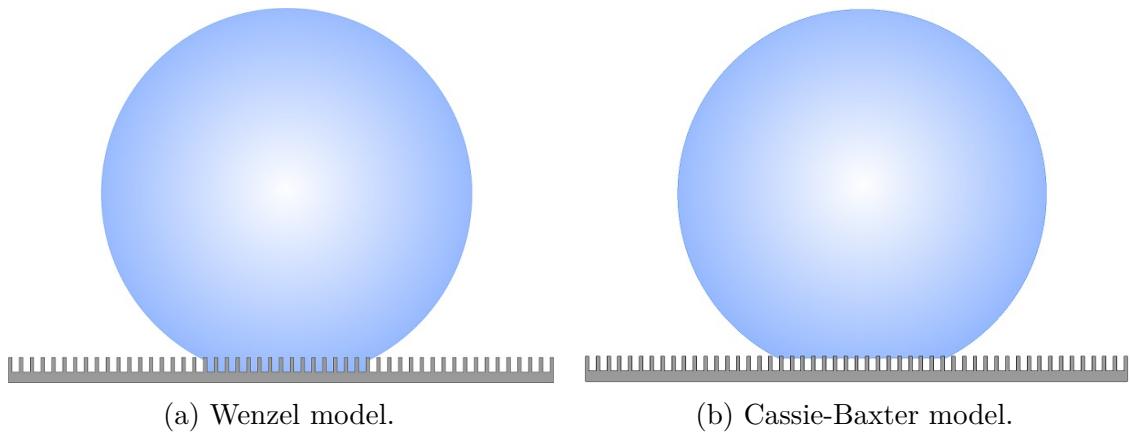


Figure 1.8: Illustrations of the Wenzel and Cassie-Baxter models.

1.9.1 Wenzel Model

In this model the roughness factor, r , is the ratio between the actual surface area and the apparent surface area (Eq.1.7)(Fig.1.9).

$$r = \frac{SA_{actual}}{SA_{apparent}} \quad (1.7)$$

Where SA_{actual} = Actual surface area

$SA_{apparent}$ = Apparent surface area

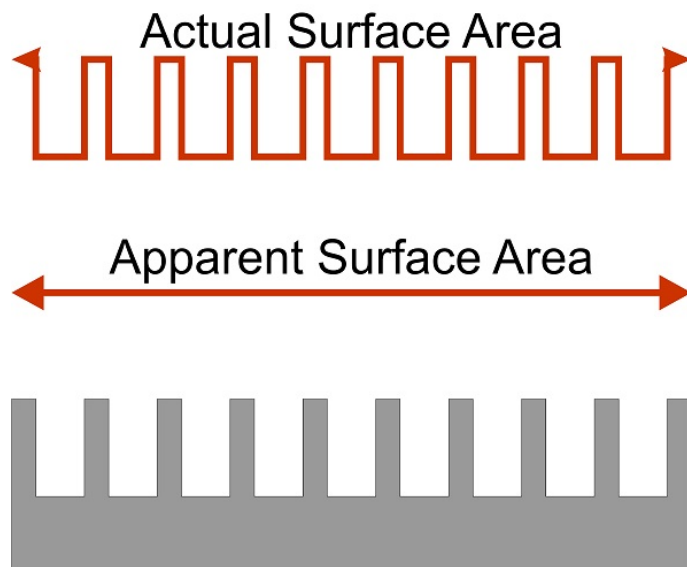


Figure 1.9: Illustration of the surface roughness. The lines represent the the 2D slice of a surface which enables the roughness to be determined in the direction of the cut.

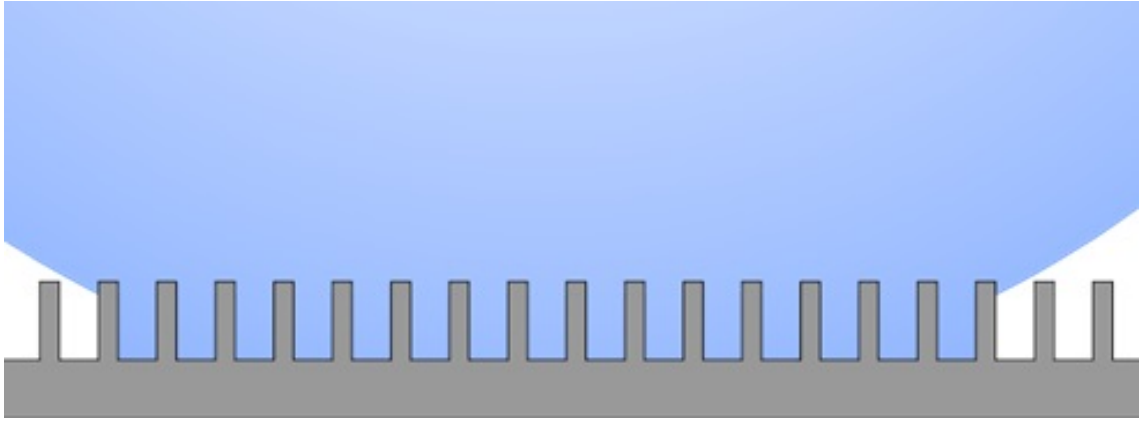


Figure 1.10: Illustration of the Wenzel wetting state where the liquid infiltrates between surface features.

Using the surface free energy approach to evaluate the rough surface in figure (Fig. 1.10) it is possible to relate Young's contact angle (section 1.5) to the apparent contact angle displayed in the Wenzel wetting case. The change in the surface free energy is

$$\Delta F = \underbrace{\gamma_{SL} r \Delta A}_{\text{gain in solid/liquid area}} - \underbrace{\gamma_{SV} r \Delta A}_{\text{loss of solid/vapour area}} + \underbrace{\gamma_{LV} \Delta A \cos \theta}_{\text{gain in liquid/vapour area}}$$

$$\Delta F = (\gamma_{SL} - \gamma_{SV}) r \Delta A + \gamma_{LV} \Delta A \cos \theta$$

Again the local equilibrium has $\Delta F = 0$, which gives

$$0 = (\gamma_{SL} - \gamma_{SV})r\Delta A + \gamma_{LV}\Delta A \cos \theta$$

$$\gamma_{LV}\Delta A \cos \theta = (\gamma_{SV} - \gamma_{SL})r\Delta A$$

$$\cos \theta = r \underbrace{\left(\frac{\gamma_{SV} - \gamma_{SL}}{\gamma_{LV}} \right)}_{\text{Sub in Eq 1.6}}$$

$$\cos \theta_W = r \cos \theta_e \tag{1.8}$$

Where θ_W is the Wenzel contact angle.

Equation 1.8 is known as the Wenzel equation [22]. It displays how roughness amplifies wettability because for all surfaces $r \geq 1$ and therefore pushes the value of $\cos \theta$ toward either 1 or -1. $\theta_e = 90^\circ$ becomes important in the Wenzel model as it is the point on the cosine graph that crosses the horizontal axis i.e. $\cos \theta = 0$. Equation 1.8 shows how with a Wenzel wetting state the angle is always pushed away from the $\theta = 90^\circ$ point. If $\theta_e < 90^\circ$ and the surface is hydrophilic, $\theta_W < \theta_e$, increasing the wetting of the surface, making it more hydrophilic. Oppositely, if the surface is hydrophobic i.e., $\theta_e > 90^\circ$, the surface becomes more hydrophobic as θ_W becomes greater in value for values of $\theta_e > 90^\circ$, and enhanced dewetting of the surface is seen. For $r = 1$ Young's equation is regained as this roughness corresponds to a flat surface.

The Wenzel state promotes complete wetting or complete non-wetting of a surface, depending on the intrinsic properties of the surface [13]. Equation 1.8 also indicates that $\cos \theta_W$ can be greater than 1. in reality this does not occur as another wetting states becomes energetically favourable.

1.9.2 Cassie-Baxter Model

In the Cassie-Baxter model the liquid is not in contact with the entire surface under the droplet (Fig. 1.11).

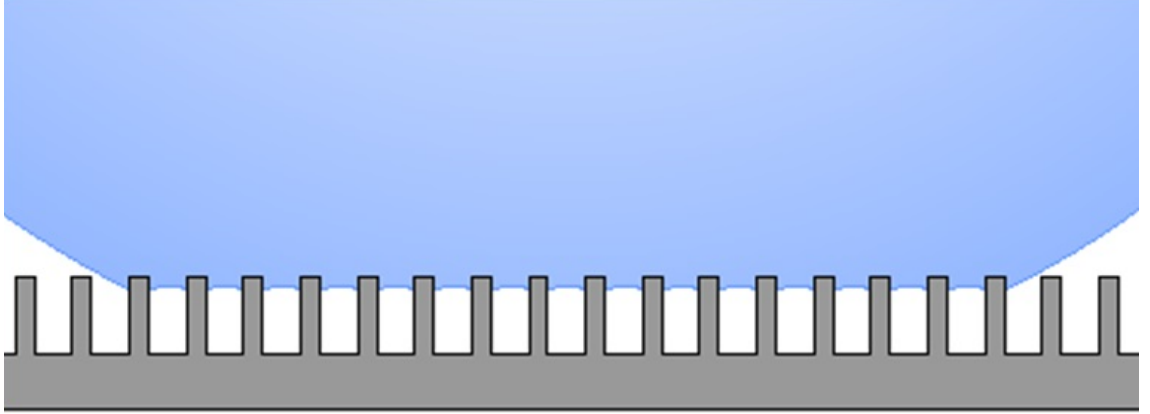


Figure 1.11: Illustration of the Cassie-Baxter wetting state where the liquid sits on top of the surface features.

As the liquid front advances on a structured surface, the liquid bridges between the features on the surface without penetrating between them. This creates air pockets between the droplet. It moves over the top of the features if the energy cost of the additional liquid/vapour interfaces is less than the energy gained from following the surface topography.

As the drop front advances by an amount ΔA , only a fraction of the surface, f_s , comes into contact with the liquid, $f_s\Delta A$. Liquid bridges form over the remainder of the surface producing liquid/vapour interfaces over an area of $(1 - f_s)\Delta A$.

By considering the change of surface free energy,

$$\Delta F = \underbrace{\gamma_{SL}f_s\Delta A}_{\text{gain in solid/liquid area}} - \underbrace{\gamma_{SV}f_s\Delta A}_{\text{loss of solid/vapour area}} + \underbrace{\gamma_{LV}(1 - f_s)\Delta A}_{\text{gain from liquid bridges}} + \underbrace{\gamma_{LV}\Delta A \cos \theta}_{\text{gain in liquid/vapour area}}$$

$$\Delta F = (\gamma_{SL} - \gamma_{SV})f_s\Delta A + \gamma_{LV}(1 - f_s)\Delta A + \gamma_{LV}\Delta A \cos \theta$$

$$\Delta F = (\gamma_{SL} - \gamma_{SV})f_s\Delta A + \gamma_{LV}\Delta A((1 - f_s) + \cos \theta)$$

At equilibrium, $\Delta F = 0$, so

$$0 = (\gamma_{SL} - \gamma_{SV})f_s\Delta A + \gamma_{LV}\Delta A((1 - f_s) + \cos \theta)$$

$$(\gamma_{SV} - \gamma_{SL})f_s\Delta A = \gamma_{LV}\Delta A((1 - f_s) + \cos \theta)$$

$$\underbrace{\left(\frac{\gamma_{SV} - \gamma_{SL}}{\gamma_{LV}}\right)}_{\text{Sub in Eq 1.6}} f_s = (1 - f_s) + \cos \theta$$

$$f_s \cos \theta_e = (1 - f_s) + \cos \theta$$

$$\cos \theta_{CB} = f_s(\cos \theta_e - (1 - f_s)) \quad (1.9)$$

Or

$$\cos \theta_{CB} = f_s(1 + \cos \theta_e) - 1$$

Equation 1.9 is known as the Cassie-Baxter equation [24]. The Cassie-Baxter angle, θ_{CB} , is always larger than the Young's angle, θ_e .

Even though the surface exhibits roughness, it does not directly appear in equation 1.9. It is the balance between the solid surface fraction and the roughness that determines when a rough surface exhibits Cassie-Baxter or Wenzel wetting characteristics.

An important feature of the Cassie-Baxter state is the sharp edges present on the features. It is at these edges that the contact line becomes pinned.

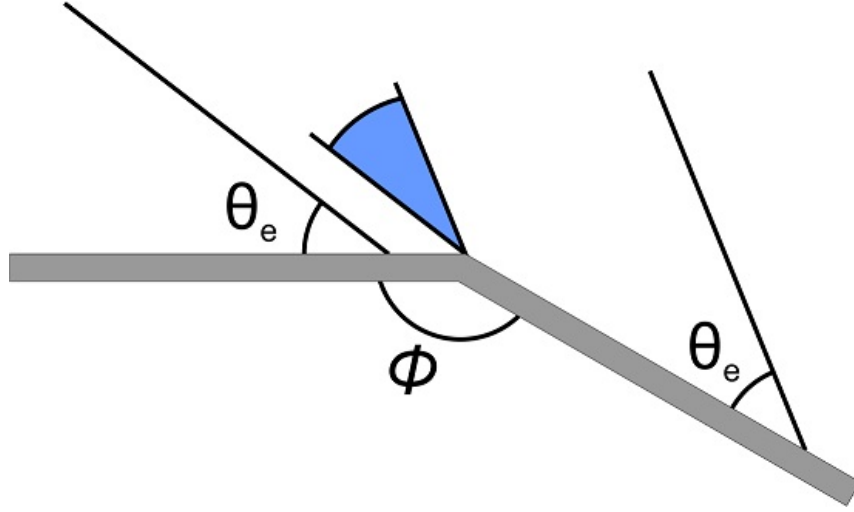


Figure 1.12: Illustration of the change in apparent contact angle as the orientation of the surface changes.

In figure 1.12 we look at the contact angle before and after a liquid front traverses a edge of angle ϕ . If the contact angle is measured from the horizontal plane, the Young's angle is $\theta_e = \theta$ before and $\theta_e = \pi - \phi + \theta$. This means that it is possible to measure angles between θ and $\pi - \phi + \theta$ when the contact line meets an edge [21, 26]. This is the reason the angle measure on a rough surface is called the apparent angle as the angle is measured from the horizontal.

1.9.3 Cassie-Baxter or Wenzel?

By comparing the surface free energy changes for the Cassie-Baxter and the Wenzel cases, a critical angle can be found which determines when each of the states is energetically favourable. The surface free energy change for the Wenzel model is given by

$$\Delta F = (\gamma_{SL} - \gamma_{SV})r\Delta A + \gamma_{LV}\Delta A \cos \theta \quad (1.10)$$

For the Cassie-Baxter state, the surface free energy change is given by

$$\Delta F = (\gamma_{SL} - \gamma_{SV})f_s\Delta A + \gamma_{LV}(1 - f_s)\Delta A + \gamma_{LV}\Delta A \cos \theta \quad (1.11)$$

By comparing equations 1.11 and 1.10 the critical for when the Cassie-Baxter state is energetically more favourable i.e., $\Delta F_W > \Delta F_{CB}$.

$$(\gamma_{SL} - \gamma_{SV})r\Delta A + \gamma_{LV}\Delta A \cos \theta > (\gamma_{SL} - \gamma_{SV})f_s\Delta A + \gamma_{LV}(1 - f_s)\Delta A + \gamma_{LV}\Delta A \cos \theta$$

$$(\gamma_{SL} - \gamma_{SV})r - (\gamma_{SL} - \gamma_{SV})f_s > \gamma_{LV}(1 - f_s) + \gamma_{LV} \cos \theta - \gamma_{LV} \cos \theta$$

$$(\gamma_{SL} - \gamma_{SV})(r - f_s) > \gamma_{LV}(1 - f_s)$$

$$\left(\frac{\gamma_{SL} - \gamma_{SV}}{\gamma_{LV}} \right) > \frac{(1 - f_s)}{(r - f_s)}$$

$$\underbrace{\left(\frac{\gamma_{SV} - \gamma_{SL}}{\gamma_{LV}} \right)}_{\text{Sub in Eq 1.6}} < - \frac{(1 - f_s)}{(r - f_s)}$$

so the Cassie–Baxter state is favourable when

$$\cos \theta_e < - \frac{(1 - f_s)}{(r - f_s)} \quad (1.12)$$

Equation 1.12 suggests that θ_e for a given surface must be greater than a critical value, θ_C , where

$$\cos \theta_C = - \frac{(1 - f_s)}{(r - f_s)} \quad (1.13)$$

in order to ensure $\cos \theta < \cos \theta_C$. Angles above the critical angle will result in a Cassie-Baxter state [17, 27–30].

For high values of r , $r \gg 1$, θ_C tends to 90° . As the surface is assumed to be hydrophobic, θ will be larger than this value e.g. for a surface covered in hairs. These types of surfaces are employed in nature by water-walking insects such as *Microvelia*. These insects have tiny hairs on its legs that obey a Cassie-Baxter state when they come into contact with water. This enables the insect to move over the surface of the water [31–33].

1.10 Methods for Changing the Hydrophobicity

Textiles and Fibres

The concept of fibre and fabric wetting was originally discussed by Wenzel [22]. Natural fibres exhibit dimensions on the microscale and have a natural roughness appropriate for changing the wettability. The use of hydrolysis of a methyldihalogenosilane as a waterproofing treatment for large material areas was first patented in 1945 [34]. It was later shown that this method can be used to hydrophobise polyester materials [35]. Improvement of the silane coating method through improved bonding techniques saw increased durability of the fabrics [36]. Plasma coatings have also been employed by the textiles industry to functionalise the fabric surfaces and change the wetting characteristics of materials [37].

With the increased interest and availability of complex carbon structures, Lui *et al.* reported a method for improving the hydrophobicity of a cotton fabric through dipping the material into a carbon nano-tube suspension to add nano-roughness to the surface [38]. Improved hydrophobicity of fabrics has also been seen through the use of plasma laser deposition of Teflon[®] films which increase the roughness of the surface [39]. Similarly, fabrics have been made superhydrophobic by infusing a textile with functionalised gold particles [40]. The inherent problem with hydrophobised fabrics is the durability of the treatment and the longevity of the wetting properties. With repeated washing cycles, the surfaces become damaged and the added roughness is worn away.

Electrospinning proves to be a promising way of tailoring the structure of individual fibres. The fibres are made from a variety of natural and synthetic polymers and the position of individual fibres can be controlled to maximise their functionality [41]. The electrospun fibres can range from nanometers to micrometers in diameter and can have different cross-sections. Contact angles as high as 172° have been recorded for these surfaces [42–44]. Through electrospinning hydrophobic polymers, both surface chemistry and roughness can be utilised to change the wetting behaviour of electrospun surfaces [45, 46]. Ogawa *et al.* found a way to add nano-scale roughness onto cellulose acetate fibres through the deposition of titanium oxide particles onto

the fibre surfaces [47]. Electropun carbon nano-fibres can also produce hydrophobic surfaces. A bonus of this surface is that it also has conductive and magnetic properties after calcination of Polyvinyl acetate with ferrous acetate [48].

Phase Separation

Rough three dimensional porous networks can be made by taking advantage of the phase separation that can occur in multicomponent mixtures. One possible route for achieving this situation is to control the temperature surrounding a mixture. At specific ambient conditions, a mixture can be made unstable which can result in the solidification of one of the constituent components. If this solid and liquid condition exists for a solution with the two parts being well mixed, it is possible to set the solid part in place to form a 3D continuous network with the liquid filling the pore spaces in the network. The liquid can then be removed, for example, through evaporation. The solid porous network can have a large area as well as a rough surface. By manipulating the ambient conditions the solidification and separation rates of the mixture can be controlled and so the pore size can be changed, predominantly in the micrometer scale [12]. If the solid material is hydrophobic, often polymers, the resulting materials can be superhydrophobic. Early work on superhydrophobic phase separated materials concentrated on using sol-gel materials [49–51]. Other surfaces have been prepared using polymers and fluoro-polymers [52–54].

Crystal Growth

By controlling the shape and size as crystals grow, needle-like structures can be formed and rough surfaces grown on a crystallising liquid. Using this method superhydrophobic crystalline surfaces can be grown from hydrophobic materials and even from hydrophilic materials if coated post-growth [12]. Tsujii *et al.* used ambient temperature control to grow alkyl ketene dimer crystalline surfaces which were able to produce contact angles of 174° [55]. Triglyceride crystalline surfaces have a contact angle of 110° but after the initial growth period, fractal structures appear on the crystals which push the contact angle up, making the surface superhydrophobic [56].

Etching

The use of etching to increase hydrophobicity focuses on increasing the roughness of a surface. This can be through plasma, chemical or laser etching.

Plasma etching can be used on its own or in combination with other patterning techniques. The plasma is generated by an electromagnetic field and depending on the gases used, different chemically reactive ions can be generated. Deep Reactive Ion Etching (DRIE) has been used on micro-scale pillar arrays to create nano-scale roughness [57]. This has produced contact angles of 173° . DRIE was also used by Kim *et al.* to produce sharp nano-scale tips on micro-features to produce a superhydrophobic surface [58]. Using a microwave plasma system it has been possible to dry etch the surface of a Polydimethylsiloxane (PDMS) surface to push it from hydrophobic to superhydrophobic [59]. By choosing an appropriate gas, surface roughness can be added to a variety of surfaces [60, 61].

By chemically etching metallic surfaces, it is possible to roughen the surface to produce superhydrophobic setting states [62].

Using laser etching techniques, Jin *et al.* added roughness to the surface of PDMS substrates with contact angles greater than 160° [63].

Diffusion Limited Growth

Using techniques such as electrodeposition or gas phase deposition, roughness can be created on surfaces as layers of material are deposited. Electro-deposition is the process by which a dissolved substance is deposited onto an electrode. During deposition the addition material bonds instantly with the surface, usually gathering at any protrusion. Growth is then concentrated at these points with branch structures appearing as growth continues. The rate of deposition is determined by the flux rate of the addition material. Metallic superhydrophobic surfaces have been created in this way [64–66]. It has also been possible to create superhydrophobic conductive polymer surfaces using these techniques [67]. Superhydrophobic surfaces have also been created using chemical vapour deposited and microwave-plasma deposited polymers, fluoro-polymers and silanes [68].

Particle Deposition

Micro and nano-particles can be used to form ordered roughness on a surface by tailoring the assembly process and size of particle. Close-packed layers of particles can be formed by taking advantage of the Van der Waals force that causes an attraction between particles. Silica particles have been used to create layers of close-packed surfaces. The particles were then functionalised with silanes to make the surface superhydrophobic [69]. Similar surfaces have been prepared using polymer spheres [70]. The added roughness from the particulate surface changes the wettability. The superhydrophobicity of these surfaces can be improved by producing hierarchical surfaces through a combination of micro and nano-particle deposits [71]. A number of different methods exist for creating superhydrophobic surfaces in this way [72]. One such method uses oxygen reactive ion etching to expose silica micro-particle layers that are embedded in a polymer matrix. Once exposed nano-particulates, in suspension, are spin-coated on the exposed surface. This is followed up with a surface coating of fluorosilane to achieve contact angles of 159° and low hysteresis, around 5° [73]. Another facile method to procure superhydrophobic surfaces was developed by Gao *et al.* [74]. They used spray coating to deposit silica nano-particles, suspended in TriethoxyHexadecylSilane (THS), onto glass. These surfaces displayed contact angles upward of 160° . A more industrial use of nano-particle coatings has been to superhydrophobise concrete surfaces. By applying a water-based emulsion of polymethyl-hydrogen siloxane and metakaolin, micro-scale roughness was added to the surface of concrete blocks. To produce hierarchical structures polyvinyl alcohol fibres were added. Using this method, contact angles of 156° were produced [75]. Zhang *et al.* used another method to produce nano-particle coatings known as Layer-By-Layer (LBL) deposition [76]. This process involves alternating the charge of a surface to build up multiple layers, at the molecular level, by immersing the substrates into solutions of the opposite charge. This allows layers of molecules to be alternatively absorbed onto the surface. Zhang *et al.* used this method to create anti-reflective coatings for the near-infra red region of the spectrum.

By functionalising the particles it is possible to adapt the particles for specific

applications. Magnetic nano-particles have been made that contain an Iron oxide core with a fluorinated silica shell. When deposited onto a substrate in the presence of a magnetic field, contact angles of up to 172° were produced [77].

Lithography

The word “lithography” derives from the ancient greek words *lithos*, meaning “stone”, and *graphein*, meaning “to write”. The term lithography covers a range of processes. These include:

- Photolithography
- Soft lithography
- Nano-imprint lithography
- Electron beam lithography
- X-ray lithography
- Colloidal lithography

Photolithography involves the irradiation of photo-sensitive polymers, usually to ultra-violet light, through a mask on which a predefined pattern has been designed. Post-exposure, the photoactive surface is developed to either remove or leave behind the exposed regions, depending on the polymer used. It has proved a useful process as it can produce well-defined, predetermined features designed to be superhydrophobic. In 1994, Kawai and Nagata used this fabrication method to produce 3D micro-patterned surfaces that changed the wetting behaviour of the photo-resist [78]. Since then a wide variety of surface features have been made using photolithography. Many of these surfaces were to examine wetting processes [79–82].

Soft lithography uses elastomer stamps, moulds and masks, often made from a master plate made using photolithography, to replicate patterns and topographies. To produce superhydrophobic surfaces using soft lithographic techniques, moulding or templating is primarily used.

Nano-imprint lithography or hot embossing involves the use of rigid stamps with topographic features to pattern a polymer surface through the application of heat and pressure [83, 84]. The rigid surfaces are often made using photolithography to have micro and nano-scale features and can produce surface displaying contact angles around 170° [85].

Electron beam lithography uses focused electron beams rather than light to pattern the surface directly. This means that a mask is not necessarily needed if the beam can accurately be controlled [86].

X-ray lithography is a very similar process to photolithography but it uses polymers sensitive to x-rays rather than the usual UV light sensitive polymers. This can allow for the production of more detailed structures below the micro scale due to the shorter wavelength of x-rays compared to UV electromagnetic waves [87].

Colloidal lithography uses micro and nano particle arrays as masks through which photo-active polymers are irradiated [72, 88]. This process can be used to form cone or pillar features and by changing the size of the particles or their arrangement different size features and array patterns can be made.

Many processes involve the use of multiple lithographic techniques to produce different size features or surface structures. Kim *et al.* use a combination of photolithography, x-ray lithography and soft lithography to produce high aspect ratio surface features [58].

Templating

Templating is a replication method whereby moulds are cast on a master surface in order to reproduce the master surface multiple times. This method can be used to produce both negatives and replicas of the master. Lithography is often used to manufacture the master substrates, which often have micro-scale features, such as spikes, cavities or strips as produced by Bico *et al.* [89]. The surface features of the master substrates were replicated using an elastomer which were in turn used to make silica features on a silicon wafer. After the deposition of a hydrophobising agent, advancing contact angles of 167° were produced on the replicated spiked surfaces.

Porous aluminium surfaces have been used as a master surface by Lee *et al.*. The nano-scale surface topography was used as a template to nano-features on polystyrene [90].

The replication of natural surfaces have also been reported. Nickel electro-forming has been utilised to make a master plate from gold coated lotus leaves which are naturally superhydrophobic. The nickel mould surface held a negative impression of the lotus leaf features from which positive impression were cast [85]. Others have also create artificial lotus leaf surfaces which display superhydrophobicity [91,92]. The replicas demonstrate high contact angles and therefore an accurate and simple way of reproducing the natural features.

1.11 Improving the Hydrophobicity of PDMS

Polydimethylsiloxane (PDMS) has proved to be a useful material for examining wetting phenomena. In its oil form, PDMS it can be produced in a variety of chain lengths, which have differing properties, such as viscosity. This enables the viscosity of the oil to be selected. It is also used as a food additive (E900), in cosmetic products, as an anti-foaming agent and as a lubricant. When the cross-linking agent is added to PDMS the polymer chains form bonds to produce a hydrophobic elastomer. The rate at which these bonds form can be controlled by regulating the ambient temperature in which the reaction is taking place. The elastomer is flexible, cheap, transparent, inert and able to replicate nano-scale features if cured on features of this size. It has been useful in the field of microfluidics, MicroElectroMechanical Systems (MEMS) and optical devices because of its replication abilities.

Soft lithography and embossing have been the primary choice of fabrication for such devices [93–101]. PDMS has also been used in the production of superhydrophobic surfaces or been made superhydrophobic. Through replication, the surface of superhydrophobic plants have been copied to produce superhydrophobic PDMS surfaces [91]. In order to create 3D mushroom-shaped features on a PDMS surface, Dufour *et al.* used photolithography to create a negative pattern on a silicon

wafer [102]. PDMS was then cast onto this surface and once cured, it was exposed to perfluorodecyltrichlorosilane (PFOTS) using Chemical Vapour Deposition (CVD). This produced contact angles of approximately 150° with high hysteresis of around 25° . Stanton *et al.* produced enhanced hydrophobic PDMS by casting directly onto sandpaper of known roughness. The PDMS negative surface achieved contact angles of 153° by simply replicating the micro-scale roughness of fine sandpaper [103].

Embossing techniques have been used by Jeong *et al.* and Cortese *et al.* to produce arrays of surface features on PDMS surfaces to change the wetting characteristics [104, 105]. Pyramidal micro-features with nano-scale roughness have been produced by replication of a silicon mould. The nano-scale roughness was added using DRIE. Using this method contact angles of 160° were observed [106]. Laser ablation techniques have also been used to change the wetting behaviour of PDMS. In 1996 Khorasani *et al.* exposed PDMS substrates to a pulsed CO_2 laser to increase the surface roughness of a substrate. This increase the contact angle of the PDMS from around 100° to approximately 170° [107]. More recently Yoon *et al.* produced hierarchical topography on PDMS using an infra red laser. The surface was exposed to the focused laser beam, $\sim 8\mu\text{m}$ in diameter, with 150fs pulse rate. This was able to create micro-scale mounds with nano-scale bumps. The added surface roughness increased the contact angle to $\sim 160^\circ$ with a hysteresis $< 5^\circ$ [108].

To create PDMS nano-structures, Xue *et al.* exposed the surface to UV light through a grid-pattern [109]. This created a cross-hatch topography with troughs $\sim 100\text{nm}$ deep. This process has potential for scale-up to produced large areas of nano-structured PDMS. It is also possible to create near-superhydrophobic surfaces using micro-particles [110]. By embedding aluminium oxide micro-particles into the surface of PDMS, a master surface was created. A negative was made of this surface using PDMS from which the original surface was replicated, again using PDMS. The replicated surfaces displayed contact angles of $\sim 149^\circ$. Gao *et al.* have also reported on a method where fumed silica is used to increasing the contact angle of PDMS. The silica is mixed with the PDMS polymer and then deposited onto glass substrates before cross-linking. The hierarchical surface produced contact angles of 147° [111].

Carbon nano-particles have been of interest in the last few years. Deng *et al.* deposited paraffin wax soot onto glass slides, which forms a fractal network as the carbon nano-particles (CNPs) are randomly deposited onto the glass. The fragile soot network was coated in a $\sim 20\text{nm}$ of silica layer using CVD and then baked at 600°C . This sealed the structure in place. The robust surface is superhydrophobic as it produces contact angles of 165° [112]. CNPs have also been produced by burning rapeseed oil. These were deposited onto metal substrates which are able of producing contact angles of 156° with a hysteresis of 3° [113]. One issue with the soot surfaces is that, without additional coatings, the surface is extremely fragile. To increase the robustness of the CNP surfaces, Yuan *et al.* embedded a thick layer of ethanol soot into thick layers of PDMS [114]. These surfaces were tested for their ability as infrared nano-sensors with self-cleaning properties, meaning that they produced contact angles over 150° with roll-off angles of 4° .

Chapter Summary

This chapter has introduced the background behind how a liquid wets a surface and how the process can be manipulated through surface modification. In the following chapters a more specific background is included in order to set the scene for the experiments performed and to give a wider understanding of where the work fits into the scientific picture.

Next is the methods chapter. It concentrate on the methods used to develop a novel flexible superhydrophobic substrate. This novel work is the basis form which the work in chapters 3, 4 and 5, where the use of the surface is tested and examined.

Chapter 2

Methods

This methods chapter concentrates on the fabrication methods trialled and adapted in order to fabricate flexible superhydrophobic thin films. The development of the superhydrophobic flexible membranes allowed the capillary origami process to be tested when surface roughness is present. It also allowed for the novel conformable surface to be tested as a possible route for superhydrophobic drag reduction as well as a potential snail repellent surface.

2.1 Development of the Superhydrophobic Thin Films

2.1.1 Trial Methods

The first step in determining the effects of superhydrophobicity on the capillary origami process was to devise a way of modifying the surface of the polydimethylsiloxane (PDMS) in order for it to display superhydrophobic properties. PDMS is a silicone that can be made to polymerize. It is available as a two-part kit (Dow Corning Sylgard 184) that, when mixed in a 10:1 elastomer to curing agent ratio, forms a flexible, inert and non-toxic silicon rubber. The curing rate of the PDMS can be controlled by changing the temperature of the environment in which it is curing. This can be anywhere between 15 minutes at 150°C to 24 hours at room temperature (approximately 20°C). It was first used as an encapsulation material for

electronic components as it is a good dielectric insulator and is capable of protecting components from the elements as it has a working temperature range of -45°C to 200°C [115]. More useful to this project is that PDMS is capable of replicating feature sizes in the micro scale but is ultimately capable of replicating feature sizes less than 10nm in size [116]. The normal procedure for making PDMS first involves mixing the elastomer and curing agent in a 10:1 ratio and then stirring vigorously for at least 5 minutes. In order to remove any bubbles introduced into the mixture from the stirring process, it is degassed in a vacuum desiccator for approximately 30 minutes. It is then ready for use. The PDMS has a working pot-life of approximately 90 minutes at room temperature.

In order to determine the ability of commercially available products to increase the hydrophobicity of the PDMS, thin layers were spin-coated onto acrylic slides, onto which the surface coatings were applied. These surface treatments claim to increase the hydrophobicity of a material by depositing a thin layer of a fluorinated compound. The first product tried was Hyrec 1405, which is available in paint or spray form, that was developed for application in the satellite industry. The paint and spray were applied to the PDMS surfaces and allowed to completely dry. The Hyrec 1405 reacted with the PDMS so was discounted as an option. The next product tested was Storm Wash-in solution. This product is marketed as a way of protecting tents from the rain. It is brushed onto a surface which is then allowed to fully dry. At this stage the material should be water resistant. Again, once the solution was brushed onto the surface, it reacted with the PDMS surface, making it unusable. A similar product is made by the company Granger's, who specialise in making products to waterproof and protect outdoor clothing and equipment. Two forms of the product were tested. The first was Granger's Supruf waterproofer, that is applied as a spray and left to dry overnight. Again, this product reacted with the PDMS surface, making it unsuitable for use. The other Granger's product is applied in a different fashion. A 20% solution of Granger's Extreme Wash-in in water was made. PDMS surfaces were completely submerged into the solution and left for 10 minutes. After being removed from the solution the substrates were placed in 60°C

oven for the surface to dry. This product deposits a fluorinated compound on the surface, making the surface more hydrophobic. Once the surfaces were fully dry, the contact angle for water was measured on the surface. The contact angles were measured using a KRUSS DSA10 Dropshape analysis system.

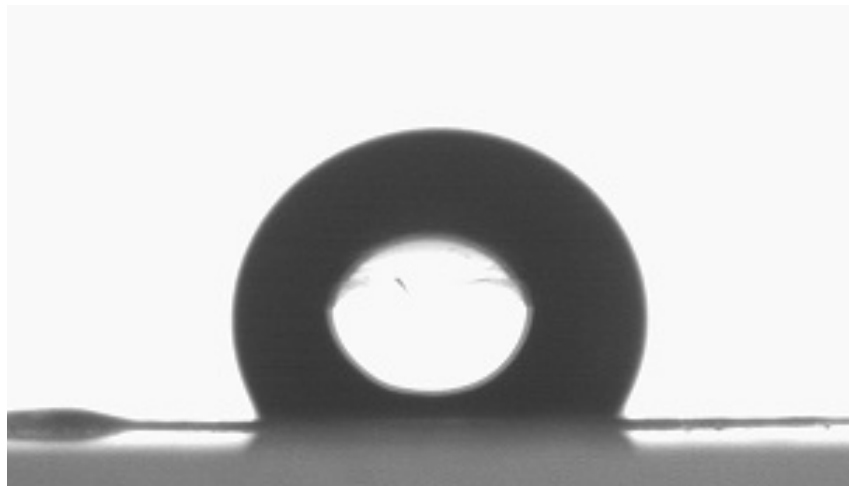


Figure 2.1: Image of a droplet of water on a PDMS surface that has been treated with Granger's.

The Granger's Extreme wash-in treatment did increase the contact angle of the PDMS surface from $\sim 100^\circ$ to $\sim 120^\circ$ (Fig. 2.1), an increase of around 20° . In order to get the contact angle sufficiently high to be considered superhydrophobic, the surface would also need to be textured on the micron scale. A quick simple test involving casting the PDMS onto a textured surface was tried. Sand paper was the surface of choice due to the fact that different grades of sandpaper are coated in different size sand grains. The FEPA (Federation of European Producers of Abrasives) classification system for sandpaper sorts different grades of sandpaper according to the diameter of the grit stuck to its surface. These range from P12 up to P2500, which correlates to an average grain size of $1815\mu m$ to $8.4\mu m$, respectively. In order to add surface roughness to the PDMS, it was cast on top of various sandpaper surfaces. Sandpaper grades ranging from P600 to P60, which is a grit size range of $269\mu m$ to $26\mu m$, respectively. Once the PDMS had fully cured on the surface of the sandpaper it was carefully peeled off. A sample of each size was then treated with the Granger's Extreme Wash-in solution. The Contact angle for each of the grades was measured (Fig.2.2) for both the uncoated and Granger's coated PDMS

to determine whether a superhydrophobic surface existed (Fig.2.3).

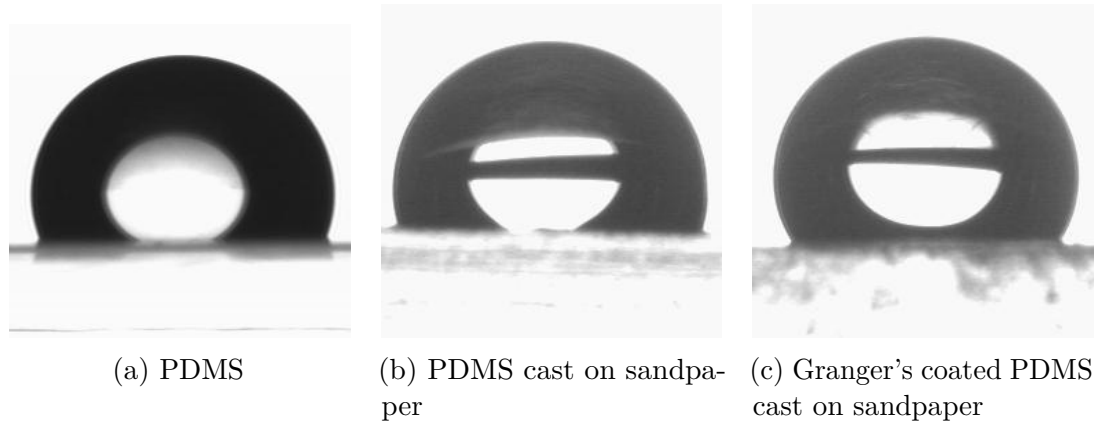


Figure 2.2: Images of water droplets on PDMS (red), PDMS cast on sandpaper (blue) and Granger's coated PDMS cast on sandpaper (green).

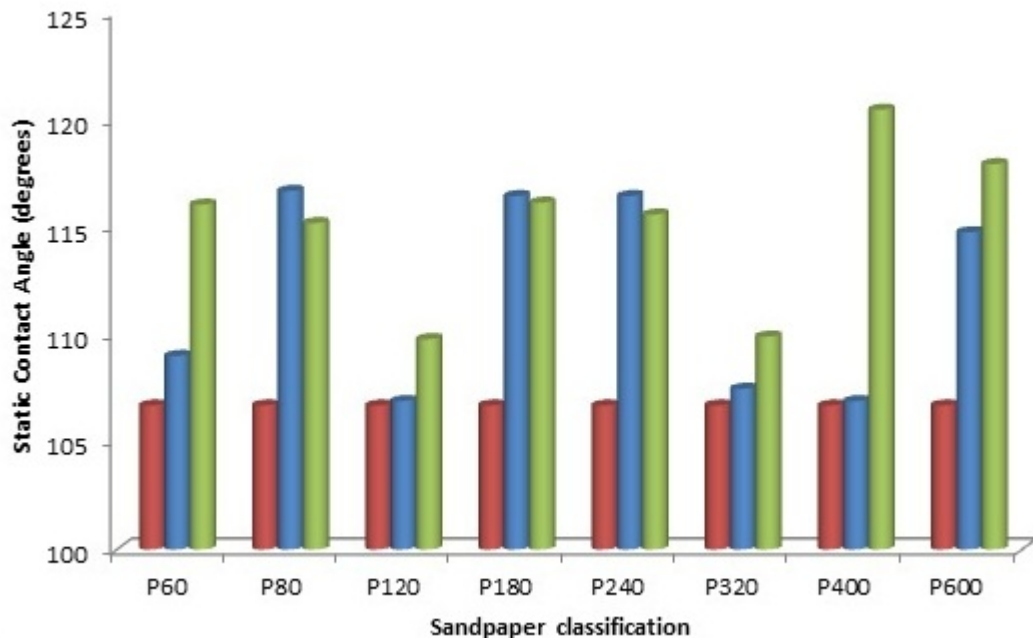


Figure 2.3: Graph of the contact angles for various grades of sandpaper for the PDMS, PDMS cast on sandpaper and Granger's coated PDMS cast on sandpaper.

Another attempt to make superhydrophobic PDMS through casting involved laser patterning acrylic plates using a Universal Laser Systems M300 40W CO₂ laser cutter. A variety of well-ordered patterns were made on the surface of acrylic plates which could then be used as negative for PDMS to be cast on. The same procedure as with the sandpaper casting was used to replicate the patterns onto a PDMS layers which were then analysed to determine whether or not an increase in hydrophobicity was present.

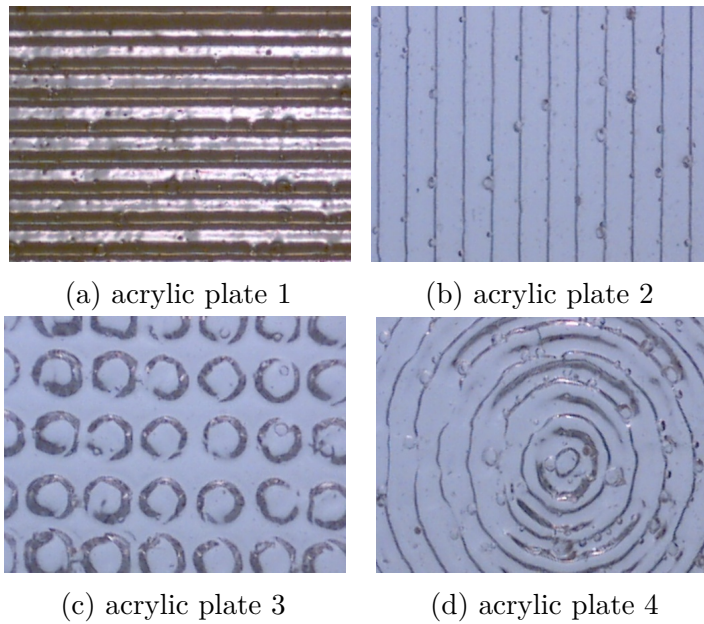


Figure 2.4: Images of laser patterned acrylic plates.

Features on the order of $200\mu m$ were designed in AutoCAD[®] and CorelDRAW[®] and were cut into the surface of the acrylic plates using the laser cutter. Multiple trial cuts were performed in order to determine the optimum settings to produce the most defined features possible using the laser system. Once the surfaces had been prepared, static contact angles were taken for the acrylic plates as well as for PDMS cast on the surfaces. A maximum increase of 10° was observed for the acrylic surfaces when compared to an unpatterned flat acrylic surface. The PDMS showed more promise with an increase of around 25° to 30° , when compared to flat PDMS, taking the contact angle up to approximately 120° (Fig.2.5). This is still not superhydrophobic but this was not surprising considering the dimensions of the features that it was possible to produce using this technique.

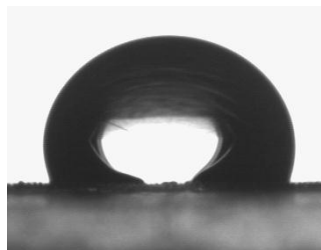


Figure 2.5: Image of a droplet of water on PDMS cast on patterned plate.

An alternative method was noticed during the acrylic patterning tests. The surface of the PDMS could be directly patterned using the laser cutter. By varying

the number of the Points Per Inch (PPI) of the pulsed infra-red laser, it was possible to make point features on a surface. Again, many trial tests were performed, in which the speed, power and the PPI were varied, in order to produce the best possible features. Using this patterning method it was possible to modify the surface of a PDMS film with the addition of concave features. The tests produced features below $100\mu m$ in size, arranged in rows, which were spaced $100\mu m$ apart, centre to centre (Fig.2.6).

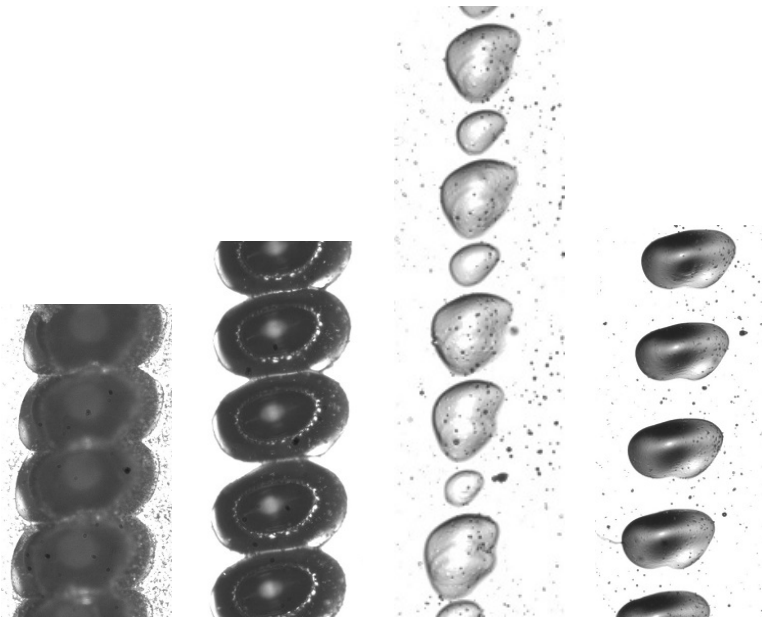


Figure 2.6: Images of laser patterned PDMS surfaces showing the concave features. The largest features (far left) are approximately $100\mu m$ wide.

Advancing and receding contact angles were taken for all samples prepared. The greatest increase was seen with power settings of 1.0%, speed of 7.5% and 240 PPI. These surface features are $80\mu m$ by $40\mu m$ in size and are approximately $100\mu m$ apart, centre to centre. The advancing contact angle was increased from $112^\circ \pm 2^\circ$ to $124^\circ \pm 2^\circ$ but the receding angle was reduced to $100^\circ \pm 2^\circ$ from $80^\circ \pm 2^\circ$. This indicates a Wenzel state is present and the droplet gets pinned by the surface features.

It is possible to modify the surface of a PDMS film as it cures if a textured surface is pressed onto its surface at the correct point during the curing process. At room temperature it can take up to 24 hours for PDMS to fully cure but by increasing the temperature to $60^\circ C$ this time can be dropped to approximately 50 minutes. PDMS can be fully cured in a matter of minutes if the curing temperature is raised

up to $150^{\circ}C$ without any adverse effect to the PDMS. In order to try and introduce surface features into the surface of the PDMS during the curing process a tool was designed that allowed a textured roller-head to be smoothly rolled over the surface of a PDMS film. For the initial tests sand grains $50 - 100\mu m$ were stuck onto the roller head to act as a textured surface. A 10:1 PDMS mixture was made and degassed in a vacuum desiccated for 30 minutes before being spun onto acrylic slides. The slides were placed into an oven at $80^{\circ}C$ and the roller was run over the surface of a slide every 2 minutes until the PDMS was fully cured. The results showed that it was possible to impart a texture onto the surface of a film but that the process was very unpredictable. It is extremely difficult to roll a texture onto the surface of a film and to have said features remain until cured. The rolling process has to be conducted in a very small time window during the curing process. If this window is missed the PDMS will be either too fluid, meaning the features are lost after rolling, or too cured so that no texture can be imparted onto the surface.

In a paper by Liang Zhang et al. entitled “A facile approach to superhydrophobic coating from direct polymerization of “Superglue[®]””, [117], the authors claim to be able to easily create superhydrophobic coatings by simply curing Ethyl CyanoAcrylate (ECA), more commonly known as Superglue[®], in a humid ammonia environment. More specifically micro-nano binary structures are formed on the surface of a substrate when the ECA polymerizes to form polyethylcyanoacrylate (PECA), through a nucleophilic attack mechanism, in the presence of a volatile initiator. This process is said to produce nano-fibres of PECA on the surface of the substrate making it superhydrophobic. If it was possible to reproduce said structures on the surface of a PDMS film, then a major hurdle in the project would be completed. The first step was to recreate the results on a glass substrate then move onto PDMS if the tests were successful. The experiment called for a chamber of approximately $5000cm^3$ with a relative humidity of 80%. A glass slide, coated with a layer of ECA is then placed inside the chamber to one side. At the same time $5ml$ of 0.8%wt ammonia solution is placed on the opposite side of the chamber. Within a few minutes the ECA film should become white in appearance and after 20 minutes the process is complete.

For the initial tests an environmental chamber was adapted to maintain the humidity required. An acrylic box was made to replicate the volume required and was placed within the chamber. With the equipment ready and the ammonia solution made, samples of Loctite® Powerflex Superglue cured in the described environment. The static contact angle for the glass slide is $25^\circ \pm 2^\circ$ but with the ECA coating it was increased to $92^\circ \pm 2^\circ$. This showed that the ECA increases the hydrophobicity but the low concentration of ECA in the glue may be responsible not producing higher angles. The Loctite® Powerflex Superglue only contained 60% ECA. More concentrated glues from No-Nonsense® and Loctite® were acquired. The No-Nonsense® glue has a concentration over 80% and Loctite® 4062 over 90%. With the more concentrated glues, the tests were repeated.

The second set of tests were more extensive. Comparisons of the two glues, comparisons of the ECA application method and a comparison against curing ECA in a normal atmosphere were conducted. In the comparison between the two glues it was not surprising that the Loctite® 4062 produced superior results to the No-Nonsense as it contains a higher concentration of ECA. The results of the deposition tests showed that thicker layers of the No-Nonsense® ECA produced larger features on the surfaces and higher contact angles. But for thinner layers the Loctite® outperformed the No-Nonsense®. The most promising result were seen for the Loctite® ECA, cured in the humid ammonia environment, that had been spun onto a glass surface. Advancing contact angles of $126.1^\circ \pm 0.4^\circ$ were recorded but as with the majority of the tests the contact line became pinned as the droplet receded. One last attempt to push the contact angle into the superhydrophobic range was tried. The Loctite® samples were coated with the Granger's® solution to see if the chemical treatment on the structured surface would increase the hydrophobicity of the thin spun layers. The resulting layers had increase advancing contact angle reaching an average of $145.9^\circ \pm 0.9^\circ$ (Fig.2.8) and a receding angle of $130.4^\circ \pm 1.9^\circ$. This was much closer to the desired 155° for superhydrophobicity but it still fell short of the goal for superhydrophobic thin flexible films.

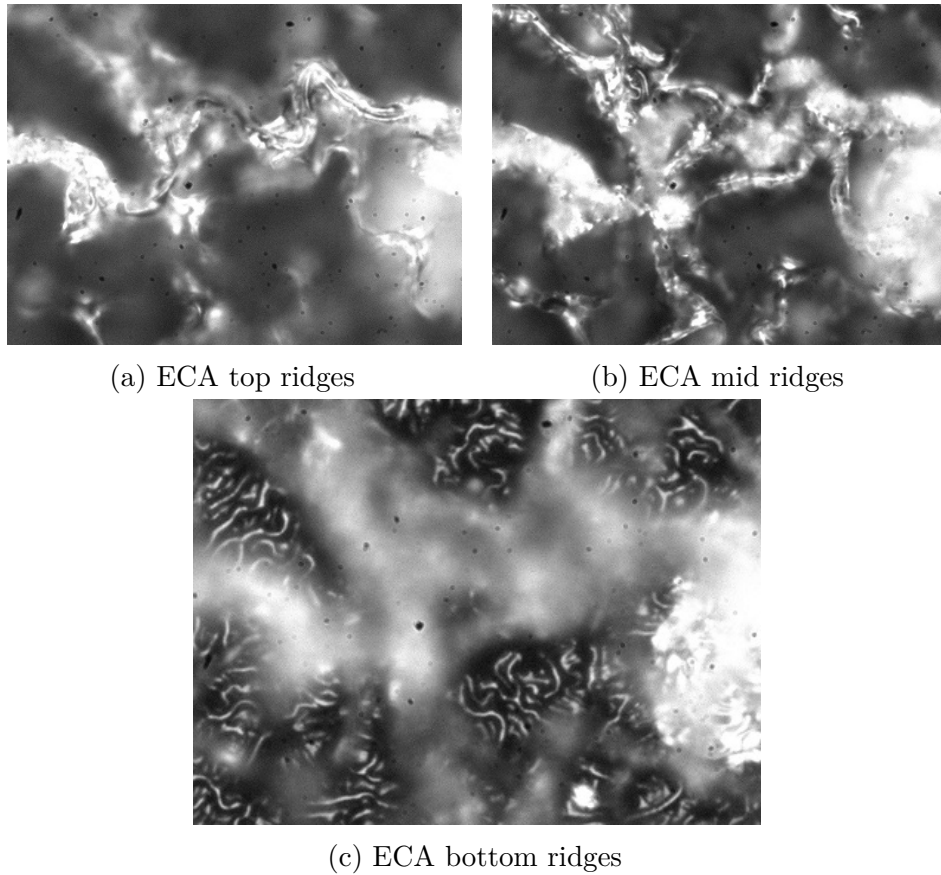


Figure 2.7: Images of a Loctite ECA Structure. There are 3 layers of ridges. The top layer is composed of the largest ridges that snake their way across the surface (top left). The middle layer is composed of a network of smaller ridges (top right). At the bottom is a layer of smaller wrinkles that cover the entire surface (bottom).

2.1.2 Development of CNP Coated PDMS

A method for the production of flexible nano-sensors is described in a paper by L. Yuan *et al.* [118]. The paper describes a method by which “highly flexible” and “robust” infrared nanosensors are fabricated on relatively thick PDMS surface with the use of Carbon Nano-Particles (CNPs). The carbon nano-particles are deposited onto ceramic strips using a simple flame synthesis process. The ceramic strips are mounted in an ethanol flame and held there until the surface of the strip went from clear to grey to matt black indicating that carbon nano-particle structures had grown and been deposited onto the surface of the strip. The soot covered strips are then placed faced down onto a partially cured PDMS substrate. Once the PDMS had fully cured the ceramic strips are peeled off leaving the carbon nano-particles attached to the surface of the PDMS. In the paper it was also reported that the PDMS with a soot layer displayed a contact angle of 150° with a sliding angle of approximately 4° .

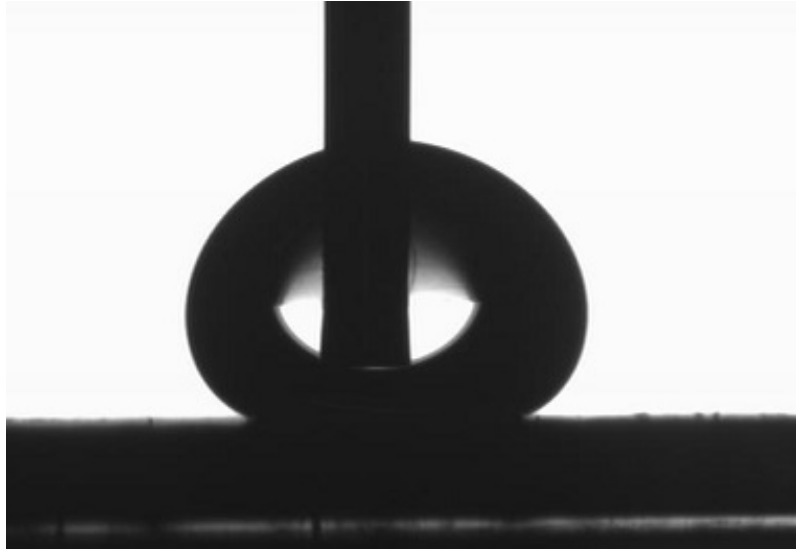


Figure 2.8: Image of an advancing droplet of water on an ECA surface.

The CNP structures that grow on the surface of the ceramic strips form a mesh-like network over the entire surface. This network becomes partially embedded into the PDMS during the curing process and is then held in place once the PDMS has fully cured. It is the nano-scale peaks and troughs, that are transferred to the PDMS, that form the necessary roughness to produce a highly hydrophobic surface. The nano-particles are not directly transferred onto the PDMS surfaces as the PDMS cures in the heat of the soot stream before a sufficient amount of nano-particles are deposited.

Initial tests of this fabrication method began with checking the validity of the hydrophobicity of the soot layer. Firstly, the flame synthesis process was recreated. Glass slides were positioned in an ethanol flame until a matt black layer of soot was seen on the surface of the slide. This took anywhere between 10 and 15 minutes. Next PDMS was mixed in a 10:1 ratio and partially cured until tacky. At this point the soot covered slides were placed face down onto the PDMS. After being fully cured advancing and receding angles were taken for the resulting soot covered PDMS. The advancing contact angle was measured at $158.8^\circ \pm 1.4^\circ$ and a receding angle of $152.8^\circ \pm 1.4^\circ$ (Fig.2.9). This is considered superhydrophobic. The drawback of this process is the slow sooting of the glass substrates.

In a paper by Mengnan Qu *et al.*, a method for producing relatively large areas of superhydrophobic films on a metal or glass surface is reported [113]. The paper

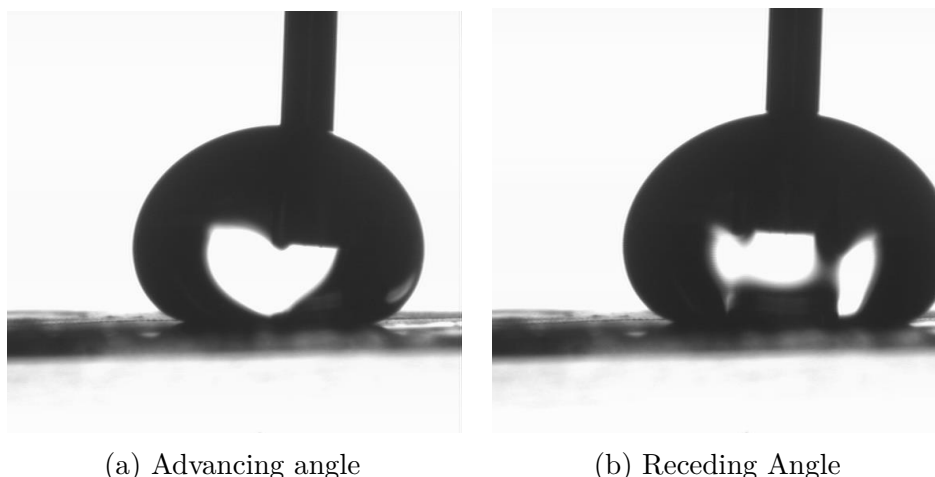


Figure 2.9: Images showing the advancing (left) and receding (right) contact angle on an ethanol soot PDMS surface.

describes a method for producing “stable anti-corrosive superhydrophobic surfaces”. The method is similar to that of Yuan *et al.* in that it involves the burning of a hydrocarbon to produce carbon nano-particles. Qu *et al.* use a longer, more complex chain hydrocarbon, more commonly known as rapeseed or Canola oil. The paper reports that 20ml of rapeseed oil is placed in a ceramic crucible with a cotton wick. This is ignited and an aluminium substrate is positioned at the top of the flame. This is held in place for 10 seconds until the surface is visibly matt black, at which point the metal block is repositioned in order to soot coat another section of the metal surface. They state that the contact angle produced is $156^\circ \pm 1^\circ$ with a sliding angle of $<3^\circ$. Again the CNP’s produce a superhydrophobic surface due to the network of particles on the surface.

By using combination of the processes developed by Yuan *et al.* and Qu *et al.* it was possible to create facile conformable superhydrophobic thin PDMS films.

2.1.3 Initial Production Method for Superhydrophobic PDMS

By combining the methods described previously, CNP coated PDMS thin films can be made. First a rolled raw cotton wick, 3cm in length and 1cm in diameter, is placed in a ceramic crucible. 20-30ml of rapeseed oil is then poured into the crucible and the wick is allowed to become saturated with the oil before the wick is lit using a naked flame. This then allowed to sit for 10 minutes to allow the flame to stabilise

and to start producing thick plumes of soot. Whilst the flame is stabilising, glass slides, $50\text{mm} \times 25\text{mm} \times 1\text{mm}$ are cleaned with distilled water and air blown dry. The glass slides are individually held at the top of the flame for between 45 to 60 seconds until the surface has become matt black. Once sooted, the substrate are placed soot side up on a heat resistant surface and allowed to cool.

The next step is to prepare the PDMS films on which the sooted glass slides will be placed. The PDMS is mixed in a 10:1 ratio and stirred vigorously for a minimum of 5 minutes. The mixture is then degassed in a vacuum desiccator for approximately 30 minutes in order to remove any air bubbles introduced into the mixture during the stirring process. Once degassed, the PDMS is spun onto acrylic slides, $75\text{mm} \times 40\text{mm} \times 4\text{mm}$ in dimension, using an Electronic Micro Systems Lmt Model 4000 Photoresist spin coater with a modified spin head. The acrylic slides are significantly larger than the sooted glass slides, 10% of the glass slide dimensions on each side, in order to negate the effects of the edge defects that occur toward the edges of the acrylic slides when the PDMS is spun on the surface. Once the PDMS films have been prepared, they are placed in the centre of a 60°C oven for between 30 and 35 minutes, until the surface has become tacky. At this stage the sooted glass slides are placed face down on the centre of the of the partially cured PDMS surfaces. The combination is then placed in another 80°C oven for at least 1 hour to ensure the PDMS has fully cured. The combined slides are allowed to cool before the glass slide is carefully removed, leaving the embedded soot CNP structure behind. The result is a CNP coated PDMS thin film that is relatively robust, flexible and superhydrophobic. The advancing contact angle for CNP coated PDMS was measured at $160^\circ \pm 2^\circ$, with a receding angle of $158^\circ \pm 1^\circ$ (Fig.2.10).

Once the process was fully developed, it was adapted for use on quartz crystal microbalances (QCM) in order to test the effect of electrowetting on superhydrophobic QCMs [119].

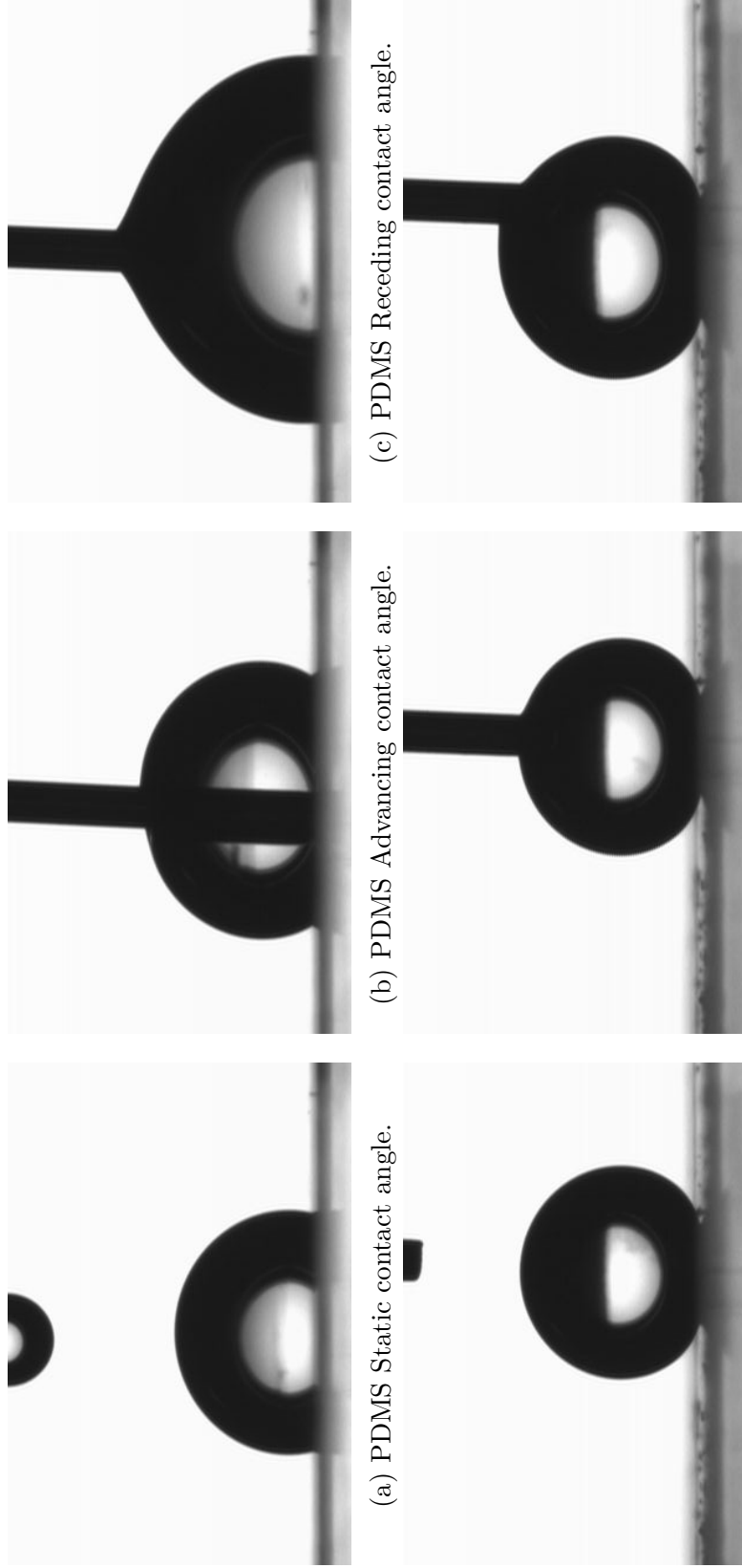


Figure 2.10: Images comparing the Static (left), the advancing (middle) and receding (right) contact angles for uncoated and CNP coated PDMS.

2.2 Suggested Work and Preliminary Tests

Alternative Ways for Soot-Coating PDMS

In order for the soot coated PDMS surface to be of future usefulness, an alternative method for their production may be needed. If it were possible to apply the PDMS directly to a surface prior to the deposition of the carbon nano-particles, it would allow for the coating of more complicated volumes without seams or issues with adhering cured PDMS to the surfaces. A spray coating method where carbon nano-particles are forced onto the partially cured PDMS surface using an air-jet may be possible [120,121]. This would allow a surface to be conformable to many different volumes and allow for the hydrophobic coating to be added directly to the object.

Another way of improving the sooting method may be to improve the soot application method. Laser printers use a charged drum to electrostatically hold a powder which is then transferred to the printing substrate after laser processing to create the image. In early versions of the technology, the ink consisted mainly of carbon and iron oxide. It may be possible for the transfer method to be adapted for use with the PDMS substrates. It would allow for a lower temperature process and a more controlled curing method. It would also mean a continuous manufacturing method may be possible if it were implemented with a rolling pre-curing process for the PDMS.

Multi-scale Roughness on PDMS Substrates

In order to create soot PDMS surfaces with a third larger scale of roughness, preliminary tests were performed whereby the method used to produce larger soot PDMS areas (section 4.2.3) is used to deposit soot onto knurled patterned metal plates, hand files used for general filing work, which is then deposited onto partially cured PDMS. Three different file types were tried, each having a different size knurling pattern. They are smooth, second and bastard cut files. One theory as to how the “bastard” file received its name is that it is neither a course file nor a fine file and therefore is the bastard of the two. The knurled pattern is created on the

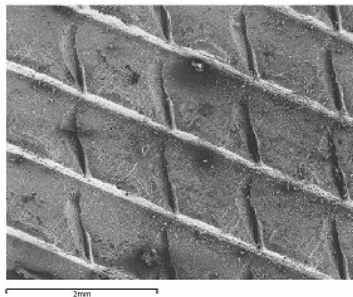
surface of the rectangular plates by rolling the plates between toothed wheels under pressure. The spacing of the teeth on the wheels determines the spacing of the ridges on the plate surface. The rolling process is performed twice on each surface in two perpendicular directions in order to create a cross-hatch pattern.

Scanning electron microscopy (SEM) was used to image the file surface, PDMS cast on the files and soot PDMS made using the files as the soot transfer plates (Fig. 2.11). The SEM images were used to determine the dimensions of the troughs on the file surface and the ridge structures produced on the PDMS and soot PDMS surfaces. The spacings and sizes are shown in table 2.1.

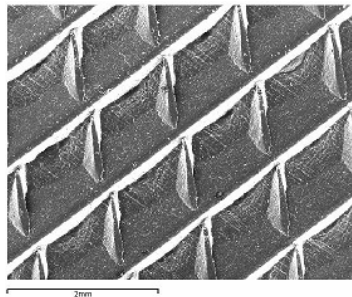
Contact angles for the soot PDMS ridged surfaces are shown in table 2.2. The contact angle measurements show that the smooth cut file produced the highest angles at 148° advancing and 146° receding. This is not quite superhydrophobic. This may be due to the production method. Further tests are needed to refine the timings for the deposition process in order to accurately recreate the surface features as well as transfer the required amount of soot in order to produce a superhydrophobic soot PDMS surface with multiple scales of roughness. There may also be an issue with the spacing of the ridges. In the literature, ridge spacing has generally been $100\mu m$ or below. The smooth surface is close to being superhydrophobic but the ridges are approximately $500\mu m$. A reduction in this distance should push the angle upward producing a superhydrophobic film.

	Ridge Separation (mm)	Error (mm)	Ridge Width (mm)	Error (mm)
Bastard File	1.030	0.005	0.137	0.008
PDMS negative of Bastard File	1.020	0.006	0.118	0.003
Soot PDMS negative of Bastard File	0.979	0.006	0.235	0.008
Second File	0.862	0.008	0.132	0.002
PDMS negative of Second File	0.807	0.004	0.129	0.005
Soot PDMS negative of Second File	0.79	0.03	0.197	0.009
Smooth File	0.511	0.007	0.051	0.003
PDMS negative of Smooth File	0.516	0.006	0.093	0.003
Soot PDMS negative of Smooth File	0.510	0.005	0.111	0.002

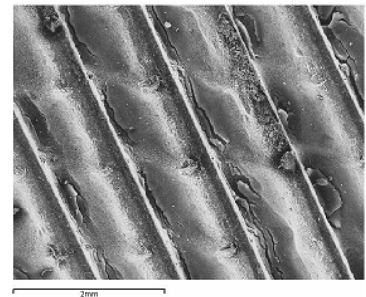
Table 2.1: Average dimensions of ridge structures on and replicated from the Bastard, Second and Smooth cut files.



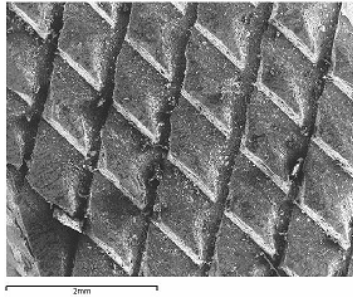
(a) Bastard cut file.



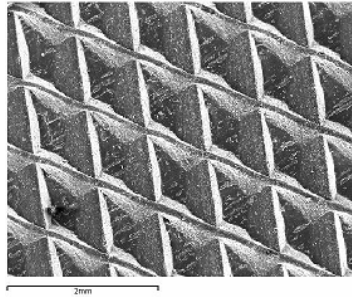
(b) PDMS cast on a bastard cut file.



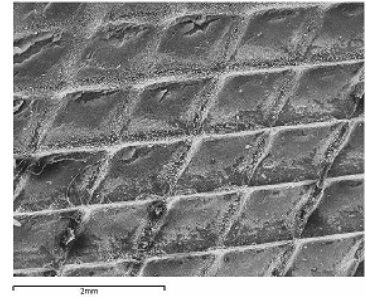
(c) Soot PDMS cast on a bastard cut file.



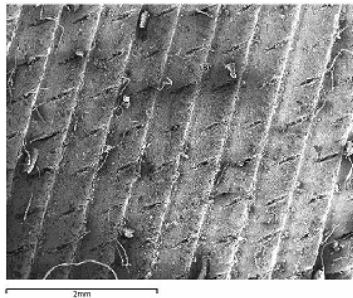
(d) Second cut file.



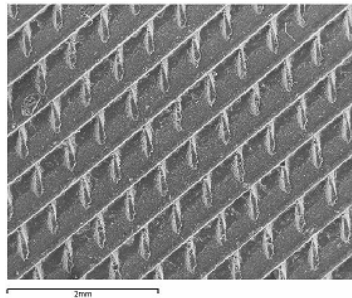
(e) PDMS cast on a second cut file.



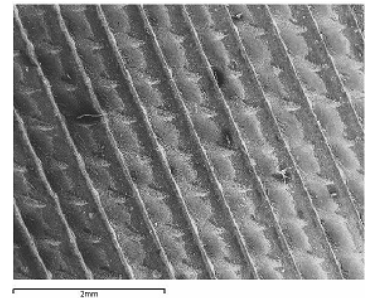
(f) Soot PDMS cast on a second cut file.



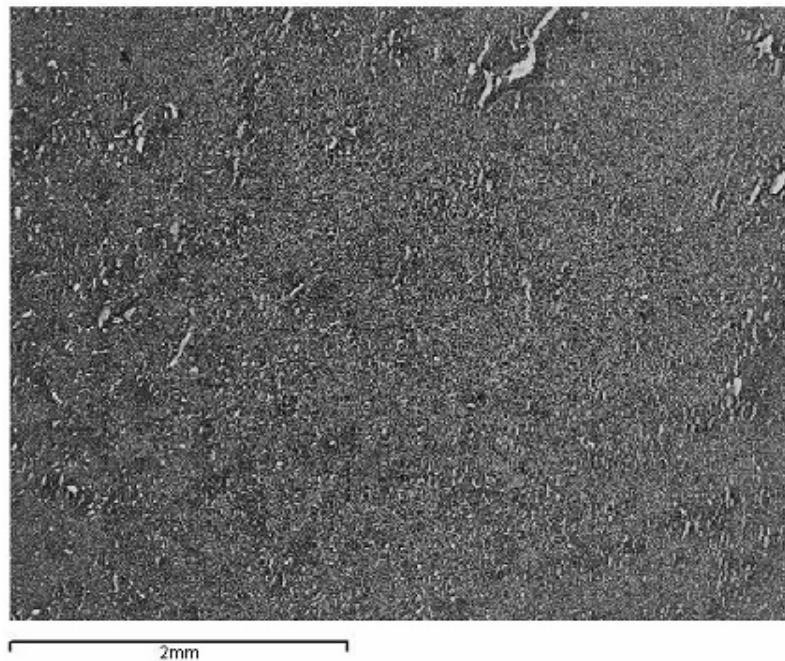
(g) Smooth cut file.



(h) PDMS cast on a smooth cut file.



(i) Soot PDMS cast on a smooth cut file.



(j) Flat soot PDMS.

Figure 2.11: SEM images of the files and the substrates cast on the different surfaces.

	Advancing Angle (degrees)	Error (degrees)	Receding Angle (degrees)	Error (degrees)
PDMS cast on a bastard cut file	137	1	PINNED	
Soot PDMS cast on a bastard cut file	143	1	141	1
PDMS cast on a second cut file	144	1	109	9
Soot PDMS cast on a second cut file	148	1	143	2
PDMS cast on a smooth cut file	139	3	99	2
Soot PDMS cast on a smooth cut file	148	1	146	1
PDMS	123	1	82	1
Flat Soot PDMS	163	1	156	1

Table 2.2: Average contact angle for PDMS and soot PDMS cast on the 3 different files and a flat surface.

Chapter Summary

This methods chapter describes the novel fabrication processes involved in the development of the flexible superhydrophobic carbon nano-particle thin substrates. This has produced a surface with increased usability due to its flexible and conformable abilities whilst maintaining the anti-wetting properties of the surface structure.

The next three chapters report on the experiments performed with the flexible surface in order to test the effects of surface roughness on the droplet wrapping capillary origami process, the possible use of the superhydrophobic surface as a method to reduce drag and as a way to repel snails.

Chapter 3

Capillary Origami

This chapter will describe the work on capillary origami and the droplet wrapping process. The background included describes the development of the field and some of its uses. It will then go on to describe how the flexible superhydrophobic surfaces were tested in the Wenzel and Cassie-Baxter wetting states and the outcomes of these tests.

3.1 Background of Self-Assembly and Capillary Origami

In 1993 Syms and Yeatman reported on a method where surface tension forces were used to fabricate 3D micro-structures [122]. Using lithography techniques, solder pads were positioned over a hinge joint between two micro-scale plates. Heating the solder caused it to melt and the surface tension of the solder caused it to form a spherical shape and adhesion with the plates caused them to move with the droplet, out of the horizontal plane. Over the next few years, this technique developed and allowed for the production of more complex hinged structures and micro-devices made of metallic and polycrystalline materials [123–125]. Other forms of self-assembly have been developed through which small-scale structures can be made. The methods include pneumatic assembly, magnetic assembly, polymer manipulation and muscular actuation [126]. Photo-sensitive polymers have also been used to create self-assembled structures. Ryu *et al.* reported that by exposing specific polymers to light, it is

possible to create a photo-chemical response which creates motion of the joints to produce 3D structures [127]. This method was termed “*Photo-Origami*”.

Elast-capillarity is the term coined to describe the interaction of liquids with flexible materials. On the macroscopic scale, capillary forces are outweighed by the gravitational forces but on the millimetric scale and below the capillary forces begin to dominate. This is because, for a given structure with dimensions of L , the gravitational forces are proportional to L^3 whilst the capillary forces are proportional to L . This means that as the dimensions reduce the capillary forces reduces at a lesser rate than the gravitational forces and eventually become dominant. This is the reason a droplet with a diameter below the capillary length, L_C (see section 1), forms a spherical shape as the surface tension forces work to reduce the surface area to volume ratio as well as dominate the gravitational forces. This is why wet hair coalesces and clumps together. Hair, being a flexible material, cannot overcome the surface tension forces which draw the hairs together [128]. Olives discussed the effects of capillarity and elasticity on thin plates and how the assumption that the surface does not deform under the influence of a liquid is not always true [129]. These effects have become of increased interest with the development of sub-millimetre devices. The construction of many MEMS involves wet lithography [130]. During these processes, as liquid layers dry-out, the capillary forces generated can deform surface structures [131, 132]. With the need for smaller and smaller devices, it has become essential to understand the processes that occur when the capillary force is dominant.

When examining the interaction of liquids with thin films, an important parameter is the elastocapillary length, L_{EC} . It is related to the bending rigidity, κ_B [133, 134], and the surface tension, γ .

$$\kappa_B = \frac{Eh^3}{12(1 - \nu^2)} \quad (3.1)$$

$$L_{EC} = \sqrt{\frac{\kappa_B}{\gamma}} = \sqrt{\frac{Eh^3}{12\gamma(1 - \nu^2)}} \quad (3.2)$$

Where E = Young's Modulus, h =thickness and ν = Poisson's spaceratio

It defines the length scale when a flexible substrate will spontaneously deform under the influence of capillary forces as it compares the forces generated by a liquid when in contact with a flexible substrate [135]. $L_{EC} \propto h^{3/2}$ so the thickness of the surface plays a crucial role when determining the wrapping characteristics of the flexible surface around a droplet.

When a wetted flexible plate of side length L , comes into contact with a similarly wetted cylinder of radius R , it will deform around the cylinder if the surface energy, γwL , overcomes the elastic energy, $\kappa_B wL/2R^2$, where w is the width of the plate [135]. Therefore, by comparing these energies we can determine when a plate will wrap a wetted cylinder [3, 136].

$$\gamma w L > \frac{\kappa_B w L}{2R^2}$$

$$2R^2 > \frac{\kappa_B}{\gamma}$$

$$\sqrt{2}R > \sqrt{\frac{\kappa_B}{\gamma}}$$

$$\sqrt{2}R > L_{EC}$$

$$R > \frac{L_{EC}}{\sqrt{2}} \tag{3.3}$$

If the cylinder is replaced with a droplet, equation 3.3 determines the minimum radius of droplet needed, for a given substrate thickness, in order for the substrate to wrap around the droplet.

Py *et al.* performed experiments with thin ribbons of PDMS in order to determine a value of L_{EC} rather than calculating the value numerically [3]. It was found that for long ribbons, the PDMS strips would completely wrap a droplet, with the ends of the ribbon making contact to form a racket-shape. Py *et al.* found that the width, d , of the racket-shape is proportional to the elastocapillary length where, $d = 0.89L_{EC}$. These racket structures have also been seen with carbon nano-tubes [137] and during simulations of graphene layers [138, 139].

For thin sheets or plates, the same processes apply. When a droplet comes into contact with a thin membrane it will deform and wrap the droplet in order to reduce the liquid/vapour area at the cost of increasing the elastic energy. Py *et al.* looked at the case where equilateral triangular substrates and square PDMS films come into contact with a droplet of water [3]. The triangular substrates had a side length of L , thickness of h and a rigidity proportional to Eh^3 . When a droplet of water was deposited onto the surface of the membranes and the side length is sufficiently

large, the membrane will wrap the droplet, with the corners of the membrane coming together to form a tetrahedron as the droplet evaporates. This occurs if the gain in surface energy, $\sim \gamma l^2$, is greater than the gain in bending energy, $\sim \kappa_B$. If the length is greater than the critical length, L_{crit} , then spontaneous wrapping will occur, where $L_{crit} \propto l_{EC}$. This value was determined experimentally for different thicknesses and Py *et al.* found that for triangular surfaces $L_{crit} \simeq 11.9L_{EC}$ and for square surfaces $L_{crit} \simeq 7.0L_{EC}$. These wrapping experiments challenge our understanding of hydrophobicity. Gao and McCarthy demonstrated how seemingly water repellent surfaces will wrap droplets if they are thin enough. They showed how films of Teflon[®] spontaneously wrap a droplet of water, even though the material is known to be hydrophobic [10]. This effect has been explained by McHale as being due to the change in the balance between the interfacial and bending energies [11]. McHale *et al.* went on to examine the effects of surface roughness on the wrapping processes for ribbon surfaces with rigid topographies [2]. By looking at the change in surface energies for the Wenzel and Cassie-Baxter wetting states, it was determined that the change in energy can be determined, where

$$\frac{\Delta F_T}{2\pi R w} = -\gamma_{LV}(\cos \theta_T + 1) + \frac{\kappa_B C_1^2}{2} \quad (3.4)$$

Where ΔF_T = change of energy depending on the wetting regime

R = radius of the droplet

w = width of the ribbon

θ_T = contact angle depending on the wetting regime

κ_B = bending rigidity

C = curvature

This is valid for textured ribbons where $L = 2\pi R$. As $C = 1/R$, equation 3.4 can be rewritten as,

$$R_C = \left(\frac{\kappa_B}{2\gamma_{LV}(\cos \theta_T + 1)} \right)^{1/2} = \left(\frac{1}{2(\cos \theta_T + 1)} \right)^{1/2} L_{EC} \quad (3.5)$$

Equation 3.5 shows that there is modified critical droplet radius, R_C , for capillary origami where rough surfaces exist. Equation 3.5 also shows that depending on the wetting regime, the wrapping process can be either enhance or suppressed. For $\theta_T > 120^\circ$ the expression in equation 3.5 before L_{EC} is greater than 1 and $R_C > L_{EC}$. Where $\theta_T < 120^\circ$ the expression is less than 1 and $R_C < L_{EC}$.

For the Cassie-Baxter state, $\cos \theta_T = \cos \theta_{CB}$ and as $\theta_{CB} \rightarrow 180^\circ$, R_C approaches infinity. This implies that in a Cassie-Baxter scenario the wrapping process is suppressed.

For the Wenzel case, $\cos \theta_T = \cos \theta_W$ which is positive when $\theta > 90^\circ$ and negative when $\theta < 90^\circ$. When θ is positive R_C is reduced as $\theta \rightarrow 0^\circ$ or as the roughness increases. The reduction in R_C implies a substrate can be wrapped into a tighter curve meaning smaller droplet radii can be used to wrap a surface due to the increased adhesion, which is an enhancement of the capillary origami process.

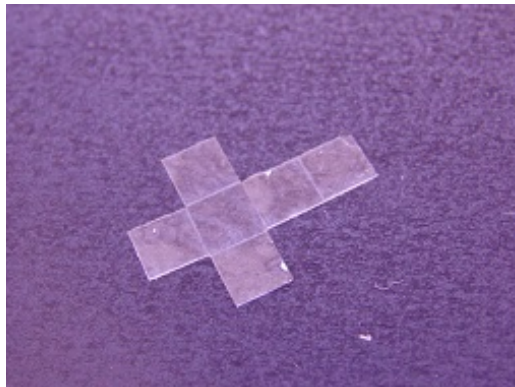
Uses of Capillary Origami

Capillary Origami has been used to produce polymer, semiconductor and metallic microstructures. Silicon nitride micro-objects, $50\mu m$ to $100\mu m$ in size, have been fabricated in combination with micromachining [140], as have silicon photovoltaic spherical objects [141]. Silicon and germanium devices have also been made for chemical sensing using capillary origami [142]. The capillary bending technique has also been exploited to form ordered carbon nano-tube surfaces and arrays of nano-tube pillars [143–145].

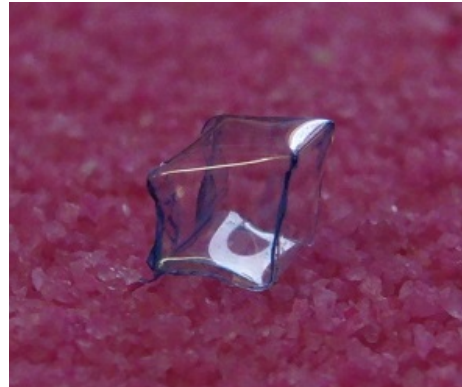
3.2 Capillary Origami with a Novel Surface

3.2.1 Initial Experiments

The first step in determining the possibility for capillary origami was to ascertain whether or not it was possible to produce thin, reproducible and tailored PDMS membranes. A variety of thicknesses were made using the spin coater. By varying the speed of the spin coater between $1000RPM$ and $2000RPM$, thicknesses ranging from $30\mu m$ to $80\mu m$ can be made. This thicknesses range of PDMS had previously been tested by C.Py *et al.* [3]. The initial challenge was to find a method for producing identical two dimensional shapes. The purpose of this was to determine if it was possible to produce membranes in the correct dimension range to test capillary origami as well as to fabricate identical membranes for repeatable systematic testing. Using the laser cutter it was possible to design, cut out and even score these shapes, using low power settings and high pass speeds (3 passes at power 1%, speed 1.8% and PPI 500 for cutting). A variety of shapes were cut and tested at this early stage, including crosses to form cubes (Fig.3.1), triangles to form tetrahedrons (Fig.3.2), and flower-shaped membranes to form sphere-like objects.



(a) PDMS cross membrane to form a cube.



(b) Cube formed through the action of the capillary force.

Figure 3.1: Formation of a cube solely through the forces generated by a droplet of water.

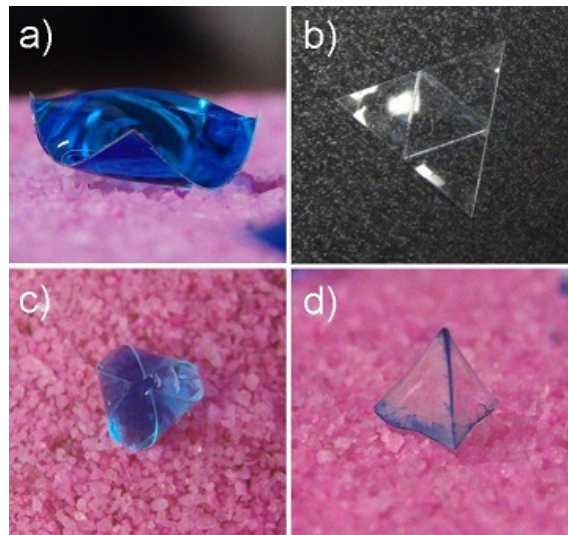


Figure 3.2: Effect of a droplet of blue-dyed water on a PDMS triangular membrane: a) blue-dye water droplet causes the edges of the membrane to bend, b) initial triangular-shaped PDMS thin film with score lines for folding, c) the evaporating droplet causes the membrane to fold around it, and d) tetrahedron left after all the liquid has evaporated [2].

3.2.2 Replication of Previous Work and Testing of Uncoated Substrates

To test the effects of hydrophobicity on the capillary origami process, it was prudent to first see if it was possible to recreate the work of C.Py *et al.* by determining the critical wrapping length for uncoated PDMS triangular substrates, whose thicknesses range from $35\mu\text{m}$ and $75\mu\text{m}$ [3]. The critical wrapping length for the substrates is the minimum side length of the triangular surface which will completely encapsulate a droplet of water as the droplet evaporates, to form a tetrahedron (Fig.3.3).



Figure 3.3: Sequence showing the six stages of a completely wrapped droplet of water on a PDMS triangular membrane as the water droplet evaporates.

In order to do this, seven different thicknesses of PDMS were made, using the standard procedure for mixing PDMS, as discussed earlier. These ranged from $33\mu\text{m}$ to $78\mu\text{m}$ thick. The thicknesses of the PDMS sheets were determined from the difference in the mass between the uncoated and coated acrylic slides, taking into account the density of the PDMS and the area of the acrylic slide. The membranes

were made on $75\text{mm} \times 40\text{mm} \times 4\text{mm}$ acrylic slides using the spin coater. Once fully cured, the triangular membranes were cut using the laser cutter. Multiple triangles, ranging in side length from 3mm to 14mm , in steps of 0.25mm , were cut out of each sheet. For one thickness at a time the substrates were laid out on a hydrophobic surface. A droplet of water was placed on the surface of each membrane, enough to completely cover the entire surface, and then observed throughout its entire evaporation process to determine whether or not the membrane completely encapsulated the droplet through its drying routine. For each substrate the outcome of the drying routine was documented.

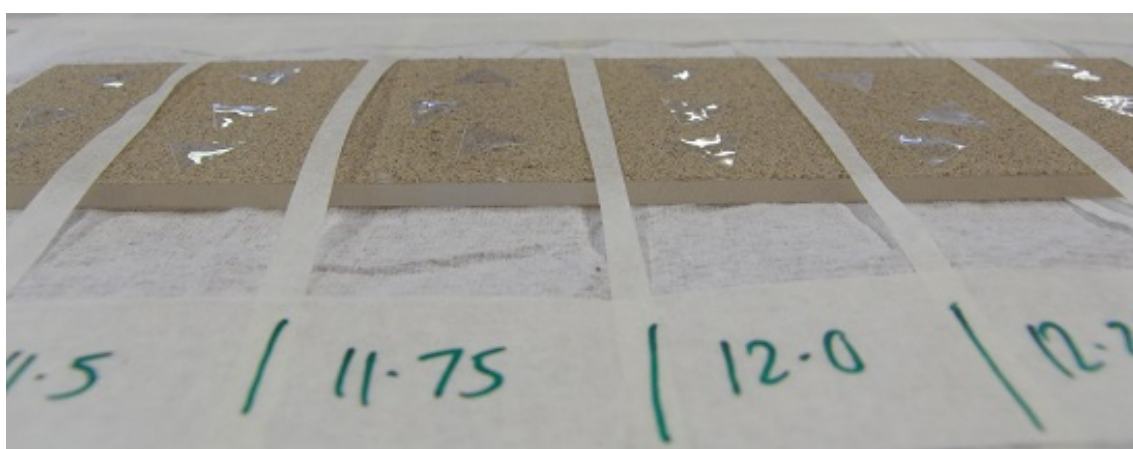


Figure 3.4: Setup for the capillary origami tests. PDMS triangles are laid out on a hydrophobic surface in side length order.

3.2.3 Superhydrophobic Modification of the Wrapping Experiments

With a way to change the hydrophobicity of the surface of the PDMS, the effects of superhydrophobicity on the origami process could now be studied. In order to make the PDMS superhydrophobic a thin CNP layer was added, using the process described previously. Once the CNP layer had been added to the surface, the same procedures for making the triangular substrates used to make the uncoated triangles was used. The thickness of the superhydrophobic films was measured using a Veeco Dektak 6M stylus profilometer. During these tests, it quickly became evident that a complete suppression of the wrapping process was present. Even with the thinnest and largest triangular substrates, those expected to wrap in every test, there was

no noticeable wrapping, or even bending, of the substrates under the influence of a water droplet (Fig 3.5).

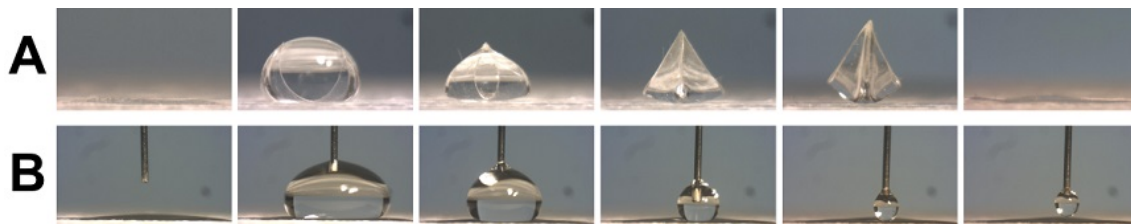


Figure 3.5: Comparison of the wrapping process for uncoated(A) and CNP-coated(B) triangular PDMS substrates over time as the water droplet evaporates.

3.2.4 Liquid Determination

The suppression of all wrapping is a result in itself but in order to test the effects of changing hydrophobicity, a liquid with a lower surface tension was needed that would allow a comparison of the uncoated and CNP coated PDMS surfaces to be conducted. A 2-propanol, aka isopropanol (IPA), solution appeared to be a good starting point. When a droplet was placed onto the CNP PDMS surface, it wetted the surface without damaging it and the superhydrophobicity was recovered once the IPA had completely evaporated away. A series of solution of IPA in water were made and the contact angles for each on superhydrophobic PDMS was measured (Fig.3.6).

For a 30% solution the contact angle is less than 90° indicating that the solution wets the surface of the PDMS. It also displayed advancing and receding angles on uncoated PDMS of $68^\circ \pm 2^\circ$ and $45^\circ \pm 3^\circ$, respectively. This would allow the solution to sufficiently wet both surfaces and to test the wrapping process. A Du Nuoy ring test of the 30% solution gave a surface tension of $26.3 \pm 0.1 mN.m^{-1}$.

The critical length for wrapping was determined, using the same methods as described in section 3.2.2, using the 30%wt IPA solution for the uncoated and soot coated PDMS substrates.

Even though it was possible to test using the IPA solution, a problem arose. As the solution evaporated, the ratio of the two constituent parts changed during the tests. This meant that the surface tension and therefore the contact angle of the solution changed during the experiments. An azeotropic solution was needed in

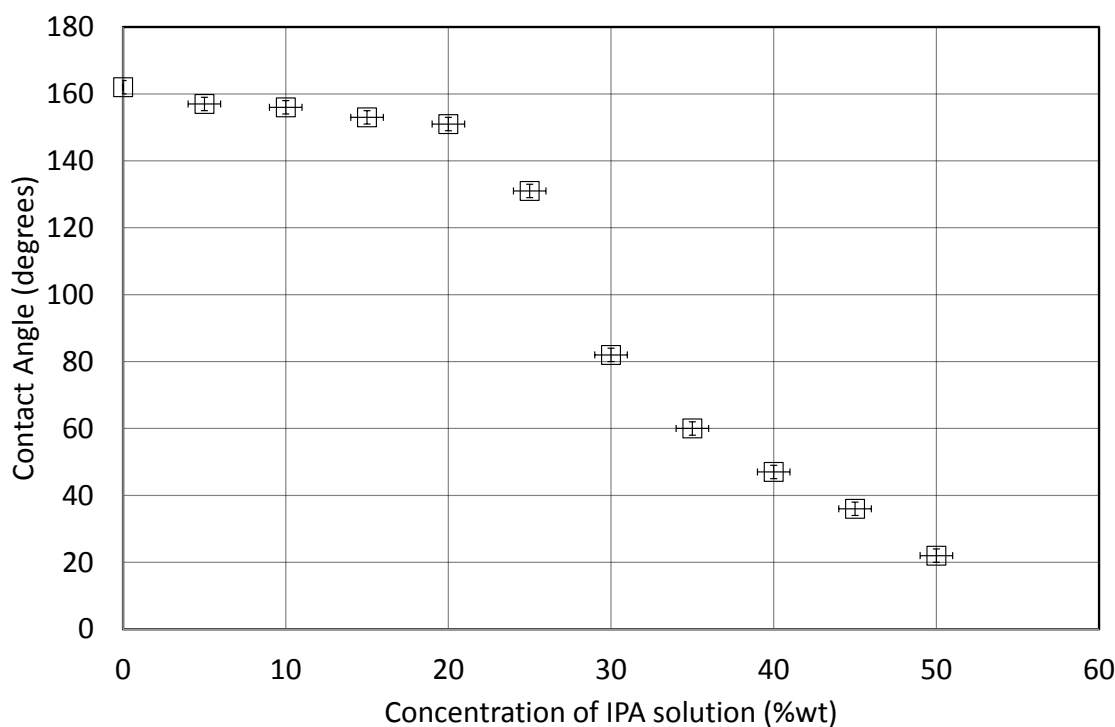


Figure 3.6: Contact angle for different concentrations of Isopropanol in water.

order to maintain these two properties throughout the tests. A two-part azeotropic solution would mean that both liquids in the solution would evaporate away in the same ratio as the solution, maintaining its properties throughout.

The azeotrope for IPA consists of 87.9%wt IPA in water. This solution completely wetted the PDMS surface and no wrapping was observed. This meant another azeotropic solution was needed. The liquids tested were

- 1-Propanol. The azeotrope is 28.1%wt 1-Propanol in water.
- 1-Butanol. The azeotrope is 47.7%wt 1-Butanol in water.
- Cyclohexanol. The azeotrope is 20%wt Cyclohexanol in water.
- Pentanone. The azeotrope is 4.6%wt Pentanone in water.
- Allyl alcohol. The azeotrope is 72.01%wt Allyl alcohol in water.

The data was found in the CRC Handbook of Chemistry and Physics [146].

When tested on the CNP coated surface only the Allyl alcohol azeotrope was appropriate. The 1-propanol solution has too low a surface tension and completely wets the surface. The 1-butanol solution is only partially miscible so the butanol

wets the surface whilst the water is left on the surface. The cyclohexanol solution has too high a surface tension and remains hydrophobic and the pentanone azeotrope is also too hydrophobic. The allyl alcohol azeotrope, on the other hand, has a surface similar to the 30%wt IPA solution, at $28.0 \pm 0.2 \text{mN.m}^{-1}$, so partially wets the surface, is fully miscible and is non-reactive with the surface. The allyl alcohol azeotrope became the solution of choice to compare the uncoated and soot coated PDMS substrates. Using the allyl alcohol azeotrope the critical length for wrapping was determined, using the same methods as described in section 3.2.2.

3.2.5 Determination of Young's Modulus for CNP Coated Surfaces

In order to calculate the elastocapillary length for each thickness of PDMS substrate, the Young's modulus was needed [3]. Since the soot coating effects the rigidity of the PDMS substrate, a way was needed to determine the modulus, E , of the surface. The cantilever deflection method was used to calculate this value.

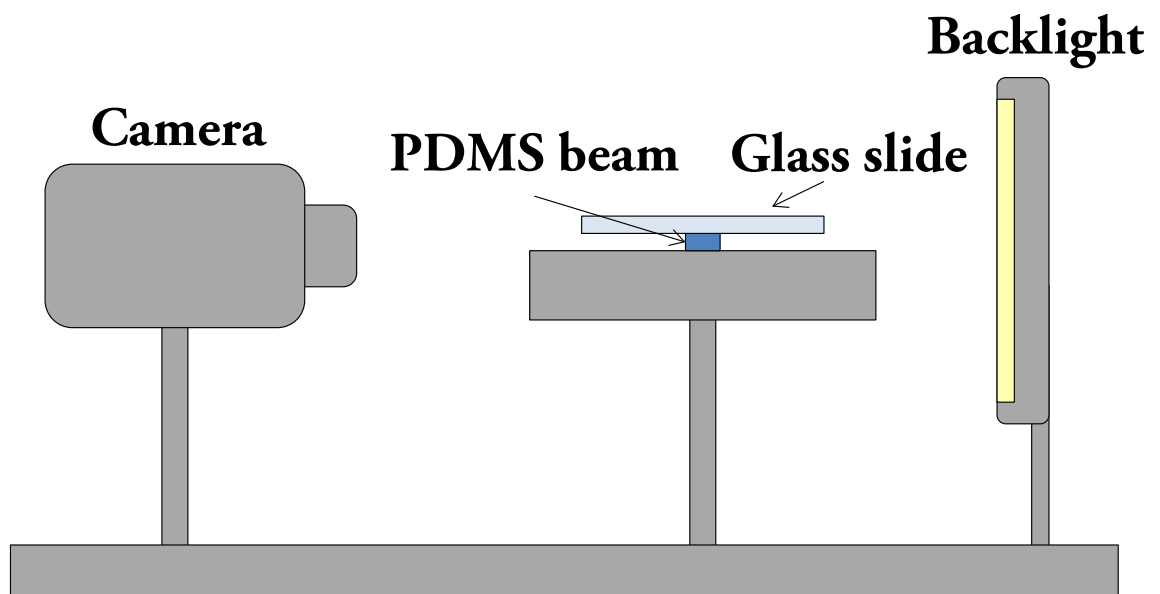


Figure 3.7: Illustration of the cantilever deflection set-up (sideview) used to measure the deflection of the PDMS beams. Both the camera and PDMS beam are mounted horizontally.

Using this method, one end of a PDMS strip is fixed horizontally, whilst the other unattached end is allowed to deflect under the influence of gravity alone. The

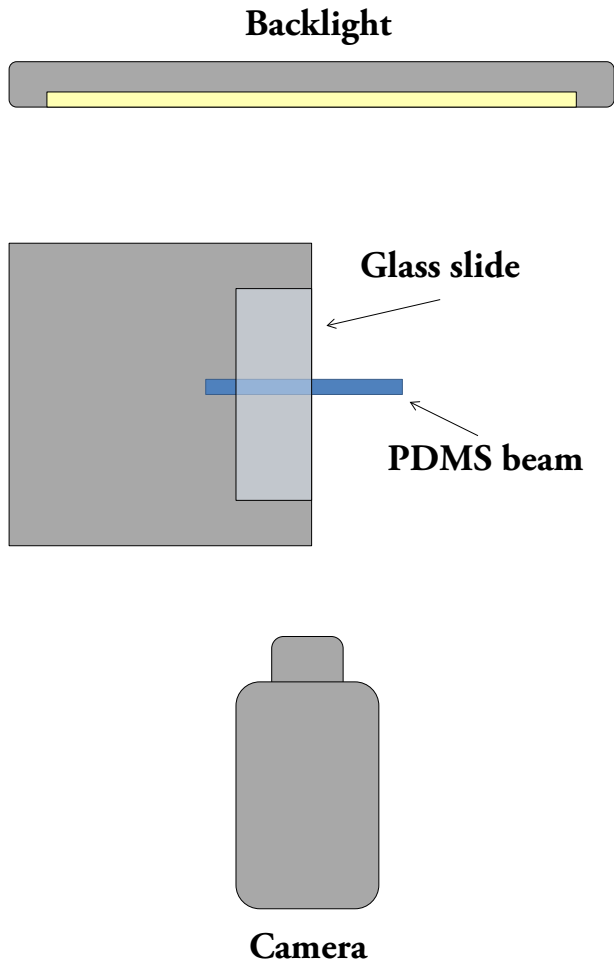


Figure 3.8: Illustration of the cantilever deflection set-up (top view) used to measure the deflection of the PDMS beams. The PDMS beam is perpendicular to the camera.

maximum deflection of the free end was measured for 1mm wide strips of PDMS and soot coated PDMS for varying strip lengths of between 4.00mm and 8.50mm ($\pm 0.06\text{mm}$). The uncoated PDMS had a thickness of $64\mu\text{m}$ and the soot coated PDMS had a thickness of $84\mu\text{m}$. In order to ensure the strips were not bent during removal from the acrylic slides, they were floated on a film of IPA, which acted as a releasing agent. Each strip was measured multiple times, facing both upward and downwards.

3.3 Results

Here the results of the various characterisation tests performed in order to determine the properties of the composite surface are included, as well as the results of the wrapping tests with different liquids on uncoated and soot coated substrates.

In order to test for the effects of a superhydrophobic surface on the capillary origami process, first the novel conformable surfaces were characterised using imaging techniques and contact angle analysis. Part of this process was to determine the Young's modulus of the coated films to account for any variation in the flexural rigidity of the substrates. Following this, the wrapping processes for triangular substrates were analysed, using the methods devised by Py *et al.* [3].

3.3.1 Determination of the Young's Modulus

PDMS and soot-coated PDMS strips, approximately 1mm in width, ranging in length from 4.00mm to 8.50mm ($\pm 0.5\text{mm}$) were tested using the cantilever deflection method. The thickness of the uncoated and soot-coated PDMS were $82\mu\text{m}$ and $64\mu\text{m}$, respectively. The thicknesses were measured using a Veeco Dektak 6M stylus profilometer. They were positioned in front of a horizontal camera and the deflection was recorded for the strips in the face up and face down positions.

The cantilever is believed to behave in a linear manner if $y_{\text{max}}/L < 0.2$ and its Young's modulus can be found using equation 3.6.

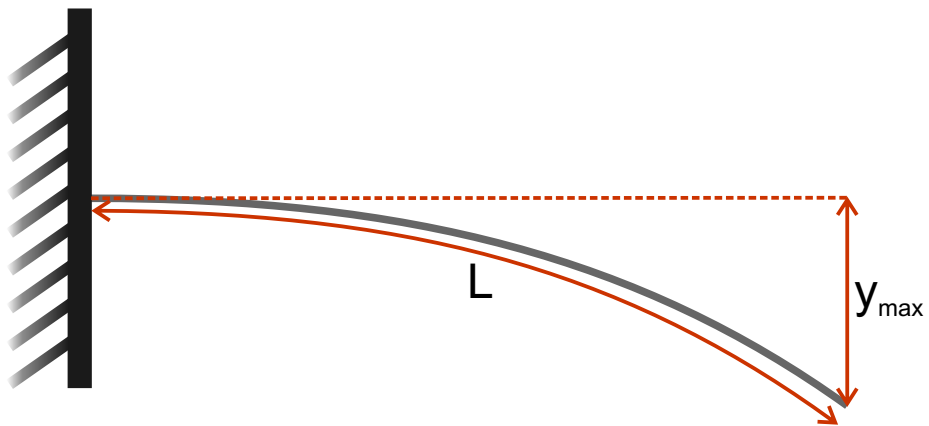


Figure 3.9: Illustration of the cantilever deflection test and key measurements.

$$y_{max} = \frac{PL^4}{8EI} = \frac{12\rho ghL^4(1-\nu^2)}{8Eh^2} = \frac{3\rho gL^4(1-\nu^2)}{2Eh^2}$$

$$\text{where } P = \rho gh \quad \& \quad EI = \frac{Eh^3}{12(1-\nu^2)}$$

$$\therefore y_{max} = \frac{12\rho ghL^4(1-\nu^2)}{8Eh^2} = \frac{3\rho gL^4(1-\nu^2)}{2Eh^2}$$

$$\therefore E = \frac{3\rho gL^4(1-\nu^2)}{2y_{max}h^2} \quad (3.6)$$

Where the deflection of the beam exceeded 20% of its length i.e. $y_{max}/L \geq 0.2$, the deflection was considered to be outside of its linear-relationship range and a large deflection correction factor can be applied in order to find the value of Young's modulus [147]. The calibration factor is found from the relationship between y_{max}/L and $PL^3/8EI$.

Equation 3.7 shows how the Young's modulus is calculated in the large deflection range.

$$EI = \frac{\rho ghL^3}{\gamma}$$

$$\text{also } EI = \frac{Eh^3}{12(1-\nu^2)}$$

$$\therefore \frac{Eh^3}{12(1-\nu^2)} = \frac{\rho ghL^3}{\gamma}$$

where γ is the correction factor calculated from Ref. [147] where $y_{max}/L > 0.2$

$$\therefore E = \frac{\rho gL^3}{12\gamma h^2(1-\nu^2)} \quad (3.7)$$

Tables 3.1 and 3.2 show the data for the uncoated and soot coated PDMS, respectively. Figures 3.10 and 3.11 are plots of the uncoated and soot PDMS beam deflections.

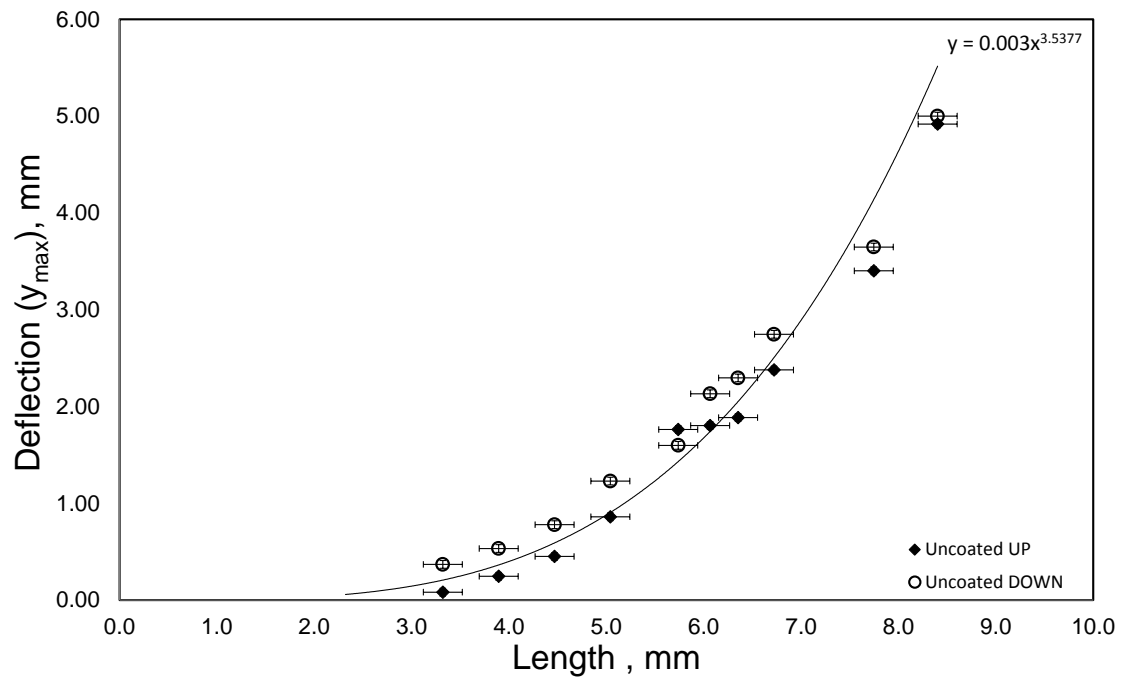


Figure 3.10: Graph of maximum deflection versus length for uncoated PDMS. The line of best fit has been added in order to compare the Uncoated PDMS with the Soot-coated PDMS in Fig.3.11.

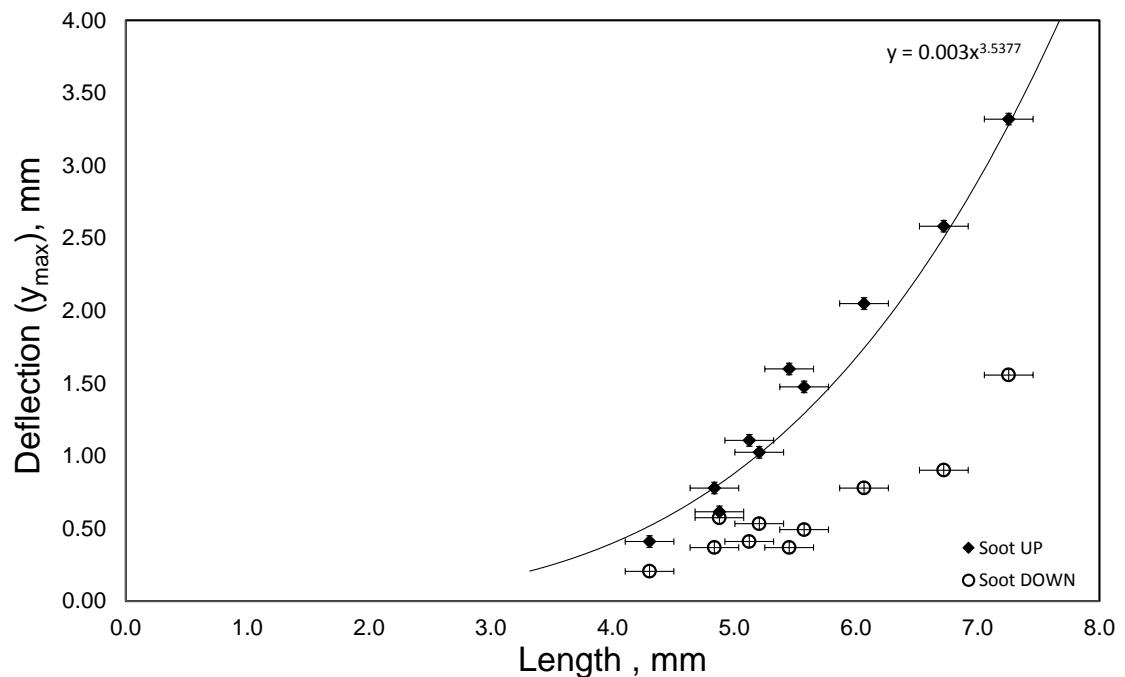


Figure 3.11: Graph of maximum deflection versus length for soot coated PDMS. The line of best fit is the same as that in Fig.3.10.

For the uncoated PDMS surface a value of $1.1 \pm 0.1 MPa$ was found. The soot

coated PDMS produced two values, depending on the direction. With the soot facing up, a value of $1.3 \pm 0.1 MPa$ and with the soot facing down a value of $3.4 \pm 0.2 MPa$ was calculated.

Length (L) (mm)	error	Deflection (y_{max})				(y_{max}/L)			
		PDMS Up	error	PDMS Down	error	PDMS Up	error	PDMS Down	error
8.4	0.2	4.92	0.04	5.00	0.04	0.59	0.02	0.60	0.02
7.7	0.2	3.40	0.04	3.65	0.04	0.44	0.01	0.47	0.01
6.7	0.2	2.38	0.04	2.75	0.04	0.35	0.01	0.41	0.01
6.4	0.2	1.89	0.04	2.30	0.04	0.30	0.01	0.36	0.01
5.7	0.2	1.76	0.04	1.60	0.04	0.31	0.01	0.28	0.01
5.0	0.2	0.86	0.04	1.23	0.04	0.17	0.01	0.24	0.01
4.5	0.2	0.45	0.04	0.78	0.04	0.10	0.01	0.17	0.01
3.9	0.2	0.25	0.04	0.53	0.04	0.06	0.01	0.14	0.01
6.1	0.2	1.80	0.04	2.13	0.04	0.30	0.01	0.35	0.01
3.3	0.2	0.08	0.04	0.37	0.04	0.02	0.01	0.11	0.01

Table 3.1: Deflection data for the uncoated PDMS.

Length (L) (mm)	Deflection (y_{max})			(y_{max}/L)			
	error	Soot Up	Soot Down	error	Soot Up	Soot Down	error
5.1	0.2	1.11	0.41	0.04	0.22	0.08	0.01
4.9	0.2	0.61	0.57	0.04	0.13	0.12	0.01
7.3	0.2	3.32	1.56	0.04	0.46	0.21	0.01
4.3	0.2	0.41	0.20	0.04	0.10	0.05	0.01
6.1	0.2	2.05	0.78	0.04	0.34	0.13	0.01
4.8	0.2	0.78	0.37	0.04	0.16	0.08	0.01
5.6	0.2	1.48	0.49	0.04	0.26	0.09	0.01
5.2	0.2	1.02	0.53	0.04	0.20	0.10	0.01
5.5	0.2	1.60	0.37	0.04	0.29	0.07	0.01
6.7	0.2	2.58	0.90	0.04	0.38	0.13	0.01

Table 3.2: Deflection data for the soot-coated PDMS.

3.3.2 Replication of Uncoated PDMS Tests

Using the method set out by Py *et al.* [3] for triangular substrates, the wrapping process was observed for film thicknesses of $33\mu\text{m}$ to $79\mu\text{m}$. Equilateral triangular membranes of side length 3.00mm to 13.00mm in steps of 0.25mm were fabricated for 7 thicknesses of uncoated PDMS. Each thicknesses was tested separately, with the triangular substrates being laid out on a hydrophobic surface to reduce adhesion to the surface. The capillary Origami process was observed throughout the entire evaporation of the applied liquid (Fig.3.12a).

For each size of triangular membranes for a given thickness, the number of membranes that followed the routine in figure 3.12a was recorded. The critical length (L_{crit}) for Capillary Origami was considered to be the side length where $\geq 50\%$ of the triangular membranes wrapped. The results for these tests are shown in figure 3.13. The data from Py *et al.* [3] has also been included for comparison.



(a) Wrapping sequence for a uncoated triangular PDMS substrate, with a side length above the critical wrapping length, where a droplet of water has been deposited on the surface.



(b) Wrapping sequence for a soot-coated triangular PDMS substrate, where a droplet of water has been deposited on the surface.



(c) Wrapping sequence for a uncoated triangular PDMS substrate, with a side length above the critical wrapping length, where a droplet of allyl alcohol azeotrope has been deposited on the surface.



(d) Wrapping sequence for a soot-coated triangular PDMS substrate, where a droplet of the allyl alcohol azeotrope has been deposited on the surface.

Figure 3.12: Wrapping sequences for uncoated and soot-coated membranes with water (a and b) and the azeotrope of allyl alcohol (c and d). Sequences b and d show how it is possible to see Cassie-Baxter and Wenzel wetting states on the same surface with the appropriate choice of liquid.

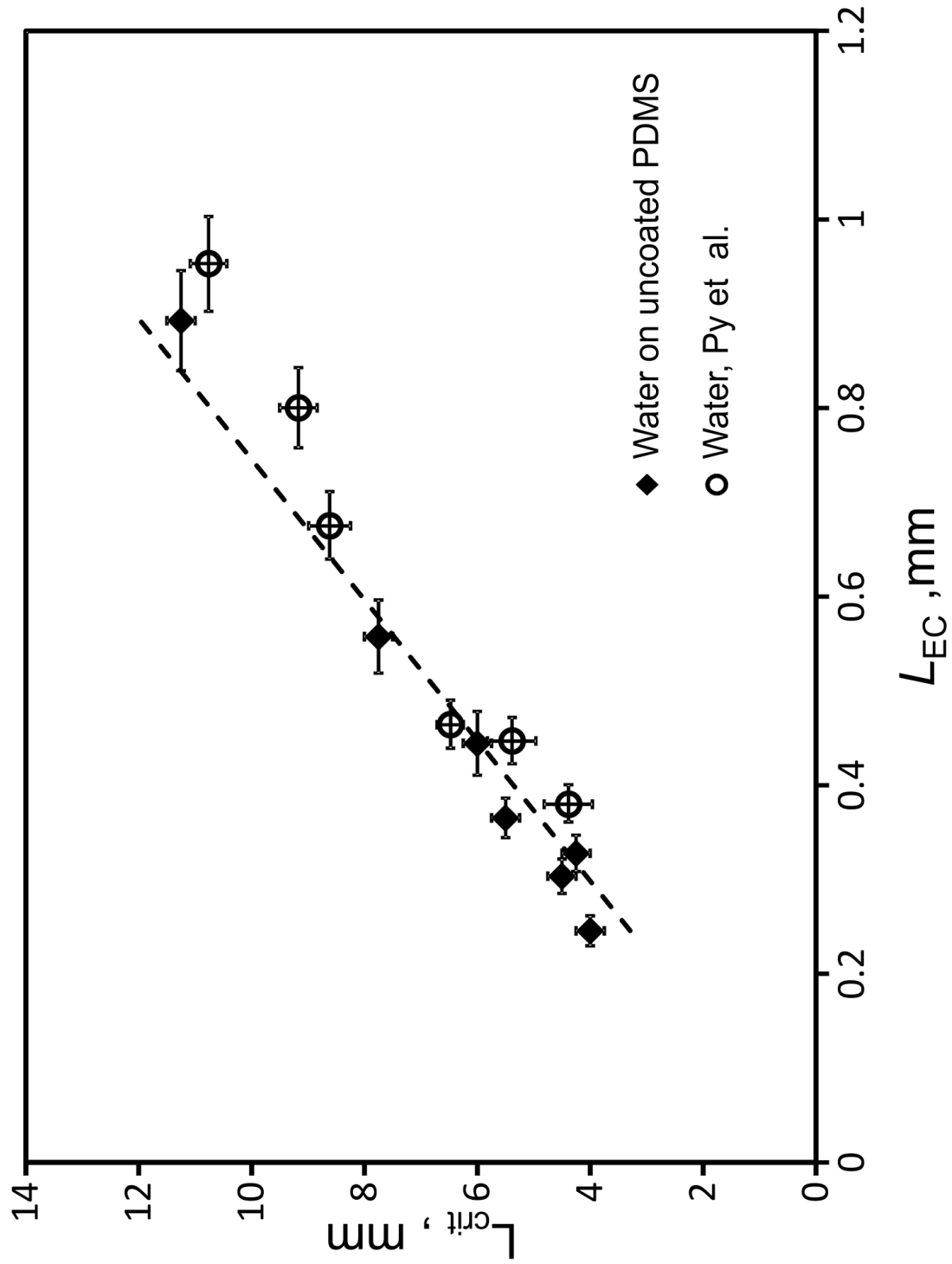


Figure 3.13: Graph of L_{crit} against L_{EC} for water on uncoated PDMS triangular membranes. The dashed line shows the line of best fit being made to cross the origin replicating that by Py *et al.* [3].

3.3.3 Characterisation of the Carbon Nano-particle PDMS Films

Contact Angles

Contact angle analysis of the uncoated and soot-coated PDMS surfaces was performed using a Drop Shape Analysis system DSA10, KRÜSS. Figure 3.21 is an image of five different water droplets sitting on the surface of the soot PDMS. The silvery appearance of the base of the droplets is the plastron air layer, which is an indication of the Cassie-Baxter state.

Table 3.3 and figures 3.15 to 3.18 show the contact angles for the two surfaces and for the two liquids, water and the azeotrope of allyl alcohol.



Figure 3.14: Image of water droplets on the soot coated PDMS surface.

		Contact Angle (degrees)		
		Advancing	Static	Receding
Water	PDMS	116±2	104±1	92±2
	Soot PDMS	159±2	156±2	153±2
Allyl Alcohol Azeo	PDMS	64±2	59±2	44±2
	Soot PDMS	56±3	38±3	~0

Table 3.3: Contact Angles for water and the azeotrope of allyl alcohol on PDMS and soot coated PDMS.

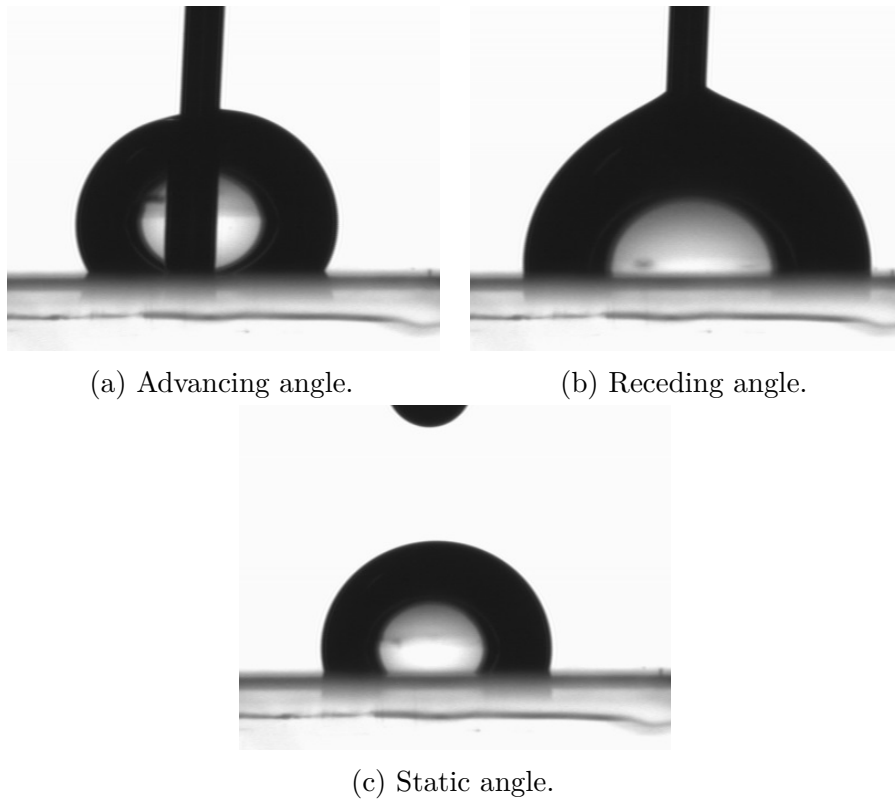


Figure 3.15: Images of the advancing, static and receding contact angles for water on PDMS.

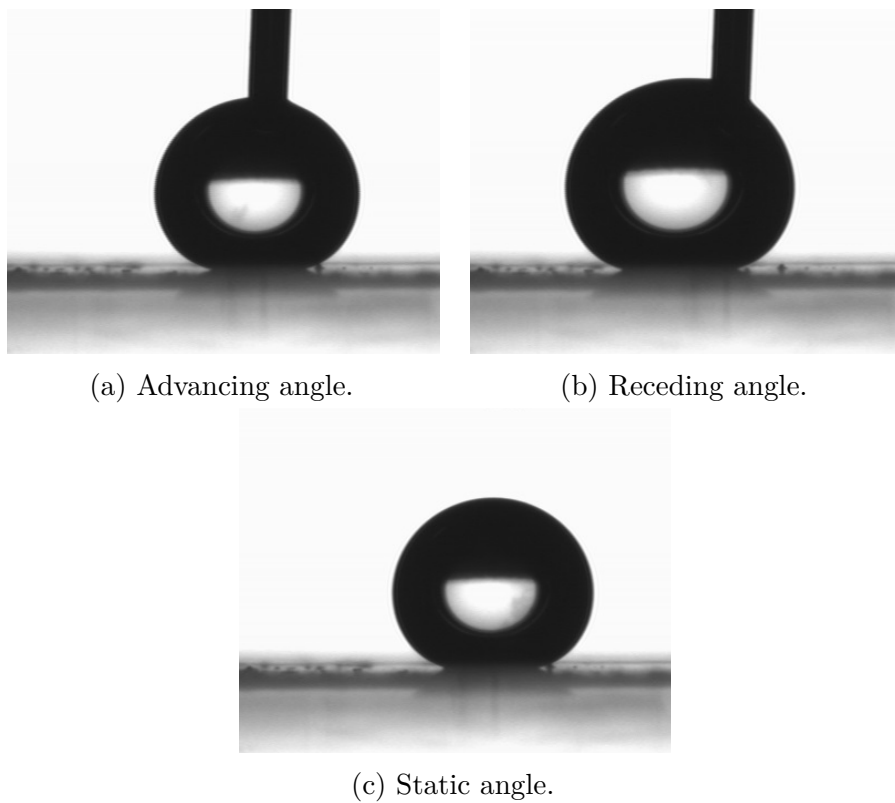


Figure 3.16: Images of the advancing, static and receding contact angles for water on soot-coated PDMS.

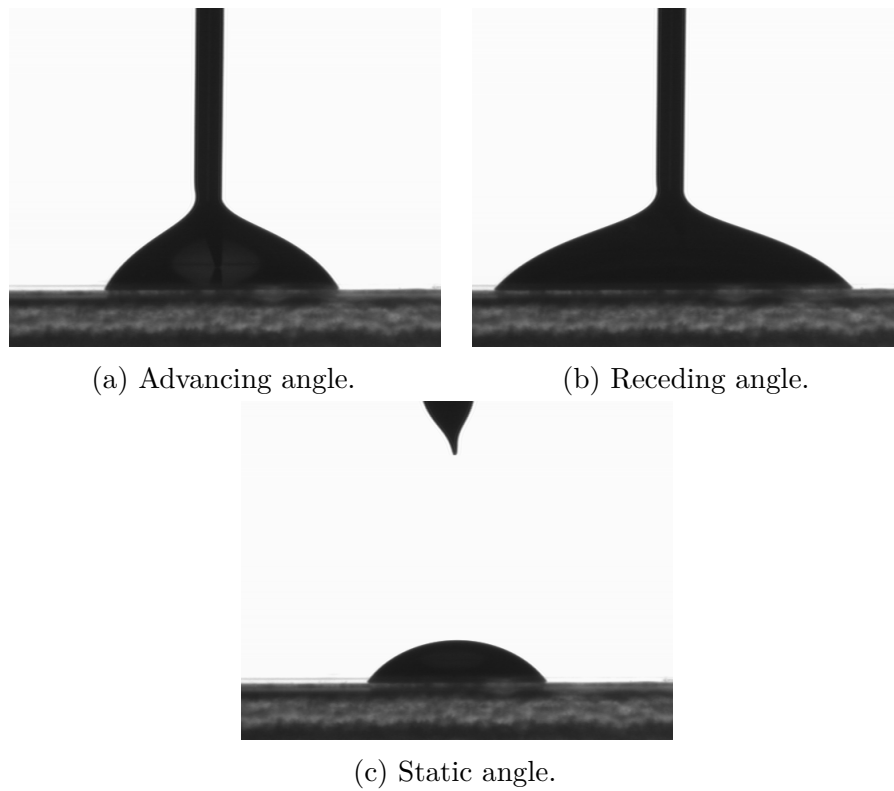


Figure 3.17: Images of the advancing, static and receding contact angles for the azeotrope of allyl alcohol on PDMS.

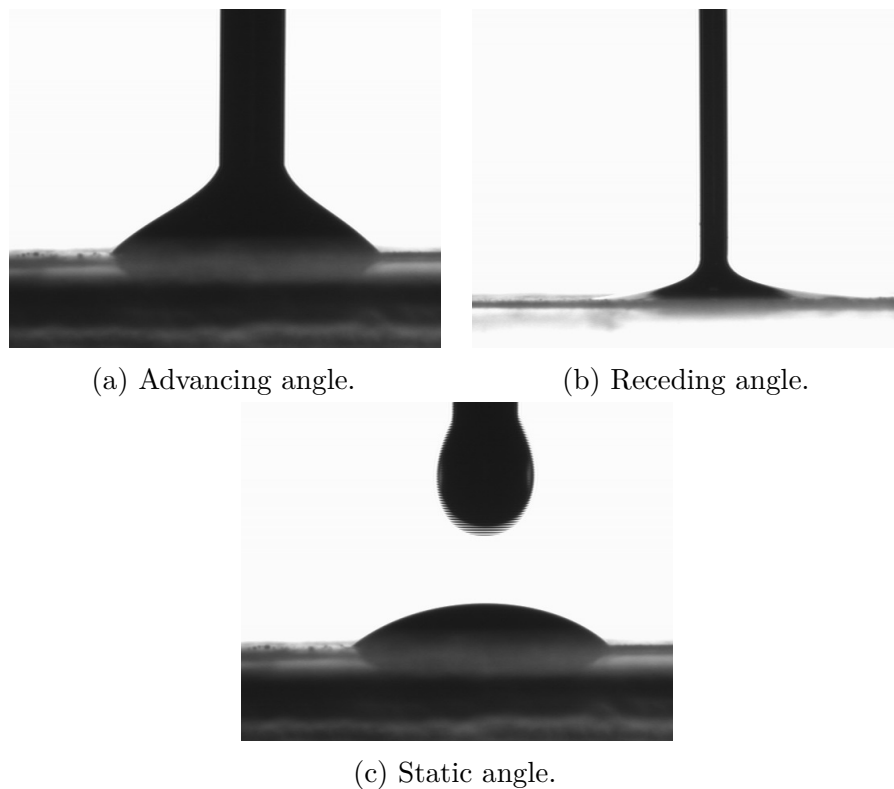


Figure 3.18: Images of the advancing, static and receding contact angles for the azeotrope of allyl alcohol on soot-coated PDMS.

Figure 3.19 is an Atomic Force Microscopy (AFM) image of the soot PDMS surface showing the micro-scale roughness of the surface. This was taken on using a Bruker FastScan AFM. The surface roughness can also be seen in figure 3.20. These images were acquired using a Jeol JSM 840A Scanning microscope.

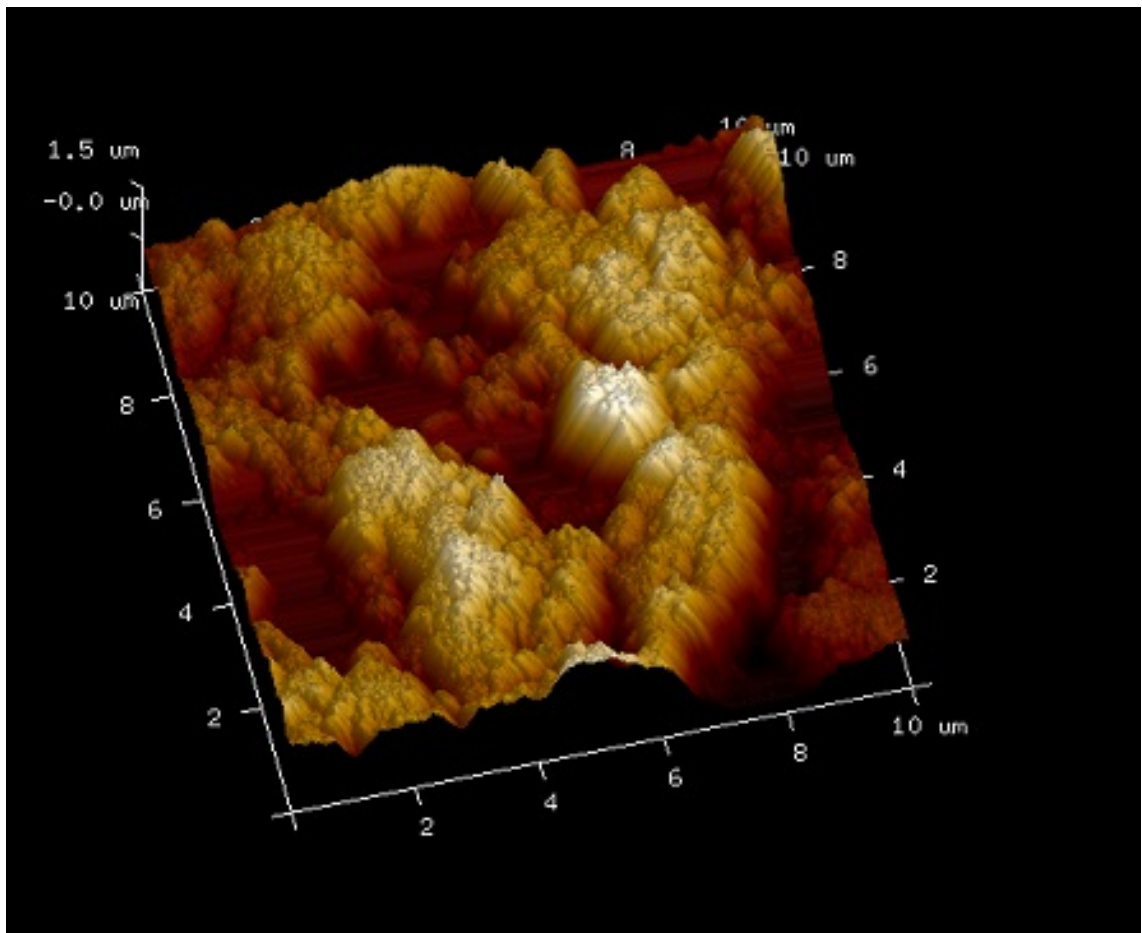
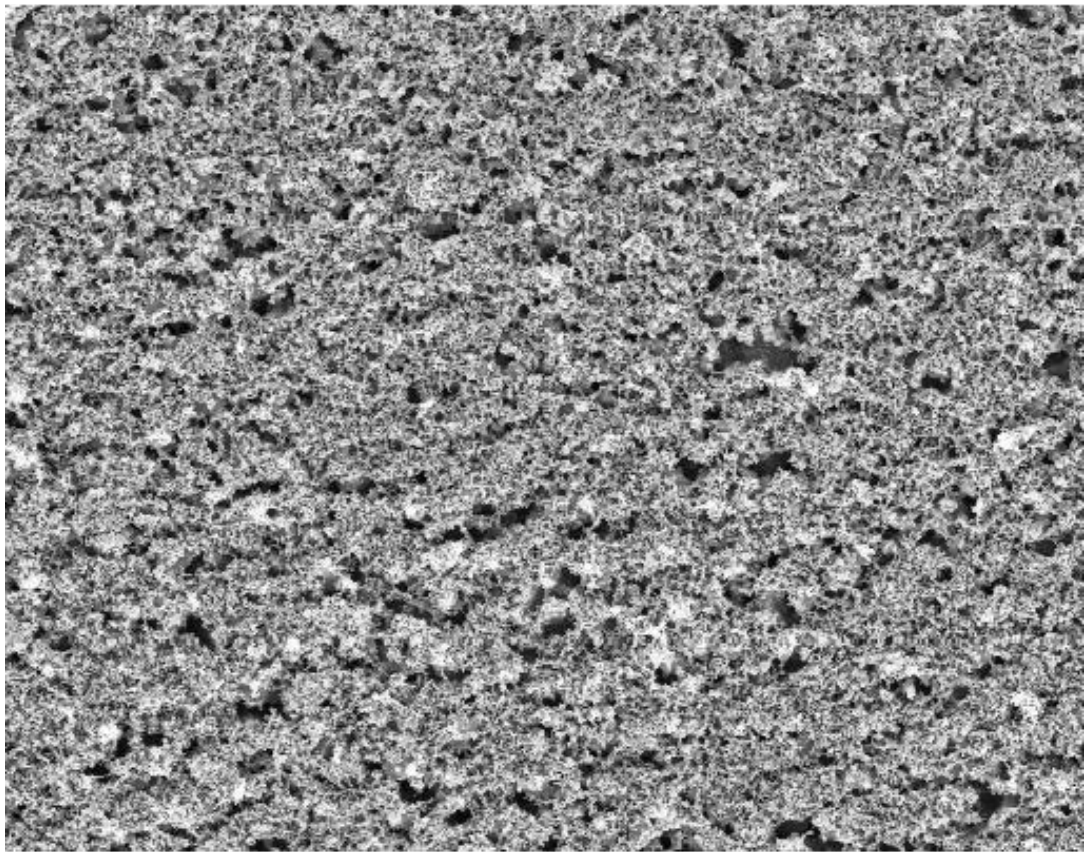
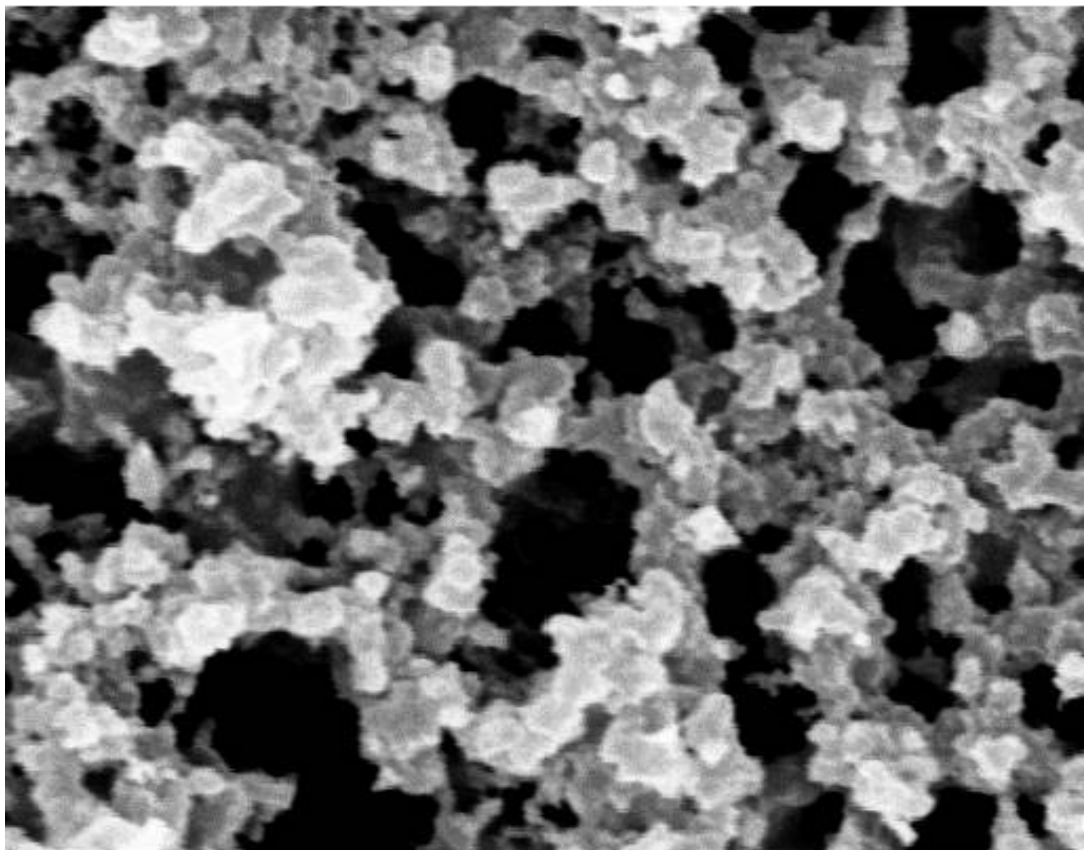


Figure 3.19: Atomic force microscopy of the soot coated PDMS surface.



100µm



10µm

Figure 3.20: Scanning electron microscopy of the soot coated PDMS surface.

3.3.4 Capillary Origami of Superhydrophobic Triangular Substrates

With the addition of the carbon nano-particles, the critical length determination tests for triangular substrates could be repeated for the superhydrophobic membranes. When tested with water a complete suppression of the wrapping process was seen for all thicknesses between $35\mu m$ and $85\mu m$ and all size triangular substrates between $3.00mm$ and $15.00mm$ (Fig.3.12b).

Isopropanol Wrapping Tests

In order to test the effects of roughness on the wrapping process, a 30% solution of Isopropanol was used because of its hydrophilic state on the soot PDMS surface. The same method that was used to determine the critical length for wrapping for the uncoated PDMS surfaces, was applied to the superhydrophobic thin films. The Isopropanol solution wets the soot surface spreading over the entire surface of the triangular films. Again, as the solution evaporates it pulls the substrate around itself if the side length of the triangular membrane is above the critical length. An issue with the IPA solution was its uneven nature to the evaporation process. The ratio of IPA to water would change during the experiments due to the different evaporation rates of the two liquids. This changed the surface tension during the tests as the IPA evaporated away at a faster rate than the water. This made the results unreliable.

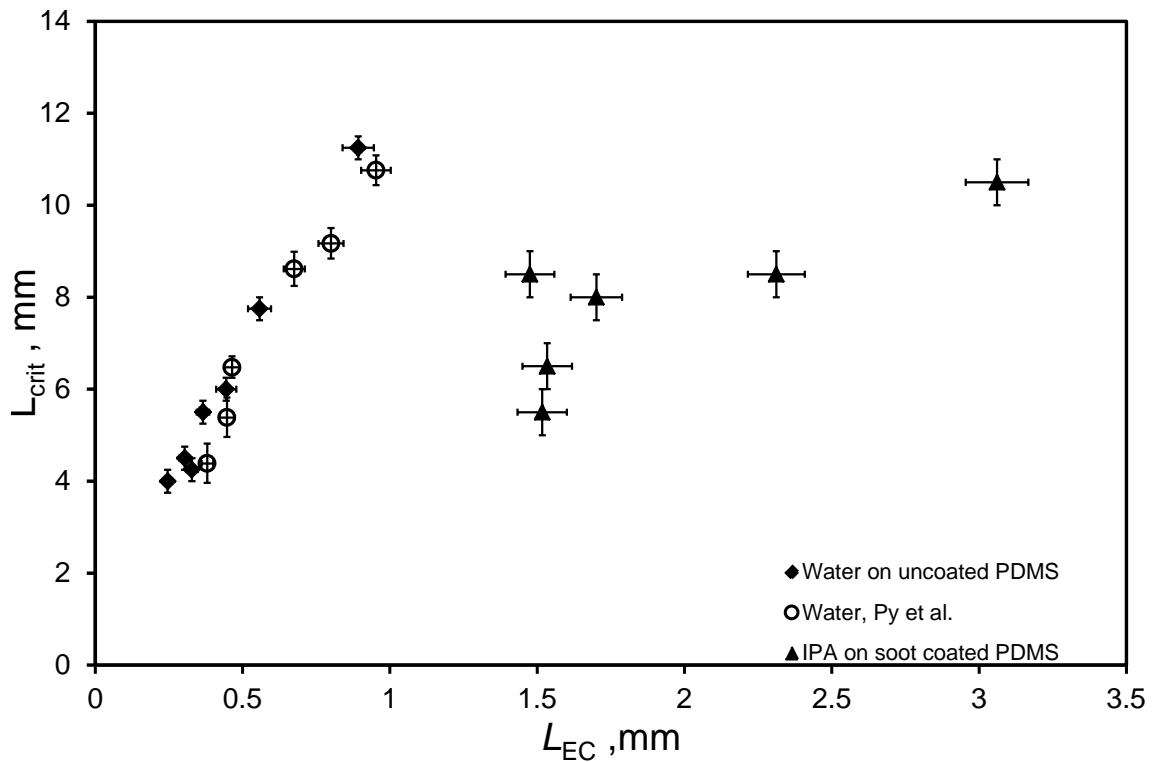


Figure 3.21: Graph of the critical length, L_{crit} , versus the elastocapillary length, L_{EC} , for the 30% Isopropanol solution on soot PDMS membranes.

Allyl Alcohol Azeotrope Wrapping Tests

The wrapping tests were repeated to determine the critical length for triangular membrane capillary origami using the azeotrope of allyl alcohol. Both uncoated and soot-coated films were tested to examine the effects of the added surface roughness. Again the allyl alcohol wet the surface of the superhydrophobic substrates behaving in a Wenzel manner (Fig.3.12c & Fig.3.12d). The evaporation issues that affected the IPA tests were not present with the azeotrope as the evaporation rate of the two constituent parts of the solution are such that the ratio of the two liquids is maintained. The critical lengths were found for film thicknesses of $33\mu m$ to $78\mu m$. The data has been plotted in graphs 3.22 and 3.23.

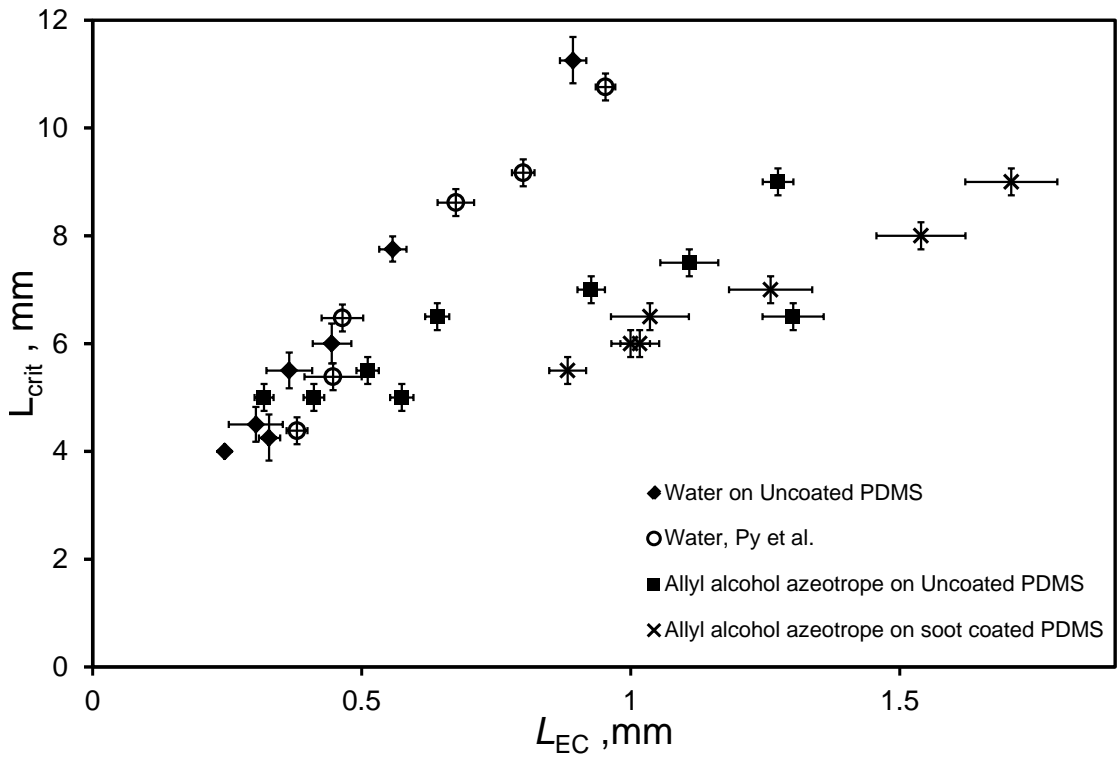


Figure 3.22: Graph of L_{crit} against L_{EC} for water and allyl alcohol on uncoated PDMS and soot coated PDMS triangular membranes.

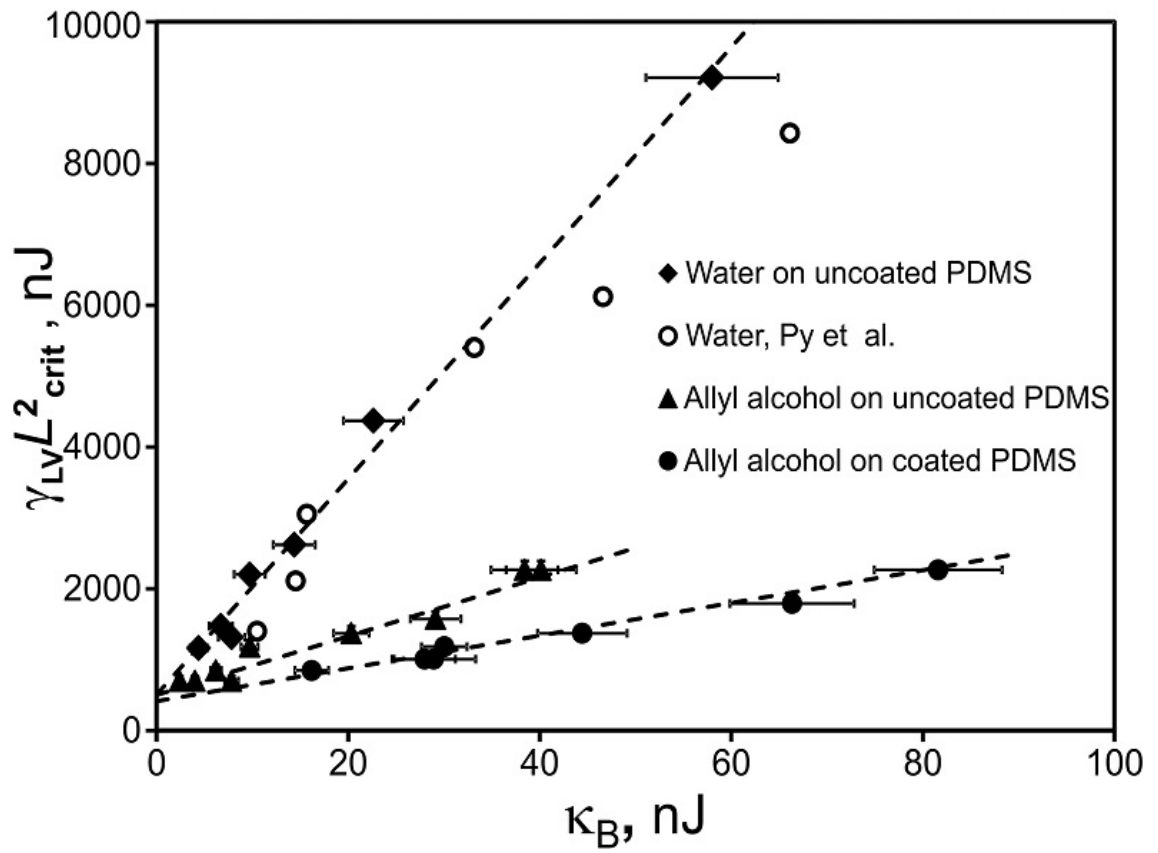


Figure 3.23: Graph of $\gamma_{LV} L_{crit}^2$ against κ_B for water and allyl alcohol on uncoated PDMS and soot coated PDMS triangular membranes.

3.4 Discussion

The cantilever deflection method proved to be a simple and accurate way to determine the Young's modulus. The values for the uncoated PDMS show the validity of the method due to the agreement with previously reported values [148,149]. The method is accurate only if the thickness (h) and the length (L) are measured accurately. The uncoated PDMS measurements were independent of the direction (within 20%) with an average of $1.1\pm 0.1\text{MPa}$. The value of for the soot up cantilever tests was $1.3\pm 0.1\text{MPa}$. This is within 18% of the uncoated value and would imply the the rigidity of the PDMS is not significantly affected when the soot surface is stretched. Conversely, when the soot surface is compressed, when the soot is face down in the cantilever deflection test, the Young's modulus value is more than doubled to $3.4\pm 0.2\text{MPa}$. This increase can be attributed to the clumping of the particles during an inward deflection. Even with the increase in rigidity the membranes are still considered highly flexible.

Figure 3.13 is a comparison of the triangular membrane data from Py *et al.* [3] and the results from the uncoated wrapping tests using water. The two sets of data are in good agreement. The linear fit of the wrapping data gives $L_{crit}=13.4L_{EC}$ compared to $L_{crit}=11.9L_{EC}$ of Py *et al.*. The dashed line shows the line on best fit as made to cross the origin as previously demonstrated by Py *et al.* [3]. The combined data indicates that this may not be the best fit and an offset may be present. The line also indicates two wrapping regions. Triangular membranes with side length below the L_{crit} at the corresponding L_{EC} will not wrap. Those with lengths above the L_{crit} will wrap a droplet. The agreement between the Py *et al.* and the collected sets of data also shows the validity of the Young's modulus value for PDMS, $E = 1.1\pm 0.1\text{MPa}$, determined from the cantilever deflection tests.

The application of a nano-particle surface coating to the PDMS membranes allows the hydrophobicity to be tailored. The added roughness to the surface lead to two possible wetting situations, a Wenzel or a Cassie-Baxter state, when a liquid makes contact with the surface. When water makes contact with the novel surface a Cassie-Baxter state is seen. This is evident in the high contact angle and low

roll-off angle. The shiny silver plastron air layer that exists is also evidence of a Cassie-Baxter state. This state means a decrease in adhesion to the surface. This lack of adhesion is the reason for the suppression of the wrapping process. An enhancement in capillary origami can be seen with the choice of an appropriate wetting liquid, such as the azeotrope of allyl alcohol. The wetting of the surface and approximately zero degree receding contact angle displays the Wenzel state present when the azeotrope is deposited on the surface of the superhydrophobic substrates. The Wenzel state means an increase in the liquid-solid surface area and an increase in the adhesion to the surface. The increase in adhesion means that surfaces with higher rigidity can be wrapped and folded.

In order to compare the wrapping processes of the two substrates by water and allyl alcohol, the dependence on the surface tension can be written in terms of the surface energy, $L_{crit} > L_{EC} = \sqrt{\kappa_B \gamma_{LV}}$. Wrapping is seen when the gain in surface energy is greater than the bending energy i.e., when $\sim \gamma_{LV} L_{crit}^2 > \kappa_B = Eh^3/12(1 - \nu^2)$. Figure 3.23 shows the variation of $\gamma_{LV} L_{crit}^2$ with κ_B for water and allyl alcohol on uncoated PDMS membranes. The slope for water is 3.7 times greater, at $152(\pm 10)$, compared to that of the allyl alcohol, at $41(\pm 4)$. The receding angles on PDMS are 92° and 44° , for water and allyl alcohol, respectively. The reduction in the slope indicates a dependence of L_{crit} on the receding contact angle. This implies a wetting liquid, with a lower receding angle can wrap the membranes into tighter curves.

The wrapping data for the soot-coated membranes with allyl alcohol is also displayed on figure 3.23. Again, this data obeys a straight line fit with a slope of $21(\pm 3)$. This is a further 1.8 times less than the uncoated PDMS. This reduction can be explained by the Wenzel wetting state present for the allyl alcohol azeotrope on the soot-coated surface. The solution penetrates the surface features, increasing the adhesion of the droplet on the surface. Therefore as the droplet evaporates, the surface tension forces are able to bend the surfaces into tighter curves as well as bend more rigid surfaces, enhancing the Capillary Origami process.

One interesting feature of the data is the non-zero intercept that occurs for

each linear fit in figure 3.23. Each fit has an intercept of $\sim 500nJ$ (to within 10%). This appears to be independent of the liquid used or the surface roughness. One explanation of this could be a dependence on the Gaussian rigidity due to the multiple radii of curvatures present with the folding of the triangular membranes.

3.5 Conclusions

The use of the cantilever deflection method in conjunction with the large deflection correction factor is a simple way to determine the Young's modulus for the thin films. The method produces results that agree with independent measurements found in the literature.

The addition of partially embedded carbon nano-particle network structures into the surface of the PDMS films adds surface roughness to the substrates producing a Cassie-Baxter state when water comes into contact with the surface. The ability to manipulate the contact angle of liquids that contact the membranes means that there is control over the capillary origami and droplet wrapping processes. With appropriate choice of liquids the two wetting states have been tested. In one extreme, a Cassie-Baxter wetting state is produced when water comes into contact with the flexible superhydrophobic substrates. The lack of adhesion with the surface means that a complete suppression of the wrapping process. Conversely, at the other extreme, using a wetting liquid with a lower surface tension, and enhanced wrapping state is seen. This is due to the Wenzel wetting state causing increased adhesion with the surface of the membranes as the liquid penetrates through the roughness on the surface increasing the contact area. This increased adhesion means the membranes can be wrapped into tighter curves.

The azeotrope of allyl alcohol has a surface tension lower than that of water. This means a difference in the contact angle when compared to water, with the azeotrope having a lower receding contact angle, on the uncoated membranes. The difference in the critical wrapping length, L_{crit} , with water having a larger L_{crit} , shows the dependence of L_{crit} on the receding contact angle.

The determination of the critical lengths for wrapping of the membranes for the differing wetting states support the idea that the wetting characteristics of a surface affect the way in which a droplet is wrapped by a flexible surface and that by changing the properties of the liquid it is possible to control the Capillary origami process. Oppositely, by reducing the receding contact angle through surface modification it is possible to more easily wrap a surface for a given surface tension if a Wenzel state is

produced or to suppress the wrapping process in the event of a Cassie-Baxter wetting state.

3.6 Suggested work

Further Capillary Origami Tests

The work on Capillary Origami can be extended for a variety of surfaces with varying hydrophobicities and hydrophilicities. This would allow for a more rigorous test of equation 3.5. If it were possible to produce flexible PDMS films with different surface roughnesses, then it would be possible to test the theory for a single liquid. For this to occur, new techniques would need to be developed in order to pattern the surface of the PDMS.

The possibility to suppress and enhance the wrapping process leads to more tailored wrapping fabrication methods. If it is possible to selectively add roughness to specific regions of a surface, it may be possible to more accurately control which parts of the surface wrap a liquid whilst leaving other regions unfolded.

With the current triangular substrates, it may be possible to test a single liquid on either side of the soot coated substrate. This would allow for two measurements of the critical length for two different roughnesses, soot coated PDMS and uncoated PDMS, from a single set of samples. As long as the Young's modulus is accurately measured for the surface in both orientations, this form of testing would reduce the uncertainty in comparing coated and uncoated PDMS surface as the results would be obtained from the same surface. The issues with manufacturing comparable thicknesses will also disappear if the same substrates are used.

The experiments performed used two different liquids with different surface tensions, water and allyl alcohol azeotrope. a simple way to extend the work would be to test the effect of surface tension and contact angle on the wrapping process.

An interesting add on would be to test the effects of electrowetting on the superhydrophobic surface and to determine whether it is possible to cause a wrapped substrate to unwrap by applying a voltage or whether it is possible to cause the

liquid on a rough non-wrapped surface to infiltrate the roughness by applying a voltage which, when the voltage is removed, will cause the liquid to retract and pull the substrate around itself.

Chapter Summary

This chapter focused on the experiments performed to test the effects of surface roughness on the droplet wrapping process in the Wenzel and Cassie-Baxter wetting regimes. It has been shown that the presence of surface structure can both inhibit and enhance the wrapping process depending on the choice of liquid.

The next chapter concentrates on the use of the conformable surface as a way to reduce drag. Superhydrophobic drag reduction has been reported with micro-scale structures but there is little on the potential of nano-scale drag reduction.

Chapter 4

Superhydrophobic Drag Reduction

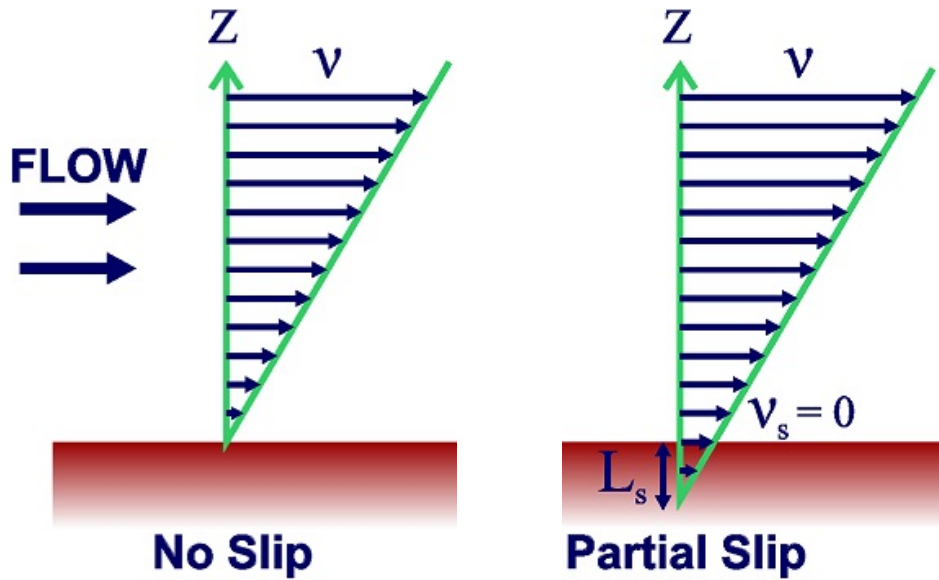
This chapter concentrates on the work that was carried out to test the capabilities of the flexible superhydrophobic surface as a way to reduce the drag force produced by an object in a laminar flow. It begins with a background to the area and describes previous work in the field, then moves on to the work performed to test the novel surface.

4.1 Background

Drag is another name for the friction caused when an object moves through a fluid or when liquid move around or through a system. At the interface where a fluid contacts a solid surface, the no-slip boundary condition has been widely accepted as the condition imposed on the solid/liquid interface (Fig.4.1a).

The validity of this model has been called into question as our understanding of surface wetting improves [150]. The concept was established by Navier in 1823 [151]. The no-slip condition states that all velocity components at the solid/liquid interface are equal to the velocity components of the corresponding solid surface at that point. Therefore if the surface is stationary the liquid will have zero velocity at the interface (Fig.4.1a).

A slip boundary proposes a non-zero value for the velocity parallel to the surface (Fig.4.1b). This velocity is known as the slip velocity, V_S and if the velocity gradient is extrapolated back to the zero velocity point into the surface, the distance into



(a) No slip condition.

(b) Partial slip condition.

Figure 4.1: Illustration of the boundary conditions between a liquid and a solid.

the surface is known as the slip length, L_s . This was first quantified by Maxwell in 1879 [152]. The slip length was found to be on the order of the mean free path of a liquid, $\sim 1\text{nm}$, and so has been considered negligible for some time. As micro and nano-fluidic devices have become more widespread it has become advantageous to increase the slip length [153]. In recent history, the effect of wettability and surface roughness on the slip length has been of interest [150, 154, 155]. In 1997, Thompson and Troian published results showing how surface hydrophobicity can increase the slip length well beyond the mean free path value [156]. This has also been found for other hydrophobic and oleophobic surfaces [157–161].

When a droplet of water is placed on a superhydrophobic surface, the lack of adhesion with the surface makes the droplet unstable [89]. The partial contact with the surface means a layer of air is present under the droplet. This air layer is known as a plastron. The presence of the plastron means a large liquid/vapour interface is present instead of the solid/liquid interface. The liquid/vapour interface presents much less friction to a liquid moving over the surface than there would be with a solid/liquid interface. Analytical approaches to this idea have been performed to determine the optimum conditions for drag reduction in the presence of a plastron [155, 162, 163]. In 2002, Kim and Kim observed the flow of water down inclined superhydrophobic

silicon micro and nano post array channels [58]. In the nano-channels, a 99% decrease in the flow resistance was seen. Ou *et al.* also performed similar experiments with various micro-post arrays and again found a reduction in the drag force due to the presence of the liquid/vapour interface below the flow of the liquid [158]. McHale *et al.* performed experiments with sand-coated acrylic spheres. The edges of the sand grains added roughness to the surface and after the application of a water-proofing compound the surface of the spheres became superhydrophobic. When immersed in water the spheres held a plastron creating an air layer around the entire ball. This air layer reduced the apparent drag by creating a slip boundary condition. The superhydrophobic spheres reached a higher terminal velocity compared to uncoated spheres or sand-coated spheres without a plastron [164]. The drag reduction is caused by circulation of air in the plastron layer (Fig.4.2) as the sphere moves through the liquid which changes the wake pattern, altering the separation point [165].

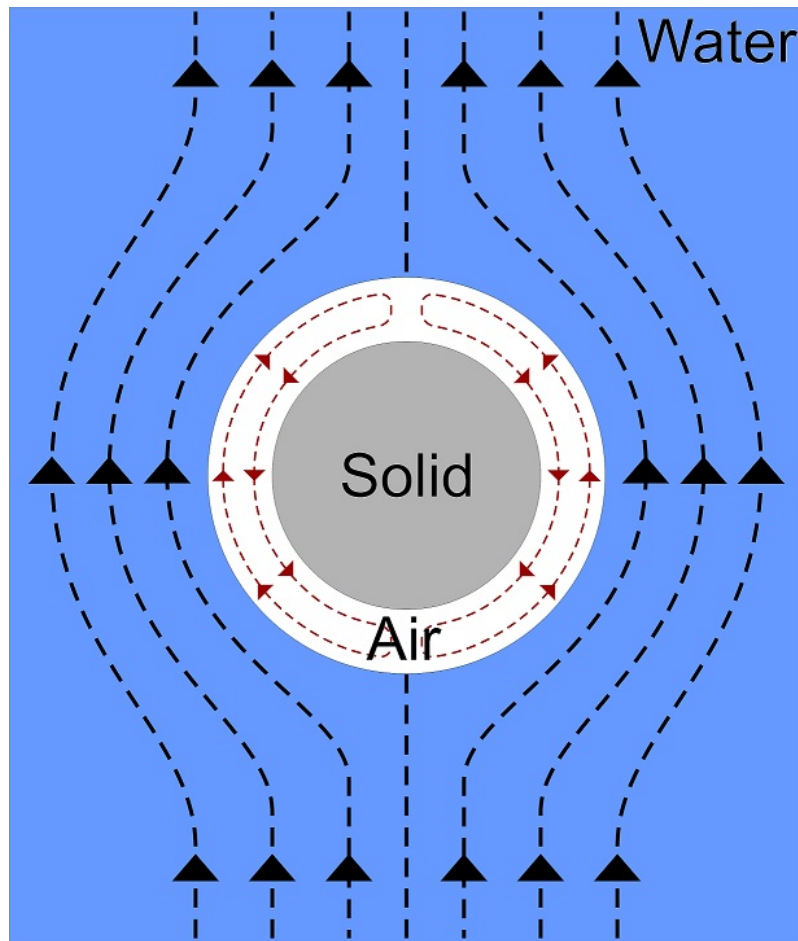


Figure 4.2: Illustration of the air circulation that occurs in the plastron layer around as water moves around the object.

Brennan *et al.* have recently conducted experiments using hydrophobic cylinders to determine the drag reduction due to the presence of a plastron. A number of brass cylinders were coated in different ranges of sand grain size, which then had a hydrophobic surface coating applied [166]. A drag reduction of 28% was demonstrated when comparing the plastron bearing rod to the same rod but without a plastron.

4.2 Drag Reduction Using CNP Coated PDMS

4.2.1 Flow Chamber Setup

To test for drag reduction properties of the CNP coated PDMS surfaces, they needed to be mounted onto brass cylinders for testing in a recirculating laminar flow chamber. The 1940's era flow chamber contains a $50\text{cm} \times 30\text{cm} \times 30\text{cm}$ laminar flow section that allows the testing of an object and their effect on flow in this region (Fig.4.3).

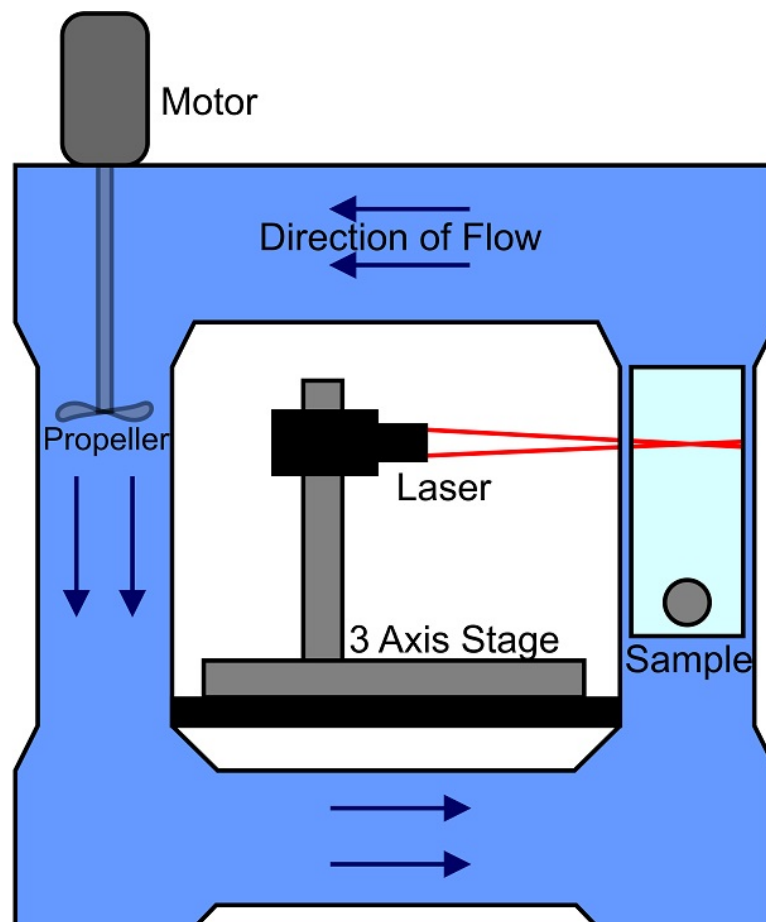


Figure 4.3: Illustration of the flow chamber used for drag reduction tests. The light blue region in which the sample is positioned, indicates the laminar flow segment of the chamber.

The drag reduction for cylinders can be found by comparison to uncoated brass cylinders of equivalent diameter. The samples are positioned at the start of the laminar region, as shown in Fig.4.3 and a 1 dimensional Laser Doppler Anemometer (LDA), mounted on a 3 axis stage, is used to record the velocity of the water at different positions, 30 cylinder diameters downstream of the sample. This produces a Gaussian profile from the flow velocities and by using the momentum deficit technique [167] the drag coefficient can be extracted.

4.2.2 Testing of Small Diameter Cylinders

The method for fabricating superhydrophobic conformable PDMS surfaces, as described in section 2.1.3, produced a maximum usable area of $50mm \times 25mm$. In order to achieve the best possible sample for testing, it was logical to have as few seams as possible on the cylinders, which would lead to increased drag, when the CNP coated PDMS was mounted onto them. $6mm$ diameter cylinders were used as they allowed to a single section of substrate to wrap around the cylinders.



Figure 4.4: Illustration of the $6mm$ diameter cylinders used for the drag reduction tests.

The cylinder surface consists of a $\sim 15cm$ superhydrophobic section, with a total length of $21.5cm$. The larger $12mm$ diameter end sections are to allow for the mounting of the cylinders to the sample holder. The cylinders were subjected to increasing flow speeds ranging from $1.45m.s^{-1}$ to $2.78m.s^{-1}$. This corresponds to a Reynolds number range of 12000 to 23000. Each cylinder was tested a minimum of 3 times.

4.2.3 Modification of the Soot Coating Process

With the flow velocity being measured 30 diameters downstream, the flow chamber test section made it possible to test larger diameter samples than the $6mm$ cylinders

being tested. With the area of the CNP coated PDMS substrates being the limiting factor, a new method for producing larger areas of superhydrophobic PDMS was needed. To achieve a large superhydrophobic area the method described in section 2.1.3 was scaled up. Instead of $50\text{mm} \times 25\text{mm}$ glass slides, $150\text{mm} \times 50\text{mm} \times 1\text{mm}$ copper master plates were made. These were suspended over a chimney, used to channel the soot plume produced by a larger rapeseed oil flame. A fan was positioned above the chimney to draw the soot through (Fig.4.5).

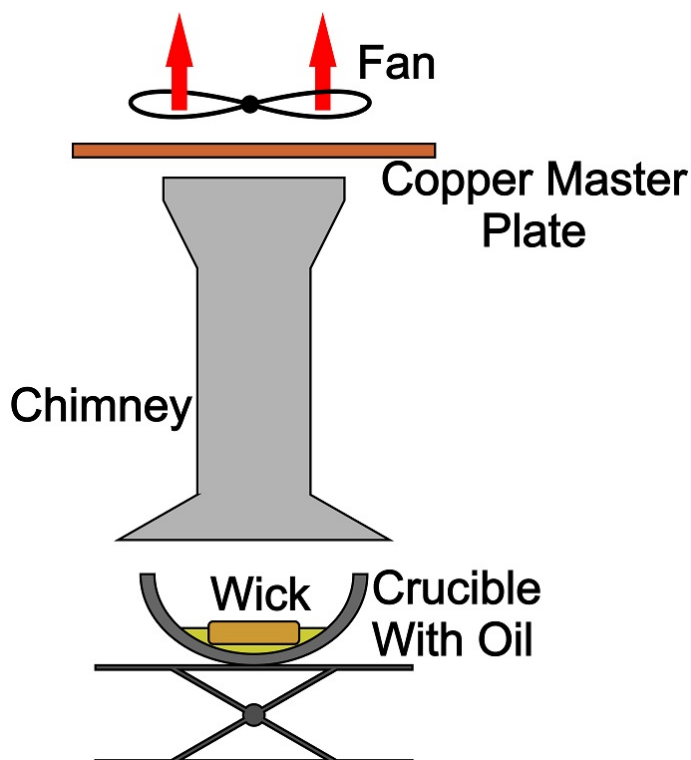


Figure 4.5: Illustration of the scaled-up sooting method.

The preparation of the larger area superhydrophobic PDMS surfaces involved multiple steps (Fig4.6). These are:

1. Preparation of the copper master plates.

The plates were cleaned using a non metallic PCB cleaning block and blown with compressed air to remove any dust or particulates remaining on the surface of the plates.

2. Ignite the rapeseed oil.

Two raw cotton wicks are placed in a ceramic crucible and 50ml to 60ml of rapeseed oil is poured over the wicks. This is ignited with a Bunsen burner.

The flame is left for 10 to 15 minutes for it to stabilise and reach a steady temperature.

3. Sooting of the copper plates.

The crucible is carefully positioned under the chimney and the fan is turned on. This helps to draw the soot through. When a steady stream can be seen the, one end of the copper plate is suspended over the plume and allowed to become covered in soot for 4 to 5 minutes. Once a thick matt black layer of soot has been deposited the copper plate is repositioned so that the next section of the copper plate can be sooted. Once complete coverage is achieved the plates are carefully remove from the plume and allowed to cool.

4. Preparation of the PDMS surfaces.

Whilst the copper plates are cooling the PDMS can be mixed. Again, a 10:1 ratio of elastomer to curing agent is used. It is vigorously mixed for 5 minutes and degassed for 30 minutes. The uncured PDMS is spread over a $180\text{mm} \times 90\text{mm}$ acrylic plate and a 1mm high spreading gauge is used to level the surface.

5. Pre-curing the PDMS.

The PDMS surfaces are placed in a 60°C oven and left for 34 to 38 minutes for the surface to become sufficiently tacky.

6. Combining the copper plates and PDMS.

The PDMS surfaces are removed from the oven and the copper plate is carefully placed face down in the centre of the acrylic plate. A steel plate, $150\text{mm} \times 50\text{mm} \times 5\text{mm}$, that has been preheated to 60°C , is placed on the back of the copper plate. This acts to spread the heat evenly over the surface of the copper plate and to add mass to the plate to push it into the surface during the remaining curing process.

7. Final cure.

The combined PDMS and copper plate are put in an 80°C oven for 1 hour for

the PDMS to fully cure. Once fully cured the surfaces are removed from the oven and allowed to cool to room temperature.

8. Plate removal and rinse.

When cool, the steel plate is first removed. The copper plate is then carefully removed from the PDMS, so as not to damage the sooted surface. The coated PDMS is then rinsed under a fast flowing tap in order to remove any loose soot still on the surface. The surface are now ready to use.

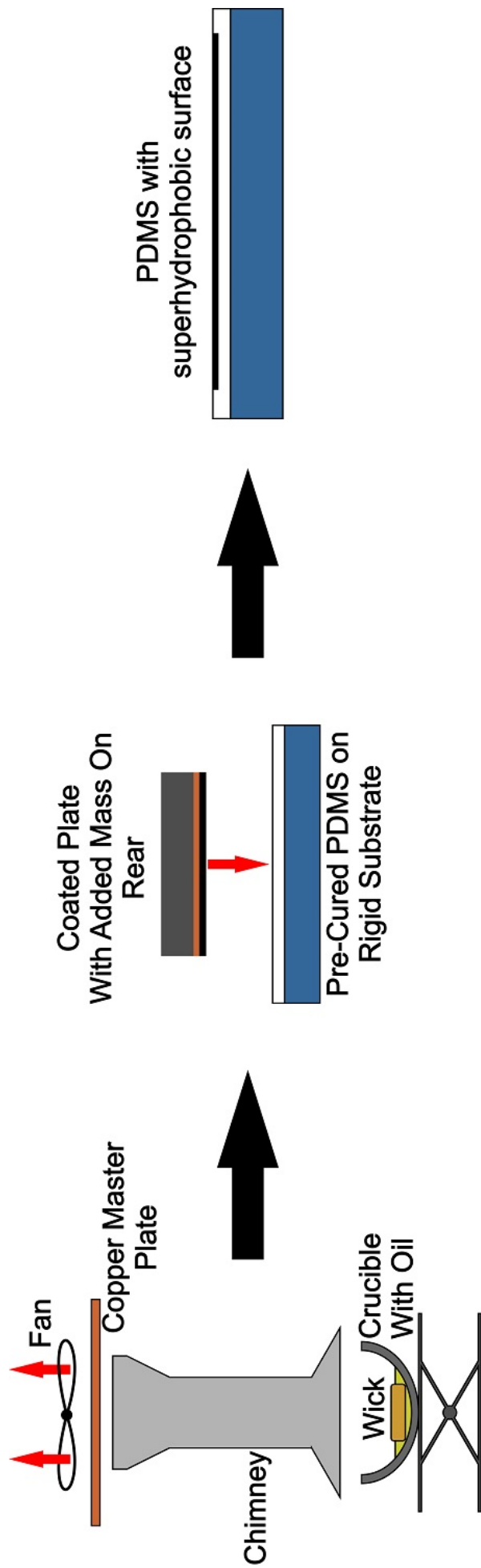


Figure 4.6: Illustration of the larger area sooting method.

4.2.4 Construction and Testing of Larger Diameter Cylinders

With the larger superhydrophobic PDMS surfaces, it was now possible to make larger diameter test cylinders to determine if the surface would be able to reduce the drag force. 10mm, 11mm and 12mm diameter brass cylinders were acquired. The PDMS surfaces were mounted onto a 10mm diameter test cylinder. First, 3 rectangular sections of superhydrophobic PDMS were cut to a width the diameter of the cylinder, 31.4mm wide, using the laser cutter. These were then placed face down on a clean glass surface, end to end. A silicon rubber primer, Loctite[®] 770, was applied to the long edge of the strips. This was allowed to dry for 1 minute before a thin layer of cyanoacrylate adhesive, Loctite[®] 4860, was applied to the PDMS, on top of the primer. The cylinder was then quickly, but carefully, placed on top. When this had sufficiently cured the PDMS was primed a quarter of the way along the PDMS sections, behind the cylinder, and adhesive applied. The cylinder was then rolled until it had covered the adhesive and then left to cure. This process was repeated until the entire rectangular PDMS sections were glued to the cylinder.

In total, 5 superhydrophobic test cylinders were made, all having diameters between 11.2mm and 11.5mm, with lengths of 215mm. These were all tested in the flow chamber a minimum of 5 times at 6 incrementally increasing flow speeds ranging from $1.45m.s^{-1}$ to $2.78m.s^{-1}$. At each speed a flow velocity profile, 30 diameters downstream, was recorded using a Laser Doppler Anemometer (LDA), Dantec Dynamic Flow explorer, mounted on a 3 axis traverse. The velocity was recorded over a length of 120mm, 60mm either side of the centre of the cylinders, perpendicular to the length of the cylinders, in steps of 3mm. The cylinders were allowed to fully dry out between each run in a cool, 60°C, oven. All experiments were also performed in a short time window to minimise the effect of changing temperature.

To determine whether or not a drag reduction was present, the superhydrophobic cylinders were compared to plain brass cylinders. 10mm, 11mm and 12mm brass cylinders were subjected to the same testing procedure as the superhydrophobic

cylinders and were each tested a minimum of 3 times.

4.3 Results

This chapter describes the results obtained from the superhydrophobic cylinder experiments in the superhydrophobic state and in a wetted state. The results are compared to those of uncoated cylinders in order to determine whether or not a reduction in drag is found.

4.3.1 Testing of Superhydrophobic Cylinders

In order to test the effect of the flexible superhydrophobic soot PDMS surface on the drag produced by cylinders, 5 soot PDMS cylinders were made with average diameters ranging from 11.2mm to 11.5mm . These were compared to uncoated brass cylinders, the same material used to mount the soot PDMS surfaces, to determine the change in drag. A 10mm , 11mm and 12mm diameter brass cylinder were tested in order to rule out changes in diameter as a factor.

Each of the soot PDMS cylinders were tested a minimum of 5 times and each uncoated brass cylinders was tested 3 times Each test involved recording the velocity profile at 6 flow rates, ranging from 1.45ms^{-1} to 2.78ms^{-1} . Figure 4.7 shows a soot PDMS covered cylinder during testing.

4.3.2 Calculation of Drag Coefficient

The 120mm velocity profile of the flow, 60mm either side of the centre of the cylinders and perpendicular to them, was measured 30 diameters down stream using an LDA. At this distance the contribution to the momentum of the water from normal stresses is negligible and the drag coefficient can be accurately calculated from a single line profile across the wake downstream of the cylinder [167]. A 120mm profile was recorded in order to ensure the free-stream velocity was found either side of the cylinders, meaning a complete traversing of the wake. Using the momentum deficit technique the drag coefficient was calculated from the Gaussian velocity profile using equation 4.1.

$$C_D = \int_{-\infty}^{\infty} \frac{U}{U_1} \left(\frac{U_1 - U}{U_1} \right) d \left(\frac{y}{d} \right) \quad (4.1)$$

U – Velocity at a given point measured using a laser doppler anemometer

U_1 – Free – stream velocity

y – Horizontal displacement

d – Diameter of the cylinder being tested

The drag coefficient (C_D) was determined as it describes the drag experienced by an object of specific shape as it passes through a fluid or as a fluid travels past it. The drag coefficient was compared to the Reynolds number (equation 4.2). The Reynolds number is a dimensionless quantity that is the ratio of the inertial forces to the viscous forces for a fluid. It takes into account the density, viscosity and characteristic dimensions of an object and is widely used to compare flow patterns in different flow situations. It allows for the characterisation of the flow for objects of any size and shape in any fluid.

$$Re = \frac{\rho U_1 d}{\eta} \quad (4.2)$$

ρ – Density of the fluid

U_1 – Free–stream velocity

d – Diameter of the cylinder

η – Viscosity of the fluid

Figure 4.8 shows the average drag coefficients determined for the uncoated 10mm,

11mm and 12mm diameter brass cylinders. The average drag coefficients determined for the soot PDMS coated brass cylinders are shown in figure 4.9 to figure 4.13.

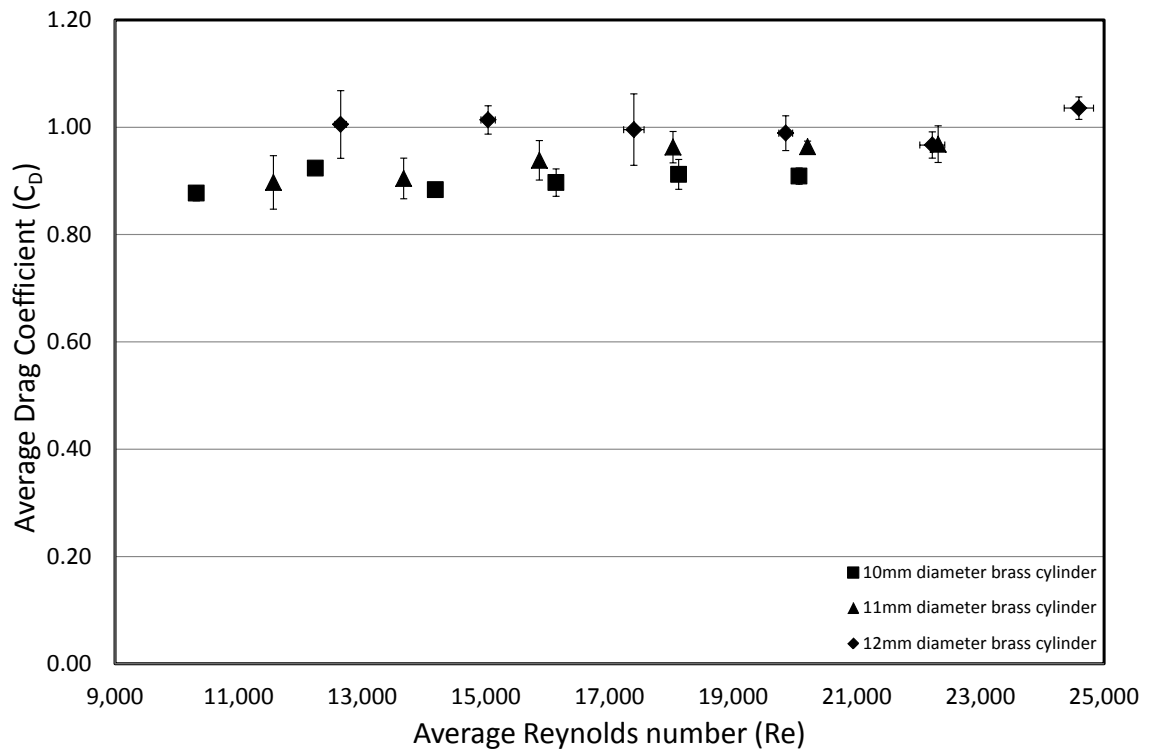


Figure 4.8: Graph showing the drag coefficient verses Reynolds number for the uncoated brass cylinders.

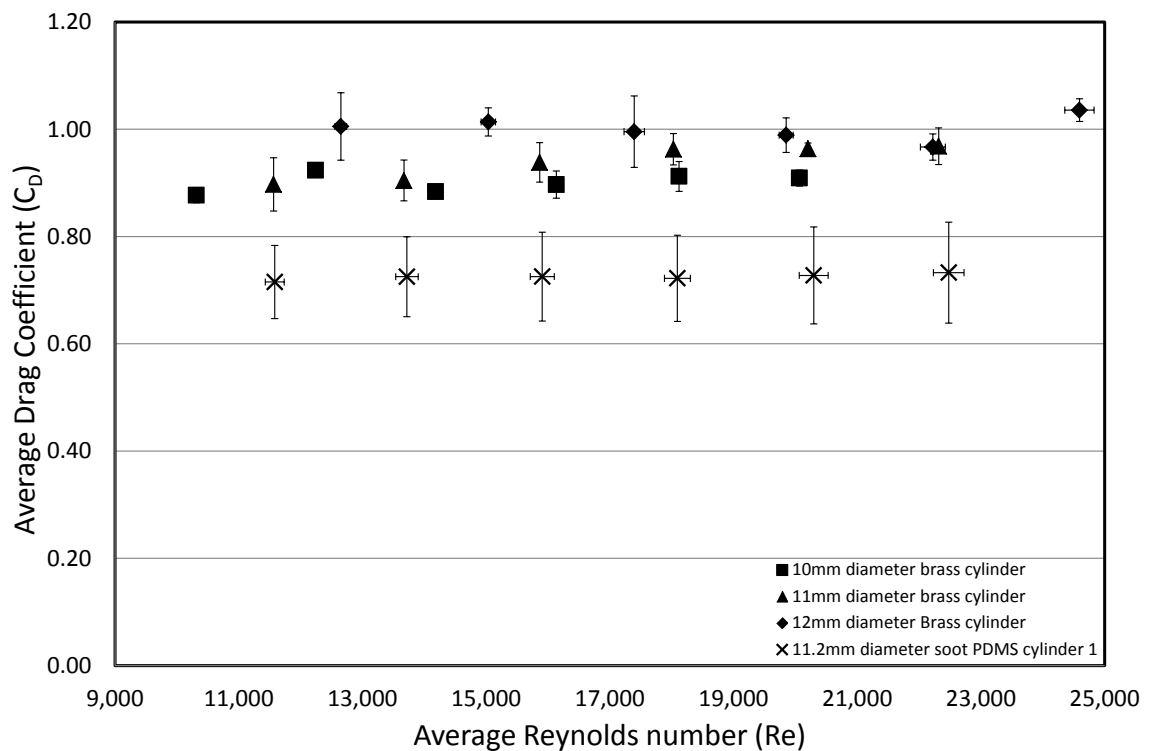


Figure 4.9: Graph showing the drag coefficient verses Reynolds number for the uncoated brass cylinders and the first soot PDMS covered cylinder.

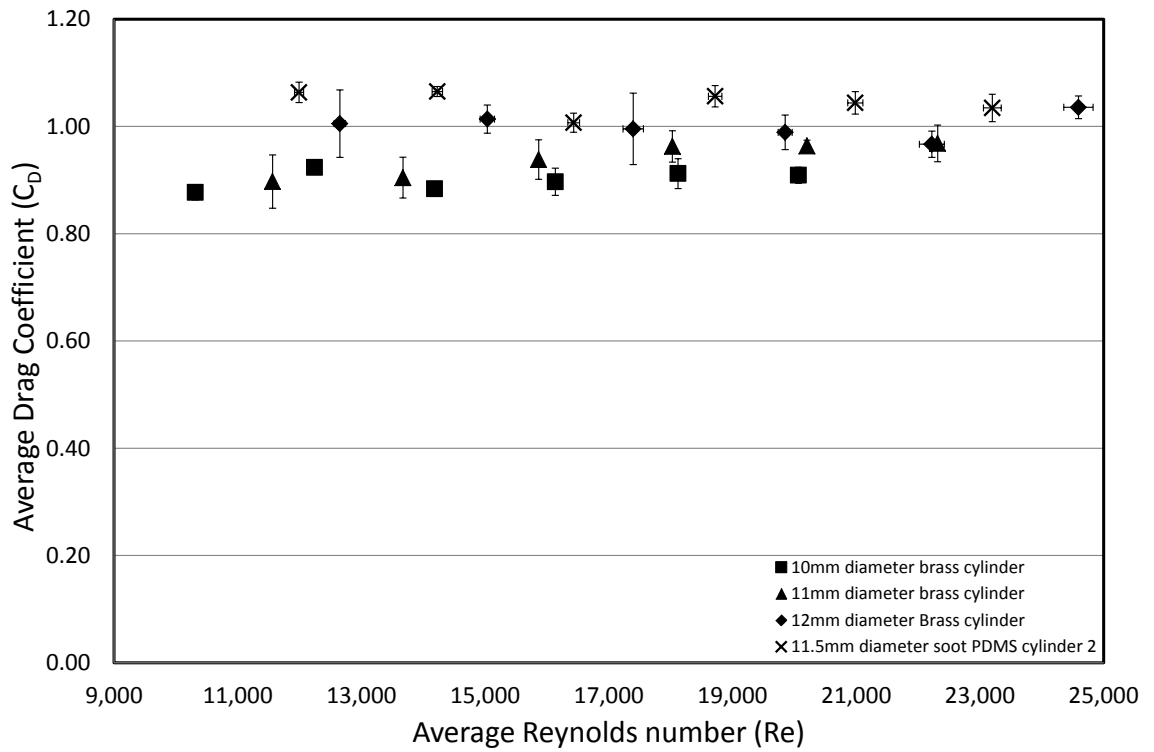


Figure 4.10: Graph showing the drag coefficient versus Reynolds number for the uncoated brass cylinders and the second soot PDMS covered cylinder.

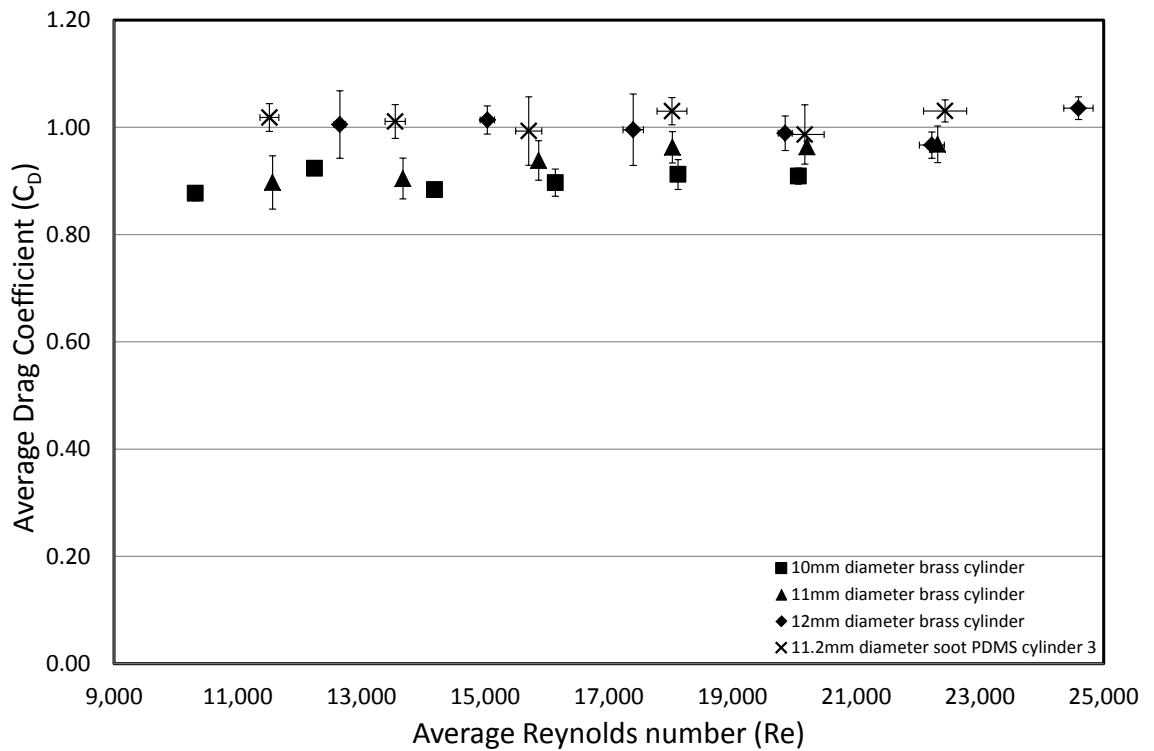


Figure 4.11: Graph showing the drag coefficient versus Reynolds number for the uncoated brass cylinders and the third soot PDMS covered cylinder.

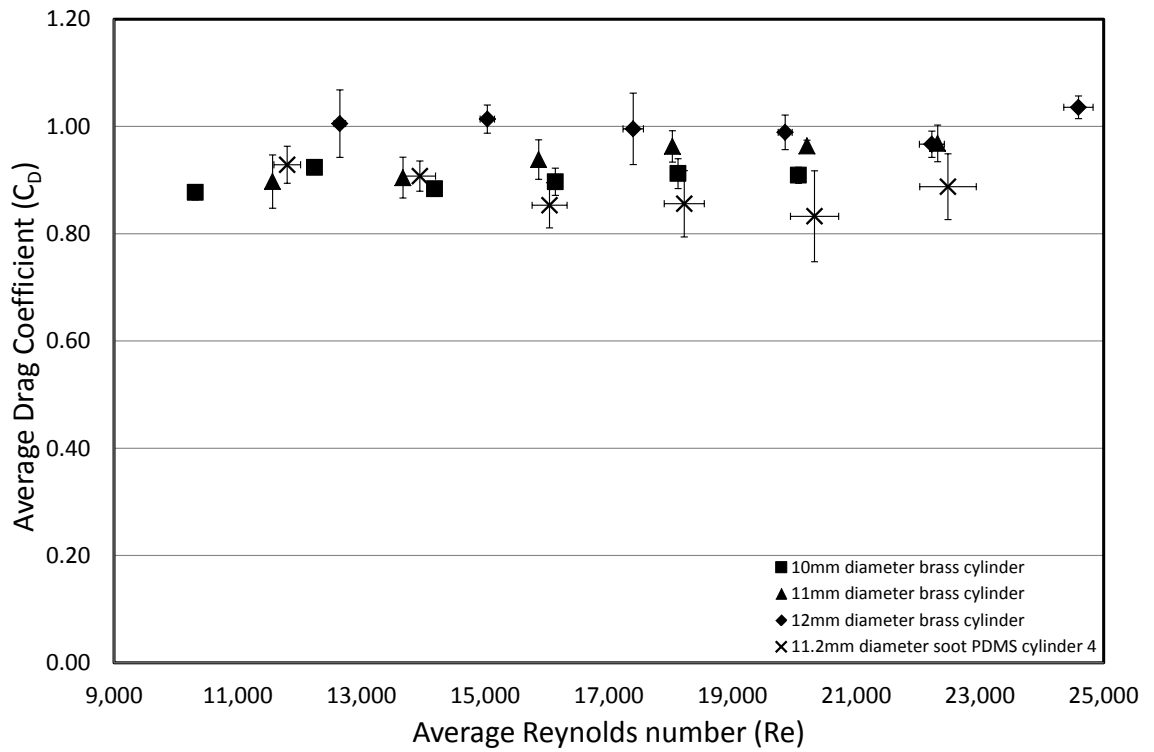


Figure 4.12: Graph showing the drag coefficient versus Reynolds number for the uncoated brass cylinders and the fourth soot PDMS covered cylinder.

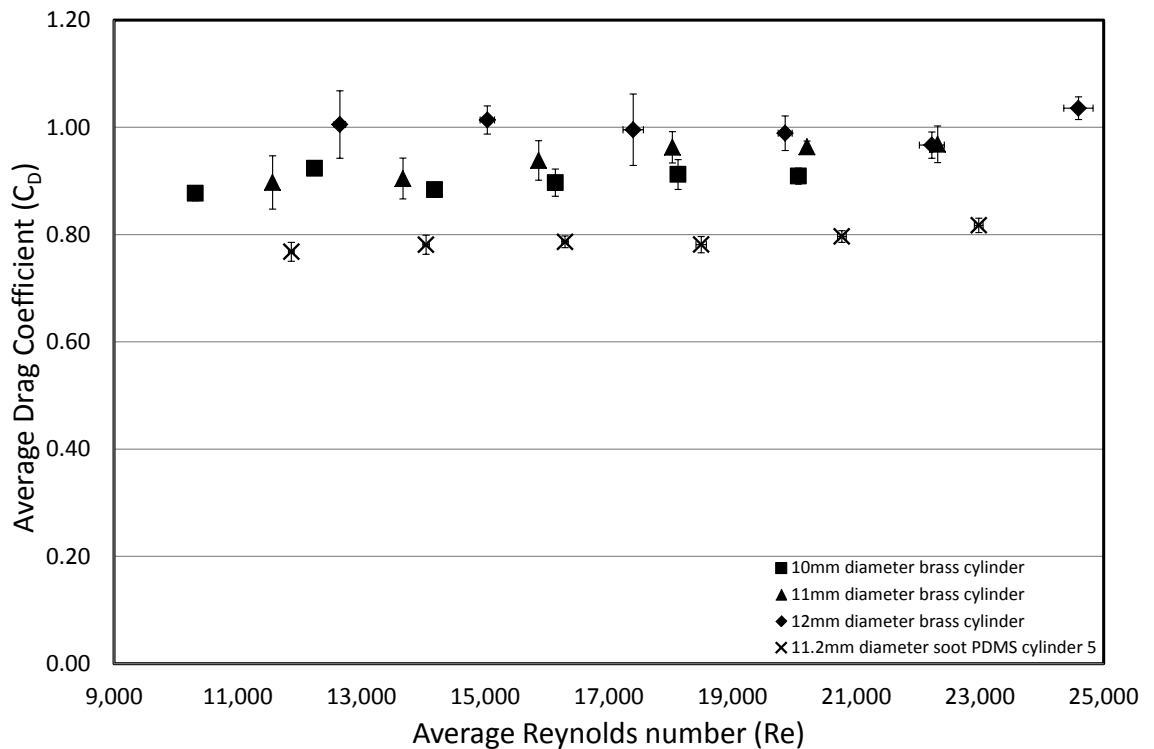


Figure 4.13: Graph showing the drag coefficient versus Reynolds number for the uncoated brass cylinders and the fifth soot PDMS covered cylinder.

The soot PDMS cylinders, numbered 1 and 2, were also tested after being rinsed in ethanol just prior to testing. This process is to remove the plastron air layer as demonstrated by McHale *et al.* [164] and Brennan *et al.* [166]. Each cylinder was tested 3 times, with an ethanol rinse prior to each test.

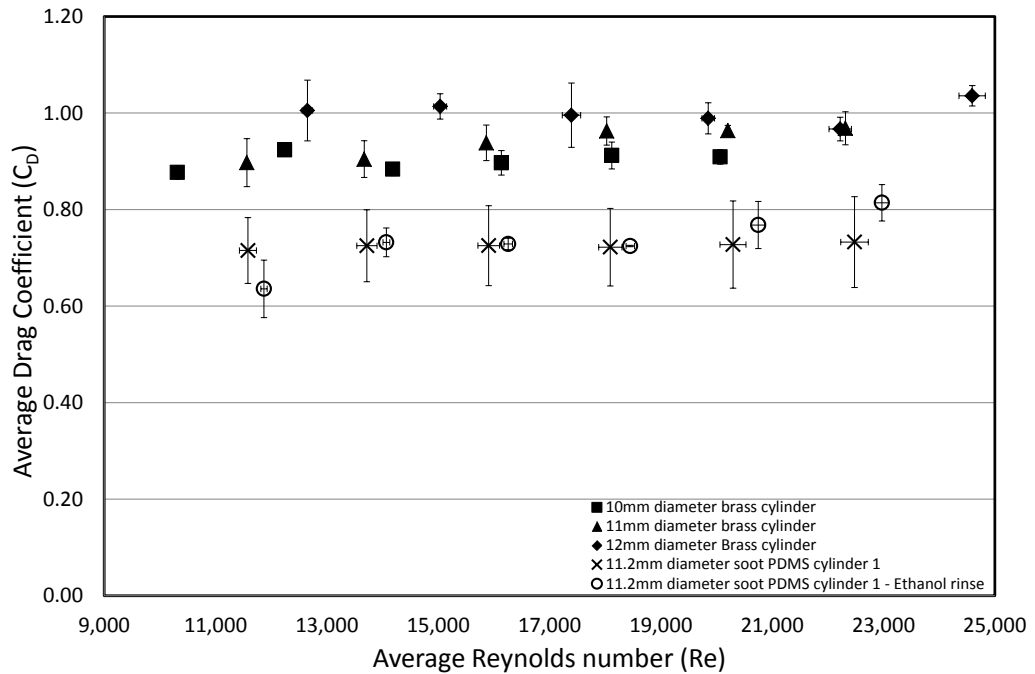


Figure 4.14: Graph showing the drag coefficient versus Reynolds number for the uncoated brass cylinders and the first soot PDMS covered cylinder after an ethanol rinse.

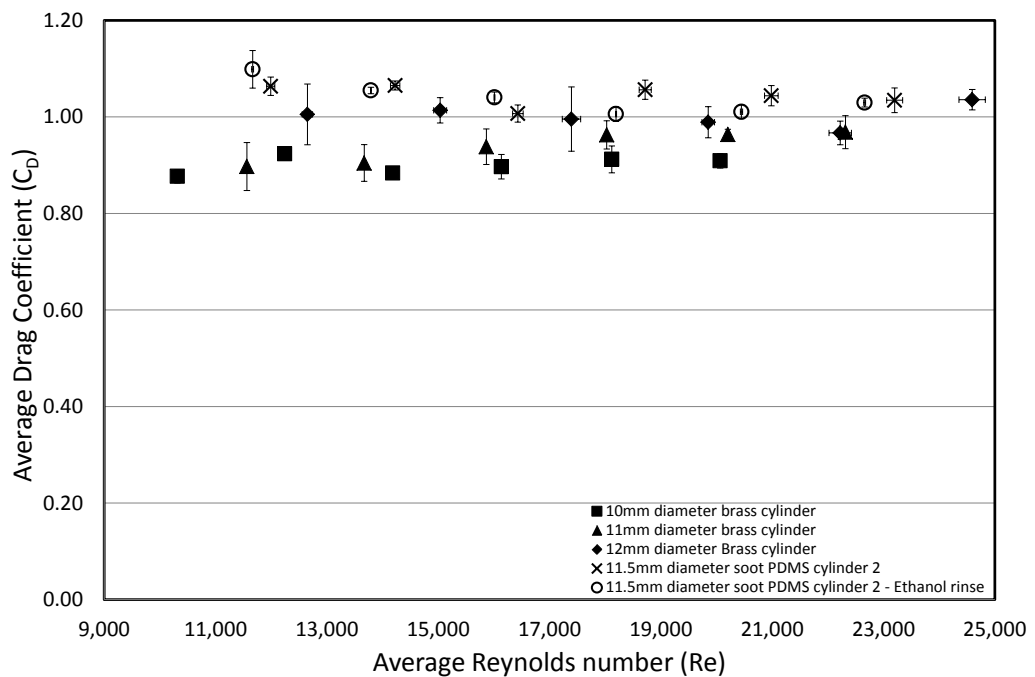


Figure 4.15: Graph showing the drag coefficient versus Reynolds number for the uncoated brass cylinders and the second soot PDMS covered cylinder after an ethanol rinse.

In order to more clearly compare all the cylinder drag coefficients determined, the average for each cylinder tested has been compared to the average drag coefficient for the brass cylinders in figure 4.16. The average drag coefficient for the cylinders that were also subjected to an ethanol rinse is shown in figure 4.17.

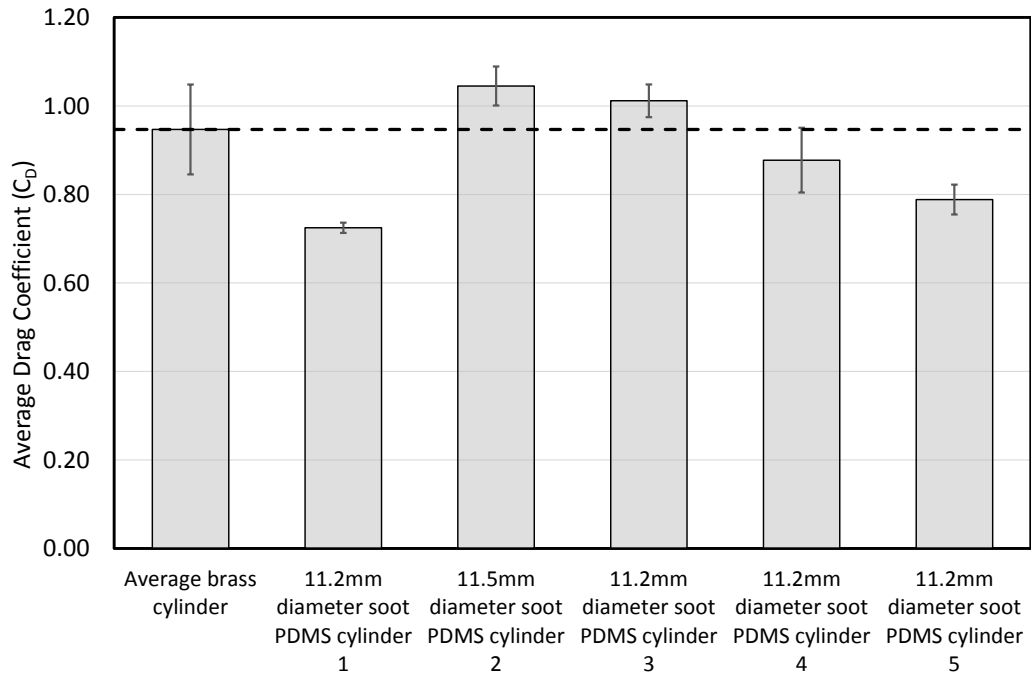


Figure 4.16: Chart comparing the average drag coefficient for the brass cylinders and the soot-coated cylinders. The dashed line shows the average drag coefficient for the brass cylinders.

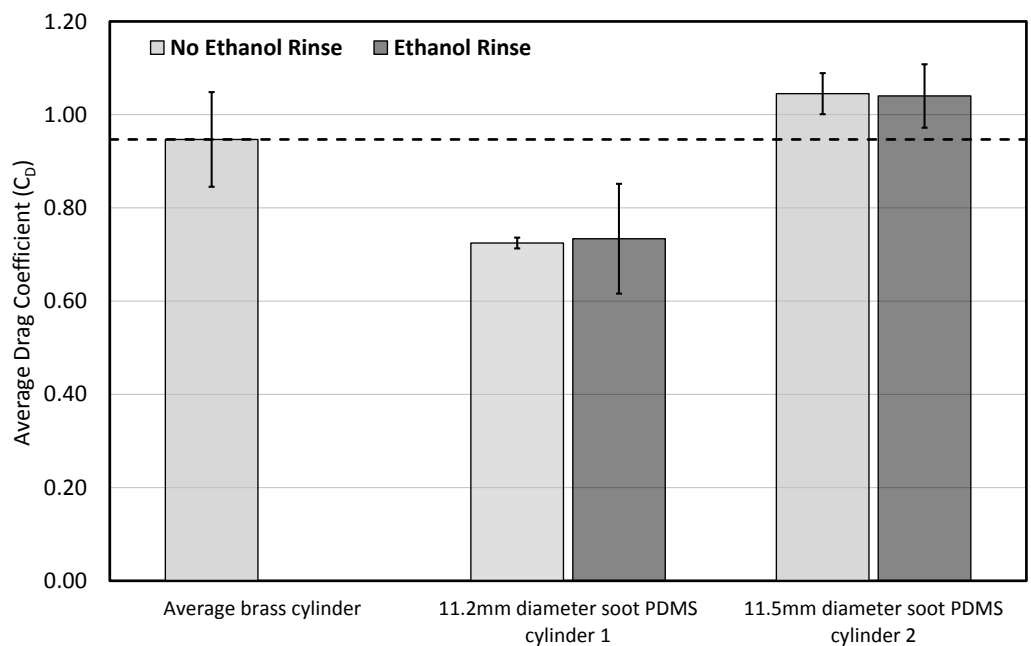


Figure 4.17: Chart comparing the average drag coefficient for the Ethanol rinsed and non-rinsed cylinders. The dashed line shows the average drag coefficient for the brass cylinders.

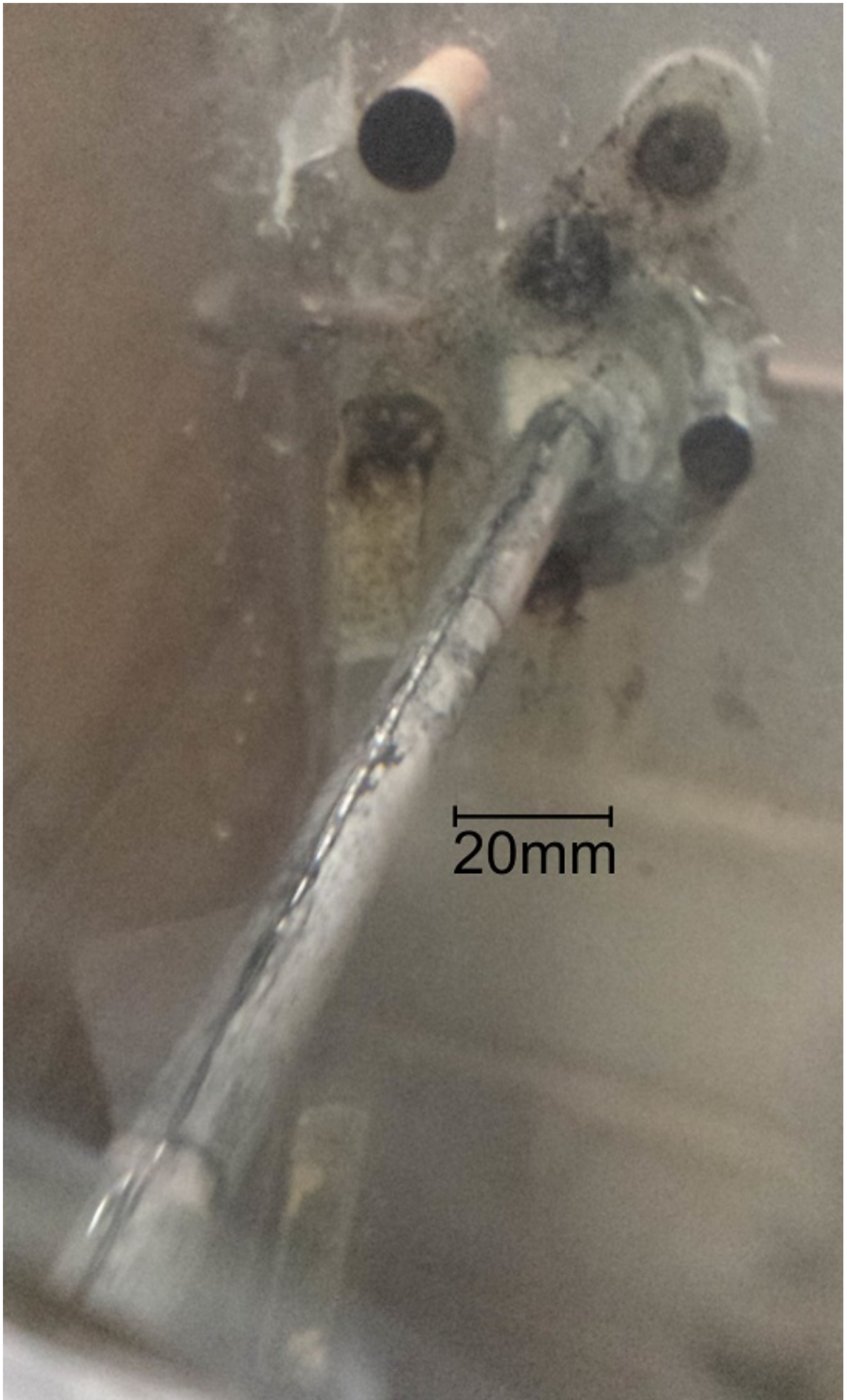


Figure 4.7: Image of a soot PDMS covered cylinder during testing. The surface appears silvery due to the presence of a plastron layer. The black lines on the cylinder are the seams where the edges of the PDMS substrates meet.

4.4 Discussion

Figure 4.8 displays the results for the uncoated plain brass cylinders. The drag coefficient is steady at ~ 0.90 for the 10mm diameter brass cylinder, ~ 0.95 for the 11mm diameter brass cylinder and ~ 1.00 for the 12mm brass cylinder. They all lie approximately, within error, around the same value. This agrees with the book value for previous work in this Reynolds number range of ~ 1 [168]. An average value of 0.95 will be used for comparison to the soot PDMS cylinder tests.

Figure 4.9 shows the results for the first soot PDMS cylinder tested. It was tested a total of 7 times and displays an average reduction in the drag coefficient of 0.22 with an drag reduction of 23% . The uncertainty in the measurements means the drag reduction for this cylinder is between 15% and 32% . For the entire Reynolds number range tested a reduction in drag is seen beyond the error range for each point. The standard error was used for the uncertainty value for all the cylinders tested.

Figures 4.10 and 4.11 show the results for the second and third soot PDMS cylinders tested. The drag coefficients found for these two cylinders was very similar to that of the uncoated brass cylinders. There is no discernible drag reduction from these results. This may be due to the preparation of the test cylinders and the condition of the seams on the cylinders (Fig. 4.18). Although the seams were lined up on the cylinders and positioned downstream during all tests, it is possible that they caused disruption to the flow, increasing the drag coefficient. The hydrophobicity of the cylinders is not believed to be in question as upon removal from the flow chamber the cylinders were dry, indicating the high contact angle and low run off angle were maintained throughout the testing procedure (Fig.4.19).

Figure 4.12 are the results for the fourth soot PDMS cylinder. Although the average drag coefficient is 0.88 , below that of the plain cylinders, the uncertainties overlap with those of the uncoated cylinders.

Figure 4.13 shows the drag coefficient of the fifth soot PDMS cylinder. An average drag coefficient of 0.8 was produced with a small uncertainty. This is below all the plain brass drag coefficients with no overlap in errors. This is an average reduction of 16% .

Soot PDMS cylinders 1 and 5 show a clear reduction in the drag coefficient which means a reduction in the drag force produced by the cylinders. Cylinder 4 also shows a reduction in the drag coefficient but this is within the uncertainty of its result and the result of the plain cylinders.

Cylinders 2 and 3 produced drag coefficients similar to or slightly above that of the plain cylinders. This indicates an increase in the drag force. This may be due to the condition of the seam on the rods. Figure 4.18 shows the condition of the seam on the third soot PDMS rod. The gaps in the seam leave areas of the brass exposed. These areas are not superhydrophobic and are unable to support a plastron (Fig.4.7). Without a plastron there can be no air circulation and therefore have no ability to reduce drag. For this reason these areas may disturb the flow around the cylinders causing increased drag.

Figure 4.14 and 4.15 show the results from soot PDMS cylinders that have been rinsed in ethanol prior to testing in an attempt to remove the plastron during testing. Each test was conducted three times and an average was found. The ethanol has a low surface tension and infiltrates the features on the surface of the cylinders. When the cylinders are then placed into the flow chamber the ethanol is replaced by water and surface is said to be “wetted out” with no air layer present on the surface. The graphs show the results for the first and second soot PDMS cylinders with and without an ethanol rinse. There appears to be very little difference between the wetted out cylinders and the superhydrophobic cylinders with all points overlapping within error. The drag reduction displayed in the figure 4.9 is maintained after the ethanol rinse, with all points overlapping within the error as shown, in figure 4.14. The wetted cylinder also shows a more consistent drag reduction over the three tests than the unrinsed cylinder results. Figure 4.15 also shows that the ethanol rinse did little to affect the drag properties of the soot PDMS surface as there is little difference between the rinsed and unrinsed cylinder tests. Figure 4.17 more clearly shows how the ethanol rinse has little effect on the drag characteristics of the soot-coated PDMS cylinders. This may be because the ethanol rinse is incapable of removing the plastron air layer and does not infiltrate into the soot CNP network

or that the ethanol evaporates from the surface before the water can replace the ethanol in the structured surface. As the testing procedure requires the test cylinders to be placed into the flow chamber empty and then it is filled, the time taken to submerge the cylinder, approximately 30 to 45 seconds, is sufficient for the substrate to recover its initial state. A modified procedure was used, where by the cylinders were immersed in ethanol and then immediately following this they were immersed in water. The tests were performed with this modified rinse procedure. Even with the modified procedure the results indicate that the surface retains its properties after the rinse and similar results are obtained for the cylinders regardless if they are wetted out or not. Post-testing it became apparent that the ethanol had caused the PDMS substrates to shrink on the cylinders, causing the seams to open and become wider 4.20. This shrinking was not present during the wetted out tests.

The negligible difference between the ethanol rinsed and superhydrophobic tests can also be seen as a positive result (Fig.4.17). Even after exposure to a liquid with a much lower surface tension which should penetrate through the features on the surface of the PDMS, the substrates maintain their properties. The effects of the penetrating liquid did not affect the drag coefficient measured for the two cylinders tested and the drag reduction displayed by the first soot PDMS cylinder is maintained. This indicates the possible robustness of the flexible soot PDMS surface. The coating is not removed after repeated test and the drag characteristics are not effected after exposure to a solvent.

The size of the cylinders tested was near the maximum possible for the flow chamber. The flow chamber has a window that is accessible up to 400mm downstream of the testing cylinders. This means that with measurements taken 30 diameters downstream, a maximum cylinder diameter of $400/30 = 13.\dot{3}mm$.

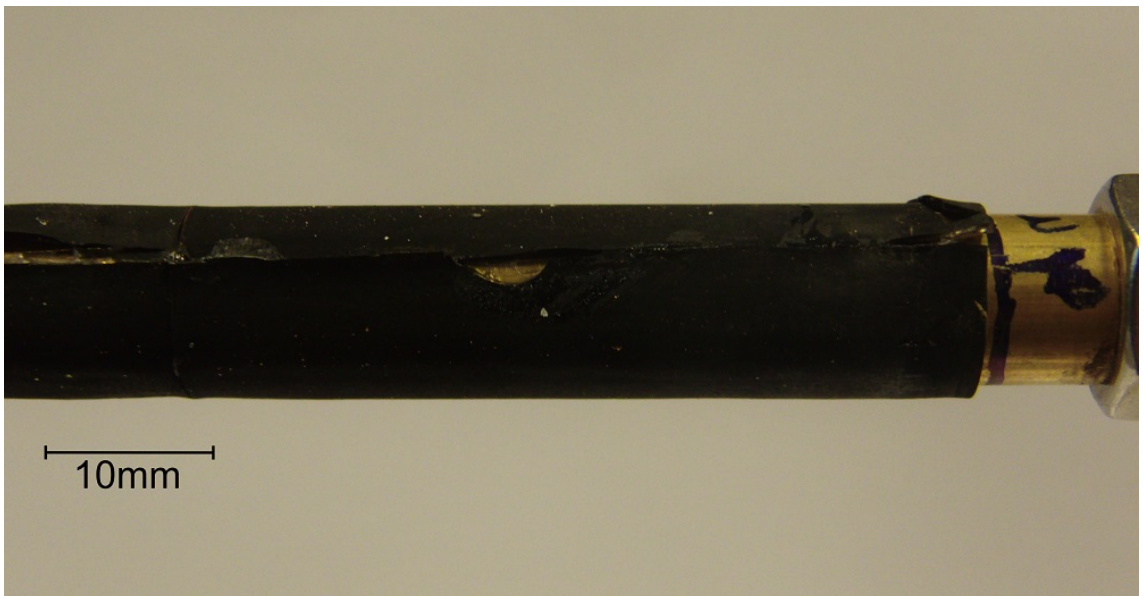
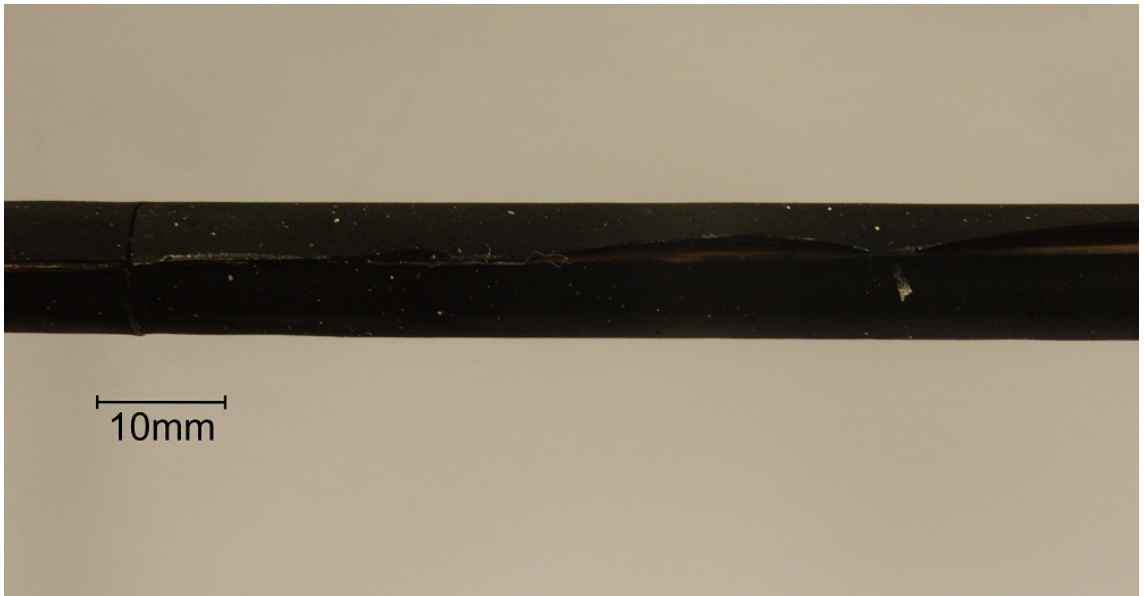
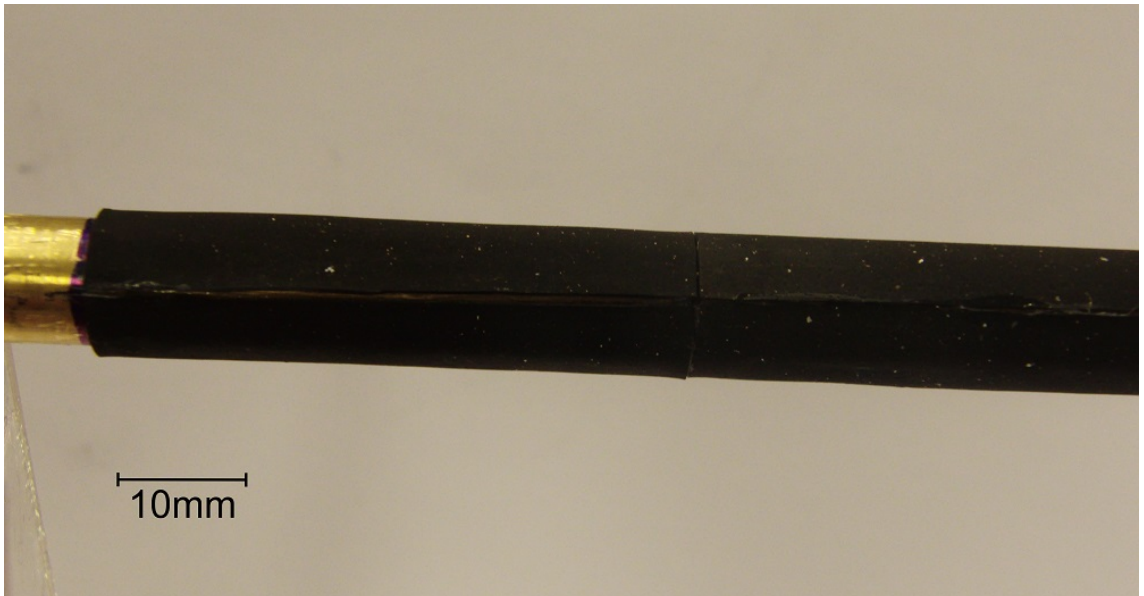


Figure 4.18: Images of the third soot PDMS cylinder after testing.



Figure 4.19: Image of a soot PDMS covered cylinder after a test in the flow chamber. The matt black surface of the cylinder shows the surface remained dry throughout the test.



Figure 4.20: Image of the second soot PDMS covered cylinder after all testing. The ethanol rinse has caused the PDMS substrate to shrink.

4.5 Conclusions

Through the application of a soot PDMS flexible surface, it is possible to make the surface of brass cylinders superhydrophobic. The surface allows a visible air layer to exist around the cylinders when submerged in water. This plastron layer is not present for the uncoated brass cylinders. In the presence of the superhydrophobic surface there is a maximum drag reduction of 28% when comparing the uncoated brass cylinders to a soot PDMS coated cylinders. The best result for a single cylinder was for the 11.2mm diameter soot PDMS cylinder 1 which had an average drag coefficient of 0.72 ± 0.01 . This is a reduction of 23%. Even with this considerable reduction only 3 of the 5 cylinders tested showed a reduction in the drag coefficient as shown in figure 4.16.

Comparing the ethanol rinse tests to the superhydrophobic tests shows that the ethanol rinse is ineffective at changing the results of the flow chamber tests. There is very little difference between the wetted out and superhydrophobic cylinder results. This shows that the properties of the surface are maintained even after exposure to a liquid with a low surface tension which penetrates the surface features.

The results of the superhydrophobic cylinders are not consistent. The construction of the coated cylinders must be improved in order to negate the effects of the seams which cause a break in the superhydrophobic surface and disrupt the flow around the test samples. Development of the sample fabrication processes are needed in order to produce superhydrophobic surface sufficiently large as to coat a cylinder with a single superhydrophobic flexible substrate.

4.6 Suggested Work

Further Testing of the Drag Reducing Properties of the Novel Surface

The development of a larger area of soot coated PDMS would also be advantageous. Problems exist with evenly curing large areas as the the curing time of PDMS is

controlled by the temperature. If the temperature is not even across the whole surface then the PDMS will be unevenly cured when the sooted plates are deposited on the surface. The current methods for precuring the PDMS surface exhibit a temperature gradient and so for larger areas these problems of uneven curing exist. If it is possible to create sooted substrates with dimensions of at least 220mm by 40mm it would be possible to test the surface for their drag reduction properties with samples with only one seam on the trailing side of the cylinder. This would reduce the possibility of any disruption to the flow other than that from the presence of the cylinder.

The development of multi-scale roughness (section 2.2) may also be advantageous for the purposes of drag reduction. Ridges on the surface can aid in plastron retention when the superhydrophobic surfaces are subjected to moving liquids and the ridged surfaces have been shown to have reduced drag [169–171]. If the surfaces can also be made superhydrophobic and of sufficient dimension to wrap a rod completely with only one seam, then the drag reduction properties of the surfaces can be tested.

Finding a way to infiltrate the soot network without damaging the surface would allow for the plastron to be removed from the surface. This would aid in the drag reduction testing as the rough surfaces could be compared to themselves with and without a plastron. This would remove any difference that may arise from the difference in diameter of the cylinders.

Chapter summary

This chapter reported the work on drag reduction using the novel superhydrophobic surface. The surface did produce a reduction in the drag coefficient when compared with uncoated samples but this was not for all samples tested. Further work is needed on the manufacturing processes in order to refine the experiments.

The next chapter describes the work on a snail repellent surface and how the novel conformable surface shows promise as a way of deterring snails.

Chapter 5

Snail Repellent Surfaces

This chapter reports the work performed in order to test the novel surface as a possible snail deterrent method. It provides a background on snail characteristics and current used methods for deterring snails.

The four different tests on the surface are described and the results of each are shown.

5.1 A Background to Snail Repellency

Gastropod Characteristics and Mucus Properties

Gastropods, more commonly known as slugs and snails, can range in size from the microscopic to nearly a metre in length. The land snail *Columella edentula* has a shell around 1mm in size whereas the largest terrestrial snail is the Giant African snail, *Achatina fulica*, which can grow to more than 20cm in length. The largest terrestrial gastropod is the *Limax cinereoniger*. This slug can grow to lengths greater than 30cm. The largest shelled gastropod known to man is the Australian trumpet, *Syrinx aruanus*, which had been found to grow to lengths of over 90cm, with weights exceeding 18kg. It is a marine gastropod and due to buoyancy the weight of the shell is no longer a limiting factor to the size of the mollusc and so much larger snails have evolved.

Snails are soft-bodied molluscs which carry a calciferous spiral shell on their backs.

They have a singular muscular foot which is their sole means of propulsion. Slugs are very similar to snails, the difference being the lack of a shell. Terrestrial gastropods are all hermaphrodites and so all have the potential to lay eggs. Once laid, the eggs have a gestation period of 2-4 weeks before hatching. Slugs reach maturity 6 months after hatching whereas snails can take up to 2 years to fully develop.

Terrestrial gastropods are most active during wet and cool periods. This is why they mostly reside in temperate regions. They avoid sunny or dry periods by hiding in damp shaded areas to reduce moisture loss which they are sensitive to. They feed on both ornamental and edible plants as well as decaying vegetation. They prefer young succulent foliage but are also attracted to ripening fruit [172,173]. They can descend on orchards and farms in large numbers to feed on crops causing considerable amounts of damage to the produce.

Helix aspersa (*Cornu aspersum*)

The common garden snail (*Helix aspersa*) is the most abundant terrestrial snail. It originates from the southern and western parts of Europe [174] but has spread worldwide to temperate and subtropical regions. It is now present on all continents except Antarctica.

Helix aspersa have a relatively large thick-walled shell that is yellowish-brown in colour with up to 5 spiral dark brown bands (Fig.5.1). The average mature snail is 35mm in height and width and have between $4\frac{1}{2}$ and 5 whirls. When fully extended the snails can grow to lengths of around 10cm. These snails are noted for their ability to repair substantial damage to their shells [175].

The snails are also edible and have become a delicacy all over the world.



Figure 5.1: Image of a common garden snail.

Methods for Snail Deterrency

The simplest method for preventing snail or slug damage is to hand-pick the pests and remove them from the affected areas before subsequent damage is caused. This method can be very effective if the molluscs are found prior to reproduction and can greatly reduce their numbers. This method may be effective but is very time-consuming and labour intensive.

Lures and Traps

Snails can be coaxed into accessible areas by providing shaded environments away from bright sunlight. This can include propped-up boards, pots, large leaves e.g. cabbage leaves or citrus peelings. When the snails gather in these sheltered areas they can then be collected up and removed. In order to entice them to congregate in these areas, dog or cat food can be used. A widely-used method to collect snails is to use beer or yeast and honey mixtures. A sunken pot is buried in affected areas and the liquid is placed inside. The snails are drawn to the pot and fall in and cannot escape.

Sharp/Jagged Edges

It is believed that placing crushed egg shells, sandpaper and diatomaceous earth around plants will deter snails. These abrasive surfaces are said to be an obstruction to the molluscs and are reluctant to travel over the materials.

Copper

Copper is known as a way of deterring snails. It is believed that the molluscs receive an electrochemical shock from the copper as the mucus reacts with the surface. The shock is unpleasant for the snails and so if copper bands are placed around the base of plants or around the trunk of a tree the snails will be deterred from eating the vegetation. The thickness of the band must be sufficiently wide so that the molluscs cannot “hoop” over the band to avoid touching the surface of the copper in order to reach the food source. If the mollusc can position a sufficient area of its foot on the other side of the band it can pull the rest of its body over the band to avoid contact with the surface. For common garden snails, this can be at least 10cm of copper and as the price of copper is quite high, this can be a costly solution.

Chemical Baits

There are two main types of chemical bait. The first is Methaldyhyde-based. These products usually come in pellet form. They are sprinkled over the ground around the plants so that as the molluscs approach the vegetation they come into the proximity of the pellets. The pellets also contain ingredients to attract the snails. As the snails devour the pellets the mollusc begins to rapidly dehydrate as the active ingredient is toxic for gastropods. If the molluscs cannot rapidly find a water source the dehydration will be fatal. An issue with this bait is it can not function after becoming wet. This means that when it rains or after watering the bait becomes ineffective. The bait can also be harmful to other animals if ingested.

The other type of chemical bait is iron phosphate based. These can be considered as less harmful and a more effective chemical bait. Iron phosphate is an organic compound that is found naturally in the soil and will break down over time into

a fertiliser. It does not readily dissolve in water so does not suffer the problem of becoming ineffective when wet. It is also usually found in pellet form for easy dispersal and again is attractive to snails. When the invertebrates eat the pellets, the iron phosphate interferes with the organism's calcium metabolism in their digestive system, causing them to completely lose their appetite and to stop eating. Eventually the molluscs die of starvation.

Predatory Snails

By introducing Decollate snails, *Rumina decollata*, to problem areas, the number of pest snails can be controlled as the decollate snails will feed on other young snails.

One issue with this solution is that Decollate snails may also eat vegetation but will do so to a lesser extent.

Snail Movement

Having only a single appendage gastropods employ adhesive locomotion in order to move. This form of movement is one of the most costly in terms of energy usage known [176]. Molluscs generate pedal mucus which they deposit on the ventral surface of the foot, over which muscular waves are produced in order to crawl over the mucus layer. This mucus layer is approximately $10\mu\text{m}$ to $20\mu\text{m}$ thick [177] and consists of between 91% and 98% water and salts. The remaining 2% to 9% is glycoprotein [178]. The glycoprotein is a polyelectrolyte that is greatly expanded by water. The presence of the glycoprotein in the mucus is responsible for its viscoelastic properties [179]. When subjected to small stresses, $0\text{-}20\text{Pa}$, the mucus behaves as an elastic solid where as at higher stresses, around 300Pa , it will begin to act as a liquid. If left unstressed it will recover its solid behaviour after approximately 0.1s [179]. Gastropod mucus is not just used for movement but is also used for adhesion to surfaces, which is advantageous in tidal or arboreal environments. It is also used for lubrication, predator repulsion and mating [178, 180]. The adhesive nature of the mollusc mucus allows the invertebrates to adhere to many different surfaces and to overcome gravity in order to travel across the underside of horizontal structures. It

also allows them to travel over low-energy non-adhesive surfaces such as PTFE and anti-adhesive hydrogels [1]. Shirtcliffe *et al.* recently tested the ability of snails to adhere to a variety of textured surfaces [1]. They performed a number of different tests to measure the adhesive properties of superhydrophobic surface to snail mucus and determined the force required to remove the snails from the surfaces. It has been proposed that the ability to pull a droplet of liquid from a surface is dependent on the receding contact angle [10]. This idea has consequences for the ability of snail mucus to adhere to superhydrophobic surfaces as the muscular wave generated on the ventral surface of a snail's foot generates a pulling force in order to move the snail forward. The adhesive properties of the mucus is likely to therefore be important to the wetting properties of the adhesive mucus and the ability of the snails to move over hydrophobic surfaces.

5.2 Investigation of CNP Coated PDMS as a Snail Deterrent Surface

5.2.1 Snail Type

The best way to determine the capability of the superhydrophobic CNP coated surfaces at deterring snails is to use live snails. The most common snail in the UK is the brown garden snail (European brown snail), *Helix aspersa* or *Cornu aspersum*, which is a plant eater (Fig.5.1). It has been disseminated to many parts of the world as a edible delicacy but also through plant movement. It can be a problem in many areas as it feeds on crops and ornamental plants. For this reason these snails were chosen for experimentation. 36 snails were acquired from H&RH Escargots, 24 mature and 12 newly hatched. These were used in a variety of experiments designed to test the deterrent properties of the surface and the snails ability to adhere to said surface.

5.2.2 Pot Comparison Tests

Three pot comparison tests were performed. The thinking behind the tests was to see whether or not, given the option between multiple food sources, if the snails would climb certain surfaces to reach their food. For the first test three pots were made. One was left uncoated, the second was covered in copper tape and the third was coated with the CNP PDMS (Fig.5.2). The three pots were then planted with small lettuce plants and placed into a closed environment. The closed environment was constructed from a 50l plastic storage box, in which a layer of moist soil had been placed. The pots were evenly spaced in the box. The pots were 150mm tall, with a diameter of 75mm. The soot pot was made by patching together rectangular areas of the PDMS and sticking them to the side of a pot, using the same primer and cyanoacrylate adhesive used for the superhydrophobic cylinder construction. The seams of the sooted surfaces were covered in 1cm wide copper tape. Copper is well known for its ability to deter snails. The exact reason for this is not precisely known, but it is believed that when a snail makes contact with a copper surface, a reaction occurs between the mucus and the copper, resulting in an electro-neural signal (similar to an electric shock) that repels the snail.

Twenty four mature snails were placed in the box and a fine netting was used to keep the snails in the container. The snails were then left for 72 hours.

The second and third pot comparison tests were very similar. The second comparison test saw the construction of a clear acrylic box, 290mm × 200mm × 200mm in size. Two new pots were made for this test, the same size as used in the first comparison test. In this comparison test, an uncoated polypropylene pot and a soot coated PDMS pot were compared (Fig.5.3a). New superhydrophobic PDMS surfaces were made for this test in order to obtain rectangular areas of approximately 150mm in length. This was to minimise the number of seams on the side of the pot. 12 immature snails were placed in the box with the two pots and again, the plan was to leave the box for 72 hours, this time with a time lapse camera taking a photo every 5 minutes (Fig.5.3b). However, after a short time, it became apparent that the snails were smarter than expected. They climbed to the roof of the box and dropped down



(a) Three pots made for comparison.



(b) Pots in the enclosure.

Figure 5.2: Images of the first of the three pot comparison tests.

onto the pots. The test was stopped at this point.

The third comparison test was identical to the second but the height of the box was doubled to 400mm . As in the second comparison test, 12 immature snails were placed in the box for 48 hours, whilst being photographed every 5 minutes using a time-lapse camera(Fig.5.4).

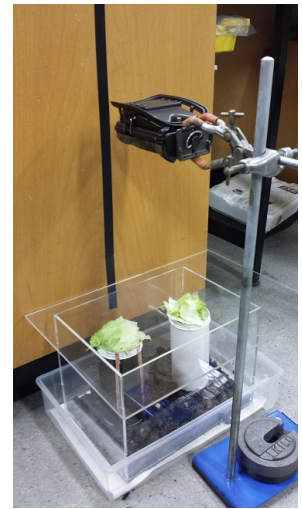
5.2.3 Maze Tests

In order to test the repellency of the soot surface, a maze test devised by Shirtcliffe *et al.* [1] was recreated. This involved the creation of a zigzag track, 3cm wide, on an A4 sheet of acrylic, with the track being surrounded by the superhydrophobic surface (Fig.5.5).

The maze was mounted vertically and a bundle of lettuce was suspended at the



(a) Two pots were made for comparison, a soot coated PDMS (superhydrophobic) pot (left) and an uncoated polypropylene pot (right).



(b) Image of the comparison setup with a time-lapse camera mounted above the box.

Figure 5.3: Images of the second of the three pot comparison tests.

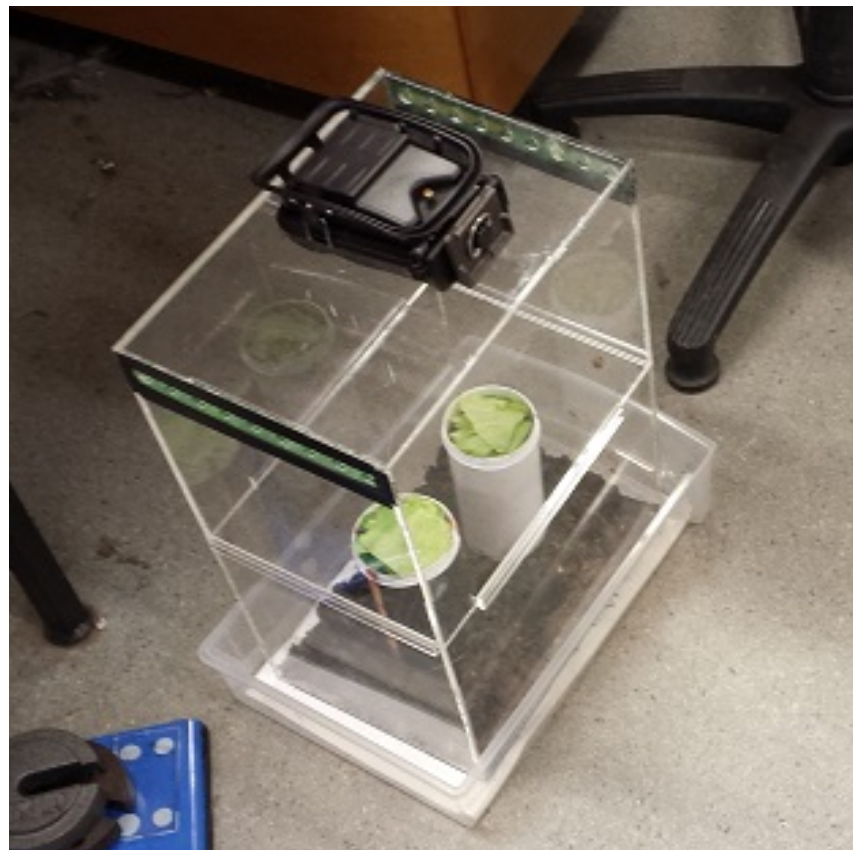


Figure 5.4: Image of the third pot comparison test.

top of the zigzag track. The immature, smaller snails were placed, individually, at the bottom of the track and their movements tracked with the time-lapse camera, taking an images every 10 seconds. 10 of the immature snails were subjected to the



Figure 5.5: Image of the zigzag maze surrounded by soot PDMS.

maze.

5.2.4 Spin Tests

In order to evaluate the extent to which snails could adhere to a variety of surfaces, Shirtcliffe *et al.* performed a series of spin tests to find the average centripetal force required, in terms of g , the gravitational force, to remove snails from a surface [1]. The same set-up was used to evaluate the CNP coated surfaces (Fig.5.6).

A spin coater was modified and connected to a variable DC power supply. As the voltage on the supply is slowly increased, so to is the speed of rotation. Custom spin heads were made to which 20cm diameter acrylic discs could be attached. These removal speed was determined for:

- Glaco[®] Zero mirror coat

This is a commercially available product designed for car windows and mirrors. It contains nanoparticles suspended in a solvent that can be wiped onto glass surfaces to increase the hydrophobicity.

- Hydrophobic sand

Sand grains, 100 μm to 150 μm in size, were stuck to an acrylic disc using a spray contact adhesive. The surface was then treated with Granger's[®] Extreme Wash-in to make it hydrophobic.

- CNP PDMS

Two variations of the superhydrophobic soot surface were tested. One with an unrinsed soot PDMS surface and another with a rinsed soot surface, which was held under a fast flowing tap for 20 seconds to remove any loose CNPs from the surface. The removal force was determined for the surface immediately after a snail was placed on the surface, and again after a period of 30 seconds.

- Hyrec 1405

This is the same product described in section 2.1.1.

- Unbound soot

Glass slides, $75\text{mm} \times 50\text{mm}$, were coated in a layer of rapeseed oil soot and stuck onto an acrylic disc.

- Superhydrophobic sand (Magic sand)

Magic sand is a commercially available product marketed as a child's toy. It is composed of sand grains that have been exposed to a hydrophobic compound which coats the surface of each grain.

- PDMS

- Acrylic

- Glass

- Polypropylene

- CNP coated PDMS saturated with Fluorinert FC70

More details on this surface can be found in section 5.2.5

To determine the removal force, a snail was first weighed and then placed 5cm from the centre of modified acrylic discs. The voltage to the spin coater was slowly increased until the snail was ejected from the surface. The revolutions per minute was then recorded using a light tachometer. The foot print of the snails was also taken (Fig. 5.7).

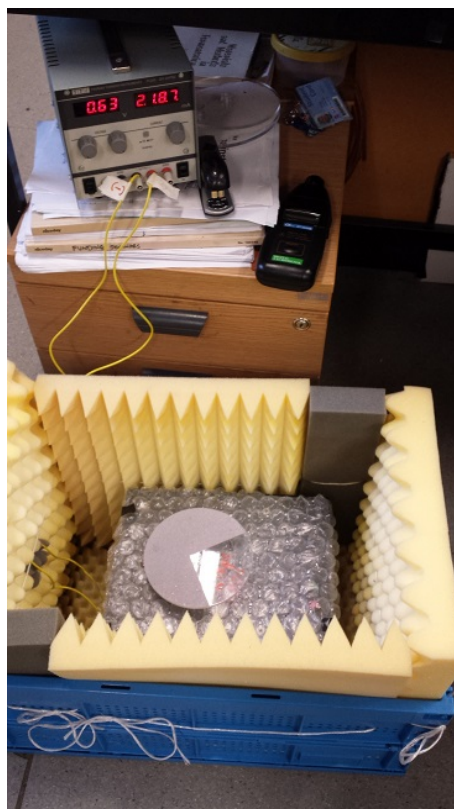


Figure 5.6: Image of the spin removal force determination experimental setup.

5.2.5 Fluorinert Modification of the Sooted Surfaces

In an article by Wong *et al.* [181], a bioinspired, self healing slippery surface is reported. The paper describes a “strategy to create self-healing, slippery liquid-infused porous surface(s) (SLIPS)”. In the article they describe the process of infiltrating a textured/porous low-energy surface with an inert liquid that is held in place by the structure that surface. One such liquid is Fluorinert FC70 from 3M. The paper demonstrates how these surfaces are capable of repelling various simple and complex liquids such as water, hydrocarbons, crude oil and blood. It also maintains a low hysteresis and is quickly able to repair itself after damage.

With the CNP structure on the surface of the PDMS forming a network of peaks and troughs, it resembles the surfaces used by Wong *et al.* and may be a another way to take advantage of the slippery repellency of the inert liquids. With the soot surfaces already being superhydrophobic and flexible, the ability to add self-repairing properties and repellency to a wider range of liquids, would make the surface even more useful.

The Fluorinert soot surfaces were made by simply pipetting $5 - 10\mu\text{l}$ per cm^2 onto



Figure 5.7: Image of a snail's footprint area being recorded.

a rinsed CNP PDMS surface. This was sufficient to infiltrate the surface features without the liquid flowing over the top of the surface.

5.2.6 Effect of Surface Tension on the Contact Angle for Different Surfaces

The advancing, receding and static contact angles were measured for various concentrations of Sodium Dodecyl Sulphate (SDS) in water. Eight different concentrations were made in order to test the effect of surface tension on six different surfaces.

These were:

- Glass
- PDMS
- soot coated PDMS
- Polypropylene
- Fluorinert saturated soot PDMS

5.3 Results

This section describes the results from the the four experiments performed to determine the capabilities of the soot PDMS surface as a snail deterrent surface have been presented.

5.3.1 Pot Comparison Tests

Test 1

Figure 5.8 shows the results of the first pot comparison test, in which a soot coated PDMS pot was compared to a copper coated and an uncoated polypropylene pot. An equal amount of lettuce was planted in each of the pots prior to testing (Fig.5.8a).

After 65 hours, the twelve mature snails had consumed all the lettuce in the uncoated polypropylene pot and were in the process of eating the lettuce in the soot coated pot as shown in Fig.5.8c. The snails appeared to have avoided the copper coated pot completely. This would indicate that the snails consumed the lettuce in the uncoated pot first, preferring to climb over the polypropylene surface before climbing the soot coated PDMS or the copper coated pots.

Test 2

The second comparison test was designed to compare the activity of ten immature snails in an enclosure in which an uncoated polypropylene pot and a soot PDMS coated pot had been placed, both having equal amounts of lettuce placed on top (Fig.5.9).

15 hours into the experiment it became apparent that the snails were not climbing the pots to get to the lettuce but were crawling over the top acrylic cover sheet and then dropping onto the pots from above (Fig.5.10). The experiment was halted at this point.

Test 3

Test 3 was very similar to the second comparison test but the height of the box was doubled, to 40cm, to discourage the snails from dropping onto the top of the pots from above. Again, ten immature snails were placed in the box with the same two

pots used in the second comparison test. Equal amounts of lettuce were placed on top of the pots and it was left for 48 hours.

Figure 5.11 shows 10 time-lapse images over the course of 48 hours. within which the test was run. Within five and a half hours of the start of the test snails had begun to climb the polypropylene pot to eat the lettuce on top (Fig.5.11b). This continued for the next $26\frac{1}{2}$ hours (Fig.5.11c,5.11d,5.11e and 5.11f). As many as 5 snails can be seen at one time on top of the uncoated Polypropylene pot. At the 32 hour point, a single snail can be seen climbing the soot PDMS pot, and remained there until the end of the test (Fig.5.11g,5.11h,5.11i and 5.11j) whilst multiple snails continued to occupy the top of the uncoated pot. The initial and final states of the two pots can be seen in figure 5.12. A large amount of lettuce had been consumed from the top of the uncoated polypropylene pot indicating a much greater amount of activity on this pot. There was very little difference in the appearance of the lettuce on top of the soot PDMS coated pot, pre and post test, indicating very little activity on the pot. With the only difference between the two pots being the surface coating, it would appear the snails were discouraged from climbing the soot PDMS pot in favour of the polypropylene pot.



(a) Image of the 3 comparison pots before placement in the test enclosure. Soot coated PDMS(left), Copper coated (middle) and Polypropylene (right).



(b) Image of the 3 pots before the snails were placed in the box. Soot coated PDMS(left), Polypropylene (middle) and Copper coated (right).



(c) Image of the 3 pots after 65 hours.

Figure 5.8: Before and after images of the first pot comparison test. Soot coated PDMS(left), Polypropylene (middle) and Copper coated (right).



(a) Images of the two test pots in the second comparison test. Soot coated PDMS (left) and Polypropylene (right).



(b) Ten immature snails were placed in the acrylic box with the pots.

Figure 5.9: Images of the second pot comparison test.



(a) Image showing a snail (circled in red) crawling on the top surface.



(b) The snail is pictured dropping onto the pot.

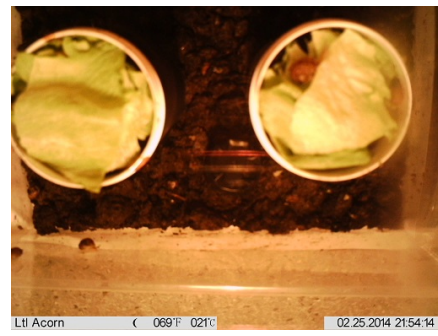


(c) The snail moving over the lettuce.

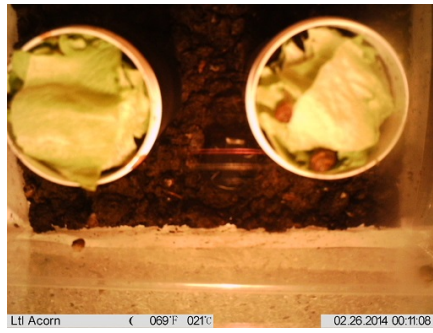
Figure 5.10: Images showing a snail dropping onto the pots from the top surface.



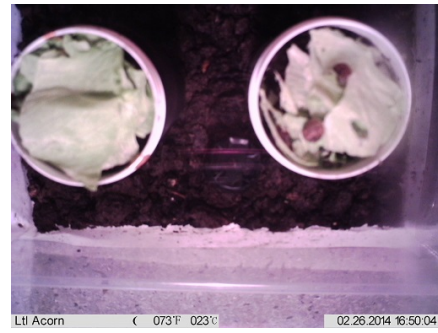
(a) Start of the comparison test.



(b) After 5 hours 20 minutes.



(c) After 7 hours 37 minutes.



(d) After 24 hours 16 minutes.



(e) After 26 hours 43 minutes.



(f) After 28 hours 14 minutes.



(g) After 32 hours 07 minutes.



(h) After 32 hours 12 minutes.

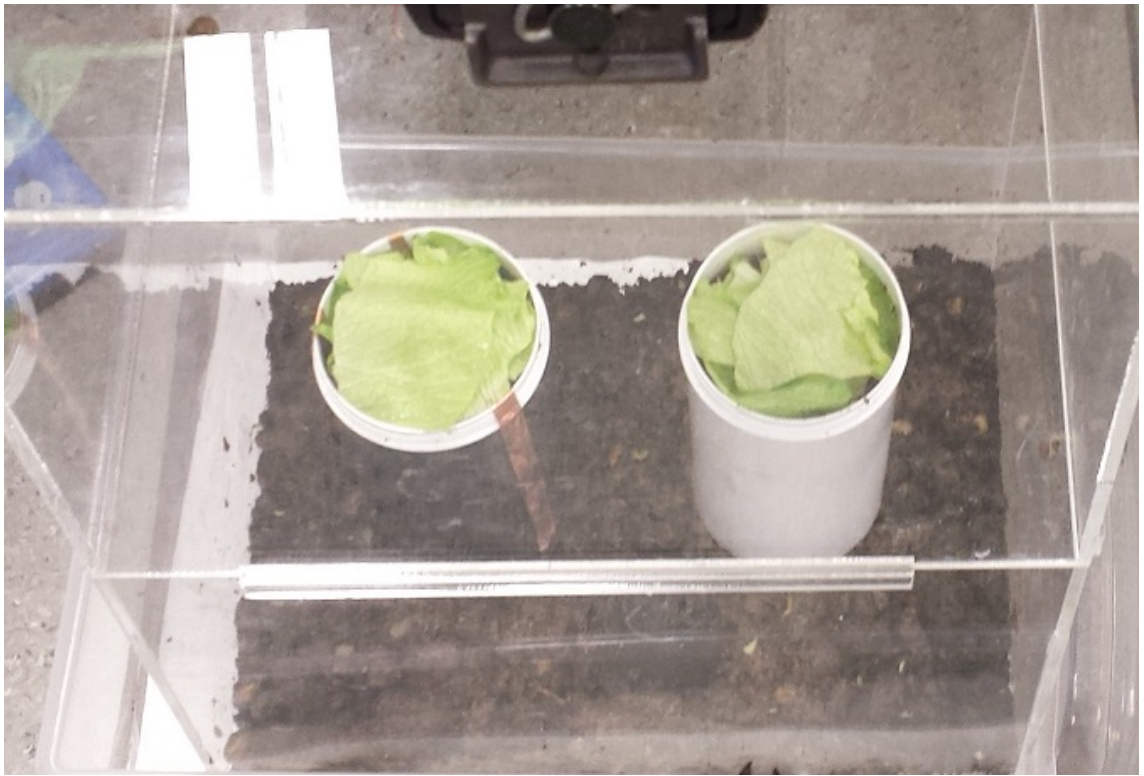


(i) After 34 hours 55 minutes.



(j) After 45 hours 59 minutes.

Figure 5.11: Time-lapse images of the third pot comparison test.



(a) Image of the pots at the start of the experiment.



(b) Image of the pots at the end of the experiment.

Figure 5.12: Before and after images of the third pot comparison test.

5.3.2 Maze Tests

Vertical Acrylic Sheet

An acrylic sheet was mounted vertically in order to determine the typical route a snail will take when located near a food source (Fig.5.13a). Seven immature snails were individually placed at the bottom of the sheet and their movements recorded. Table 5.1 shows the results of these tests and figure 5.14 illustrates, using time-lapse imaging, one snail's movements, which was a recurring result for all snails in this set of tests.

Vertical Maze Test

Sixteen immature snails tested with the soot PDMS maze in the vertical position. The snails were positioned at the bottom of the path and a food source was placed at the top, to attract the snails to the other end of the path. Table 5.2 shows the results of these tests. For tests 1, 2, 3, 4, 5, 6, 7, 8, 14 and 15 the snail avoided the soot PDMS surface and remained on the path for the duration of the test. Figure 5.15 shows the path of the snail in test 1. During test 9 the snail left the path for the first time. Its path is shown in figure 5.16. In test 10, 12 and 13 the snails followed the same path over the soot as the snail in test 9. This can also be seen in test 10 and 16. The snail left a path over the soot in test 10 which was then followed by the snail in test 16.

Horizontal Maze Test

Nine immature snails had their movements recorded with the soot PDMS path in the horizontal plane. Only in tests 3, 6 and 8 did the snails avoid moving over the soot surface (see Table 5.3). In all the other tests the snails moved over the soot surface. This occurred multiple times in test 2.



(a) Vertical acrylic sheet used to observe the typical path of a snail when presented with a food source. (b) Zig-Zag acrylic path enclosed by soot PDMS.

Figure 5.13: Images of maze test setup.

test no.	Description
1	Snail travelled in a straight line to the lettuce
2	Snail travelled in a straight line to the lettuce
3	Snail travelled in a straight line to the lettuce
4	Snail travelled in a straight line to the lettuce
5	Snail travelled in a straight line to the lettuce
6	Snail travelled in a straight line to the lettuce
7	Snail travelled in a straight line to the lettuce

Table 5.1: Table of results for the vertical acrylic sheet tests.

Test no.	Did the snail avoid the soot PDMS?	Description
1	Yes	The snail stayed on the path from start to end
2	Yes	The snail travelled a third of the path length before stopping
3	Yes	The snail travelled two thirds of the path length before stopping
4	Yes	The snail travelled two thirds of the path length before stopping
5	Yes	The snail travelled two thirds of the path length before stopping
6	Yes	The snail travelled half of the path length before stopping
7	Yes	The snail stayed on the path from start to end
8	Yes	The snail stayed on the path from start to end
9	No	The snail travelled two thirds of the path before crawling over the soot PDMS
10	No	The snail followed the path over the soot PDMS of the previous snail
11	No	The snail left the path at the first corner and crawled over the soot PDMS
12	No	The snail followed the path over the soot PDMS of the previous snail
13	No	The snail followed the path over the soot PDMS of the previous snail
14	Yes	The snail travelled a third of the path length before stopping
15	Yes	The snail stayed on the path from start to end
16	No	The snail left the path at the first corner

Table 5.2: Table of results for the vertical soot PDMS maze tests.

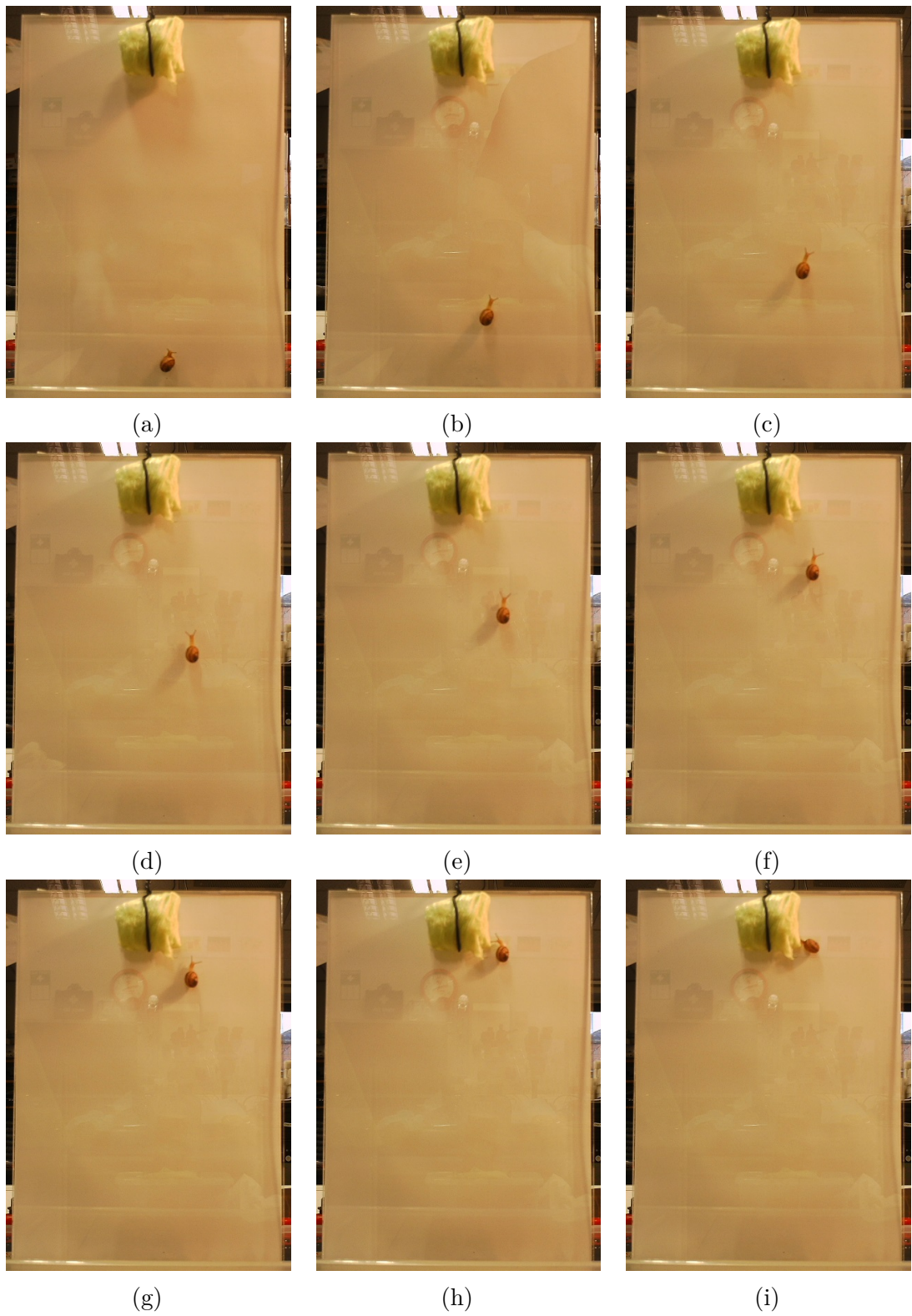


Figure 5.14: Time-lapse images of a snail travelling upward on a vertically mounted sheet of acrylic.



(a) Image of a snail at the start of the soot PDMS vertical path.



(b) Snail approaches the first corner.



(c) Snail investigates the soot surface for a possible route.



(d) Snail makes its way along the path.



(e) Snail makes its way along the path.



(f) Snail approaching the second corner.



(g) Snail investigating the surfaces at on corner.



(h) Snail crawls toward the lettuce.



(i) The snail has made it the entire way along the path.

Figure 5.15: Time-lapse images of a snail travelling the length of the path enclosed by soot PDMS.

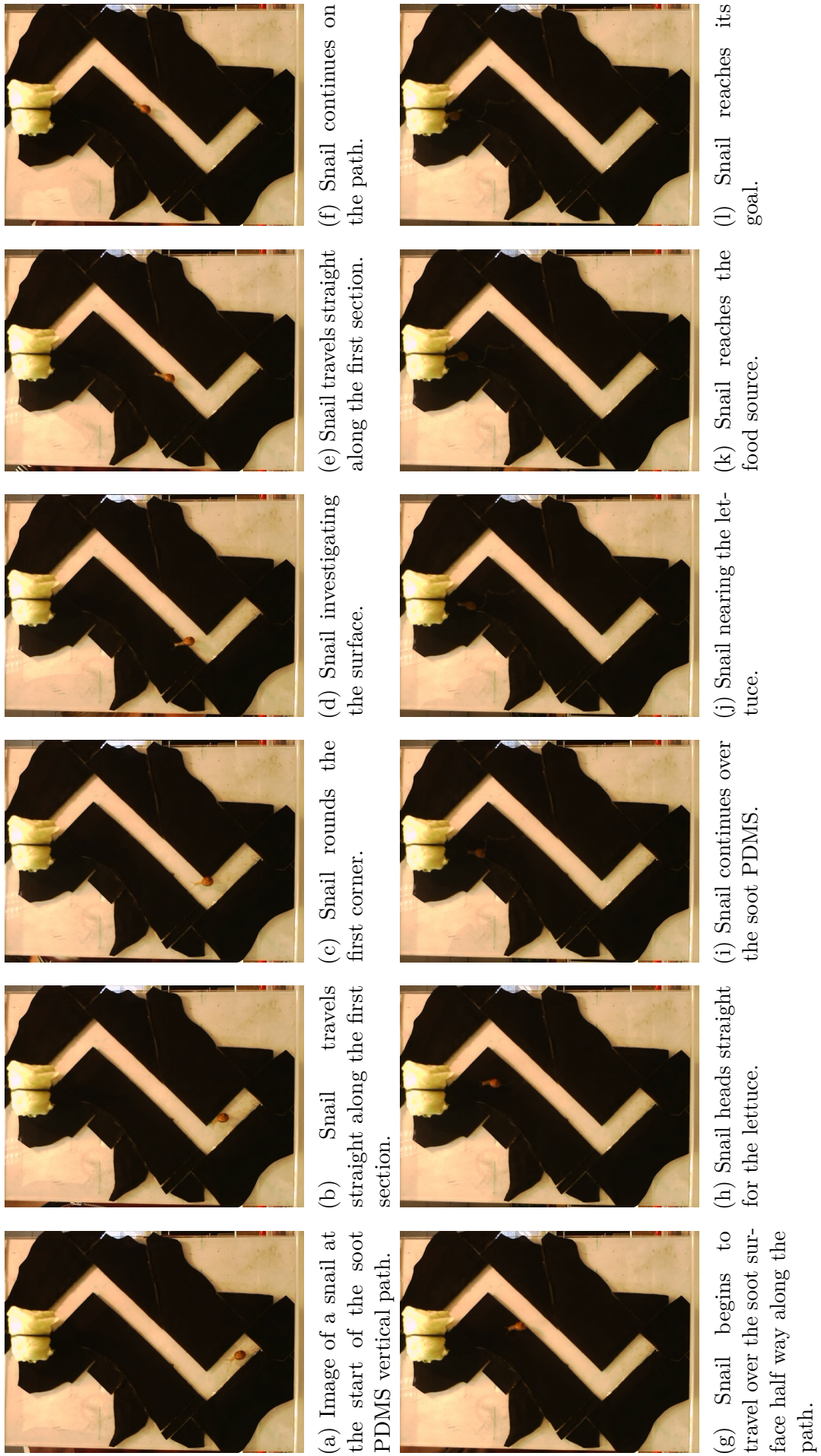


Figure 5.16: Time-lapse images of a snail travelling over the soot surface during a vertical maze test.

Test no.	Did the snail avoid the soot PDMS?	Description
1	No	Snail travelled two thirds of the path before leaving the path
2	No	Snail left the path multiple times before reaching the lettuce
3	Yes	Stayed on the path from start to end
4	No	Snail travelled two thirds of the path before leaving the path
5	No	Snail travelled straight on at the first corner
6	Yes	Stayed on the path from start to end
7	No	Left the path at the start
8	Yes	Travelled to the first corner and back to the start
9	No	Snail travelled straight on at the first corner and left the sheet

Table 5.3: Table of results for the horizontal soot PDMS maze tests.

5.3.3 Spin Tests

In order to determine the extent to which a snail can adhere to a surface, spin tests, described in section 5.2.4, were conducted. The RPM at which the snails were ejected from a surface was recorded and converted into a centripetal force using equation 5.1. A minimum of 9 snails were spun on each surface and the average removal force was determined for each surface (Table 5.4).

$$F = \frac{4\pi^2(RPM)^2rm}{3600} \quad (5.1)$$

Where RPM = Revolutions Per Minute r = radius m = mass

Figure 5.17 shows a graph of the removal force, sorted from highest to lowest force, for each surface.

Brown garden snails take six months to reach maturity. All spin tests were conducted in a 4 week period and in this time the snails size significantly increased. In order to account for this the snails mass and footprint area were recorded (Fig.5.18). There graph indicates a linear relationship between the footprint area and the mass of the snails. This relationship was used to determine the footprint area for each snail tested. The removal force was then divided by the footprint area to negate the influence of size and mass changes during the testing period.

Figure 5.19 shows that the soot PDMS surfaces all required less than $200N/m^2$ in order to remove the snails from the surface, with only the Magic Sand[®] and loose

soot performing just as well. All other surfaces required over $600N/m^2$ for snail ejection. These results indicate that the snails cannot adhere well to the soot surface.

Surface	$\langle Force \rangle (N)$	error
Polypropylene	0.072	0.010
Fluorinert soot pdms	0.07	0.01
Zero	0.034	0.006
Glass	0.033	0.009
PDMS	0.033	0.004
Sand (Graingers)	0.033	0.003
Acrylic	0.028	0.007
Soot PDMS (rinsed - 30 sec)	0.009	0.002
Magic Sand	0.007	0.002
Soot PDMS (Rinsed)	0.004	0.001
Soot PDMS (Unrinsed)	0.003	0.001
Soot (loose on glass)	0.003	0.001
Soot PDMS (unrinsed - 30 sec)	0.0026	0.0004

Table 5.4: Table showing the average force required to eject a snail from a given surface.

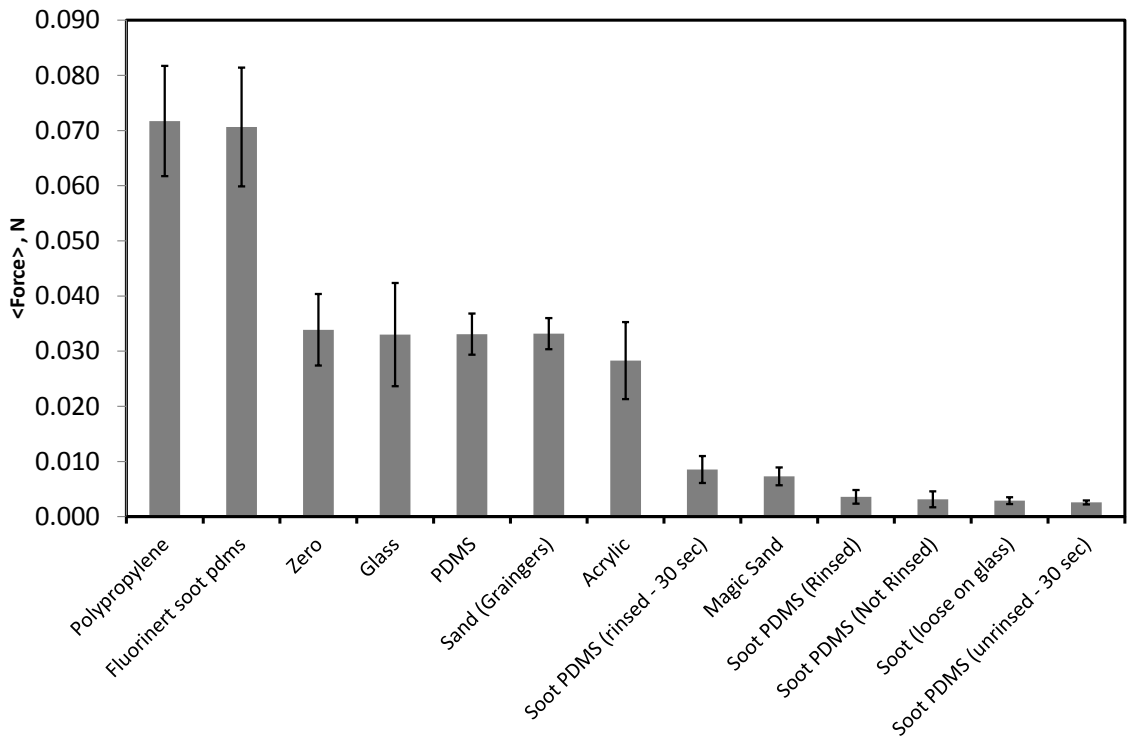


Figure 5.17: Graph showing the average removal force for a given surface.

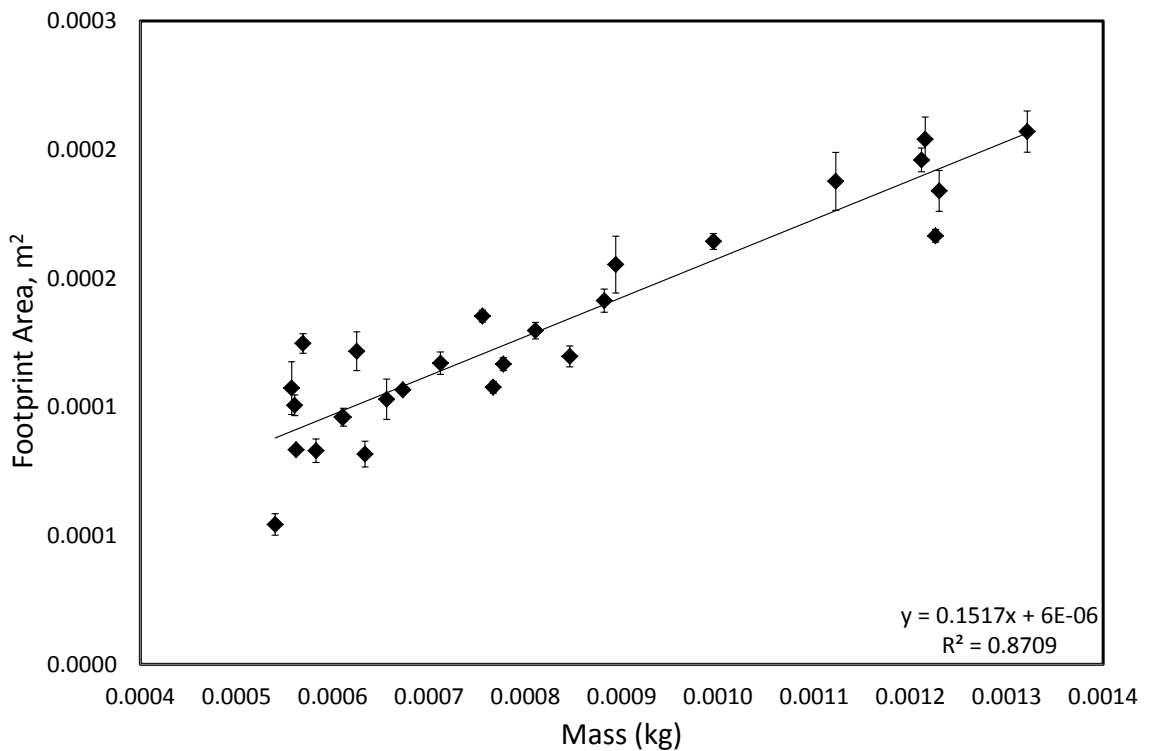


Figure 5.18: Graph showing the variation in footprint area with mass for maturing common garden snails.

Test Surface	$\langle Force \rangle / \langle Area \rangle$ (N/m^2)	error
Zero	1163	238
Acrylic	1026	265
PDMS	996	124
Sand (Grangers)	808	78
Fluorinert soot PDMS	790	129
Polypropylene	785	117
Glass	700	207
Soot PDMS (rinsed - 30 second wait)	189	56
Magic Sand	170	39
Soot PDMS (Rinsed)	134	48
Soot PDMS (Unrinsed)	117	55
Soot (loose on glass)	72	16
Soot PDMS (Unrinsed - 30 second wait)	63	10

Table 5.5: Table showing the average force per square metre to remove the snails from a given surface.

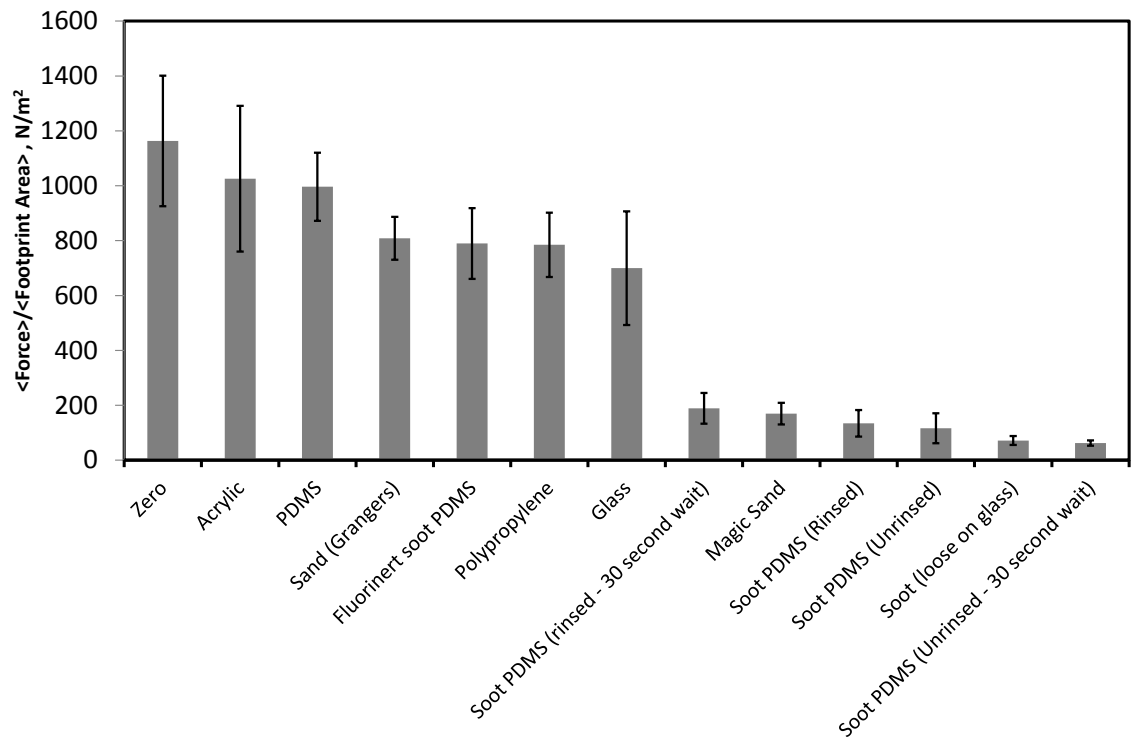


Figure 5.19: Graph showing the difference in removal force, divided by the footprint area, for all test surfaces.

5.3.4 Surface Tension Tests

One hypothesis by Shirtcliffe *et al.* [1] was that the ability of a snail to adhere and move over a wide variety of surfaces is due to the presence of a weak bio-surfactant that reduces the receding contact angle and creates a high contact angle hysteresis. This implies that a snail repellent superhydrophobic surface would have to exhibit a high receding angle at reduced surface tensions. SDS, an anionic surfactant, was an appropriate way to vary the surface tension of water in order to find the receding angles for a variety of surfaces. The results are shown in figure 5.20. The data for Hyrec 1440 from [1] has been added for comparison. The soot PDMS surface maintained a high receding angle until the surface tension dropped below 40 mN/m .

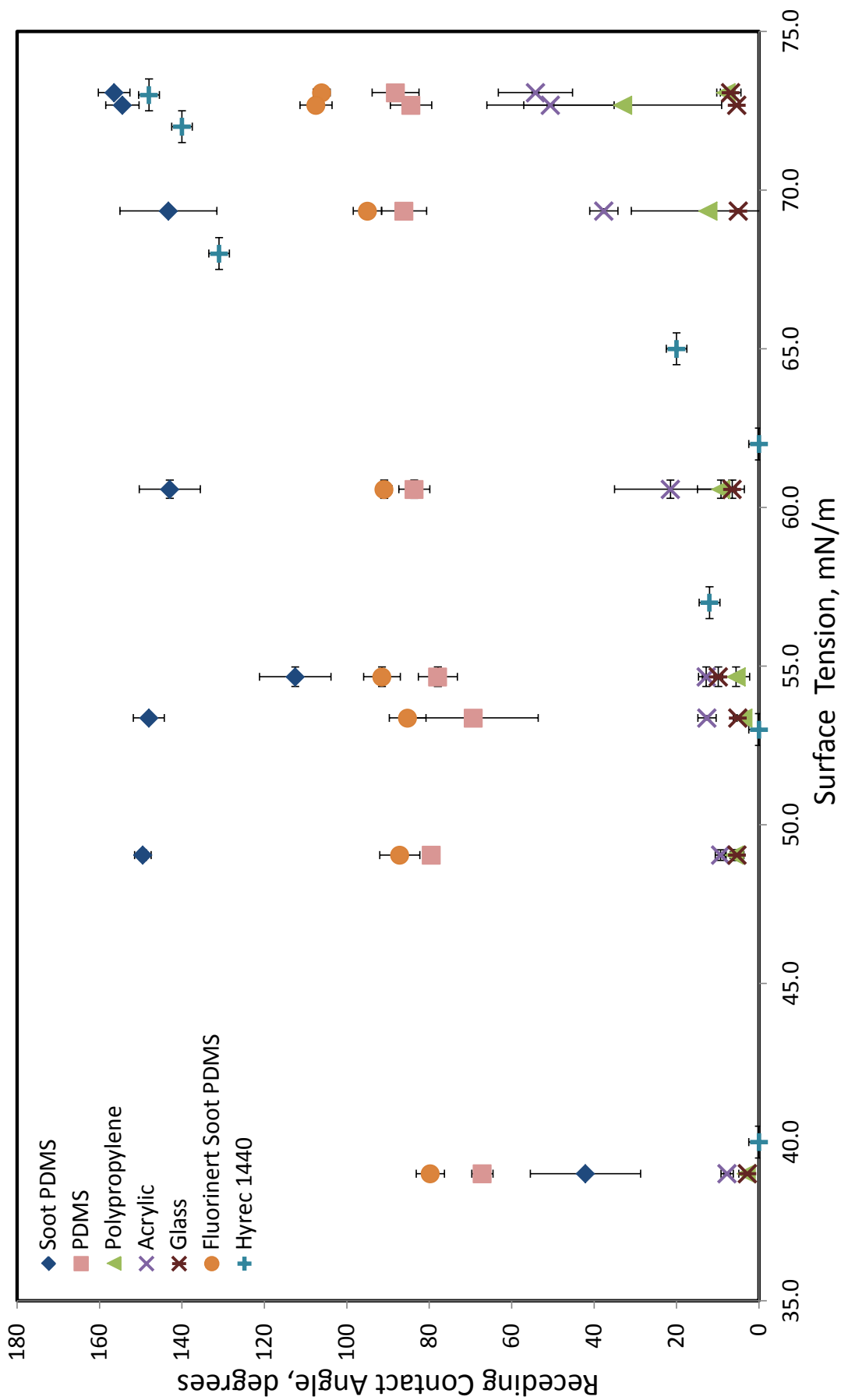


Figure 5.20: Graph of receding contact angle against surface tension for various surfaces.

5.4 Discussion

The simple pot comparison tests demonstrated that the soot PDMS has snail deterrent properties. Test 1 showed that the snails preferred to completely devour the lettuce on top of the uncoated pot before choosing the Soot PDMS pot over the copper coated pot. Copper is a well known snail deterrent but the cost of copper makes it an expensive and impractical option. Test 3 demonstrated the deterrent properties of the soot surface more definitively. Over the 48 hours of the experiment as many as 5 snails were active on the uncoated polypropylene pot at any one time where as a single snail was recorded on the top of the soot PDMS pot over the entire duration of the experiment. The pot tests presented the snails with very few food sources. One question is whether or not, in the wild, the snails would still attempt to climb the soot PDMS surface or would they continue to search elsewhere for an easier to reach food source.

The vertical maze tests showed that the snails are reluctant to move over the soot PDMS surface. This was evident in the way they followed the path bound by the soot rather than travelling in a straight line, as they would on the acrylic surface. However, once a snail had traversed the superhydrophobic surface, the trail of mucus left behind it allowed following snails to travel over the same path. The horizontal maze tests demonstrated the snails ability to move over nearly any surface, including razor sharp edges, due to the mucus layer upon which it crawls.

When performing the spin removal force tests Shirtcliffe *et al.* [1] compared the removal force using an average snail mass. This was possible as they used adult brown garden snails that were not changing size during the testing period, which in turn meant that their footprint area did not change. The larger size of the snail did however make it more difficult to determine an accurate radial distance for the centre of mass for the snail, leading to larger experimental errors. The use of the smaller immature snails made determining their position from the centre of the spin discs more accurate but their changing size, and in turn their footprint area, meant that in order to get an accurate removal force, the footprint area was recorded. This proved to have a strong correlation to the mass of the snails and a relationship

was determined, as shown in figure 5.18. This allowed for a calculation of removal force per unit area, which may be more informative than a simple ' γ ' value used by Shirtcliffe *et al.* [1]. In order to compare this new data to the previously published results, common surfaces such as acrylic, glass and loose soot were tested. Again the loose soot required little force for removal and this was closely followed by the unrinsed soot PDMS and the rinsed soot PDMS surfaces. All the soot surfaces performed significantly better than the commercial products tested by Shirtcliffe *et al.* [1].

With the soot PDMS maintaining a high receding contact angle down to surface tension values around 48mN/m, it should be able to deter snails from adhering to it, based on the hypothesis of Shirtcliffe *et al.* [1]. It out performed the next best commercially available coating, Hyrec 1440[®], tested by Shirtcliffe *et al.* [1], which maintained a high receding angle above surface tensions of 68mN/m. This may indicate the presence of a critical receding contact angle for the snail mucus above which snail mucus cannot achieve sufficient adhesion.

5.5 Conclusions

In a controlled environment, when presented with two sources of food on top of equally tall polypropylene pots, one coated in soot PDMS and the other left uncoated, the vast majority of snails will first consume the food on top of the uncoated polypropylene pot. This indicates an unwillingness of the snails to climb the superhydrophobic soot surface. This conclusion is further supported by the results of the maze tests where the snails avoided taking a direct path to a food source in favour of a route without soot PDMS to crawl over. The lack of willingness to crawl on a vertical soot surface implies the snails cannot sufficiently adhere to the soot PDMS surface in order to overcome gravity.

The spin tests show that the force required to eject a snail from a soot PDMS surface is much smaller than the uncoated PDMS, acrylic, polypropylene or glass surfaces. This again shows the lack of ability of the snails to adhere to the sooted surfaces. These results, together with the SDS tests, show the anti-adhesive properties of the novel surface. The results of the SDS tests show the soot surfaces maintaining a high receding contact angle as the surface tension of the SDS solutions decreases. This demonstrates the ability of the soot PDMS surface to resist the ingress of the anionic surfactant into the rough surface, which would reduce the receding contact angle. This supports the hypothesis of Shirtcliffe *et al.* [1]. The hypothesis states that an effective anti-adhesive snail resistant superhydrophobic is one that can maintain a high receding contact angle in the presence of an anionic surfactant.

5.6 Suggested Work

In order to further this work it would be interesting to further examine the relationship between the footprint area and mass of the snails as well as how this relates to the adhesive abilities of the snails. If this were tested through out the life cycle of the snails, it would lead to a better understanding of the snail attachment properties.

Chapter Summary

In this chapter we have seen how the novel soot-coated surface has been tested and demonstrated its potential as a way of deterring snails. The pot tests and the maze tests showed the reluctance of the snails to travel on the surface. The spin tests showed how the snails are not able to well adhere to the surface and the SDS test demonstrated how the surface is able to maintain a high receding angle as surface tension is reduced.

The following chapter will round up the major conclusions of all the work described in this report.

Chapter 6

Summary

The major hurdle in this project was the development of a superhydrophobic surface on a sufficiently thin flexible film. Using the method of partially embedding carbon nano-particles into thin, $30\mu m$ to $90\mu m$, PDMS substrates, it has been possible to increase the roughness of the PDMS surfaces and increase the hydrophobicity to make the membranes superhydrophobic with a static contact angle of 156° with low hysteresis. This method allows for the production of a novel conformable surface. The first experiments performed with the new substrate were to test its droplet wrapping properties. It was determined that it is possible to tailor the outcome of the Capillary Origami droplet wrapping process through modification of the surface roughness and appropriate choice of wrapping liquid. The tests show it is possible to more easily wrap a membrane using a wetting liquid on a structured surface to form a Wenzel state. The wrapping can also be suppressed when a Cassie-Baxter state is produced.

The analysis of the Capillary Origami experiments required the Young's modulus to be found. It was determined that this was possible for the composite substrate using the cantilever deflection method and with the application of the large deflection correction, an accurate value of the modulus could be determined, with values agree with published literature.

Further development of the manufacturing process allowed for the production of larger areas, approximately $100cm^2$, of usable superhydrophobic substrate. These were used to test the change in the drag coefficient in the presence of the novel

surface. it was determined that a soot PDMS coating is capable of reducing the drag coefficient experienced by cylinders, at Reynolds numbers between 9000 and 25000. By coating the cylinders in the soot PDMS membrane it was possible to reduce the drag coefficient by a maximum of 28%. Through the course of these experiments it was found that the soot PDMS surface is resilient to immersion in ethanol and is capable of retaining its drag properties after multiple immersions in the liquid.

The final tests of the novel superhydrophobic material were to determine its ability as a snail repellent surface. During the pot comparison tests the soot PDMS surface shows promise as a snail repellent surface. A snail will avoid the soot PDMS surface if presented with an alternative option which has a lower receding contact angle. The surface was found to agree with the hypothesis of Shirtcliffe *et al.* [1] whereby an effective snail repellent surface shows anti-adhesive properties and maintains a high receding contact angle in the presence of an anionic surfactant.

References

- [1] N.J. Shirtcliffe, G. McHale, and M.I. Newton. Wet adhesion and adhesive locomotion of snails on anti-adhesive non-wetting surfaces. *PloS one*, 7(5):e36983, January 2012.
- [2] G. McHale, M.I. Newton, N.J. Shirtcliffe, and N.R. Geraldi. Capillary origami: superhydrophobic ribbon surfaces and liquid marbles. *Beilstein Journal of Nanotechnology*, 2:145–151, March 2011.
- [3] C. Py, P. Reverdy, L. Doppler, J. Bico, B. Roman, and C. Baroud. Capillary Origami: Spontaneous Wrapping of a Droplet with an Elastic Sheet. *Physical Review Letters*, 98(15):2–5, April 2007.
- [4] P.G. De Gennes, F. Brochard-Wyart, and D. Quéré. *Capillarity and wetting phenomena: drops, bubbles, pearls, waves*. Springer, 2004.
- [5] P.S. de Laplace. *Complete Works of Laplace: Volume 4*. Paris : Duprat [u.a.], 1805.
- [6] W.D. Harkins and F.E. Brown. The Determination Of Surface Tension (Free Surface Energy), And The Weight Of Falling Drops: The Surface Tension Of Water And Benzene By The Capillary Height Method. *Journal of the American Chemical Society*, 41(4):499–524, April 1919.
- [7] T. Young. An essay on the cohesion of fluids. *Philosophical Transactions of the Royal Society of London*, 95:65–87, 1805.
- [8] Shafrin E.G. and Zisman W.A. *Upper Limits to the Contact Angles of Liquids on Solids*, chapter 10, pages 145–157. American Chemical Society, 1964.
- [9] E.B. Dussan and R.T.P. Chow. On the ability of drops or bubbles to stick to non-horizontal surfaces of solids. *Journal of Fluid mechanics*, 137:1–29, 1983.

- [10] L. Gao and T.J. McCarthy. Teflon is hydrophilic. Comments on definitions of hydrophobic, shear versus tensile hydrophobicity, and wettability characterization. *Langmuir*, 24(17):9183–8, September 2008.
- [11] G. McHale. All solids, including teflon, are hydrophilic (to some extent), but some have roughness induced hydrophobic tendencies. *Langmuir*, 25(13):7185–7, July 2009.
- [12] P. Roach, N.J. Shirtcliffe, and M.I. Newton. Progress in superhydrophobic surface development. *Soft Matter*, 4(2):224, 2008.
- [13] G. McHale, N.J. Shirtcliffe, and M.I. Newton. Super-hydrophobic and super-wetting surfaces: Analytical potential? *The Analyst*, 129(4):284, 2004.
- [14] W. Barthlott and C. Neinhuis. Purity of the sacred lotus, or escape from contamination in biological surfaces. *Planta*, 202(1):1–8, April 1997.
- [15] C. Neinhuis and W. Barthlott. Characterization and Distribution of Water-repellent, Self-cleaning Plant Surfaces. *Annals of Botany*, 79(6):667–677, June 1997.
- [16] Y.Y. Yan, N. Gao, and W. Barthlott. Mimicking natural superhydrophobic surfaces and grasping the wetting process: A review on recent progress in preparing superhydrophobic surfaces. *Advances in Colloid and Interface Science*, 169(2):80–105, September 2011.
- [17] N.J. Shirtcliffe, G. McHale, S. Atherton, and M.I. Newton. An introduction to superhydrophobicity. *Advances in colloid and interface science*, 161(1-2):124–38, December 2010.
- [18] N.J. Shirtcliffe, G. McHale, and M.I. Newton. Learning from superhydrophobic plants: the use of hydrophilic areas on superhydrophobic surfaces for droplet control. *Langmuir*, 25(24):14121–8, December 2009.
- [19] L. Gao and T.J. McCarthy. How Wenzel and cassie were wrong. *Langmuir*, 23(7):3762–5, March 2007.
- [20] G. McHale. Cassie and Wenzel: were they really so wrong? *Langmuir*, 23(15):8200–5, July 2007.

- [21] D. Quéré. Wetting and Roughness. *Annual Review of Materials Research*, 38(1):71–99, August 2008.
- [22] R.N. Wenzel. Resistance Of Solid Surfaces To Wetting By Water. *Industrial & Engineering Chemistry*, 28(8):988–994, August 1936.
- [23] R.N. Wenzel. Surface Roughness and Contact Angle. *The Journal of Physical and Colloid Chemistry*, 53(9):1466–1467, September 1949.
- [24] A.B.D. Cassie and S. Baxter. Wettability of porous surfaces. *Transactions of the Faraday Society*, 40(5):546, 1944.
- [25] A.B.D. Cassie. Contact angles. *Discuss. Faraday Soc.*, 3:11–16, 1948.
- [26] J.F. Oliver, C. Huh, and S.G. Mason. Resistance to spreading of liquids by sharp edges. *Journal of Colloid and Interface Science*, 59(3):568 – 581, 1977.
- [27] J. Bico, U. Thiele, and D. Quéré. Wetting of textured surfaces. *Colloids and Surfaces A: Physicochemical and Engineering Aspects*, 206(1-3):41–46, July 2002.
- [28] G. Alberti and A. DeSimone. Wetting of rough surfaces: a homogenization approach. *Proceedings of the Royal Society A: Mathematical, Physical and Engineering Sciences*, 461(2053):79–97, January 2005.
- [29] N. Gao and Y. Yan. Modeling Superhydrophobic Contact Angles and Wetting Transition. *Journal of Bionic Engineering*, 6(4):335–340, December 2009.
- [30] Y.Q. Zu, Y.Y. Yan, J.Q. Li, and Z.W. Han. Wetting Behaviours of a Single Droplet on Biomimetic Micro Structured Surfaces. *Journal of Bionic Engineering*, 7(2):191–198, June 2010.
- [31] J.W.M. Bush, D.L. Hu, and M. Prakash. The Integument of Water-walking Arthropods : Form and Function. *Advances in Insect Physiology*, 34(07), 2008.
- [32] N R Bernardino, V Blickle, and S Dietrich. Wetting of surfaces covered by elastic hairs. *Langmuir*, 26(10):7233–41, May 2010.
- [33] M.L. Blow and J.M. Yeomans. Superhydrophobicity on hairy surfaces. *Langmuir*, 26(20):16071–83, October 2010.

- [34] F.J. Norton. Waterproofing treatment of materials, October 9 1945. US Patent 2,386,259.
- [35] L. Gao and T.J. McCarthy. The“lotus effect” explained - two reasons why two length scales of topography are important. *Langmuir*, 22(7):2966–2967, 2006. PMID: 16548542.
- [36] W.A. Daoud, J.H. Xin, and X. Tao. Superhydrophobic silica nanocomposite coating by a low-temperature process. *Journal of the American Ceramic Society*, 87(9):1782–1784, 2004.
- [37] J. Zhang, P. France, A. Radomyselskiy, S. Datta, J. Zhao, and W. van Ooij. Hydrophobic cotton fabric coated by a thin nanoparticulate plasma film. *Journal of Applied Polymer Science*, 88(6):1473–1481, 2003.
- [38] Y. Liu, J. Tang, R. Wang, H. Lu, L. Li, Y. Kong, K. Qi, and J. H. Xin. Artificial lotus leaf structures from assembling carbon nanotubes and their applications in hydrophobic textiles. *J. Mater. Chem.*, 17:1071–1078, 2007.
- [39] Walid a. Daoud, John H. Xin, Yi He Zhang, and C.L. Mak. Pulsed laser deposition of superhydrophobic thin Teflon films on cellulosic fibers. *Thin Solid Films*, 515(2):835–837, October 2006.
- [40] T. Wang, X. Hu, and S. Dong. A general route to transform normal hydrophilic cloths into superhydrophobic surfaces. *Chem. Commun.*, pages 1849–1851, 2007.
- [41] Y.A. Dzenis and D.H. Reneker. Polymer hybrid micro/nano composites. *Proc. Am. Soc. Compos*, pages 657–665, 1994.
- [42] N. Bolgen, Y.Z. Menciloglu, K. Acatay, I. Vargel, and E. Piskin. In vitro and in vivo degradation of non-woven materials made of poly(ϵ -caprolactone) nanofibers prepared by electrospinning under different conditions. *Journal of Biomaterials Science, Polymer Edition*, 16(12):1537–1555, 2005.
- [43] G. Srinivasan and D.H. Reneker. Structure and morphology of small diameter electrospun aramid fibers. *Polymer International*, 36(2):195–201, 1995.
- [44] A.E. Zachariades, R.S. Porter, J. Doshi, G. Srinivasan, and D.H. Reneker. High modulus polymers. *Polymer News*, 20(7):206–206, 1995.

- [45] M. Ma, R.M. Hill, J.L. Lowery, S.V. Fridrikh, and G.C. Rutledge. Electrospun poly(styrene-block-dimethylsiloxane) block copolymer fibers exhibiting superhydrophobicity. *Langmuir*, 21(12):5549–5554, 2005.
- [46] S. Agarwal, S. Horst, and M. Bognitzki. Electrospinning of fluorinated polymers: Formation of superhydrophobic surfaces. *Macromolecular Materials and Engineering*, 291(6):592–601, 2006.
- [47] T. Ogawa, B. Ding, Y. Sone, and S. Shiratori. Super-hydrophobic surfaces of layer-by-layer structured film-coated electrospun nanofibrous membranes. *Nanotechnology*, 18(16):165607, 2007.
- [48] Y. Zhu, J.C. Zhang, J. Zhai, Y.M. Zheng, L. Feng, and L. Jiang. Multifunctional carbon nanofibers with conductive, magnetic and superhydrophobic properties. *ChemPhysChem*, 7(2):336–341, 2006.
- [49] A. Nakajima, K. Abe, K. Hashimoto, and T. Watanabe. Preparation of hard super-hydrophobic films with visible light transmission. *Thin Solid Films*, 376(1-2):140 – 143, 2000.
- [50] A.V. Rao and M.M. Kulkarni. Hydrophobic properties of tmos/tmes-based silica aerogels. *Materials Research Bulletin*, 37(9):1667 – 1677, 2002.
- [51] N. J. Shirtcliffe, G. McHale, M. I. Newton, and C. C. Perry. Intrinsically superhydrophobic organosilica sol-gel foams. *Langmuir*, 19(14):5626–5631, 2003.
- [52] H.Y. Erbil, A. Demirel, Y. Avci, and O. Mert. Transformation of a simple plastic into a superhydrophobic surface. *Science*, 299(5611):1377–1380, 2003.
- [53] N. Zhao, J. Xu, Q. Xie, L. Weng, X. Guo, X. Zhang, and L. Shi. Fabrication of biomimetic superhydrophobic coating with a micro-nano-binary structure. *Macromolecular Rapid Communications*, 26(13):1075–1080, 2005.
- [54] M. Yamanaka, K. Sada, M. Miyata, K. Hanabusa, and K. Nakano. Construction of superhydrophobic surfaces by fibrous aggregation of perfluoroalkyl chain-containing organogelators. *Chem. Commun.*, pages 2248–2250, 2006.

- [55] S. Shibuichi, T. Onda, N. Satoh, and K. Tsujii. Super water-repellent surfaces resulting from fractal structure. *The Journal of Physical Chemistry*, 100(50):19512–19517, 1996.
- [56] W. Fang, H. Mayama, and K. Tsujii. Spontaneous formation of fractal structures on triglyceride surfaces with reference to their super water-repellent properties. *The Journal of Physical Chemistry B*, 111(3):564–571, 2007.
- [57] Y. Kwon, N. Patankar, J. Choi, and J. Lee. Design of surface hierarchy for extreme hydrophobicity. *Langmuir*, 25(11):6129–6136, 2009.
- [58] J. Kim and C.J. Kim. Nanostructured surfaces for dramatic reduction of flow resistance in droplet-based microfluidics. In *Proceedings, IEEE micro electro mechanical systems*, pages 479–482, 2002.
- [59] S.J Hwang, D.J Oh, P.G. Jung, S.M. Lee, J.S. Go, J.H. Kim, K.Y. Hwang, and J.S. Ko. Dry etching of polydimethylsiloxane using microwave plasma. *Journal of Micromechanics and Microengineering*, 19(9):095010, 2009.
- [60] Z. Guo, F. Zhou, J. Hao, and W. Liu. Effects of system parameters on making aluminum alloy lotus. *Journal of Colloid and Interface Science*, 303(1):298 – 305, 2006.
- [61] T. Baldacchini, J.E. Carey, M. Zhou, and E. Mazur. Superhydrophobic surfaces prepared by microstructuring of silicon using a femtosecond laser. *Langmuir*, 22(11):4917–4919, 2006.
- [62] B. Qian and Z. Shen. Fabrication of superhydrophobic surfaces by dislocation-selective chemical etching on aluminum, copper, and zinc substrates. *Langmuir*, 21(20):9007–9009, 2005.
- [63] M. Jin, X. Feng, J. Xi, J. Zhai, K. Cho, L. Feng, and L. Jiang. Superhydrophobic pdms surface with ultra-low adhesive force. *Macromolecular Rapid Communications*, 26(22):1805–1809, 2005.
- [64] N.J. Shirtcliffe, G. McHale, M.I. Newton, and C.C. Perry. Wetting and wetting transitions on copper-based super-hydrophobic surfaces. *Langmuir*, 21(3):937–943, 2005.

- [65] Y. Jiang, Z. Wang, X. Yu, F. Shi, H. Xu, X. Zhang, M. Smet, and W. Dehaen. Self-assembled monolayers of dendron thiols for electrodeposition of gold nanostructures: toward fabrication of superhydrophobic/superhydrophilic surfaces and ph-responsive surfaces. *Langmuir*, 21(5):1986–1990, 2005.
- [66] M. Li, J. Zhai, H. Liu, Y. Song, L. Jiang, and D. Zhu. Electrochemical deposition of conductive superhydrophobic zinc oxide thin films. *The Journal of Physical Chemistry B*, 107(37):9954–9957, 2003.
- [67] L. Xu, W. Chen, A. Mulchandani, and Y. Yan. Reversible conversion of conducting polymer films from superhydrophobic to superhydrophilic. *Angewandte Chemie International Edition*, 44(37):6009–6012, 2005.
- [68] A. Hozumi and O. Takai. Preparation of ultra water-repellent films by microwave plasma-enhanced cvd. *Thin Solid Films*, 303(1-2):222 – 225, 1997.
- [69] P.S. Tsai, Y.M. Yang, and Y.L. Lee. Fabrication of hydrophobic surfaces by coupling of langmuir-blodgett deposition and a self-assembled monolayer. *Langmuir*, 22(13):5660–5665, 2006.
- [70] J.Y. Shiu, C.W. Kuo, P. Chen, and C.Y. Mou. Fabrication of tunable superhydrophobic surfaces by nanosphere lithography. *Chemistry of materials*, 16(4):561–564, 2004.
- [71] W. Ming, D. Wu, R. van Benthem, and G. De With. Superhydrophobic films from raspberry-like particles. *Nano letters*, 5(11):2298–2301, 2005.
- [72] N. Gao and Y.Y. Yan. Characterisation of surface wettability based on nanoparticles. *Nanoscale*, 4(7):2202–18, 2012.
- [73] P. Jiang and M.J. McFarland. Large-scale fabrication of wafer-size colloidal crystals, macroporous polymers and nanocomposites by spin-coating. *Journal of the American Chemical Society*, 126(42):13778–13786, 2004.
- [74] N. Gao, Y.Y. Yan, X.Y. Chen, and X.F. Zheng. Superhydrophobic Composite Films Based on THS and Nanoparticles. *Journal of Bionic Engineering*, 7:S59–S66, September 2010.

- [75] I. Flores-Vivian, V. Hejazi, M.I. Kozhukhova, M. Nosonovsky, and K. Sobolev. Self-assembling particle-siloxane coatings for superhydrophobic concrete. *ACS applied materials & interfaces*, 5(24):13284–94, December 2013.
- [76] L. Zhang, Y. Li, J. Sun, and J. Shen. Layer-by-layer fabrication of broad-band superhydrophobic antireflection coatings in near-infrared region. *Journal of colloid and interface science*, 319(1):302–308, 2008.
- [77] J. Fang, H. Wang, Y. Xue, X. Wang, and T. Lin. Magnet-induced temporary superhydrophobic coatings from one-pot synthesized hydrophobic magnetic nanoparticles. *ACS applied materials & interfaces*, 2(5):1449–1455, 2010.
- [78] A. Kawai and H. Nagata. Wetting behavior of liquid on geometrical rough surface formed by photolithography. *Japanese Journal of Applied Physics*, 33(9A):L1283, 1994.
- [79] N.J. Shirtcliffe, S. Aqil, C. Evans, G. McHale, M.I. Newton, C.C. Perry, and P. Roach. The use of high aspect ratio photoresist (su-8) for superhydrophobic pattern prototyping. *Journal of Micromechanics and Microengineering*, 14(10):1384, 2004.
- [80] D. Öner and T.J. McCarthy. Ultrahydrophobic surfaces. effects of topography length scales on wettability. *Langmuir*, 16(20):7777–7782, 2000.
- [81] L. Zhu, Y. Feng, X. Ye, and Z. Zhou. Tuning wettability and getting superhydrophobic surface by controlling surface roughness with well-designed microstructures. *Sensors and Actuators A: Physical*, 130:595–600, 2006.
- [82] C. Dorrer and J. Rühle. Advancing and receding motion of droplets on ultrahydrophobic post surfaces. *Langmuir*, 22(18):7652–7657, 2006.
- [83] B.D. Gates, Q. Xu, M. Stewart, D. Ryan, C.G. Willson, and G.M. Whitesides. New approaches to nanofabrication: molding, printing, and other techniques. *Chemical reviews*, 105(4):1171–1196, 2005.
- [84] N. Bogdanski, H. Schulz, M. Wissen, H.C. Scheer, J. Zajadacz, and K. Zimmer. 3d-hot embossing of undercut structures—an approach to micro-zippers. *Microelectronic engineering*, 73:190–195, 2004.

- [85] S.M. Lee and T.H. Kwon. Effects of intrinsic hydrophobicity on wettability of polymer replicas of a superhydrophobic lotus leaf. *Journal of Micromechanics and Microengineering*, 17(4):687, 2007.
- [86] T.R. Groves, D. Pickard, B. Rafferty, N. Crosland, D. Adam, and G. Schubert. Maskless electron beam lithography: prospects, progress, and challenges. *Microelectronic engineering*, 61:285–293, 2002.
- [87] W. Ehrfeld and H. Lehr. Deep x-ray lithography for the production of three-dimensional microstructures from metals, polymers and ceramics. *Radiation Physics and Chemistry*, 45(3):349–365, 1995.
- [88] X. Zhang, J. Zhang, Z. Ren, X. Li, X. Zhang, D. Zhu, T. Wang, T. Tian, and B. Yang. Morphology and wettability control of silicon cone arrays using colloidal lithography. *Langmuir*, 25(13):7375–7382, 2009.
- [89] J. Bico, C. Marzolin, and D. Quéré. Pearl drops. *EPL (Europhysics Letters)*, 47(2):220, 1999.
- [90] W. Lee, M.K. Jin, W.C. Yoo, and J.K. Lee. Nanostructuring of a polymeric substrate with well-defined nanometer-scale topography and tailored surface wettability. *Langmuir*, 20(18):7665–7669, 2004.
- [91] M. Sun, C. Luo, L. Xu, H. Ji, Q. Ouyang, D. Yu, and Y. Chen. Artificial lotus leaf by nanocasting. *Langmuir*, 21(19):8978–81, September 2005.
- [92] B. Liu, Y. He, Y. Fan, and X. Wang. Fabricating super-hydrophobic lotus-leaf-like surfaces through soft-lithographic imprinting. *Macromolecular rapid communications*, 27(21):1859–1864, 2006.
- [93] Y. Xia, E. Kim, X.M. Zhao, J.A. Rogers, M. Prentiss, and G.M. Whitesides. Complex optical surfaces formed by replica molding against elastomeric masters. *Science*, 273(5273):347–349, 1996.
- [94] H. Cong and T. Pan. Microfabrication of conductive PDMS on flexible substrates for biomedical applications. *2009 4th IEEE International Conference on Nano/Micro Engineered and Molecular Systems*, pages 731–734, 2009.

- [95] D. Armani, C. Liu, and N. Aluru. Re-configurable fluid circuits by pdms elastomer micromachining. In *Micro Electro Mechanical Systems, 1999. MEMS'99. Twelfth IEEE International Conference on*, pages 222–227. Ieee, 1999.
- [96] Y. Xia and G.M. Whitesides. Soft lithography. *Annual review of materials science*, 28(1):153–184, 1998.
- [97] Y. Lu, B. Lin, and J. Qin. Patterned paper as a low-cost, flexible substrate for rapid prototyping of PDMS microdevices via "liquid molding". *Analytical chemistry*, 83(5):1830–5, March 2011.
- [98] B.H. Jo, L.M. Van Lerberghe, K.M. Motsegood, and D.J. Beebe. Three-dimensional micro-channel fabrication in polydimethylsiloxane (PDMS) elastomer. *Journal of Microelectromechanical Systems*, 9(1):76–81, March 2000.
- [99] J. Tong, C. Simmons, and Y. Sun. Precision patterning of PDMS membranes and applications. *Journal of Micromechanics and Microengineering*, 18(3):037004, March 2008.
- [100] X. Ye, H. Liu, Y. Ding, H. Li, and B. Lu. Research on the cast molding process for high quality PDMS molds. *Microelectronic Engineering*, 86(3):310–313, March 2009.
- [101] V.N. Goral, Y.C. Hsieh, O.N. Petzold, R. a Faris, and P.K. Yuen. Hot embossing of plastic microfluidic devices using poly(dimethylsiloxane) molds. *Journal of Micromechanics and Microengineering*, 21(1):017002, January 2011.
- [102] R. Dufour, M. Harnois, Y. Coffinier, V. Thomy, R. Boukherroub, and V. Senez. Engineering sticky superomniphobic surfaces on transparent and flexible PDMS substrate. *Langmuir*, 26(22):17242–7, November 2010.
- [103] M.M. Stanton, R.E. Ducker, J.C. MacDonald, C.R. Lambert, and W.G. McGimpsey. Super-hydrophobic, highly adhesive, polydimethylsiloxane (PDMS) surfaces. *Journal of colloid and interface science*, 367(1):502–8, February 2012.
- [104] Hoon Eui Jeong, Sung Hoon Lee, Jae Kwan Kim, and Kahp Y Suh. Nano-engineered multiscale hierarchical structures with tailored wetting properties. *Langmuir*, 22(4):1640–5, February 2006.

- [105] B. Cortese, S. D'Amone, M. Manca, I. Viola, R. Cingolani, and G. Gigli. Superhydrophobicity due to the hierarchical scale roughness of PDMS surfaces. *Langmuir*, 24(6):2712–8, March 2008.
- [106] X.S. Zhang, F.Y. Zhu, M.D. Han, X.M. Sun, X.H. Peng, and H.X. Zhang. Self-cleaning poly(dimethylsiloxane) film with functional micro/nano hierarchical structures. *Langmuir : the ACS journal of surfaces and colloids*, 29(34):10769–75, August 2013.
- [107] M.T. Khorasani, H. Mirzadeh, and P.G. Sammes. Laser induced surface modification of polydimethylsiloxane as a super-hydrophobic material. *Radiation Physics and Chemistry*, 47(6):881–888, 1996.
- [108] T.O. Yoon, H.J. Shin, S.C. Jeoung, and Y.I. Park. Formation of superhydrophobic poly (dimethylsiloxane) by ultrafast laser-induced surface modification. *Optics express*, 16(17):12715–12725, 2008.
- [109] C.Y. Xue, W. Zhang, W.H.S. Choo, and K.L. Yang. Simplest Method for Creating Micropatterned Nanostructures on PDMS with UV Light. *Langmuir*, 27(22):13410–4, November 2011.
- [110] D.W. Jeong, S.J. Kim, J.K. Park, S.H. Kim, D.W. Lee, and J.M. Kim. A simple route to morphology-controlled polydimethylsiloxane films based on particle-embedded elastomeric masters for enhanced superhydrophobicity. *ACS applied materials & interfaces*, 6(4):2770–6, February 2014.
- [111] N. Gao, Y.Y. Yan, X.Y. Chen, and D.J. Mee. Superhydrophobic surfaces with hierarchical structure. *Materials Letters*, 65(19-20):2902–2905, October 2011.
- [112] X. Deng, L. Mammen, H.J. Butt, and D. Vollmer. Candle soot as a template for a transparent robust superamphiphobic coating. *Science (New York, N.Y.)*, 335(6064):67–70, January 2012.
- [113] M. Qu, J. He, and B. Cao. Facile fabrication of large-scale stable superhydrophobic surfaces with carbon sphere films by burning rapeseed oil. *Applied Surface Science*, 257(1):6–9, October 2010.

- [114] L. Yuan, J. Dai, X. Fan, T. Song, Y.T. Tao, K. Wang, Z. Xu, J. Zhang, X. Bai, P. Lu, J. Chen, J. Zhou, and Z.L. Wang. Self-cleaning flexible infrared nanosensor based on carbon nanoparticles. *ACS nano*, 5(5):4007–13, May 2011.
- [115] Dow Corning Corporation. *Product Information - Sylgard 184*, 2014. Form No. 11-3184B-01.
- [116] S.R. Quake and A. Scherer. From micro-to nanofabrication with soft materials. *Science*, 290(5496):1536–1540, 2000.
- [117] L. Zhang, N. Zhao, X. Li, Y. Long, X. Zhang, and J. Xu. A facile approach to superhydrophobic coating from direct polymerization of “super glue”. *Soft Matter*, 7(8):4050, 2011.
- [118] Z. Yuan, H. Chen, J. Zhang, D. Zhao, Y. Liu, X. Zhou, S. Li, P. Shi, J. Tang, and X. Chen. Preparation and characterization of self-cleaning stable superhydrophobic linear low-density polyethylene. *Science and Technology of Advanced Materials*, 9(4):045007, December 2008.
- [119] K.D. Esmerlyan, G. McHale, C.L. Trabi, N.R. Geraldi, and M.I. Newton. Manipulated wettability of a superhydrophobic quartz crystal microbalance through electrowetting. *Journal of Physics D: Applied Physics*, 46(34):345307, 2013.
- [120] D.W. Jeong, S.J. Kim, J.K. Park, S.H. Kim, D.W. Lee, and J.M. Kim. A simple route to morphology-controlled polydimethylsiloxane films based on particle-embedded elastomeric masters for enhanced superhydrophobicity. *ACS applied materials & interfaces*, 6(4):2770–6, February 2014.
- [121] T.M. Schutzius, I.S. Bayer, J. Qin, D. Waldroup, and C.M. Megaridis. Water-based, nonfluorinated dispersions for environmentally benign, large-area, superhydrophobic coatings. *ACS applied materials & interfaces*, 5(24):13419–25, December 2013.
- [122] R.R.A. Syms and E.M. Yeatman. Self-assembly of three-dimensional microstructures using rotation by surface tension forces. *Electronics Letters*, 29(8):662–664, 1993.

- [123] P.W. Green, R.R.A. Syms, and E.M. Yeatman. Demonstration of three-dimensional microstructure self-assembly. *Microelectromechanical Systems, Journal of*, 4(4):170–176, 1995.
- [124] R.R.A. Syms. Surface tension powered self-assembly of 3-D micro-optomechanical structures. *Journal of Microelectromechanical Systems*, 8(4):448–455, 1999.
- [125] R.R.A. Syms, E.M. Yeatman, V.M. Bright, and G.M. Whitesides. Surface tension-powered self-assembly of microstructures - The state-of-the-art. *Journal of Microelectromechanical Systems*, 12(4):387–417, August 2003.
- [126] T.G. Leong, A.M. Zarafshar, and D.H. Gracias. Three-dimensional fabrication at small size scales. *Small*, 6(7):792–806, 2010.
- [127] J. Ryu, M. D’Amato, X. Cui, K.N. Long, H.J. Qi, and M.L. Dunn. Photo-origami - Bending and folding polymers with light. *Applied Physics Letters*, 100(16):161908, 2012.
- [128] J. Bico, B. Roman, L. Moulin, and A. Boudaoud. Adhesion: elastocapillary coalescence in wet hair. *Nature*, 432(7018):690, December 2004.
- [129] J. Olives. Capillarity and elasticity. the example of the thin plate. *Journal of Physics: Condensed Matter*, 5(14):2081, 1993.
- [130] M.J. Madou. *Fundamentals of microfabrication: the science of miniaturization*. CRC press, 2002.
- [131] T. Tanaka, M. Morigami, and N. Atoda. Mechanism of resist pattern collapse during development process. *Japanese journal of applied physics*, 32(12S):6059, 1993.
- [132] N. Chakrapani, B. Wei, A. Carrillo, P.M. Ajayan, and R.S. Kane. Capillarity-driven assembly of two-dimensional cellular carbon nanotube foams. *Proceedings of the National Academy of Sciences*, 101(12):4009–4012, 2004.
- [133] L.D. Landau and E.M. Lifshitz. Theory of elasticity, 1986. *Course of Theoretical Physics*, 1986.

- [134] S. Timoshenko, S. Woinowsky-Krieger, and S. Woinowsky-Krieger. *Theory of plates and shells*, volume 2. McGraw-hill New York, 1959.
- [135] B. Roman and J. Bico. Elasto-capillarity: deforming an elastic structure with a liquid droplet. *Journal of physics. Condensed matter : an Institute of Physics journal*, 22(49):493101, November 2010.
- [136] C. Py, P. Reverdy, L. Doppler, J. Bico, B. Roman, and C. N. Baroud. Capillarity induced folding of elastic sheets. *The European Physical Journal Special Topics*, 166(1):67–71, February 2009.
- [137] A.E. Cohen and L. Mahadevan. Kinks, rings, and rackets in filamentous structures. *Proceedings of the National Academy of Sciences of the United States of America*, 100(21):12141–6, October 2003.
- [138] S. Cranford, D. Sen, and M.J. Buehler. Meso-origami: folding multilayer graphene sheets. *Applied physics letters*, 95(12):123121, 2009.
- [139] N. Patra, B. Wang, and P. Král. Nanodroplet activated and guided folding of graphene nanostructures. *Nano letters*, 9(11):3766–71, November 2009.
- [140] J. W. van Honschoten, J. W. Berenschot, T. Ondarc̃suhu, R. G. P. Sanders, J. Sundaram, M. Elwenspoek, and N. R. Tas. Elastocapillary fabrication of three-dimensional microstructures. *Applied Physics Letters*, 97(1):014103, 2010.
- [141] X. Guo, H. Li, B.Y. Ahn, E.B. Duoss, K.J. Hsia, J. Lewis, and R.G. Nuzzo. Two- and three-dimensional folding of thin film single-crystalline silicon for photovoltaic power applications. *Proceedings of the National Academy of Sciences of the United States of America*, 106(48):20149–54, December 2009.
- [142] M. Yu, M. Huang, D.E. Savage, M.G. Lagally, and R.H. Blick. Local-wetting-induced deformation of rolled-up si/si-ge nanomembranes: a potential route for remote chemical sensing. *Nanotechnology, IEEE Transactions on*, 10(1):21–25, 2011.
- [143] M. De Volder, S.H. Tawfick, S.J. Park, D. Copic, Z. Zhao, W. Lu, and A.J. Hart. Diverse 3D microarchitectures made by capillary forming of carbon nanotubes. *Advanced materials (Deerfield Beach, Fla.)*, 22(39):4384–9, October 2010.

- [144] S. Tawfick, M. De Volder, and A.J. Hart. Structurally programmed capillary folding of carbon nanotube assemblies. *Langmuir*, 27(10):6389–94, May 2011.
- [145] S. Tawfick, J. Hart, and M. De Volder. Capillary bending of Janus carbon nanotube micropillars. *Nanoscale*, 4(13):3852–6, July 2012.
- [146] D.R. Lide. *CRC Handbook of Chemistry and Physics*. CRC Press Inc, 86 edition, 2005.
- [147] A. Ohtsuki. An Innovative Own-Weight Cantilever Method for Measuring Young’s Modulus in Flexible Thin Materials Based on Large Deflections. *Applied Mechanics and Materials*, 24-25:371–377, June 2010.
- [148] D. Fuard, T. Tzvetkova-Chevolleau, S. Decossas, P. Tracqui, and P. Schiavone. Optimization of poly-di-methyl-siloxane (pdms) substrates for studying cellular adhesion and motility. *Microelectronic Engineering*, 85(5):1289–1293, 2008.
- [149] M.C. Lopes and E. Bonaccorso. Evaporation control of sessile water drops by soft viscoelastic surfaces. *Soft Matter*, 8(30):7875–7881, 2012.
- [150] E. Lauga, M. Brenner, and H. Stone. Microfluidics: the no-slip boundary condition. *Springer handbook of experimental fluid mechanics*, pages 1219–1240, 2007.
- [151] C.L.M.H. Navier. Mémoire sur les lois du mouvement des fluides. *Mémoires de l’Académie Royale des Sciences de l’Institut de France*, 6:389–440, 1823.
- [152] J.C. Maxwell. On stresses in rarified gases arising from inequalities of temperature. *Philosophical Transactions of the royal society of London*, 170:231–256, 1879.
- [153] J.P. Rothstein. Slip on Superhydrophobic Surfaces. *Annual Review of Fluid Mechanics*, 42(1):89–109, January 2010.
- [154] O.I. Vinogradova. Slippage of water over hydrophobic surfaces. *International journal of mineral processing*, 56(1):31–60, 1999.
- [155] A. Busse, N.D. Sandham, G. McHale, and M.I. Newton. Change in drag, apparent slip and optimum air layer thickness for laminar flow over an idealised

- superhydrophobic surface. *Journal of Fluid Mechanics*, 727:488–508, June 2013.
- [156] P.A. Thompson and S.M. Troian. A general boundary condition for liquid flow at solid surfaces. *Nature*, 389(6649):360–362, 1997.
- [157] C. Cottin-Bizonne, J.L. Barrat, L. Bocquet, and E. Charlaix. Low-friction flows of liquid at nanopatterned interfaces. *Nature materials*, 2(4):237–240, 2003.
- [158] J. Ou, B. Perot, and J.P. Rothstein. Laminar drag reduction in microchannels using ultrahydrophobic surfaces. *Physics of Fluids (1994-present)*, 16(12):4635–4643, 2004.
- [159] C.H. Choi and C.J. Kim. Large slip of aqueous liquid flow over a nanoengineered superhydrophobic surface. *Physical review letters*, 96(6):066001, 2006.
- [160] C. Ybert, C. Barentin, C. Cottin-Bizonne, P. Joseph, and L. Bocquet. Achieving large slip with superhydrophobic surfaces: Scaling laws for generic geometries. *Physics of Fluids (1994-present)*, 19(12):123601, 2007.
- [161] D Jing and B Bhushan. Boundary slip of superoleophilic, oleophobic, and superoleophobic surfaces immersed in deionized water, hexadecane, and ethylene glycol. *Langmuir*, 29(47):14691–14700, 2013.
- [162] G. McHale, M.R. Flynn, and M.I. Newton. Plastron induced drag reduction and increased slip on a superhydrophobic sphere. *Soft Matter*, 7(21):10100, 2011.
- [163] B.R.K. Gruncell, N.D. Sandham, and G. McHale. Simulations of laminar flow past a superhydrophobic sphere with drag reduction and separation delay. *Physics of Fluids*, 25(4):043601, 2013.
- [164] G. McHale, N.J. Shirtcliffe, C.R. Evans, and M.I. Newton. Terminal velocity and drag reduction measurements on superhydrophobic spheres. *Applied Physics Letters*, 94(6):064104, 2009.
- [165] G. McHale, M.I. Newton, and N.J. Shirtcliffe. Immersed superhydrophobic surfaces: Gas exchange, slip and drag reduction properties. *Soft Matter*, 6(4):714, 2010.

- [166] J.C. Brennan, D.J. Fairhurst, R.H. Morris, G. McHale, and M.I. Newton. Investigation of the drag reducing effect of hydrophobized sand on cylinders. *Journal of Physics D: Applied Physics*, 47(20):205302, May 2014.
- [167] R.A. Antonia and S. Rajagopalan. Determination of drag of a circular cylinder. *AIAA Journal*, 28(10):1833–1834, October 1990.
- [168] P. Catalano, M. Wang, G. Iaccarino, and P. Moin. Numerical simulation of the flow around a circular cylinder at high reynolds numbers. *International Journal of Heat and Fluid Flow*, 24(4):463–469, 2003.
- [169] B.R.K. Gruncell. *Superhydrophobic surfaces and their potential application to hydrodynamic drag reduction*. PhD thesis, University of Southampton, 2014.
- [170] R.J. Daniello, N.E. Waterhouse, and J.P. Rothstein. Drag reduction in turbulent flows over superhydrophobic surfaces. *Physics of Fluids (1994-present)*, 21(8):085103, 2009.
- [171] R. Truesdell, A. Mammoli, P. Vorobieff, F. van Swol, and C.J. Brinker. Drag reduction on a patterned superhydrophobic surface. *Physical review letters*, 97(4):044504, 2006.
- [172] A. Panigrahi and S.K. Raut. *Thevetia peruviana* (family: Apocynaceae) in the control of slug and snail pests. *Memórias do Instituto Oswaldo Cruz*, 89(2):247–250, 1994.
- [173] G.M. Barker. *Molluscs as crop pests*. CABI, 2002.
- [174] A. Guiller and L. Madec. Historical biogeography of the land snail *Cornu aspersum*: a new scenario inferred from haplotype distribution in the Western Mediterranean basin. *BMC evolutionary biology*, 10:18, January 2010.
- [175] H. Janus. *Illustrated guide to molluscs*. Harold Starke Publishers, 1982.
- [176] M. Denny. Locomotion: the cost of gastropod crawling. *Science (New York, N.Y.)*, 208(4449):1288–90, June 1980.
- [177] M. Denny. The role of gastropod pedal mucus in locomotion. *Nature*, 285(5761):160–161, May 1980.

- [178] M. Denny. Mechanical properties of pedal mucus and their consequences for gastropod structure and performance. *American Zoologist*, 24(1):23–36, 1984.
- [179] M. Denny and J.M. Gosline. The physical properties of the pedal mucus of the terrestrial slug, *ariolimax columbianus*. *The Journal of Experimental Biology*, 88(1):375–394, 1980.
- [180] M. Denny. Molecular biomechanics of molluscan mucous secretions. *The mollusca*, 1:431–465, 1983.
- [181] T. Wong, S.H. Kang, S.K.Y. Tang, E.J. Smythe, B.D. Hatton, A. Grinthal, and J. Aizenberg. Bioinspired self-repairing slippery surfaces with pressure-stable omniphobicity. *Nature*, 477(7365):443–7, September 2011.

Published Work

1. G. McHale, M.I. Newton, N.J. Shirtcliffe, N.R. Geraldi. Capillary origami: superhydrophobic ribbon surfaces and liquid marbles. *Beilstein J. Nanotechnol.* 2, 145-51 (2011).
2. N.R. Geraldi, F.F. Ouali, R.H. Morris, G. McHale, M.I. Newton. Capillary origami and superhydrophobic membrane surfaces. *Appl. Phys. Lett.* 102, 214104 (2013).
3. K.D. Esmeryan, G. McHale, C.L. Trabi, N.R. Geraldi, M.I. Newton. Manipulated wettability of a superhydrophobic quartz crystal microbalance through electrowetting. *J. Phys. D. Appl. Phys.* 46, 345307 (2013).
4. N.R. Geraldi, R.H. Morris, G. McHale, M.I. Newton. Snail Deterrent Properties of a Soot based Flexible Superhydrophobic Surface. *Proc. 1st Int. Electron. Conf. Mater.* (MDPI, 2014).

Capillary origami: superhydrophobic ribbon surfaces and liquid marbles

Glen McHale^{*§}, Michael I. Newton, Neil J. Shirtcliffe and Nicasio R. Gerardi

Full Research Paper

Open Access

Address:
School of Science and Technology, Nottingham Trent University,
Clifton Lane, Nottingham NG11 8NS, UK

Email:
Glen McHale* - glen.mchale@ntu.ac.uk

* Corresponding author
§ Tel: +44 (0)115 8483383

Keywords:
capillary origami; Cassie; contact angle; superhydrophobic; Wenzel

Beilstein J. Nanotechnol. 2011, 2, 145–151.
doi:10.3762/bjnano.2.18

Received: 18 December 2010
Accepted: 10 February 2011
Published: 10 March 2011

This article is part of the Thematic Series "Biomimetic materials".

Guest Editors: W. Barthlott and K. Koch

© 2011 McHale et al; licensee Beilstein-Institut.
License and terms: see end of document.

Abstract

In the wetting of a solid by a liquid it is often assumed that the substrate is rigid. However, for an elastic substrate the rigidity depends on the cube of its thickness and so reduces rapidly as the substrate becomes thinner as it approaches becoming a thin sheet. In such circumstances, it has been shown that the capillary forces caused by a contacting droplet of a liquid can shape the solid rather than the solid shaping the liquid. A substrate can be bent and folded as a (pinned) droplet evaporates or even instantaneously and spontaneously wrapped on contact with a droplet. When this effect is used to create three dimensional shapes from initially flat sheets, the effect is called *capillary origami* or *droplet wrapping*.

In this work, we consider how the conditions for the spontaneous, capillary induced, folding of a thin ribbon substrate might be altered by a rigid surface structure that, for a rigid substrate, would be expected to create Cassie–Baxter and Wenzel effects. For smooth thin substrates, droplet wrapping can occur for all liquids, including those for which the Young's law contact angle (defined by the interfacial tensions) is greater than 90° and which would therefore normally be considered relatively hydrophobic. However, consideration of the balance between bending and interfacial energies suggests that the tendency for droplet wrapping can be suppressed for some liquids by providing the flexible solid surface with a rigid topographic structure. In general, it is known that when a liquid interacts with such a structure it can either fully penetrate the structure (the Wenzel case) or it can bridge between the asperities of the structure (the Cassie–Baxter case).

In this report, we show theoretically that droplet wrapping should occur with both types of solid–liquid contact. We also derive a condition for the transition between the Cassie–Baxter and Wenzel type droplet wrapping and relate it to the same transition condition known to apply to superhydrophobic surfaces. The results are given for both droplets being wrapped by thin ribbons and for solid grains encapsulating droplets to form liquid marbles.

Introduction

In wetting, the usual implicit assumption is that a solid substrate is sufficiently thick or rigid, that it does not deform or change shape due to the interfacial forces that arise when it contacts a droplet of a liquid, however, in many natural systems this is not the case. Depositing a small droplet onto a smooth substrate and measuring the contact angle in side-profile view gives the contact angle, θ , which is assumed (to within contact angle hysteresis) to approximate to the Young's law value, θ_e , given by the interfacial tensions, i.e., $\cos\theta_e = (\gamma_{SV} - \gamma_{SL})/\gamma_{LV}$ where the γ_{ij} are the interfacial tensions between the solid, liquid and vapor phases. However, the bending rigidity of a solid elastic plate scales with the cube of its thickness and this assumption can become erroneous [1]. When a droplet has a radius, R , larger than the elastocapillary bending length [2], $L_{EC} = (\kappa_b/\gamma_{LV})^{1/2}$ the solid can become deformed and shaped by the liquid. In practice, this effect has been given the name “*capillary origami*” based on experiments showing how films of polydimethylsiloxane (PDMS) shaped in two-dimensions can be folded by evaporating droplets of water to produce a designed three-dimensional shape [3,4]; an effect stronger than the dimpling of an elastomer surface by a deposited droplet [5]. *Capillary origami* is more than a curiosity and has implications for technological applications in creating three-dimensional structures from initially flat films through the capillary forces during liquid evaporation and drying [6-8]. The effect of capillary forces due to nanodroplets in activating and guiding the folding of planar graphene ribbons has recently been simulated [9].

Figure 1 illustrates *capillary origami* concepts and effects based on original ideas by Py et al [3,4]. When a PDMS (Sylgard 184) substrate of reduced thickness is contacted by a droplet of water (containing blue food dye) capillary forces bend it out of its initial planar shape (Figure 1a). When the substrate thickness is reduced to 45 μm and cut into a triangular shape (10 mm side lengths) and scored with a laser (Universal Laser Systems 30W CO₂ laser cutter) to create fold-lines (Figure 1b), contact with a large droplet of water can create a three-dimensional shape (Figure 1d). On contact by the droplet the sheet is bent (Figure 1c) and after droplet evaporation a tetrahedron is formed (Figure 1d). Whilst this is an example of the shaping of a solid substrate by capillary forces, the final shape relies on evaporation to complete the process.

Figure 2 illustrates a number of effects as a droplet contacts a thin PDMS strip substrate (“ribbon”) hanging vertically. If a droplet is deposited on a long ribbon it causes substrate deformation, but is unable to wrap or fold the substrate around itself and, as evaporation proceeds, the deformation decreases (Figure 2a). However, when the length of ribbon below the

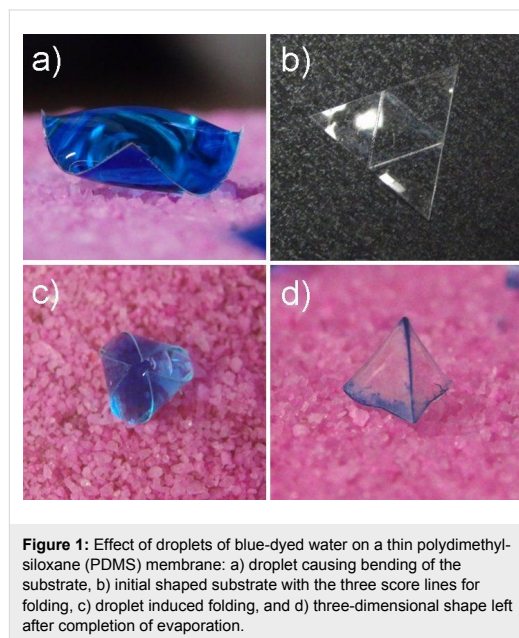


Figure 1: Effect of droplets of blue-dyed water on a thin polydimethylsiloxane (PDMS) membrane: a) droplet causing bending of the substrate, b) initial shaped substrate with the three score lines for folding, c) droplet induced folding, and d) three-dimensional shape left after completion of evaporation.

droplet contact point is sufficiently short, the contacting droplet can quickly fold the ribbon up against gravity and wrap itself. Figure 1 and Figure 2 are illustrative of the ability of capillary forces to deform, fold and bend substrates. The concepts of *capillary origami* and *droplet wrapping* also have implications for our understanding of the definition of hydrophobicity and its relationship to adhesion. Gao and McCarthy demonstrated that spontaneous and complete droplet wrapping occurs, without the need for evaporation, with a thin film of Teflon® even though this material would normally have a contact angle to water greater than 90° and so be regarded as hydrophobic [10]; an effect one of the current authors explained on the basis of the changes in the balance between interfacial and bending energies [11].

In a previous report, McHale argued from surface free energy considerations that, when the bending energy is small, all solids should demonstrate droplet wrapping and so can, in an absolute sense, be considered hydrophilic [11]. That work also discussed why for a partially wetting droplet to be observed there is necessarily an assumption of some rigidity of the substrate, so that the usual definition of relative hydrophobicity (and relative hydrophilicity) through contact angle measurement includes a structural non-surface chemistry based assumption about the solid. It was also suggested that a set of loose spherical grains could be considered to be the extreme case of a solid with no bending energy, thus relating the concept of droplet wrapping to

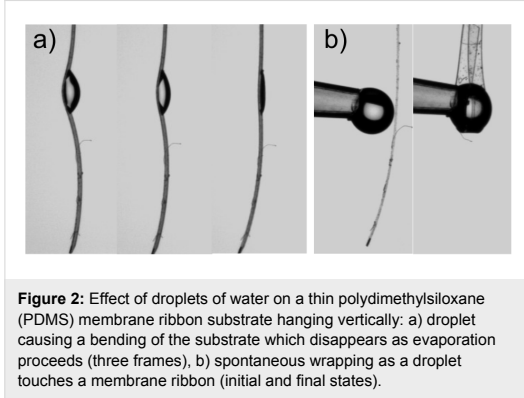


Figure 2: Effect of droplets of water on a thin polydimethylsiloxane (PDMS) membrane ribbon substrate hanging vertically: a) droplet causing a bending of the substrate which disappears as evaporation proceeds (three frames). b) spontaneous wrapping as a droplet touches a membrane ribbon (initial and final states).

that of the formation of liquid marbles [12,13]. It was further argued that when the flexible solid surface possessed rigid surface roughness or the solid grains had a rigid surface roughness, droplet wrapping might, under defined conditions for the surface chemistry defined contact angle, be suppressed. Since wrapping a spherical droplet requires both bending and stretching of the solid, in this report, we consider the simpler, but experimentally realizable, cases of wrapping of a droplet of water by a thin ribbon and the assembly of solid grains to form a liquid marble. For both cases, we extend the previous theoretical consideration to ribbon-type substrates and disconnected solid grains with a rigid surface structure. We review the case for surface roughness that has low aspect ratio so that the liquid can penetrate into the structure – the Wenzel case [14,15]. We then consider whether droplet wrapping can occur without penetration into the surface structure – the Cassie–Baxter case [16,17]. We show that droplet wrapping should occur with both types of configuration and we derive a condition for the transition between these two cases; this condition is the same as for the Wenzel to Cassie–Baxter transition on a superhydrophobic surface [18,19].

Results and Discussion

1. Droplet wrapping theory

To assess whether it is energetically favourable for a liquid to become wrapped in a solid we consider the change in interfacial energy as the solid–vapor interface is replaced by a solid–liquid interface together with the increase in bending energy as the solid deforms from a planar ribbon, similar to those shown in Figure 2, of width $w \ll R$, where R is the droplet radius. The use of a ribbon substrate allows the problem to be simplified to a quasi-two dimensional situation. Assuming there is no spontaneous curvature of the solid film, the initial energy is given by the sum of the energy associated with the liquid in contact with the vapor and the surfaces of the solid in contact with the vapor (Figure 3a),

$$F^i = A_{LV}^i \gamma_{LV} + r_W A_{SV}^p \gamma_{SV} + A_{SV}^{lower} \gamma_{SV} \quad (1)$$

where A_{LV}^i is the initial liquid–vapor interfacial area, A_{SV}^p is the initial planar projection of the area of the upper surface of the solid film, r_W is the Wenzel roughness of the surface, and the γ_{ij} are the interfacial tensions; the lower surface of the film is assumed to have an area A_{SV}^{lower} . The initial liquid–vapor area is $A_{LV}^i = 4\pi R^2$, where R is the droplet radius, and after wrapping it is assumed that the shape is spherical with the same radius R . This means that a planar projected area $2\pi R w$ of the ribbon’s area is involved in the wrapping. For simplicity in the following, we limit the initial ribbon length to $2\pi R$, so that $A_{SV}^p = 2\pi R w$ is assumed.

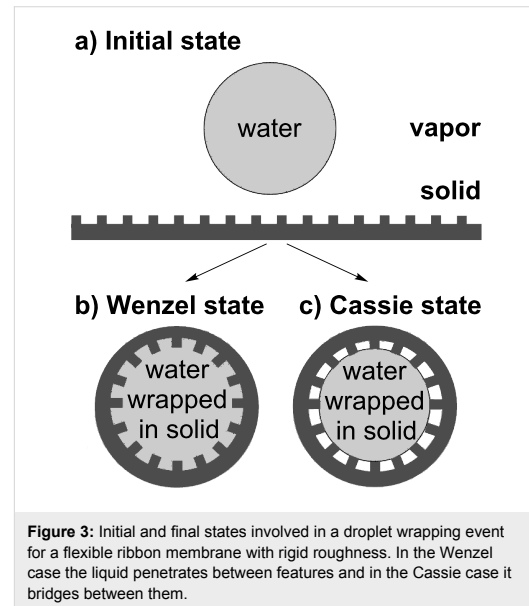


Figure 3: Initial and final states involved in a droplet wrapping event for a flexible ribbon membrane with rigid roughness. In the Wenzel case the liquid penetrates between features and in the Cassie case it bridges between them.

The energy per unit area, f_b , associated with bending and stretching a thin membrane substrate is related to the principal radii of curvatures of the substrate,

$$f_b = \frac{\kappa_b (c_1 + c_2)^2}{2} + \kappa_G c_1 c_2 \quad (2)$$

where κ_b is the elastic bending rigidity and κ_G is the Gaussian bending modulus [20]. For a film of thickness h , the bending rigidity is given by $\kappa_b = Eh^3/12(1-\nu^2)$, where E is Young’s modulus and ν is Poisson’s ratio; the Gaussian bending modulus relates to any stretching or compression of the film. The coefficients c_1 and c_2 are the principal radii of curvature, which for a

spherical droplet are $c_1 = c_2 = 1/R$. For a ribbon bending only along its length $c_1 = 1/R$ and $c_2 = 0$ so that for a radius of R the bending energy per unit area is,

$$f_b = \frac{\kappa_b c_1^2}{2} = \frac{\kappa_b}{2R^2} \quad (3)$$

When the liquid comes into contact with the ribbon, assuming the ribbon can bend, and that the roughness remains unchanged, we can imagine two types of wrapping scenarios. In the Wenzel case, the liquid may penetrate between the surface features and retain contact with the ribbon at all points along its surface (Figure 3b). In the alternative Cassie–Baxter case, the surface structure combined with the surface chemistry may be such that the liquid bridges between the tops of the surface features leaving vapor between them (Figure 3c).

1.1 Wenzel case

In the Wenzel case, the liquid penetrates between surface features (Figure 3b) and the difference in energy between the final and the initial state related to the attachment of the droplet to the ribbon is given by,

$$\frac{\Delta F_W}{2\pi R w} = r_W (\gamma_{SL} - \gamma_{SV}) - \gamma_{LV} + \frac{\kappa_b c_1^2}{2} \quad (4)$$

which can be rewritten using the definition of the Young's law equilibrium contact angle on a rigid surface of $\cos\theta_e = (\gamma_{SV} - \gamma_{SL})/\gamma_{LV}$, as,

$$\frac{\Delta F_W}{2\pi R w} = -\gamma_{LV} (r_W \cos\theta_e + 1) + \frac{\kappa_b c_1^2}{2} \quad (5)$$

For liquids which on a rigid smooth solid substrate are considered to be partially wetting the cosine satisfies $-1 < \cos\theta_e < 1$ and θ_e gives a finite Young's law contact angle. However, for those liquids which completely wet and form films, the combination $(\gamma_{SV} - \gamma_{SL})/\gamma_{LV}$ has a value greater than 1. The combination of the roughness, r_W , multiplying $\cos\theta_e$ immediately introduces the Wenzel contact angle,

$$\frac{\Delta F_W}{2\pi R w} = -\gamma_{LV} (\cos\theta_W + 1) + \frac{\kappa_b c_1^2}{2} \quad (6)$$

One assumption in Equation 6 is that the final radius of the wrapped portion of the droplet is approximately the same as the initial droplet radius.

1.2 Cassie–Baxter case

In the Cassie–Baxter case, complete penetration of liquid between surface features does not occur (Figure 3c). The liquid only contacts a fraction ϕ_s of the surface thus leaving a fraction $(r_W - \phi_s)$ of the solid surface in contact with the vapor. In addition, the liquid bridges between surface features, thus providing a set of menisci, here approximated by a fraction $(1 - \phi_s)$ of the surface with a liquid–vapor interface. The difference in energy between the final and the initial state related to the attachment of the droplet to the ribbon is then given by,

$$\frac{\Delta F_{CB}}{2\pi R w} = \phi_s \gamma_{SL} + (1 - \phi_s) \gamma_{LV} + (r_W - \phi_s) \gamma_{SV} - r_W \gamma_{SV} - \gamma_{LV} + \frac{\kappa_b c_1^2}{2} \quad (7)$$

Cancelling terms involving the roughness factor r_W and using the definition of the equilibrium contact angle on a rigid substrate of $\cos\theta_e = (\gamma_{SV} - \gamma_{SL})/\gamma_{LV}$ gives,

$$\frac{\Delta F_{CB}}{2\pi R w} = -\gamma_{LV} (\phi_s \cos\theta_e - (1 - \phi_s) + 1) + \frac{\kappa_b c_1^2}{2} \quad (8)$$

Defining the Cassie–Baxter combination $\cos\theta_{CB} = \phi_s \cos\theta_e - (1 - \phi_s)$, which is familiar from the modelling of droplets on superhydrophobic surfaces, gives,

$$\frac{\Delta F_{CB}}{2\pi R w} = -\gamma_{LV} (\cos\theta_{CB} + 1) + \frac{\kappa_b c_1^2}{2} \quad (9)$$

The similarity of Equation 6 and Equation 9 can be revealed by writing,

$$\frac{\Delta F_T}{2\pi R w} = -\gamma_{LV} (\cos\theta_T + 1) + \frac{\kappa_b c_1^2}{2} \quad (10)$$

where the subscript T defines the topographic assumption of the liquid either in a Wenzel (“penetrating”) or Cassie–Baxter (“skating”) state. In the form presented by Equation 10, the principal radius of curvature c_1 is given by $1/R$ and so the energy change per unit area of the ribbon substrate depends on the droplet size.

1.3 Wrapping and transitions with roughness

The wrapping state will be stable provided the energy change given by Equation 10 is negative, i.e.,

$$\cos\theta_T > -1 + \frac{\kappa_b c_1^2}{2\gamma_{LV}} \quad (11)$$

Defining the dimensionless curvature elastocapillary number $n_{EC} = \kappa_b c_1^2 / 2\gamma_{LV}$, Equation 11 can be written as,

$$\cos\theta_T > -1 + n_{EC} \quad (12)$$

A ribbon substrate that is unable to bend in response to contact with the liquid will have an elastocapillary number that tends to infinity and so wrapping will not occur. When the elastocapillary number has a finite value, wrapping will occur, but will depend on the volume and shape of the liquid. For a droplet with a spherical shape of radius R , the elastocapillary number is $n_{EC} = \kappa_b / 2\gamma_{LV} R^2 = 1/2 (L_{EC}/R)^2$, where $L_{EC} = (\kappa_b / \gamma_{LV})^{1/2}$ is the characteristic elastocapillary length. Equation 12 then becomes,

$$\cos\theta_T > -1 + 2 \left(\frac{L_{EC}}{R} \right)^{1/2} \quad (13)$$

This condition for droplet wrapping depends upon the state of contact of the wrapped liquid with the solid surface, i.e., penetrating or skating. For the Cassie–Baxter state with its air-pockets to be thermodynamically stable compared to the Wenzel state, requires $\Delta F_{CB} < \Delta F_W$ in addition to $\Delta F_{CB} < 0$. Since the curvature energy contributes the same to both, Equation 10 implies $\cos\theta_W < \cos\theta_{CB}$, which gives a condition on the relationship between the Young’s law contact angle θ_e , and the roughness r_W and solid surface fraction ϕ_s ,

$$\cos\theta_e < - \left(\frac{1 - \phi_s}{r_W - \phi_s} \right) = \cos\theta_c \quad (14)$$

where θ_c is a critical contact angle for thermodynamic stability of the Cassie–Baxter state; when the Young’s law contact angle exceeds the critical contact angle the Cassie–Baxter state is favoured over the Wenzel state. Equation 14 is exactly the same as the condition derived by Bico et al., for the thermodynamic stability of the Cassie–Baxter state on a superhydrophobic surface [18,19]. As noted by these authors, when $90^\circ < \theta_e < \theta_c$, the Cassie–Baxter state may exist due to, e.g., pinning on sharp edges of features, but it is a metastable state.

Here we have also only considered a simple model that assumes either a Wenzel state or a Cassie–Baxter state. However, surfaces with curvature can effectively have a combination of

both Wenzel and Cassie–Baxter properties with the solid surface fraction becoming a function of the Young’s law contact angle [21]. Re-entrant surfaces have been shown to be particularly effective in producing suspended droplets of liquids with low surface tensions [22]. Following the superhydrophobic literature, we can also anticipate that if the surface chemistry tends towards hydrophilic (i.e., $\theta_e < 90^\circ$) there might be a hemi-wicking effect with the liquid invading the surface texture, but wetting the asperities of the topographic features. A simple two-dimensional model consideration of the energy changes as a liquid invades a structure on a thin substrate suggests that the critical Young’s law contact angle for hemi-wicking will be shifted to values lower than θ_c due to the contribution of bending energy.

1.4 Drop size and contact angle effects

The inclusion of the energy associated with the curvature of a substrate introduces a characteristic elastocapillary length and results in drop size effects. For a ribbon film substrate, Equation 10 implies wrapping requires the droplet radius R to be greater than a critical radius, R_c , given by,

$$R_c = \left(\frac{\kappa_b}{2\gamma_{LV} (\cos\theta_T + 1)} \right)^{1/2} = \left(\frac{1}{2(\cos\theta_T + 1)} \right)^{1/2} L_{EC} \quad (15)$$

which can be compared to the condition $R > L_{EC}/\sqrt{2}$ given by Py et al [3]. Thus, there is a critical radius which depends on the Young’s law contact angle, θ_e , and the topographic structure via the surface roughness, r_W , or solid surface fraction, ϕ_s .

In the Cassie–Baxter case, $\cos\theta_T = \cos\theta_{CB}$, and θ_{CB} can approach 180° from below and, as it does so, the critical radius for wrapping tends to infinity; a strongly superhydrophobic ribbon will not result in droplet wrapping because the energy gain cannot overcome the bending energy. In the Wenzel case, $\cos\theta_T = \cos\theta_W$, and this is positive when $\theta_e < 90^\circ$, but negative when $\theta_e > 90^\circ$. In the former case, the critical radius becomes smaller as the Young’s law contact angle tends to zero or as the roughness increases; a film can be wrapped in a tighter curve and, hence, a smaller droplet radius is needed. It should also be noted that $\cos\theta_e$ is defined by a combination of the interfacial tensions and this combination can be greater than unity; this corresponds to a film of liquid on a smooth and rigidly flat surface. In the considerations above, no account has been taken of the finite mass of the substrate on the critical volume of liquid required for wrapping; a problem recently considered experimentally and theoretically for square and triangular sheets of PDMS by Chen et al [23].

2. Liquid marbles and topographically structured grains

When a solid in the form of a thin ribbon wraps around a droplet it only needs to bend, whereas when the solid is a sheet it needs to either stretch and deform or to crumple and fold. Such a situation could be considered, but additional energies relating to these effects would need to be included unless the contribution from these is at no energy cost. One possible situation that conceptually is similar to a substrate able to deform and conform to a liquid surface, but without any bending or stretching energy cost, is the adhesion of a collection of solid grains to a liquid surface to encapsulate it and form a liquid marble (Figure 4a and Figure 4b) [12,13,24]. In an abstract sense, a collection of grains assembled in a close-packed form onto a liquid–vapor interface is the extreme limit of a flexible solid possessing no curvature (or stretching) energy and, hence, a vanishing elastocapillary length. In the study of liquid marbles, the simplest assumption is that each grain is spherical in shape and has no particular surface topography. As a consequence all grains, irrespective of their surface chemistry, will adhere to the water–air interface; a similar conclusion to that regarding the absolute hydrophobicity of solids when their curvature energy is zero. The effect of surface chemistry, characterised through the Young’s law contact angle, is to determine the strength of the adhesion to the air–water interface with maximum strength corresponding to $\theta_e = 90^\circ$; if $\theta_e > 90^\circ$ more than half the grain projects out of the interface into the air. In practice, the surfaces of the grains do not need to be smooth and can have a topographic structure. For example, pollen grains come in a variety of shapes, commonly spherical, ovoid or disc-like with lengths in the order of 10–100 μm and their surfaces (exine) under scanning electron microscopy vary from relatively smooth to mesh-like and ones adorned with sharp spikes (see, e.g., [25]).

By considering the changes in interfacial areas as a spherical grain of radius R_g with a roughness r_w attaches to a droplet of radius R (Figure 4c), we deduce the change in surface free energy ΔF_T^M ,

$$\Delta F_T^M = -A_{\text{cap}} \gamma_{LV} (1 + \cos \theta_T) \quad (16)$$

where $A_{\text{cap}} = \pi R_g^2 (1 + \cos \theta_T)$ is the spherical cap area of the solid grain of radius R_g intersecting the droplet and θ_T is either the Wenzel contact angle or the Cassie–Baxter contact angle, depending on whether the liquid penetrates between the topographic features on the surface of the grain or whether it bridges between the asperities (and is therefore only in contact with a fraction of the solid area, ϕ_s). In a similar manner to droplet wrapping, Equation 14 defines a minimum Young’s law contact

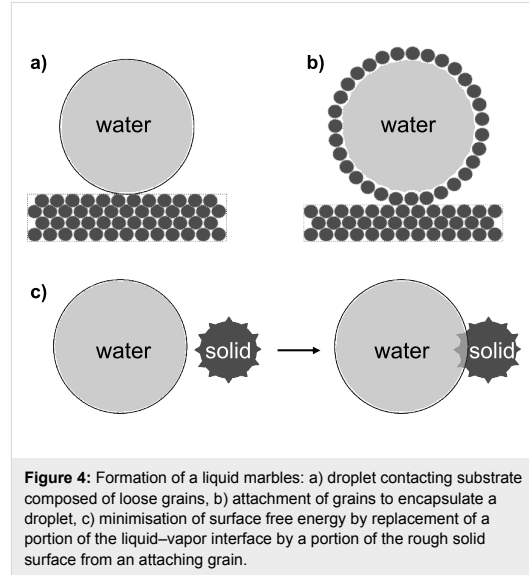


Figure 4: Formation of a liquid marbles: a) droplet contacting substrate composed of loose grains, b) attachment of grains to encapsulate a droplet, c) minimisation of surface free energy by replacement of a portion of the liquid–vapor interface by a portion of the rough solid surface from an attaching grain.

angle for the Cassie–Baxter state to be thermodynamically stable over the Wenzel state. The idea of a solid film that tends to a non-adhesive surface for liquids can be extended to non-stick granular or powder systems. All smooth spherical grains adhere to the liquid interface because $(1 + \cos \theta_e)$ can never be negative. However, when the surface of a grain is structured it can become superhydrophobic and it will then only weakly attach to the surface of the liquid.

Conclusion

In this work, we have focused on a rigid surface structure on a thin flexible substrate, but the inverse situation of a flexible surface structure on a rigid substrate has recently also been modelled [26,27]. A result of that work is an understanding that elastocapillary effects can provide additional stability for Cassie-type suspended liquid states involved in, e.g., plastron respiration [27–29]. It therefore seems likely that to fully understand superhydrophobic surfaces, the flexible nature of elements of surfaces needs to be understood. Using a model of a thin ribbon (strip) substrate we have shown that relaxing the assumption of a rigid substrate allows a contacting droplet to shape and bend the substrate provided the droplet radius is larger than a critical value. When the flexible substrate has a surface with a rigid topographic structure, the critical droplet radius at which droplets wrap depends on both the elastocapillary length and a function of either the Wenzel or the Cassie–Baxter contact angle dependent on the state of the contact. We have argued that liquid marbles can be thought of as such a system, but with a vanishing elastocapillary length. Manipulating the surface structure therefore provides a method,

complementary to control of substrate thickness, to tune the balance of adhesive forces between liquids and solids both within *capillary origami* and granular systems.

Acknowledgements

One of the authors (NG) is grateful to Nottingham Trent University for providing a PhD scholarship.

References

- Olives, J. J. *Phys.: Condens. Matter* **1993**, *5*, 2081–2094. doi:10.1088/0953-8984/5/14/007
- Bico, J.; Roman, B.; Moulin, L.; Boudaoud, A. *Nature* **2004**, *432*, 690. doi:10.1038/432690a
- Py, C.; Reverdy, P.; Doppler, L.; Bico, J.; Roman, B.; Baroud, C. N. *Phys. Rev. Lett.* **2007**, *98*, No. 156103. doi:10.1103/PhysRevLett.98.156103
- Py, C.; Reverdy, P.; Doppler, L.; Bico, J.; Roman, B.; Baroud, C. N. *Eur. Phys. J. Special Topics* **2009**, *166*, 67–71. doi:10.1140/epjst/e2009-00880-4
- Pericet-Camara, R.; Auernhammer, G. K.; Koynov, K.; Lorenzoni, S.; Raiteri, R.; Bonaccorso, E. *Soft Matter* **2009**, *5*, 3611–3617. doi:10.1039/b907212h
- De Volder, M.; Tawfick, S. H.; Park, S. J.; Copic, D.; Zhao, Z.; Lu, W.; Hart, A. J. *Adv. Mater.* **2010**, *22*, 4384–4389. doi:10.1002/adma.201001893
- Ahn, B. Y.; Shoji, D.; Hansen, C. J.; Hong, E.; Dunand, D. C.; Lewis, J. A. *Adv. Mater.* **2010**, *22*, 2251–2254. doi:10.1002/adma.200904232
- van Honschoten, J. W.; Berenschot, J. W.; Ondarçuhu, T.; Sanders, R. G. P.; Sundaram, J.; Elwenspoek, M.; Tas, N. R. *Appl. Phys. Lett.* **2010**, *97*, No. 014103. doi:10.1063/1.3462302
- Patra, N.; Wang, B.; Král, P. *Nano Lett.* **2009**, *9*, 3766–3771. doi:10.1021/nl9019616
- Gao, L.; McCarthy, T. J. *Langmuir* **2008**, *24*, 9183–9188. doi:10.1021/la8014578
- McHale, G. *Langmuir* **2009**, *25*, 7185–7187. doi:10.1021/la900597a
- Aussillous, P.; Quéré, D. *Nature (London)* **2001**, *411*, 924–927. doi:10.1038/35082026
- McHale, G.; Herbertson, D. L.; Elliott, S. J.; Shirtcliffe, N. J.; Newton, M. I. *Langmuir* **2007**, *23*, 918–924. doi:10.1021/la061920j
- Wenzel, R. N. *Ind. Eng. Chem.* **1936**, *28*, 988–994. doi:10.1021/ie50320a024
- Wenzel, R. N. *J. Phys. Colloid Chem.* **1949**, *53*, 1466–1467. doi:10.1021/j150474a015
- Cassie, A. B. D.; Baxter, S. *Trans. Faraday Soc.* **1944**, *40*, 546–551. doi:10.1039/tf9444000546
- Cassie, A. B. D. *Discuss. Faraday Soc.* **1948**, *3*, 11–16. doi:10.1039/df9480300011
- Bico, J.; Thiele, U.; Quéré, D. *Colloids Surf., A* **2002**, *206*, 41–46. doi:10.1016/S0927-7757(02)00061-4
- Quéré, D. *Annu. Rev. Mater. Res.* **2008**, *38*, 71–99. doi:10.1146/annurev.matsci.38.060407.132434
- Boal, D. H. *Mechanics of the Cell*; Cambridge University Press: New York, 2002.
- Shirtcliffe, N. J.; McHale, G.; Atherton, S.; Newton, M. I. *Adv. Colloid Interface Sci.* **2010**, *161*, 124–138. doi:10.1016/j.cis.2009.11.001
- Tuteja, A.; Choi, W.; Ma, M.; Mabry, J. M.; Mazzella, S. A.; Rutledge, G. C.; McKinley, G. H.; Cohen, R. E. *Science* **2007**, *318*, 1618–1622. doi:10.1126/science.1148326
- Chen, L.; Wang, X.; Wen, W.; Li, Z. *Appl. Phys. Lett.* **2010**, *97*, No. 124103. doi:10.1063/1.3492834
- Shirtcliffe, N. J.; McHale, G.; Newton, M. I.; Pyatt, F. B.; Doerr, S. H. *Appl. Phys. Lett.* **2006**, *89*, No. 094101. doi:10.1063/1.2339072
- Shaheen, N.; Khan, M. A.; Hayat, M. Q.; Yasmin, G. J. *Med. Plants Res.* **2009**, *3*.
- Bernardino, N. R.; Blicke, V.; Dietrich, S. *Langmuir* **2010**, *26*, 7233–7241. doi:10.1021/la904345r
- Blow, M. L.; Yeomans, J. M. *Langmuir* **2010**, *26*, 16071–16083. doi:10.1021/la101847b
- McHale, G.; Newton, M. I.; Shirtcliffe, N. J. *Soft Matter* **2010**, *6*, 714–719. doi:10.1039/b917861a
- Shirtcliffe, N. J.; McHale, G.; Newton, M. I.; Perry, C. C.; Pyatt, F. B. *Appl. Phys. Lett.* **2006**, *89*, No. 104600. doi:10.1063/1.2347266

License and Terms

This is an Open Access article under the terms of the Creative Commons Attribution License (<http://creativecommons.org/licenses/by/2.0>), which permits unrestricted use, distribution, and reproduction in any medium, provided the original work is properly cited.

The license is subject to the *Beilstein Journal of Nanotechnology* terms and conditions: (<http://www.beilstein-journals.org/bjnano>)

The definitive version of this article is the electronic one which can be found at:
doi:10.3762/bjnano.2.18



Capillary origami and superhydrophobic membrane surfaces

N. R. Gerald, ¹ F. F. Ouali, ^{1,a)} R. H. Morris, ¹ G. McHale, ² and M. I. Newton ¹

¹*School of Science and Technology, Nottingham Trent University, Clifton Lane, Nottingham NG11 8NS, United Kingdom*

²*Faculty of Engineering & Environment, Northumbria University, Ellison Place, Newcastle upon Tyne NE1 8ST, United Kingdom*

(Received 2 May 2013; accepted 14 May 2013; published online 31 May 2013)

Capillary origami uses surface tension to fold and shape solid films and membranes into three-dimensional structures. It uses the fact that solid surfaces, no matter how hydrophobic, will tend to adhere to and wrap around the surface of a liquid. In this work, we report that a superhydrophobic coating can be created, which can completely suppress wrapping as a contacting water droplet evaporates. We also show that using a wetting azeotropic solution of allyl alcohol, which penetrates the surface features, can enhance liquid adhesion and create more powerful Capillary Origami. These findings create the possibility of selectively shaping membrane substrates. © 2013 AIP Publishing LLC. [<http://dx.doi.org/10.1063/1.4808015>]

The initial development of microsystems technology suffered from the problem that liquid photoresist would often result in capillary bridges between microscale surface features that caused them to deform and clump together. Eventually, this effect was put to positive use to assemble three-dimensional shapes from planar (two-dimensional) fabricated structures by rotating surface features using molten solder.^{1–4} The same effect causes the hairs on a wet brush to clump together.⁵ An extension of these ideas has been to use contact with a liquid, typically an evaporating droplet, to completely fold up a membrane substrate into a pre-determined three-dimensional shape—an effect called *Capillary Origami*.^{6–8} This liquid adhesive effect depends on the ratio of the elastic forces maintaining the rigidity of the substrate to the surface tension forces of the liquid trying to shape the substrate. It is now well understood that the controlling parameter for these processes is the elastocapillary length, $L_{EC} = (\kappa_B/\gamma_{LV})^{1/2}$, where κ_B is the bending rigidity of the substrate and γ_{LV} is the surface tension of the liquid, and this sets the critical length scale at which substrates of a given thickness can be shaped by a liquid. Applications of this include the fabrication of micropillars,⁹ iridophores,¹⁰ and assembling carbon nanotubes¹¹ (see also the review by Roman and Bico¹²).

A potentially surprising aspect of *Capillary Origami* is that the liquid adhesion is not suppressed by substrate hydrophobicity. As demonstrated by Gao and McCarthy,¹³ even what is normally regarded as hydrophobic Teflon[®], when made into a thin membrane, will spontaneously wrap itself around a water droplet. This can be explained by considering the surface free energies of an initial non-wrapped and a final wrapped state.¹⁴ For a smooth membrane substrate with no bending energy, the final wrapped state is always the lower energy state provided the Young's law contact angle is less than 180°. However, this situation is predicted to change when the surface is rough and this introduces a dependence on the contact angle into the problem.^{14,15} In one limit, liquid can be assumed to not penetrate into the surface structure

(a Cassie-Baxter type state) and this allows a non-adhesive state to be achieved. In the other limit, liquid can be assumed to penetrate into the surface structure (a Wenzel state) enhancing the liquid adhesion so that substrates of greater stiffness can be deformed. A key challenge in suppressing liquid adhesion occurring in *Capillary Origami* is to produce a completely non-wetting (superhydrophobic) surface coating that does not substantially increase the substrate rigidity.

In this report, we consider the capillary-induced wrapping of triangular shaped films of polydimethylsiloxane (PDMS) possessing a thin surface coating. We use evaporation of a deposited liquid droplet to determine the critical side length at which wrapping occurs. We follow the method of Py *et al.*⁶ by examining a sequence of equilateral triangular shaped membranes with decreasing side lengths to determine the critical side length, L_{crit} , for which an evaporating droplet can no longer completely fold up the membrane around itself; Py *et al.* argued that the critical length should be proportional to the *elastocapillary* length, i.e., $L_{crit} \propto L_{EC} = (\kappa_B/\gamma_{LV})^{1/2}$. We show that suppression of capillary-induced folding or enhancement of folding a rough membrane substrate consisting of a thin PDMS film with a soot coating¹⁶ can be achieved depending on the wetting properties of the liquid. We report the development of a carbon nanoparticle (soot) coating that is superhydrophobic for water, but is wetted by allyl alcohol and so provides a system in which both non-penetrating (Cassie-Baxter) and penetrating (Wenzel) states to be studied. Allyl alcohol is chosen as a wetting liquid because it can form an azeotropic mixture with water and, therefore, its concentration remains constant during evaporation.

To create a flexible superhydrophobic substrate, we attempted a wide range of techniques (laser etching, casting against rigid substrates, etc.) to produce nano- and micro-structured superhydrophobic surfaces on membranes but with little success. The approach that was eventually successful combined the production of rapeseed oil nanoparticles¹⁶ with a process initially developed to transfer a layer of carbon nanoparticles from a glass surface onto a rigid PDMS surface to produce superhydrophobicity.¹⁷ In our work, we combined these two methods using the soot covered glass transfer

^{a)} Author to whom correspondence should be addressed. Electronic mail fouzia.ouali@ntu.ac.uk

method with the rapeseed oil nanoparticles. The advantage of using rapeseed oil, rather than ethanol, in a flame synthesis approach is that it produces much thicker smoke, reduces coating times, and can produce large surface areas displaying superhydrophobicity.

In our method, rapeseed oil was placed into a ceramic bowl with a wick and left burning for 5–7 min in order for a stable flame to develop. Glass slides were then placed in the flame for between 30 s and 60 s in order to coat the entire surface of the slide with a layer of matt black rapeseed oil soot. PDMS was mixed in a 10:1 ratio and degassed in a vacuum desiccator to remove any air bubbles trapped in the mixture. After approximately 30 min of degassing, the PDMS was spun onto acrylic slides to the required thickness determined by the spin speed. A prebake time of 30–35 min was required at a temperature of 60 °C for the PDMS to become sufficiently tacky for the soot to adhere to it without becoming completely engulfed by the PDMS. When the PDMS had partially cured to a tacky state, the glass slide was gently positioned, soot side down, onto the centre of the PDMS coated slides. These were then returned to a 60 °C environment until fully cured. Once cured, the samples were allowed to cool and then the glass slides were carefully peeled from the PDMS surface leaving the soot attached to the PDMS membrane surface as a nanoparticle coating. Excess soot was removed under running water to ensure the observed superhydrophobicity was not a liquid marble effect.^{18,19} The thickness of the membranes h were measured using a Veeco Dektak 6 M stylus profilometer determined to within 2 μm for smooth layers, and to within 3 μm for the soot-coated layers.

PDMS and soot-coated PDMS membranes were first characterized by measuring the static, advancing and receding contact angles with droplets of water ($\gamma_{LV} = 72.8 \text{ mN m}^{-1}$) and azeotropic mixtures of allyl alcohol ($\gamma_{LV} = 28.0 \text{ mN m}^{-1}$ and concentration of 72%) prior to detaching them from the acrylic slides. For water, the advancing and receding angles on soot-coated PDMS were $\theta_A = 159^\circ \pm 2^\circ$ and $\theta_R = 153^\circ \pm 2^\circ$, respectively, compared to $\theta_A = 116^\circ \pm 2^\circ$ and $\theta_R = 92^\circ \pm 2^\circ$, respectively, for uncoated PDMS. For allyl alcohol, the advancing and receding angles on soot-coated PDMS were $\theta_A = 56^\circ \pm 3^\circ$ and $\theta_R \sim 0^\circ$, respectively, compared to $\theta_A = 64^\circ \pm 2^\circ$ and $\theta_R = 44^\circ \pm 2^\circ$, respectively, for uncoated PDMS. Particularly relevant to the wrapping is the receding contact angle. Allyl alcohol with a near zero receding contact on soot-coated membrane is consistent with a Wenzel state in which the liquid penetrates between the

surface features of the soot. For water, on the other hand, the soot is superhydrophobic with high advancing contact angle and low contact angle hysteresis so is consistent with a Cassie-Baxter in which the liquid does not penetrate into the features of the soot-coated surface.

To determine the effect of the soot coating on the rigidity of the PDMS membrane, the Young's modulus, E , was determined using a cantilever deflection method. In the method used, one end of a strip of PDMS was fixed whilst the other, free end, was deflected under the action of its own weight. Measurements of the maximum vertical deflections of the free end, y_{max} , were carried out on PDMS membranes with widths $W = 1 \text{ mm}$ and varying lengths ℓ from 4.00 to 8.50 mm (to within 0.06 mm). The thickness h was 64 μm and 82 μm for uncoated and soot-coated membranes, respectively. To ensure minimal residual bending during peeling from the slides, the membranes were first floated in isopropyl alcohol (IPA) before careful removal. For each length, measurements were carried out with a given surface of the membrane facing both upwards and downwards. Deflection was independent of direction (to within 20%) for uncoated PDMS, and y_{max} was taken to be the average value of the two measurements. However, deflections for soot-coated PDMS were smaller by a factor ~ 2.5 when the coated-side of membranes was facing downwards than when facing upwards.

Since uncoated PDMS is a flexible material with E varying in the range 50 kPa–4 MPa,^{20,21} y_{max} is expected to exceed $\sim 20\%$ of the beam lengths in long cantilevers. The linear small deflections equation for uniformly loaded beams which gives $y_{\text{max}} = P\ell^4/8EI$, where $P = \rho gh$ is the weight of the membrane per unit length and unit width, $\kappa_B = EI$ is the bending rigidity of the beam, and ρ and g are the density of the cantilever and acceleration due to gravity, respectively, is not applicable for $y_{\text{max}}/\ell > 0.2$. In our case $h \ll W$, and so the cantilevers can be considered as thin plates with $EI = Eh^3/12(1 - \nu^2)$ ($\nu \sim 1/2$ is the Poisson ratio) which in turn gives $y_{\text{max}} = 3(1 - \nu^2)\rho g\ell^4/2Eh^2$ for small deflections, so E can be determined from y_{max} provided ℓ and h are measured accurately. For large deflections with $y_{\text{max}}/\ell > 0.2$, we used the non-linear calibration curve relating y_{max}/ℓ to $P\ell^3/8EI$ to determine E .^{22,23} For uncoated membranes, we determined $E = (1.1 \pm 0.1) \text{ MPa}$, a value consistent with the 10% concentration of cross linker and the baking times reported by Furad *et al.*²⁰ and Lopes and Bonaccorso.²¹ The soot coating induces a 20% increase in rigidity of PDMS to $E = (1.3 \pm 0.1) \text{ MPa}$ when facing upwards but a threefold increase to $E = (3.4 \pm 0.2) \text{ MPa}$

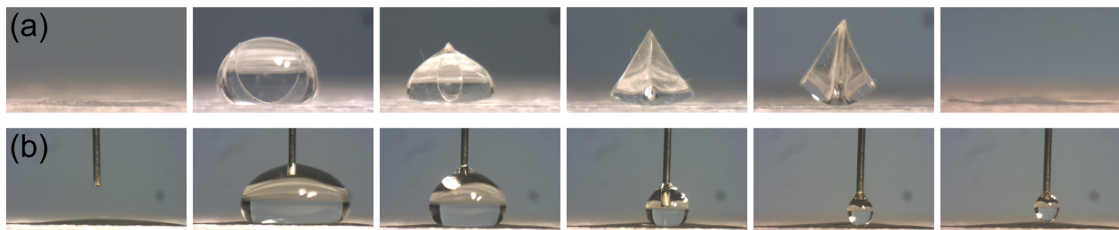


FIG. 1. (a) Image sequence showing a triangle of uncoated PDMS folding to a tetrahedral pyramid as a droplet of water evaporates. (b) Image of a droplet of water on soot-coated (superhydrophobic) PDMS membrane showing suppression of folding.

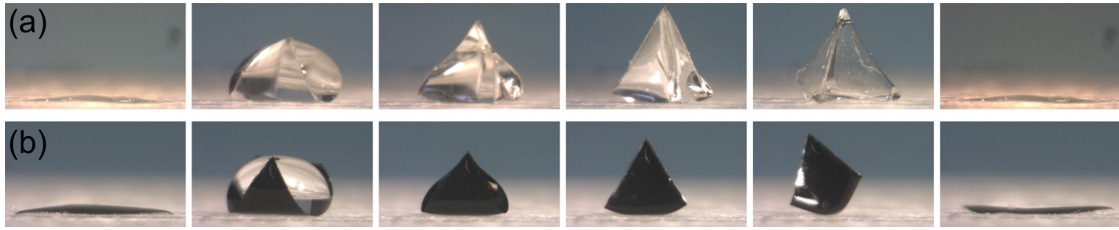


FIG. 2. Image sequence showing (a) a triangle of uncoated PDMS, and (b) soot-coated PDMS folding as a droplet of azeotropic solution of allyl alcohol evaporates.

when facing downwards. This latter value is relevant for droplet wrapping. The increased rigidity may be attributable to jamming of the nanoparticles under large inward deflections. This increase in E , nevertheless, leaves the coated PDMS as a flexible membrane.

To determine the critical length, L_{crit} , for capillary-induced droplet wrapping, equilateral triangular shaped membranes of PDMS and soot-coated PDMS membranes varying in thickness between $35\ \mu\text{m}$ and $85\ \mu\text{m}$ were produced. For each thickness of PDMS, a range of triangle edge lengths, L , in steps of $0.25\ \text{mm}$, were cut using a laser cutter. Each thickness was placed on a hydrophobic surface (to minimize adhesion to the supporting surface) and was observed over the entire evaporation process following the deposition of a droplet of water or an azeotropic solution of allyl alcohol of sufficient size to cover the surface of the triangle. When droplets of water were allowed to evaporate from sufficiently large uncoated PDMS membranes (Figure 1(a)) or when droplets of allyl alcohol were allowed to evaporate from uncoated or soot-coated PDMS membranes (Figures 2(a) and 2(b), respectively), they induced a wrapping transition. As the thickness of the PDMS was increased, the wrapping transition moved to larger volume droplets with lower curvature (and hence bending energy). The drying regime for each size was recorded in order to determine the critical length; here, we define this as the smallest side length for which 50% of the triangles of that size folded. However, when water drops were deposited on soot-coated (superhydrophobic) PDMS membranes, wrapping was completely suppressed for all thicknesses h and for triangles of lengths up $L = 15\ \text{mm}$ (Figure 1(b)).

In order to make a direct comparison with the measurements of Py *et al.*⁶ for wrapping of PDMS by droplets of water, the elastocapillary length L_{EC} was determined for each thickness h using $L_{EC} = \sqrt{\kappa_B/\gamma_{LV}} = \sqrt{Eh^3/12\gamma_{LV}(1-\nu^2)}$, with a value of $E = 1.1\ \text{MPa}$ obtained from our cantilever deflection measurements. Figure 3 shows the dependence of L_{crit} on L_{EC} for uncoated PDMS together with those of Py *et al.* for comparison. The dashed line divides triangular samples into two types: those above the line are wrapped by evaporating droplets, whilst those below are not. For all membranes and both liquids, $L_{EC} \ll L_C$, where $L_C = \sqrt{\gamma_{LV}/\rho_L g}$ is the capillary length (ρ_L is the density of the liquid), so gravity effects are not expected to be important. There is a good agreement between the two sets of data with a linear fit of our data giving $L_{crit} = 13.4 L_{EC}$ (to within 10%) compared to $L_{crit} = 11.9 L_{EC}$ for Py *et al.* This gives us

confidence that our estimate of E is reasonably accurate. Interestingly, both data sets can be better fitted by a non-zero intercept straight line.

In order to compare the wrapping of uncoated membranes by water and allyl alcohol, the dependence on surface tension, the wrapping condition $L_{crit} > L_{EC} = \sqrt{\kappa_B/\gamma_{LV}}$ can be written in terms of energy. Wrapping occurs when the gain in surface energy ($\sim \gamma_{LV} L_{crit}^2$) is greater than the bending energy κ_B , i.e., when $\gamma_{LV} L_{crit}^2 > \kappa_B = Eh^3/12(1-\nu^2)$. Figure 4 shows the variation of $\gamma_{LV} L_{crit}^2$ with κ_B on uncoated PDMS both for water and for allyl alcohol. The dashed lines show linear fits of $\gamma_{LV} L_{crit}^2$ with κ_B having a slope of $152 (\pm 10)$ for water ($\theta_R = 92^\circ$) compared to $41 (\pm 4)$ for allyl alcohol ($\theta_R = 44^\circ$). The 3.7 times decrease in the slope between the two liquids indicates a dependence of L_{crit} on receding contact angle; a wetting liquid with a lower receding contact angle can wrap the membrane into a tighter curve. The wrapping of soot-coated PDMS membranes in Figure 4 (with $E = 3.4\ \text{MPa}$) also obeys a linear fit but with a further 1.8 times decrease in slope to $21 (\pm 3)$ compared to uncoated PDMS. Allyl alcohol on soot-coated membranes ($\theta_R \sim 0^\circ$) is a Wenzel state, and so penetrates the features of the surface, thus enhancing adhesion of the drop which, in turn, produces more powerful *Capillary Origami* as observed. We have thus succeeded in creating a flexible superhydrophobic coating which suppresses wrapping of a droplet of a non-wetting liquid (water) and enhances wrapping of droplet of a wetting liquid (allyl alcohol). One unexpected feature of the data, however, is the non-zero intercept value for all graphs $\sim 500\ \text{nJ}$ (to within 10%), which seems

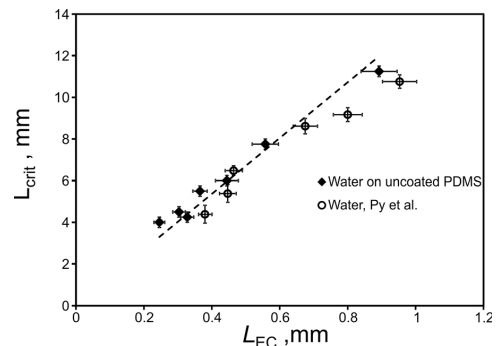


FIG. 3. The dependence of L_{crit} for wrapping water droplets on uncoated PDMS on L_{EC} (filled diamonds). The open circles show the corresponding data of Py *et al.*⁶ for comparison.

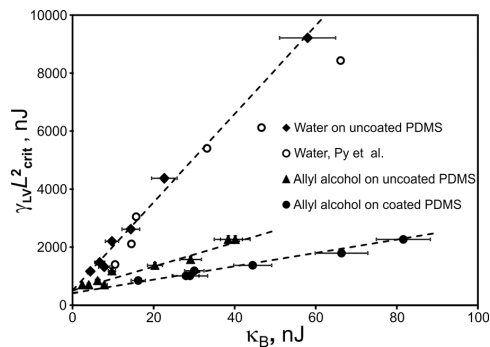


FIG. 4. The variation of $\gamma_{LV}L^2_{crit}$ with κ_B for water on uncoated PDMS (filled diamonds), and allyl alcohol on uncoated PDMS (filled triangles) and coated PDMS (filled circles). The open circles show data of Py *et al.*⁶ for comparison.

to be independent of the liquid used or surface topography and cannot be accounted for by variations in thickness of PDMS. Re-plotting the data of Py *et al.* gives an offset value of 670 nJ which is within 30% of the value obtained in this experiment. One possibility is that the experimental method using the wrapping of a triangular shaped membrane results in a dependence on the Gaussian bending rigidity.

In this work, we have shown that the contact angle can be used to control *Capillary Origami* and droplet wrapping. At one extreme, we have developed a method to create a flexible PDMS membrane with a superhydrophobic surface supporting a Cassie-Baxter type suspended droplet state. Water completely fails to wrap the membrane. At the other extreme, we have shown that using a wetting liquid (an azeotropic solution of allyl alcohol) enhances wrapping of the membrane by the liquid, supporting a Wenzel type penetrating droplet state. We have also shown that the critical lengths for wrapping triangular-shaped uncoated PDMS membranes are larger for water than allyl alcohol, thereby demonstrating dependence on the receding contact angle.

These measurements support the idea that wetting properties of the substrate affect its ability to wrap a droplet and that a flexible substrate can wrap more easily for smaller receding contact angles at a given surface tension of liquid and topography of surface.

This work has been supported by the U.K. Engineering & Physical Sciences Research Council (EPSRC) under Grant EP/E063489/1. NRG is grateful to Nottingham Trent University for provision of a Ph.D. studentship.

- ¹R. R. A. Syms and E. M. Yeatman, *Electron. Lett.* **29**, 662 (1993).
- ²P. W. Green, R. R. A. Syms, and E. M. Yeatman, *J. Microelectromech. Syst.* **4**, 170 (1995).
- ³R. R. Syms, *J. Microelectromech. Syst.* **8**, 448 (1999).
- ⁴R. R. A. Syms, E. M. Yeatman, V. M. Bright, and G. M. Whitesides, *J. Microelectromech. Syst.* **12**, 387 (2003).
- ⁵J. Bico, B. Roman, L. Moulin, and A. Boudaoud, *Nature* **432**, 690 (2004).
- ⁶C. Py, P. Reverdy, L. Droppler, J. Bico, B. Roman, and C. N. Baroud, *Phys. Rev. Lett.* **98**, 156103 (2007).
- ⁷C. Py, P. Reverdy, L. Doppler, J. Bico, B. Roman, and C. N. Baroud, *Eur. Phys. J. Spec. Top.* **166**, 67 (2009).
- ⁸H. Li, X. Guo, R. G. Nuzzo, and K. J. Hsia, *J. Mech. Phys. Solids* **58**, 2033 (2010).
- ⁹A. Takei, Y. Yoshihata, and I. Shimoyama, *J. Micromech. Microeng.* **21**, 085009 (2011).
- ¹⁰S. Manaksethram, J. A. Taylor, and T. N. Krupenkin, *Appl. Phys. Lett.* **99**, 144102 (2011).
- ¹¹S. Tawfik, A. J. Hart, and M. De Volder, *Nanoscale* **4**, 3852 (2012).
- ¹²B. Roman and J. Bico, *J. Phys. Condens. Matter* **22**, 493101 (2010).
- ¹³L. Gao and T. J. McCarthy, *Langmuir* **24**, 9183 (2008).
- ¹⁴G. McHale, *Langmuir* **25**, 7185 (2009).
- ¹⁵G. McHale, M. I. Newton, N. J. Shirtcliffe, and N. R. Geraldi, *Beilstein J. Nanotechnol.* **2**, 145 (2011).
- ¹⁶M. Qu, J. He, and B. Cao, *Appl. Surf. Sci.* **257**, 6 (2010).
- ¹⁷L. Y. Yuan, J. J. Dai, X. H. Fan, T. Song, Y. T. Tao, K. Wang, Z. Xu, J. Zhang, X. D. Bai, P. X. Lu, J. Chen, J. Zhou, and Z. L. Wang, *ACS Nano* **5**, 4007 (2011).
- ¹⁸P. Aussillous and D. Quéré, *Nature* **411**, 924 (2001).
- ¹⁹G. McHale and M. I. Newton, *Soft Matter* **7**, 5473–5481 (2011).
- ²⁰D. Fuard, T. Tzvetkova-Chevolleau, S. Decossas, P. Tracqui, and P. Schiavone, *J. Microelectron. Eng.* **85**, 1289 (2008).
- ²¹M. C. Lopes and E. Bonaccorso, *Soft Matter* **8**, 7875 (2012).
- ²²J. T. Holden, *Int. J. Solids Struct.* **8**, 1051 (1972).
- ²³A. Ohtsuki, *Appl. Mech. Mater.* **24–25**, 371 (2010).

Manipulated wettability of a superhydrophobic quartz crystal microbalance through electrowetting

K D Esmeryan¹, G McHale², C L Trabi², N R Gerald³ and M I Newton³

¹ Georgi Nadjakov Institute of Solid State Physics, 72, Tzarigradsko Chaussee Blvd., 1784 Sofia, Bulgaria

² Faculty of Engineering and Environment, Northumbria University, Ellison Place, Newcastle upon Tyne, NE1 8ST, UK

³ School of Science and Technology, Nottingham Trent University, Clifton Lane, Nottingham, NG11 8NS, UK

Received 1 May 2013, in final form 4 July 2013

Published 9 August 2013

Online at stacks.iop.org/JPhysD/46/345307

Abstract

The liquid phase response of quartz crystal microbalances (QCMs) with a thin coating ($\sim 9 \mu\text{m}$) of epoxy resin with and without a carbon nanoparticles top layer is reported. The nanoparticles convert the epoxy surface to a superhydrophobic one with a high static contact angle ($\sim 151^\circ$ – 155°) and low contact angle hysteresis ($\sim 1^\circ$ – 3.7°) where droplets of water are in the suspended Cassie–Baxter state. The frequency decrease of the fully immersed QCM with the superhydrophobic surface is less than with only epoxy layer, thus indicating a decoupling of the QCM response. A wettability transition to a liquid penetrating into the surface roughness state (for droplets a high contact angle hysteresis Wenzel state) was triggered using a molarity-of-ethanol droplet test (MED) and electrowetting; the MED approach caused some surface damage. The electrowetting-induced transition caused a frequency decrease of 739 Hz at a critical voltage of ~ 100 V compared to the QCM in air. This critical voltage correlates to a contact angle decrease of 26° and a high contact angle hysteresis state in droplet experiments. These experiments provide a proof-of-concept that QCMs can be used to sense wetting state transitions and not only mass attachments or changes in viscosity–density products of liquids.

(Some figures may appear in colour only in the online journal)

1. Introduction

Quartz crystal microbalances (QCMs) provide a simple and effective method to detect changes of physical properties of thin films adhering to their surfaces. Sauerbrey first discovered that a film deposited to the surface of a piezoelectric quartz crystal resonator will cause a decrease in the resonance frequency proportional to the mass per unit area of the film attached [1]. The Sauerbrey equation is valid under the condition that the film is thin, smooth and rigidly coupled to the oscillatory motion of the crystal surface. In 1982 Nomura and Okuhara showed that the QCM can oscillate in, and detect properties of, a liquid environment [2]. Its utility as a liquid phase sensor has been demonstrated for many applications in electrochemistry [3] and immunology [4]. When the crystal surface is brought into a contact with

a liquid, a viscous entrainment of liquid near the surface occurs due to the acoustic wave, thus causing both a frequency decrease and an energy loss depending on the viscosity–density product of the liquid [5, 6]. This phenomenon is described by the Kanazawa and Gordon equation and it is valid under a no slip boundary condition, which implies that the velocity of displacement of the quartz substrate and the liquid at the solid–liquid interface match. However, if the crystal surface has an appropriate hydrophobic chemistry and consists of high-aspect-ratio surface roughnesses, the effect of hydrophobicity will be amplified to superhydrophobicity (SH) [7]. When such a solid surface has protrusions, which are tall enough and sufficiently close, water does not penetrate between them. In this situation the droplets ball up and are effectively suspended on the tips of the surface features. Moreover due to the small number of contact points with the solid they become extremely

mobile and roll off easily. This type of surface is often called ‘slippy’ and is described by the Cassie–Baxter equation [8]. If sufficient pressure is applied, water will penetrate into the gaps between surface features and will contact the solid surface everywhere including the bottom part of the surface structure and up the sides and across the tops of the surface features. A droplet may still ball up but it will become immobile and unable to roll. The surface is said to be ‘sticky’ and is described by the Wenzel equation [8]. Liquid-phase QCMs sense interactions via the liquid close to the QCM surface within the shear wave penetration depth

$$\delta = (\eta/\pi f \rho)^{1/2}, \quad (1)$$

where f is the resonance frequency of the crystal and ρ and η are the density and viscosity of the liquid. For a 5 MHz device immersed in water $\delta \sim 250$ nm. According to the considerations above, it can be expected that the sensor response of QCM operating in a liquid environment will depend on the wetting state, Cassie–Baxter or Wenzel, of the quartz surface and should be able to detect wetting transitions between these two states. Up to now, the monitoring of wetting transitions on SH surfaces has usually been based on optical methods, electrochemical impedance spectroscopy and using ultrasound [9–11]. Recently, it has been reported that through a superhydrophobization of the QCM’s surface it is possible to decouple the sensor response [12–15].

Therefore, in this paper we consider whether a sensor can be designed such that a small change in hydrophobicity triggers a complete switching of the wetting state; an idea speculated upon but not previously reported [16]. In principle, such a change could be due to the attachment of specific molecules, but the detection would not depend on the detectability of the mass change, but would be via their effect on the wetting state. To study the QCM response to a change in the wetting state of a superhydrophobic surface, several other trigger mechanisms are possible including temperature, surface tension, mechanical, optical and magnetic changes or applied voltage via an electrowetting effect [17–20]. The two mechanisms studied in this paper are a surface tension induced switching using increasing concentrations of ethanol (molarity-of-ethanol droplet (MED) test) and electrowetting. Electrowetting involves application of electrical potential across liquid/dielectric/electrode sandwich structure to charge the solid–liquid interface. For a droplet, the charge induced imbalance of forces near the liquid/dielectric contact line results in a decrease in the observed liquid contact angle; on a superhydrophobic surface the electrocapillary pressure can cause a switch from the Cassie–Baxter suspended state to a Wenzel penetrating state [21]; an effect recently shown to provide a locally reversible transition [22, 23].

In section 2, we first review the results of a model of QCM liquid response under the assumption of a no slip boundary condition and confirm that our experimental setup can provide results for glycerol/water solutions consistent with the Kanazawa and Gordon equation. We then describe a new method to create a superhydrophobic surface using an epoxy resin–soot composite surface coating; the advantage of this surface coating is its ability to simultaneously act as

the dielectric insulator for electrowetting. We also describe how MED tests can be used to switch wetting states and we characterize droplet contact angle changes for both the electrowetting and MED switching methods. In section 3, we investigate the possible relationship between QCM response and the wetting state transition of the superhydrophobic QCM device triggered by using MED tests and electrowetting.

2. Experimental setup

2.1. Calibration of the QCM

The liquid phase sensor response of QCM, which operates in a liquid environment, is usually expressed as proportional to the square root of the viscosity–density product of the liquid according to the Kanazawa and Gordon equation [5]. In our work, gold electrode quartz crystals with a fundamental frequency of 5 MHz and diameter of 25 mm were used, with frequency spectra being monitored using an Agilent Technologies 8712ET network analyser over the range of 5.01–5.02 MHz. Resonance characteristics were measured at room temperature for crystal in air and in aqueous glycerol solutions with concentrations in the range of 0–90% per weight and fitted to a Butterworth–van-Dyke (BVD) model using Lab View 10.1. A brief description of the BVD model is available in [12].

2.2. Decoupling of the sensor response of the QCM

It is expected that a superhydrophobic QCM surface could efficiently decouple its sensor response [12, 24]. If this occurs, the crystal resonance spectra of the device should become relatively less sensitive to the viscous properties of the liquid. Thus both the resonance frequency decrease and bandwidth increase would be lower than that predicted by Kanazawa and Gordon. One example of using this physical property is the development of a SH QCM sensor device for examination of volatile organic compounds in aqueous mixtures [25]. Many strategies to create superhydrophobic surfaces have been put forward including wax solidification, lithography, vapour deposition, template methods, polymer reformation, sublimation, plasma, electro spinning, sol–gel processing, electrochemical methods, hydrothermal synthesis, layer-by-layer deposition and one pot reactions [26]. Each method has particular advantages and disadvantages e.g. multistep procedures and harsh conditions, requirement of specialized reagents and equipment, durability and robustness of coating or applicability only to small areas of flat surfaces or specific materials [27]. The method we developed, suitable for our intended application, was based on the incomplete combustion of carbon nanoparticles (CNPs) contained in a rapeseed oil mixture [28] or in candle soot [29] deposited on an epoxy coating layer. The method is facile and time-efficient and did not require specialized equipment, dangerous reagents or complex process control. In previous use of the soot approach, the main drawback is the fragility of the structure because the particle–particle interactions are only physical and weak. Therefore when a droplet of water rolls off the surface, the drop carries soot particles with it until almost all of the

soot deposit is removed and the drop undergoes a wetting transition. Increase in the structural robustness has previously been achieved by the development of a composite soot-polydimethylsiloxane (PDMS)-based layer [30]. However for our QCM application, PDMS, which belongs to the family of rubbery polymers [31], could complicate the QCM response reducing the quality of resonance and rigid response interpretation. Moreover, PDMS does not easily adhere to gold surfaces so an additional thin adhesive layer would be required. We therefore modified the superhydrophobic coating approach to use a soot-epoxy resin composite layer. The liquid epoxy resin is transparent, rigid and has good surface adhesion and low viscosity, which allows a spin coating deposition technique, and thus the opportunity to form very thin rigid layers. The fully cured epoxy resin is rigid so the QCM can be expected to have low damping and higher operational frequency compared to using PDMS.

2.2.1. Epoxy resin preparation and spin coating deposition.

MAS epoxy resin with slow hardener in a ratio 2 : 1 was mixed for 2 min. After mixing, the prepared solution with viscosity $\eta_e = 600$ cps was placed in a vacuum oven for 30 min to extract any air. The oven was set up to maintain a maximal pressure of 0.1 MPa and constant temperature of 21 °C. Then the quartz crystals were mounted one at the time in an Emhart spin coater and liquid epoxy resin was deposited by pipette onto their surfaces. The spin coating procedure was conducted with a spin velocity of 5000 rpm and spin duration of 50 s. The thickness of the layer achieved with these working parameters was $\sim(9 \pm 0.5)$ μm .

2.2.2. Fabrication of epoxy resin-soot composite SH QCM.

After spin coating deposition of the epoxy resin, the process parameters required to create a superhydrophobic crystal surface were determined. First a few soot-coated SH glass slides were prepared exposing them over a flame of a burning wick, immersed in rapeseed oil [28]. Then, to achieve uniform and homogeneous SH surfaces, the soot-coated glass slides were bound with the pre-cured epoxy coated quartz crystals [30]. Since the viscosity of the epoxy resin is highly temperature- and time-sensitive [32] it was very important to find the best pre-curing time prior to soot deposition that resulted in a non-engulfed, but attached, soot layer. It was found that the optimal pre-curing time in room temperature is 4 h and 20 min. For a complete and uniform transfer, an additional mechanical force is required by pressing a finger on the glass slides. Eventually the soot-coated glass samples were carefully peeled off from the epoxy resin coated QCMs and the quartz crystal patterns were held in room temperature conditions until full cure was reached. For the used resin the full curing time is approximately 11 h. The process was repeated for five from seven available QCMs. The other two QCMs, one with an uncoated surface and the other with an epoxy coated surface, were used as reference devices. After full cure of the epoxy resin-soot coated QCM we verified the wettability of surfaces using static contact angle (SCA) and contact angle hysteresis (CAH) measurements for droplets of water. These were found to be in the range of 151°–155° and

1°–3.7°, respectively, thereby confirming a superhydrophobic surface with mobile droplet behaviour [33].

2.3. Investigation and control of the wetting state transition of an SH QCM

When the superhydrophobic QCMs had been obtained, we investigated the triggering of the wetting state transition and its detection by variations in the resonance frequency response and/or the dissipation factor. During investigations the QCMs were placed in a quartz crystal holder and their sensing surface was fully immersed in a liquid of interest (water or aqueous ethanol solution). The holder had a liquid capacity of approximately 2 ml, therefore, the liquid volume used in each experimental setup was 2 ml. The first triggering mechanism used was based on surface tension changes using ethanol-water solutions with different concentrations. The MED, which is sometimes referred to as critical surface tension or % ethanol test, is widely applied to determine the level of water repellency for soils and other porous and granular patterns [34]. Drops of aqueous ethanol solutions with decreasing surface tension are placed onto different areas of the sample surface until a solution with sufficiently low surface tension is reached that just allows the drops to penetrate in. The % ethanol concentration at which the drops penetrate the porous surface is then taken to characterize the level of hydrophobicity of the surface. In our case we investigated the wettability of SH QCM with increasing concentrations of ethanol-water solutions. First a 5 MHz gold electrode quartz crystal with diameter of 25 mm and uncoated surface was used as a reference device with the aim of verifying the QCM's response in aqueous ethanol solutions. Its frequency spectra were monitored using an Agilent technologies 8712ET network analyser over the range of 5.018–5.020 MHz. The sensor response was measured at room temperature for QCM in air and in ethanol solutions in concentration range of 0–90% per weight and then fitted to a BVD model using Lab View 10.1. Subsequently, an SH quartz crystal was tested for lower concentration range of 0–12.5% per weight and again fitted to the BVD model. By analysing the resonance frequency shifts for both sets it was possible to assess whether the QCM is capable of detecting the wetting state transition.

Four further SH QCMs with resonance frequency of 5 MHz were used and their wettability was manipulated through electrowetting. An epoxy coated QCM was used as a reference device in order to evaluate whether the observed frequency shifts were caused by a wetting state transition or by e.g. change in the piezoelectric stiffness of the crystal. A 30 MHz synthesized function generator DS345 was connected via coaxial cable to the input of a voltage amplifier TREK PZD 700A and used to set up the input parameters of the signal. The output of the device was combined with two branches. The first one was a metal needle immersed in the liquid, in which the SH QCM was immersed, while the second (the ground electrode) was a connection with the surface electrode of the crystal, thus creating a droplet/dielectric/electrode capacitive structure. In this electrowetting investigation ac voltage at frequency 10 kHz was used. We initially measured the

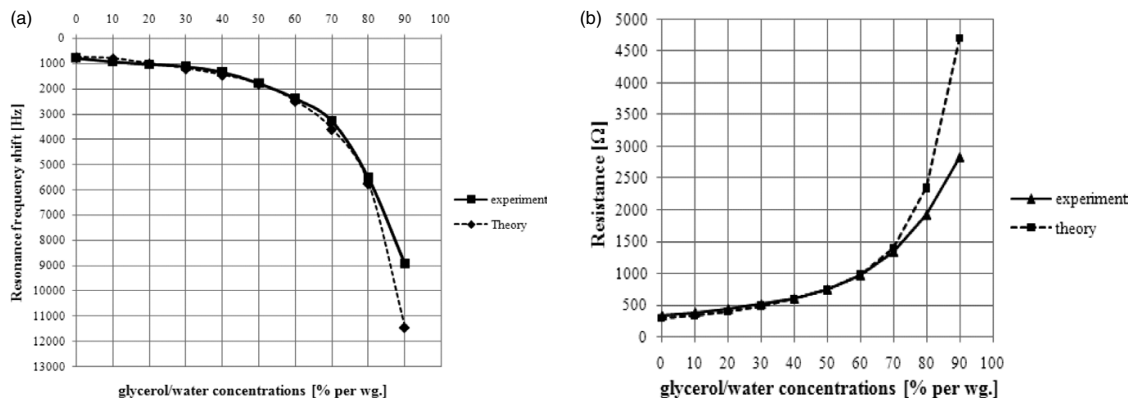


Figure 1. (a) Resonance frequency and (b) resistance of an uncoated QCM operating in glycerol/water solutions with different concentrations.

Table 1. Electrical characteristics in air of the QCM prior to and after deposition of epoxy–soot SH layer.

QCM No	QCM status	f_r (MHz)	BW (kHz)	Q factor	Insertion losses (dB)	R (Ω)
1	Prior to	5.028655	0.214	23500	-7.7	118
	After SH	4.953138	6.199	799	-0.77	1130
2	Prior to	5.022336	0.213	23500	-6.58	136
	After SH	4.942000	6.197	797	-0.72	1210
3	Prior to	5.019909	0.211	23800	-6.39	137
	After SH	4.946988	9.5	520	-0.54	1600
4	Prior to	5.025575	0.212	23700	-8.51	109
	After SH	4.935535	9.5	519	-0.55	1600
5	Prior to	5.028312	0.211	23800	-5.55	157
	After SH	4.964032	11.84	419	-0.425	2025

resonance frequency of the SH crystal in air. Then the crystal surface was fully immersed in water and the sensor response was measured again. After that an alternating voltage with step increases of 25 V was applied until a threshold voltage of 100 V was reached, at which a large frequency shift was observed. Subsequently, the voltage was increased with steps of 100 V until it reached the second threshold of 500 V. At this critical value a dielectric breakdown occurred and the experiment was terminated. After each voltage step, the crystal was disconnected from the amplifier and connected to an Agilent 8712ET network analyser. The resonance frequency was recorded and fitted to a BVD model. The experiment was repeated for the three further SH QCMs, but with an upper voltage applied not exceeding 400 V, thus avoiding the dielectric breakdown occurrence.

3. Results and discussions

3.1. Investigation of QCM resonance behaviour in air

Figures 1(a) and (b) illustrates the resonance frequency and the resistance shifts of an uncoated 5 MHz QCM against glycerol/water solutions with different concentrations. The dotted lines represent the theoretical values calculated by the Kanazawa and Gordon equation, while the solid lines are the values obtained by the experiment. The frequency and resistance shifts in the range of 0–70% follow the predictions of

Kanazawa and Gordon. A slight difference between theory and experiment is observed for concentrations over 70%, which is most likely due to the hygroscopic nature of glycerol, which tends to absorb water molecules from the ambient air and the fact measurements were performed in an open lab.

Table 1 reveals the electrical characteristics of five QCMs, operating in air at the same fundamental frequency of approximately 5 MHz, after the superhydrophobic coating was applied. The deposition of composite epoxy–soot SH layer on the crystal surface leads to a proportional frequency down shift in the range of 64–90 kHz (12 800–18 000 ppm), an increase in the bandwidth by an average value of 8.4 kHz and a corresponding increase in the insertion loss of 6.2 dB.

Figure 2 compares the resonance spectra behaviour of QCM with (a) uncoated, (b) epoxy coated and (c) superhydrophobic surface. For the case of an uncoated surface the quartz crystal operates at a fundamental frequency of approximately 5 MHz and supports a narrow bandwidth of 211 Hz. The deposition of an epoxy resin coating leads to a frequency downshift of 64 kHz and an increase in insertion loss to 3 dB, although the sensor still maintained a narrow bandwidth of 730 Hz; this increase in damping was likely to be caused by the rougher surface of the epoxy compared to the polished crystal surface. The superhydrophobic coating causes a more substantial increase in the level of insertion loss to 8 dB and increases the bandwidth to 6.19 kHz. This can be

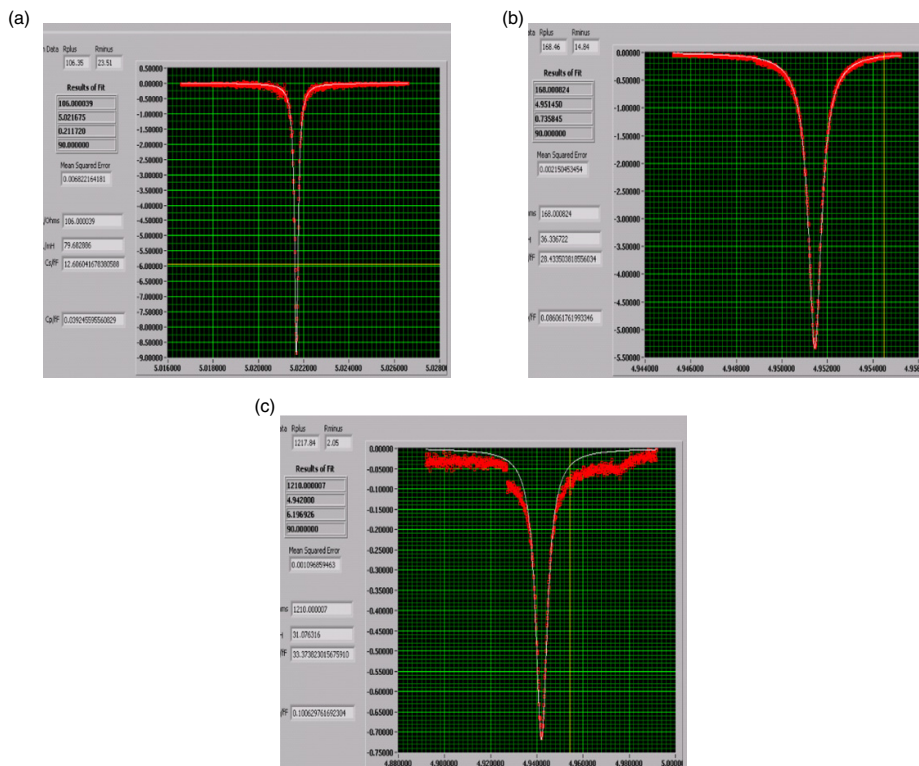


Figure 2. Resonance spectra of a 5 MHz QCM in air with (a) uncoated, (b) epoxy resin coated and (c) SH surface and their fits (white curves) achieved by the BVD fitting model.

interpreted as an additional dissipation of energy in air due to the high level of surface roughness [35].

All SH coated devices continued to operate with well-behaved single mode resonance and good sensitivity. The thickness of the epoxy coating was measured via profilometer Bruker AXS Dektak XT and compared to the value obtained by the theoretical calculation through Sauerbrey’s equation using an assumed density of the epoxy resin/hardener mixture, which is $\rho_{ep} = 1.0863 \text{ g cm}^{-3}$. The experimentally measured thickness was in the range of $9 \pm 0.5 \mu\text{m}$, while the theoretical calculations gave a thickness $d \sim 11 \mu\text{m}$.

3.2. Wetting state transition triggered using ethanol–water mixtures

Figure 3 shows the resonance frequency shifts of a 5 MHz gold electrode QCM with an uncoated surface versus different aqueous ethanol solutions, obtained by experiment and by theoretical calculation according to the Kanazawa and Gordon equation. The graphical dependence shows that the resonance frequency shifts achieved by experiment and theoretically calculated are in consistency with slight deviation of the experimental data set at some concentrations.

Since the experiments were performed in an open lab, there was a slight temperature deviation in the range of 20–26 °C, therefore the experimental data were corrected

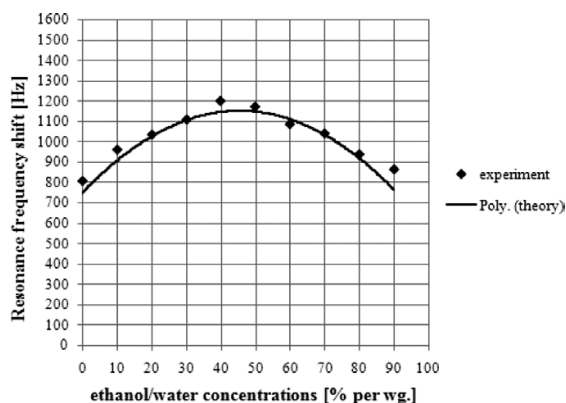


Figure 3. Experimental resonance frequency shift (dotted curve) of 5 MHz QCM with an uncoated surface and its theoretical second-order polynomial fit (solid curve) versus % ethanol concentrations in the range of 0–90% per weight.

with the pre-factor for the ethanol, which is $8.49 \times 10^{-11} \text{ cm}^3 \text{ s}^{-1}/\text{molecule}$. The resonance spectra of the first SH QCM was observed at % ethanol concentrations in the range of 0–12.5% per weight. For comparison, glass microscope slides were also coated with a superhydrophobic epoxy–soot layer and the contact angle variation of droplets with different ethanol concentrations was investigated. The

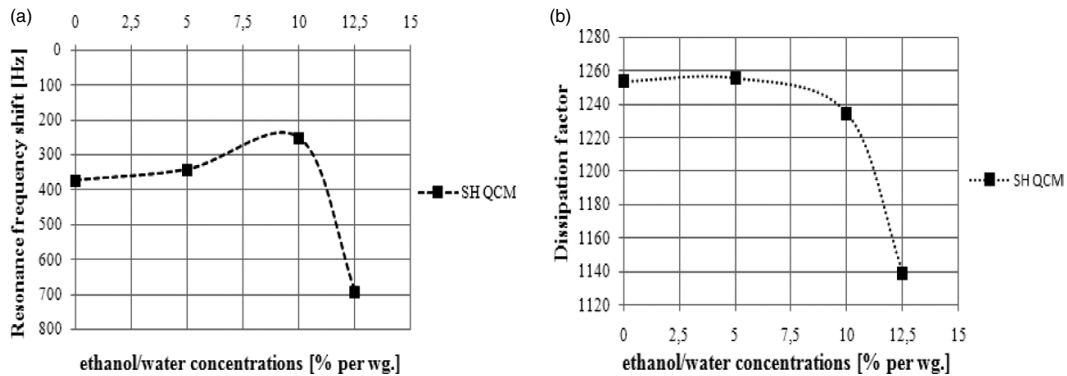


Figure 4. (a) Frequency response and (b) dissipation factor of the SH QCM for % ethanol concentrations in the range of 0–12.5% per weight.

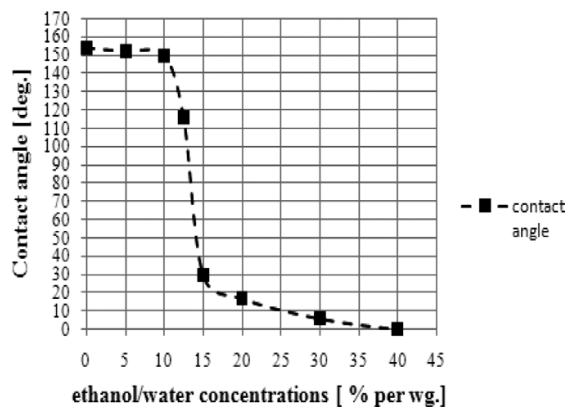


Figure 5. Contact angle variation of droplets of aqueous ethanol solutions on epoxy-soot coated surfaces with different concentrations.

results are summarized in figures 4 and 5. At concentrations between 0% and 10% the resonance frequency shifts are almost the same and 2.5 times lower compared to these obtained through the QCM with an uncoated surface (see experimental curve in figure 3). This effect can be attributed to the efficient decoupling of the sensor response achieved by the superhydrophobization of the crystal surface; the same tendency is reported in [12]. Also, the dissipation factor and the resonance frequency shifts keep approximately constant values in this range of concentrations. Further increase of the ethanol concentration leads to a large 700 Hz frequency downshift of the QCM at 12.5% concentration of ethanol accompanied by decrease in the dissipation factor at the same concentration. Contact angle measurements show that at this concentration of ethanol on epoxy-soot coated surfaces there is a large contact angle change from 155° to 116°, indicating this is critical concentration at which the surface undergoes a transition from the superhydrophobic Cassie-Baxter state to a more hydrophilic state.

The decrease in dissipation accompanying the decrease in frequency shift and the change to a hydrophilic state suggests the observed transition is not a simple Cassie-Baxter to Wenzel

wetting state transition. After removal from the ethanol solution the surface was observed to have a SCA to water of 116° and so was no longer superhydrophobic. Moreover, the crystal surface appeared to the eye to be a brighter black colour and a deposited droplet of water adhered to it, thus indicating a much higher CAH. Using a hydrophobic chemical treatment, an SCA of 152° could be recovered together with a low CAH of 1.3°. We further examined the quartz crystal surface using a scanning electron microscope (SEM). Figure 6 compares a surface exposed to the ethanol solution and an area of surface not exposed to the ethanol solution. The comparison shows that the peak features are more rounded after exposure to the ethanol. These results suggest that the application of aqueous ethanol solution with 12.5% concentration may cause both surface chemical and structural damage. Despite the apparent structural damage, SH of such surfaces could be recovered by applying a hydrophobic chemical treatment.

3.3. Wetting state transition triggered using electrowetting

To achieve a wetting state transition, which on drying the crystal could be reversed, we considered applying a voltage using an electrowetting configuration. The results of the electrical performance of these devices are summarized in table 2.

Table 2 shows the electrical characteristics of four SH QCMs during electrowetting presented as average data from eight independent electrowetting measurement cycles. It was found that the experimental data had good reproducibility from device to device and the frequency shift deviations were within 80 Hz (16 ppm). Figure 7 compares the resonance frequency shifts of (a) an SH quartz crystal with (b) that of an epoxy coated QCM. The inclusion of an epoxy coated QCM as a comparison device allows us to evaluate whether possible frequency shifts are caused by a transition in the wetting state or by changes, such as in the piezoelectric stiffness. For the SH QCM, a step change in frequency is observed between 75 and 100 V with little change in dissipation. Above this voltage the frequency decreased only slightly. Moreover, throughout the experiment the dissipation remained broadly constant at the initial value measured on immersion. This is

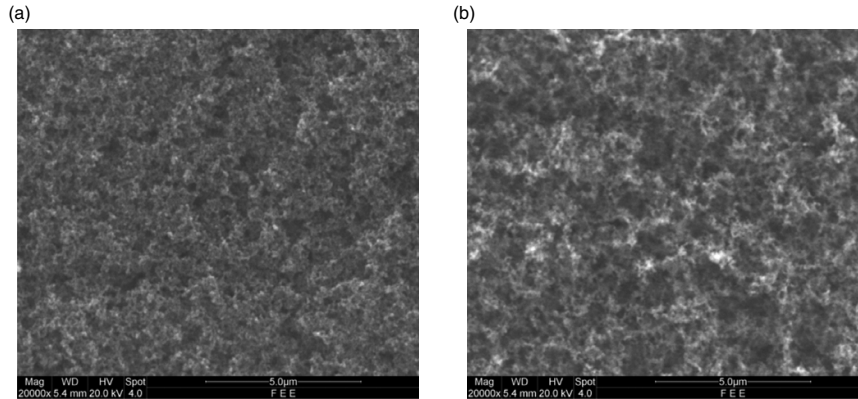


Figure 6. Scanning electron microscopy of (a) the affected and (b) unaffected area of the superhydrophobic QCM.

Table 2. Average electrical characteristics of four SH QCMs during electrowetting.

State of the QCM	Resonance frequency f_r (MHz)	Resistance R (Ω)	Bandwidth BW (kHz)	$\Delta f = f_{\text{air}} - f_{\text{rEW}}$ (Hz)	$D = \text{BW}/f_r$
QCM in air	4.952165	1424.4	8.29	0	1674×10^{-6}
QCM in water	4.951863	1523.9	8.47	302	1710×10^{-6}
QCM at 25 V	4.951845	1525.1	8.47	320	1710×10^{-6}
QCM at 50 V	4.951820	1529.3	8.46	345	1708×10^{-6}
QCM at 75 V	4.951807	1530.1	8.47	358	1710×10^{-6}
QCM at 100 V	4.951426	1542.4	8.48	739	1713×10^{-6}
QCM at 200 V	4.951425	1546.6	8.49	740	1715×10^{-6}
QCM at 300 V	4.951402	1547.6	8.48	763	1713×10^{-6}
QCM at 400 V	4.951387	1544.6	8.49	778	1715×10^{-6}

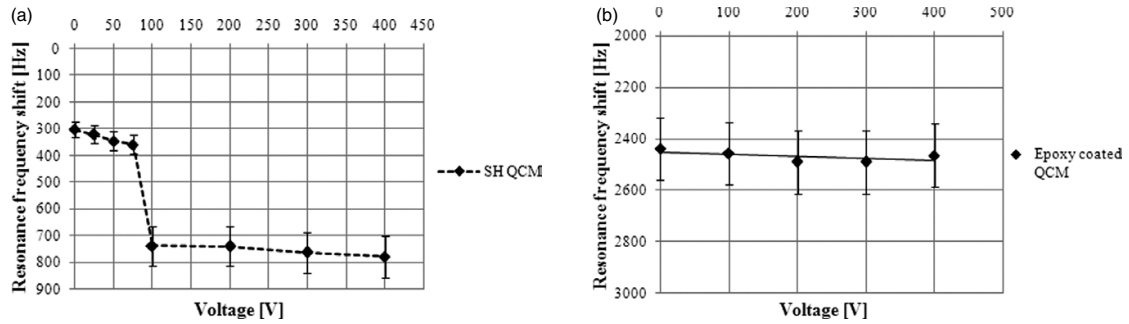


Figure 7. Resonance frequency downshift of (a) an SH and (b) epoxy coated QCM with its linear fit (solid curve).

contrary to the results reported in [36], where the change in the dynamical state of the film is accompanied by a change both in the resonance frequency and in the dissipation of the QCM. However, that work related to a change from sub-monolayer coverage towards monolayer coverage of a sliding film on a smooth crystal. In our case, liquid fully or partially penetrates between surface features on a length scale less than the shear wave penetration depth. It is therefore likely the penetrating liquid is locked with the surface motion and behaves acoustically in a manner more similar to rigid mass. In our measurements the epoxy layer suffered irreversible damage at a threshold voltage of 500 V. Interestingly, the initial

frequency downshift on immersion of the SH QCM in water is only 302 Hz and is 2.5 times lower than the case of a QCM with an uncoated surface (see figures 1(a) and 3). We also note that the epoxy coated crystal did not show any significant step changes or variations in the resonance frequency behaviour as voltage was increased; the shifts were within 56 Hz. One interpretation of the data is that the superhydrophobic coating decouples the QCM response compared to the uncoated and epoxy coated QCM and that a wetting state transition is detected at between 75 and 100 V.

To investigate the hypothesis of a wetting state transition, the droplet contact angle behaviour over the same range of

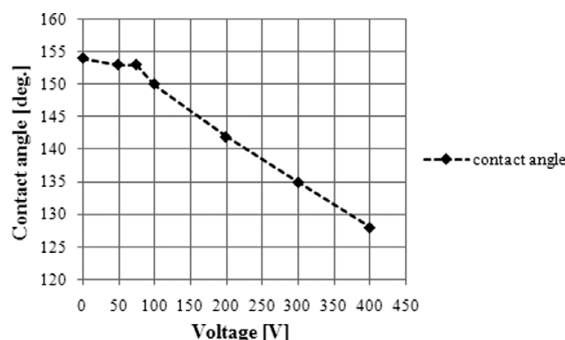


Figure 8. Contact angle variations of water droplet resting upon gold coated SH glass slide during electrowetting.

voltages was studied. The basic equation for droplet contact angle changes using electrowetting is

$$\cos \theta = \cos \theta_Y + \left(\frac{\epsilon_0 \epsilon_d}{2d\gamma_{LV}} \right) V^2, \quad (2)$$

where $\cos \theta_Y$ is the initial contact angle, ϵ_0 is the dielectric permittivity in vacuum, ϵ_d is the dielectric permittivity of the layer, d is its thickness, γ_{LV} is the interfacial energy between liquid and vapour (surface tension) and V is the applied voltage. This relation shows that, for a given dielectric layer, an applied voltage will reduce the contact angle causing improved wettability. We also know from previous studies that the associated electrocapillary pressure can cause a droplet in a suspended Cassie–Baxter state to collapse into a penetrating Wenzel state [21]. Figure 8 reveals the contact angle behaviour of a water droplet resting upon gold coated SH glass slide.

From 0 to 100 V there are no significant changes in the contact angle, but upon passing to 200 V a decrease in the contact angle is observed. Further voltage increase leads to further decrease in the contact angle and for 400 V the contact angle has reduced by 26°. Moreover, the CAH also increased and droplet mobility was observed to reduce. During the electrowetting an overall proportional frequency downshift of 778 Hz was observed when the voltage was increased from 0 to 400 V. Upon decreasing the voltage from 400 to 0 V the resonance frequency shift recovered to its initial value within a slight downward deviation of 157 Hz. This correlates well with the CAH, which appears to be 8° for the same range of voltages (154° prior to and 146° after applied voltage). A locally Cassie to Wenzel reversible switching of state using an electrowetting approach was reported in [22] and further modelled in [23]. In our experiments, we did not determine whether the acoustic changes related to a deformation of the meniscus or locally reversible transitions to the Wenzel state. Moreover, the surface structure is a relatively disordered one rather than, e.g. a regular pillar or cavity array, and so applicability of an electrohydrodynamic model such as in [23] is less clear. To check the chemical and surface structure had not been altered by electrowetting, crystals were dried after the QCM experiments and SCA and CAH measurements performed. Prior to and after electrowetting the SCA was in the range of 151°–155° and the CAH was 1°–3.7° (table 3).

Table 3. Contact angle of four SH QCMs prior to and after electrowetting.

QCM No	CA status	Static CA (°)	Advancing CA (°)	Receding CA (°)	CAH (°)
QCM.2	Prior to	152.4	156.7	153	3.7
	After EW	152.0	155.0	152.7	2.3
QCM.3	Prior to	155.2	150.3	149.3	1
	After EW	154.6	153.3	151.7	1.6
QCM.4	Prior to	152.4	153.0	150.8	2.2
	After EW	151.9	153.4	151.2	2.2
QCM.5	Prior to	150.8	156.2	153.4	2.8
	After EW	151.7	153.2	150.8	2.4

4. Conclusions

In this work we have presented results from systematic experimental investigation on the wetting state response of quartz crystals possessing a superhydrophobic soot–epoxy coating. Possible triggering of wetting state transitions using ethanol solutions and electrowetting has been developed. The first of these methods was found to cause surface changes, but the second method appeared to trigger a wetting state transition without surface damage. This wetting state transition appears to be observable as an electrowetting-induced frequency downshift of 778 Hz. The transition voltage is consistent with droplet contact angle decreases on similar surfaces. The step change in frequency was not accompanied by any significant change in the QCM dissipation. The proof-of-concept that an acoustic wave signal change, here a quartz crystal resonance frequency, can be observed when a superhydrophobic surface wetting state change is triggered, may provide an additional sensor mechanism to the usual mass or viscosity–density induced changes. The optimization of such superhydrophobic coated sensors may allow the development of a new acoustic wave based sensor with controllable wettability for detecting changes in hydrophobicity of surfaces.

Acknowledgments

The authors wish to gratefully acknowledge Dr Guillaume Zoppi and Mr Pietro Maiello from the University of Northumbria at Newcastle (UK) for the assistance with the laboratory equipment. KE also thanks the EU for financial support under its Erasmus Exchange programme.

References

- [1] Sauerbrey G Z 1959 *Physics* **155** 206–22
- [2] Nomura T and Okuhara M 1982 *Anal. Chim. Acta* **142** 281–4
- [3] Buttry D A 1991 *Electroanal. Chem.* **17** 1–58
- [4] Muratsugu M, Ohia F, Miya Y, Hosokawa T, Kurosawa S, Kamo N and Ikeda H 1993 *Anal. Chem.* **65** 2933–7
- [5] Kanazawa K K and Gordon J G 1985 *Anal. Chem.* **57** 1770–2
- [6] Bruckenstein S and Shay M 1985 *Electrochim. Acta* **30** 1295–300
- [7] Shirtcliffe N J, McHale G, Atherton S and Newton M I 2010 *Adv. Colloid Interface Sci.* **161** 124–38
- [8] Quere D, Lafuma A and Bico J 2003 *Nanotechnology* **14** 1109–12
- [9] Rathgen H and Mugele F 2010 *Faraday Discuss.* **146** 49–56

- [10] Tuberquia J C, Song W S and Jennings G K 2011 *Anal. Chem.* **83** 6184–90
- [11] Saad N *et al* 2012 *Int. Symp. on Ultrasound in the Control of Industrial Processes (UCIP 2012) IOP Conf. Ser.: Mater. Sci. Eng.* **42** 012052
- [12] Roach P, McHale G, Evans C R, Shirtcliffe N J and Newton M I 2007 *Langmuir* **23** 9823–30
- [13] Evans C R, McHale G and Shirtcliffe N J 2005 *Sensors Actuators A* **123–124** 73–6
- [14] Fujita M, Muramatsu H and Fujihira M 2005 *Japan. J. Appl. Phys. Part 1* **44** 6726–30
- [15] Kwoun S J, Lee R M, Cairncross R A, Shah P and Brinker C J 2006 *IEEE Trans. Ultrason. Ferroelectr. Freq. Control* **53** 1400–3
- [16] Thompson M, McHale G and Newton M I 2005 *Canadian Patent Application* CA2451413
- [17] Shirtcliffe N J, McHale G, Newton M I, Perry C C and Roach P 2005 *Chem. Commun.* **25** 3135–7
- [18] Shirtcliffe N J, McHale G, Newton M I, Perry C C and Roach P 2007 *Mater. Chem. Phys.* **103** 112–7
- [19] Verplanck N, Coffinier Y, Thomy V and Boukherroub R 2007 *Nanoscale Res. Lett.* **2** 577–96
- [20] Mugele F and Baret J C 2005 *J. Phys.: Condens. Matter* **17** R705
- [21] Herbertson D L, Evans C R, Shirtcliffe N J, McHale G and Newton M I 2006 *Sensors Actuators A* **130–131** 189–93
- [22] Manukyan G, Oh J M, Ende D, Lammertink R G H and Mugele F 2011 *Phys. Rev. Lett.* **106** 014501
- [23] Oh J M, Manukyan G, Ende D and Mugele F 2011 *Eur. Phys. Lett.* **93** 56001
- [24] McHale G, Roach P, Evans C R, Shirtcliffe N J, Elliot S J and Newton M I 2008 *IEEE Frequency Control Symp. (Honolulu, HI)* pp 698–704
- [25] Andreeva N, Ishizaki T, Baroch P and Saito N 2012 *Sensors Actuators B* **164** 15–21
- [26] Zhang X, Shi F, Niu J, Jiang Y and Wang Z 2008 *Mater. Chem.* **18** 621–33
- [27] Levkin P A, Svec F and Frechet J M 2009 *Adv. Funct. Mater.* **19** 1993–8
- [28] Qu M, He J and Cao B 2010 *Appl. Surf. Sci.* **257** 6–9
- [29] Deng X, Mammen L, Butt H J and Volmer D 2012 *Science* **335** 67–70
- [30] Yuan L *et al* 2011 *ACS Nano* **5** 4007–13
- [31] Lotters J C, Olthuis W, Veltink P H and Bergveld P 1997 *Micromech. Microeng.* **7** 145–7
- [32] Brostow W and Glass N M 2003 *Mater. Res. Innov.* **7** 125–32
- [33] Roach P, Shirtcliffe N J and Newton M I 2008 *Soft Matter* **4** 224–40
- [34] King P M 1981 *Aust. J. Soil Res.* **19** 275–85
- [35] Wu S, Shi L, Garfield L B, Tabor R F, Striolo A and Grady B P 2011 *Langmuir* **27** 6091–8
- [36] Bruschi L, Carlin A and Mistura G 2002 *Phys. Rev. Lett.* **88** 046105



<http://sciforum.net/conference/ecm-1>

Article

Snail Deterrent Properties of a Soot Based Flexible Superhydrophobic Surface

Nicasio R Gerald¹, Robert H Morris¹, Glen McHale² and Michael I Newton^{1*}

¹ Nottingham Trent University, School of Science and Technology, Clifton Lane, Nottingham NG11 8NS UK

² Northumbria University, Faculty of Engineering & Environment, Newcastle upon Tyne NE1 8ST, UK

* Author to whom correspondence should be addressed; E-Mail: michael.newton@ntu.ac.uk; Tel.: +44-115-848-3365; Fax: +44-115-848-6636.

Received: 7 March 2014 / Accepted: 17 May 2014 / Published: 26 May 2014

Abstract: Snails enjoying eating the leaves of many garden plants. Detering this pest without resorting to chemicals can present a significant challenge. A previous report (PLoS ONE 7(5): e36983) suggested that loose soot was a surface to which snails found adhesion difficult. Soot may also be embedded into a PDMS substrate making a flexible membrane with superhydrophobic properties (Appl. Phys. Lett. 102 (21) 214104). In this article we investigate whether the embedded soot has the same anti-adhesive properties to snails as the loose soot, so giving the possibility of a facile method for protecting crops from this pest. Data is presented showing the force required to remove snails from the soot/PDMS surfaces using a simple spinning technique. The receding contact angles have also been measured for various concentrations of an anionic surfactant on the soot/PDMS surface and compared to the data presented in the PLoS ONE article. In addition, simple time lapse video demonstrations are presented that show the reluctance of the snails to move over the soot based surfaces suggesting that the soot/PDMS structure does indeed provide a level of deterrence to this garden pest.

Keywords: superhydrophobic; snail; contact angle; anti-adhesive; soot;

1. Introduction

Snails move using a process called adhesive locomotion by producing a thin layer of mucus and using its non-linear properties to create a pedal wave. Adhesive locomotion is one of the most effective but energetically expensive methods of locomotion known in biology [1]. The snails have a single foot and the mucus acts both as an adhesive and in propulsion. Pedal mucus, which has 91% to 98% of its content as water, has mechanical properties dependent on how fast the material is deformed [2]. Recent work has used rheometers to assess the properties of snail mucus and attempted to find substances that mimic the same properties [3]. With such high water content, it may seem appropriate to consider the very water repellent properties of superhydrophobic surfaces [4] as possible repelling surfaces for snails. Superhydrophobicity occurs when a chemically hydrophobic surface also has high aspect ratio surface roughness or texture [5]. Using a range of commercially available superhydrophobic coating, Shirtcliffe et al [6] investigated the ability of such coatings to repel snails. One result that did not receive much comment in that article was the data showing that loose soot provided one of the most snail resistant surfaces; the durability of loose soot making it impractical as a snail deterrent. In this work we look at the snail deterrent properties of a novel type of superhydrophobic surface produced by embedding the soot from burning rapeseed oil in a PDMS substrate, thus making a flexible membrane with superhydrophobic properties; a type of surface which has recently been reported for use in Capillary Origami [7].

2. Results and Discussion

In figure 1 we show some simple tests that demonstrate the reluctance of snails to cross the soot/PDMS surfaces. Figure 1a shows a simple acrylic zigzag track bounded by soot/PDMS, mounted vertically with some snail food at the top. The figure shows a sequence of overlaid images taken as a snail ascends up the track. Figure 1b shows two polypropylene containers, one with a soot/PDMS coating and one without any coating, both with snail food on top. Snails were admitted to the enclosure and the containers were photographed again after 24 hours (figure 1c). None of the food on the soot/PDMS coated container was consumed after 24 hours, although eventually after 2 days one snail climbed the soot. These simple tests show that a soot/PDMS coating has deterrent properties to snails.

Shirtcliffe et al [6] used a technique to spin snails adhering to a horizontal surface to find the speed at which they were removed and from this calculated the force for removal using an average snail mass. Our spinning technique was identical however we also recorded the foot area for the young snails as they grew. This is shown in figure 2 and provides a strong linear relationship between footprint area and mass of snail. This enabled the removal force per unit area of footprint to be estimated for a range of surfaces and these are shown in figure 3. This may be a more informative measure than the simple 'g' value used by Shirtcliffe et al [6]. To allow comparison between the two data sets, we measured a number of standard surfaces that they also reported (glass, loose soot and acrylic). As with the Shirtcliffe et al data, the loose soot was found to require the least force to remove the snails (figure 3) closely followed by the unrinsed soot/PDMS surface and then the rinsed soot/PDMS, all being significantly better than the commercial products tested by Shirtcliffe et al [6].

Figure 1. (a) Overlaid images of a snail moving up a vertical track bounded by the PDMS/soot material. (b) Two pots, one polypropylene and one PDMS/soot coated, both with snail food on top. (c) The same pots 24 hours after snails were admitted to the enclosure showing only the food on the polypropylene has been eaten.

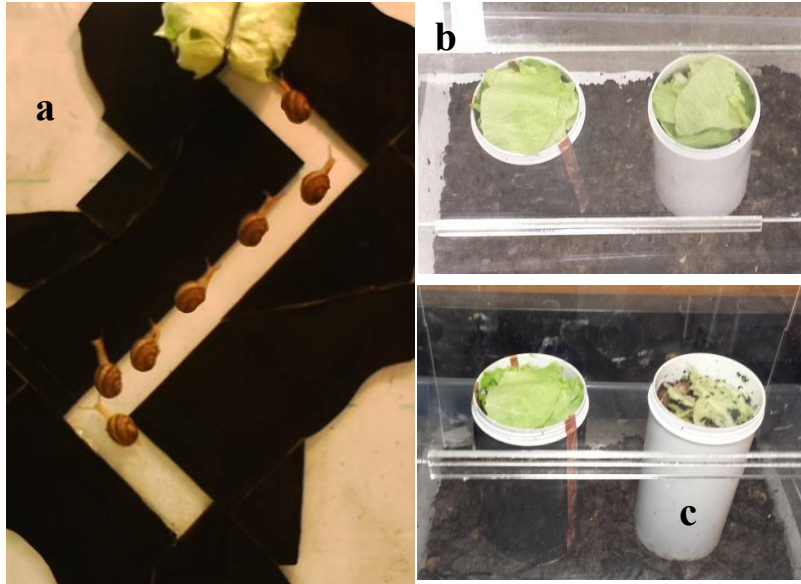
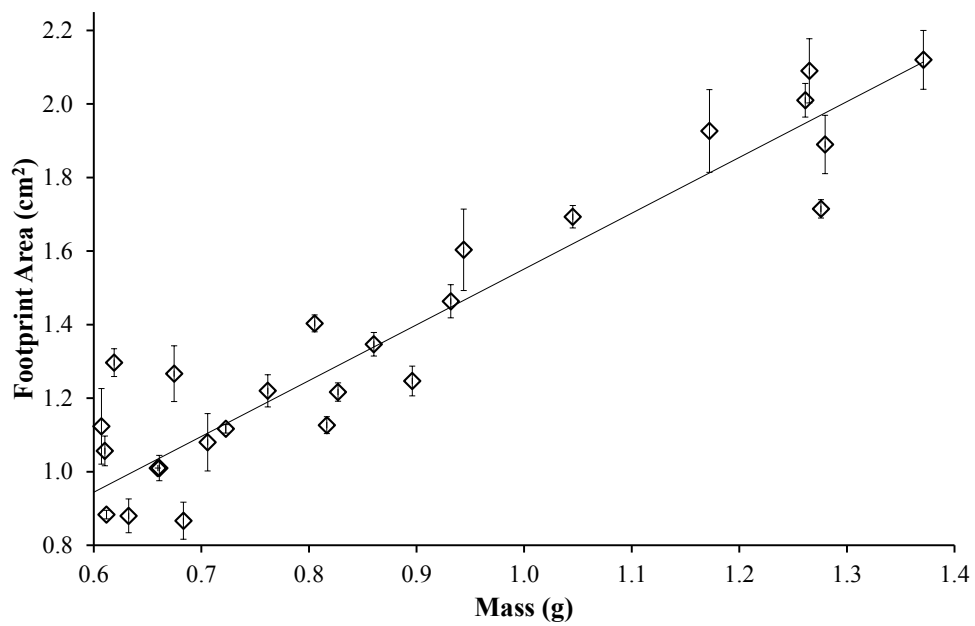


Figure 2. The footprint area for young *helix aspersa* as a function of body mass.



One hypothesis by Shirtcliffe et al for the effectiveness of snails to adhere to and traverse a wide range of surfaces was that the mucus included a weak bio surfactant that was able to reduce the receding contact angle and create high contact angle hysteresis. The implication of this hypothesis is that a snail resistant superhydrophobic surface should be one that is able to maintain a high receding contact angle even when challenged by an appropriate surfactant. To characterise the wettability of the various surfaces, the receding contact angles various concentration of the anionic surfactant sodium dodecyl sulfate (SDS) were measured and the results are shown in figure 4. The most snail repellent material tested by Shirtcliffe et al (HIREC) is included in figure 4 and showed a high receding contact angle for low surfactant concentrations. However, as the surface tension of the SDS solution was reduced to below 68mN/m a transition occurred to a low receding contact angle. Soot/PDMS retains the high receding contact angle all the way down to an SDS solution surface tension of 48 mN/m before such a transition. This transition is consistent with the liquid entering the roughness of the superhydrophobic surface, which given the 10's nm length scales of the roughness for the soot surface can be expected to require higher concentrations of surfactant [8, 9].

3. Experimental Section

The soot/PDMS surfaces were produced in a similar method to previously described [8]. Rapeseed oil was left burning several minutes, using a wick, until a stable flame developed. Copper sheets were then placed at the top of a chimney, with a fan used to draw the soot up the chimney, until the entire surface of the copper was coated with a thick layer of matt black rapeseed oil soot. PDMS was mixed in a 10:1 ratio and degassed in a vacuum desiccator to remove any air bubbles trapped in the mixture. After approximately 30 minutes of degassing the PDMS was spread onto acrylic slides to the required thickness of 1mm. A prebake time of 30-35 minutes was used at 80°C until the PDMS became tacky. The soot coated slides were gently positioned, soot side down, onto the PDMS and a mass placed on top to ensure contact across the whole surface. These were then returned to an oven at 60°C for at least an hour. After cooling the acrylic slides and copper sheets were carefully removed from the PDMS surface leaving a PDMS membrane with a nanoparticle coating. Excess soot was then removed under running water in most samples although some were spin tested with the loose soot attached as shown in figure 3.

A zigzag track was produced on an acrylic sheet using sections of the soot/PDMS to mark the borders. Young snails, *helix aspersa* (obtained from H & RH Escargots Kent UK) were placed at the bottom of the vertically mounted track and filmed with a video camera. A polypropylene container was covered by the soot/PDMS material and placed with an identical but uncoated container in an enclosure with fresh lettuce on top of each; these were also filmed over a period of 24 hours.

The snail centrifuge was a modified spin coated (Electronic Micro Systems Ltd. Salisbury UK) with a dc power supply used to power the motor and a tachometer used to measure the speed. A snail was placed 50mm from the center and the speed slowly increased until the snail was removed. This process was repeated for several snails on each of the different surfaces tested. Advancing and receding contact angles of sodium dodecyl sulfate (>99% Aldrich) in deionized water were measured using a Krüss DSA10 contact angle meter.

Figure 3. The removal force calculated from the spin speed at which the snails detached from a rotating horizontal disc, the snail mass and data from figure 2 for the footprint area for the different surfaces tested.

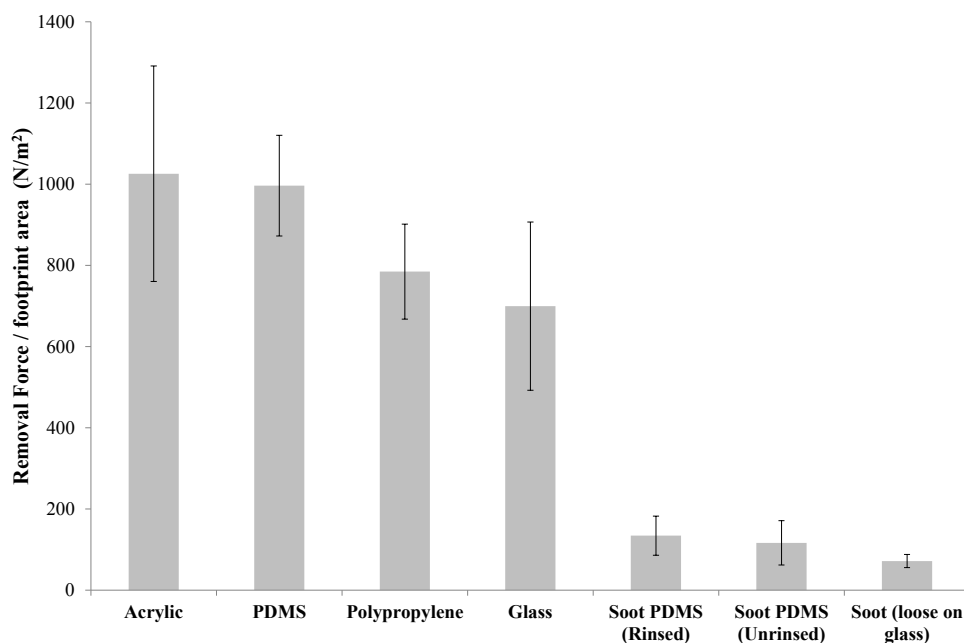
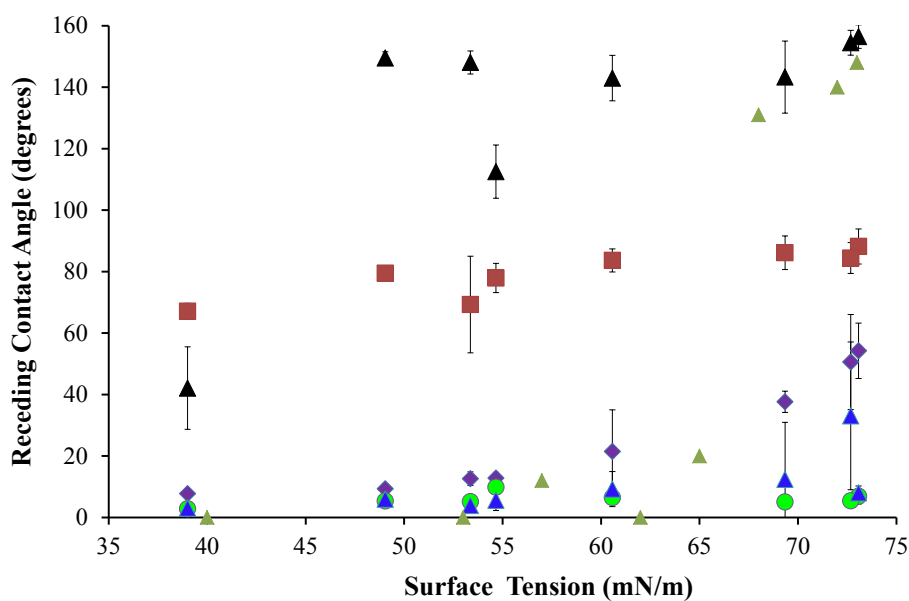


Figure 4. The receding contact angle of sodium dodecyl sulfate (SDS) solutions on PDMS/soot (black triangles), PDMS (red squares), polypropylene (blue triangles), Acrylic (purple diamonds), glass (green circles) and HIREC data from reference [6] (green triangles).



4. Conclusions

Soot/PDMS flexible membrane surfaces can be constructed and that they show excellent anti-adhesive properties. Moreover, they also perform particularly well in resisting the ability of the anionic surfactant SDS to reduce the receding contact angle. This supports the hypothesis that an effective anti-adhesive snail resistant superhydrophobic surface is one that can maintain a high receding contact angle when challenged by an anionic surfactant, such as SDS.

Acknowledgments

NRG acknowledges Nottingham Trent University for provision of a PhD bursary.

Conflicts of Interest

The authors declare no conflict of interest.

References and Notes

1. Denny, M.W. The role of gastropod pedal mucus in locomotion. *Nature* **1980**, *285*, 160–161
2. Denny, M.W. Mechanical Properties of Pedal Mucus and Their Consequences for Gastropod Structure and Performance. *American Zoologist* **1984**, *24*, 23–36.
3. Ewoldt, R.H.; Clasen, C.; Hosoi, A.E.; McKinley, G.H. Rheological fingerprinting of gastropod pedal mucus and synthetic complex fluids for biomimicking adhesive locomotion. *Soft Matter* **2007**, *3*, 634–643
4. Roach, P.; Shirtcliffe, N.J.; Newton, M.I. Progress in superhydrophobic surface development. *Soft Matter* **2008**, *4*, 224–240
5. Shirtcliffe, N.J.; Atherton, S.; Newton, M.I.; McHale, G. An Introduction to Superhydrophobicity. *Advances in Colloid and Interface Science* **2010**, *161*, 124–138
6. Shirtcliffe, N.J.; McHale, G.; Newton, M.I. Wet Adhesion and Adhesive Locomotion of Snails on Anti-Adhesive Non-Wetting Surfaces *PLOS ONE* **2012**, *7*, e36983
7. Geraldi, N.R.; Ouali, F.F.; Morris, R.H.; McHale, G.; Newton, M.I. Capillary origami and superhydrophobic membrane surfaces. *Applied Physics Letters* **2013**, *102*, 214104
8. Mohammadi, R.; Wassink, J.; Amirfazli, A. Effect of Surfactants on wetting of superhydrophobic surfaces. *Langmuir* **2004**, *20*, 9657–9662
9. Ferrari, M.; Ravera, F. Surfactants and wetting at superhydrophobic surfaces: Water solutions and non aqueous liquids. *Advances in Colloid and Interface Science* **2010**, *161*, 22–28

© 2014 by the authors; licensee MDPI, Basel, Switzerland. This article is an open access article distributed under the terms and conditions of the Creative Commons Attribution license (<http://creativecommons.org/licenses/by/3.0/>).